

**Beyond the first Generation:  
Extending the Science Range of the  
Gravitational Wave Detector GEO 600.**

Von der Fakultät für Mathematik und Physik  
der Gottfried Wilhelm Leibniz Universität Hannover  
zur Erlangung des Grades

**Doktor der Naturwissenschaften**  
– Dr. rer. nat. –

genehmigte Dissertation von

**Dipl.-Phys. Stefan Hild**

geboren am 1. April 1978 in Celle.

2007

Referent: Prof. K Danzmann  
Korreferent: Prof. R Schnabel  
Tag der Promotion: 2. Februar 2007

## Summary

During recent years, the first generation of large-scale laser-interferometric gravitational wave (GW) detectors has been commissioned and is now in operation. This worldwide network of gravitational wave observatories collects the most GW-sensitive data to date.

The gravitational wave detector GEO 600 near Hannover, is the first large-scale instrument already now using second generation technology, such as electro-static actuators and signal recycling. The use of signal recycling allows to improve the sensitivity but at the cost of a significantly more complex detector. A new method was developed that allowed, for the first time, the realization of tuned signal recycling in a large interferometer. In Chapter 2 a comparison of tuned and detuned signal recycling operation is given and related problems are discussed. It is found that the combination of heterodyne readout and detuned signal recycling is unfavourable in many respects. This supports the decisions to operate the LCGT detector with tuned signal recycling, and advanced LIGO in detuned signal recycling, but with a homodyne readout. The concept of detuned signal recycling with a DC-readout scheme might actually also have advantages for GEO 600 as described in Chapter 6.

One of the main noise sources encountered during the commissioning of 1st generation detectors is stray light. The actual sensitivity of GEO 600 can already be degraded by stray light contributions of the order  $10^{-20}$  W. Since second generation GW detectors will operate with significantly higher light powers, and aim for increased sensitivities, stray light could be even more problematic. Chapter 3 describes the experience that was gained by studying stray light in GEO 600. A guide is given to help avoid, identify and eliminate stray light noise.

GEO 600 is not only an excellent test facility for second generation technologies, but also provides sensitive data with a high duty cycle. Currently a peak strain sensitivity of  $2.5 \cdot 10^{-22}/\sqrt{\text{Hz}}$  is achieved. In order to allow the data from GEO 600 to be used for multi-detector analysis, a high calibration accuracy is required. In an attempt to validate the official calibration routines, photon pressure calibrators are used in GEO 600 and LIGO. As shown in Chapter 4, several problems have been encountered during the commissioning of the GEO photon pressure calibrator. In particular, at frequencies above 1 kHz, a large discrepancy between the official calibration and that derived from the photon pressure calibrator was observed. This can be explained by photon pressure induced test mass deformation.

In Chapter 5 a new statistical veto method is presented employing an amplitude consistency check. This technique allows the derivation of safe statistical vetoes from interferometer channels which can contain traces of GW signal. This veto was applied to S5 data of the GEO 600 detector and was found to give veto efficiencies between 5 % and 20 % and a use-percentage of up to 80 %. This new veto method can easily be applied to the data from other GW detectors.

**Key words:** *Gravitational wave detector, signal recycling, stray light, photon pressure calibrator, statistical veto, DC-readout*





## Zusammenfassung

Die großen laser-interferometrischen Gravitationswellendetektoren (GWD) der ersten Generation haben ihren Betrieb aufgenommen und bilden ein weltweites Netzwerk von Gravitationswellen-Observatorien. Die aufgenommenen Daten haben die beste Empfindlichkeit, die bisher erreicht wurde.

Der Gravitationswellendetektor GEO 600 bei Hannover ist das erste große Instrument, das bereits jetzt Technologien der zweiten Generation einsetzt, wie z.B. elektrostatische Aktuatoren oder Signal-Recycling (SR). Der Gebrauch von SR erhöht die Empfindlichkeit des Interferometers, steigert aber gleichzeitig auch die Komplexität des Systems. Eine neue Methode wurde entwickelt, mit der es erstmals möglich ist, tuned SR in einem großen Interferometer zu realisieren. In Kapitel 2 werden detuned und tuned SR verglichen und die damit verbundenen Probleme diskutiert. Es zeigt sich, dass eine Kombination aus Heterodyndetektion und detuned SR in mehrfacher Hinsicht unvorteilhaft ist. Dies bestätigt die Entscheidung, LCGT im tuned SR modus und Advanced LIGO mit einer Homodyndetektion zu betreiben. Die Konfiguration, detuned SR mit Homodyndetektion, kann auch für GEO 600 von Vorteil sein (siehe Kapitel 6).

Eine der Hauptrauschquellen der GWD der ersten Generation stellt Streulicht dar. Die Empfindlichkeit von GEO 600 kann schon von Streulichtbeiträgen in der Größenordnung von  $10^{-20}$  W limitiert werden. Da die Detektoren der zweiten Generation mit deutlich größeren Lichtleistungen und gleichzeitig besserer Empfindlichkeit betrieben werden, kann die Streulichtproblematik in Zukunft sogar noch verstärkt auftreten. Kapitel 3 beschreibt die Erfahrungen, die in GEO 600 mit Streulicht gemacht wurden. Es werden Methoden beschrieben, wie Streulicht gefunden und eliminiert, bzw. vermieden werden kann.

Mit GEO 600 können nicht nur Technologien der zweiten Generation hervorragend getestet werden, sondern GEO 600 nimmt auch Daten mit hoher Empfindlichkeit und großem Dutycycle auf. Aktuell wird eine Empfindlichkeit von  $2.5 \cdot 10^{-22}/\sqrt{\text{Hz}}$  erreicht. Damit GEO-Daten für Multi-Detektor-Analysen eingesetzt werden können, ist eine hohe Kalibrationsgenauigkeit erforderlich. GEO 600 und LIGO versuchen, Strahlungsdruckkalibratoren zu entwickeln, um die offiziellen Kalibrationen zu überprüfen. Wie in Kapitel 4 dargestellt wird, treten dabei aber mehrere Probleme auf. Besonders bei Frequenzen oberhalb von 1 kHz wird eine große Abweichung der Strahlungsdruckkalibration von der offiziellen Kalibration gefunden, die durch eine vom Strahlungsdruck induzierte Verformung der Testmasse erklärt werden kann.

In Kapitel 5 wird eine neue Methode zur Gewinnung statistischer Vetos beschrieben, die einen Amplitudenschwellwert benutzt. Diese Technik erlaubt das Erstellen von zuverlässigen Vetos auch aus Interferometerkanälen, die Spuren von Gravitationswellensignalen enthalten können. Die Vetomethode wurde auf Daten vom GEO-Detektor mehrfach angewendet und hat sich als leistungstark erwiesen.

**Schlüsselwörter:** *Gravitationswellendetektor, Signal-Recycling, Streulicht, Strahlungsdruckkalibrator, Statistisches Veto, Homodyndetektion*



# Contents

<b>Summary</b>	<b>i</b>
<b>Zusammenfassung</b>	<b>iii</b>
<b>Table of Contents</b>	<b>v</b>
<b>List of Figures</b>	<b>ix</b>
<b>List of Tables</b>	<b>xv</b>
<b>Abbreviations and Symbols</b>	<b>xvii</b>
<b>1. Introduction</b>	<b>1</b>
1.1. Detection of Gravitational waves . . . . .	1
1.2. A world wide network of large-scale gravitational wave detectors . . . .	3
1.3. A brief description of the GEO 600 GW detector . . . . .	3
<b>2. Demonstration and comparison of tuned and detuned signal recycling</b>	<b>7</b>
2.1. Introduction . . . . .	7
2.2. Control scheme for signal recycling in GEO 600 . . . . .	11
2.3. A new method for locking tuned signal recycling . . . . .	15
2.3.1. Simulation of the control parameters for tuned signal recycling .	16
2.3.2. Calibration of the actuator strength . . . . .	18
2.4. Measurements of optical gain . . . . .	18
2.5. Reduction of the RF amplitude modulation . . . . .	21
2.6. Comparison of noise transfer functions for tuned and detuned signal re- cycling . . . . .	21
2.7. Calibrated detector sensitivity for tuned signal recycling . . . . .	24

2.8. Comparison of detuned signal recycling for upper and lower operating point	25
2.9. Summary . . . . .	29
<b>3. Scattered light problems in interferometric gravitational wave detectors</b>	<b>31</b>
3.1. Introduction . . . . .	31
3.2. Controlled stray light injections . . . . .	33
3.2.1. How to produce stray light sowing up in $H$ at 1 kHz . . . . .	33
3.2.2. A device for controlled stray light generation . . . . .	34
3.2.3. Low frequency large amplitude scenario . . . . .	37
3.2.4. High frequency low amplitude scenario . . . . .	37
3.2.5. Combination of the two scenarios . . . . .	38
3.2.6. Summary of the stray light injections . . . . .	39
3.3. Indications for a stray light limited sensitivity . . . . .	39
3.4. The filter experiment: A reliable method to identify the source of stray light . . . . .	43
3.4.1. Limitations of the filter experiment . . . . .	45
3.5. Experience of stray light problems in GEO . . . . .	46
3.6. The cat's eye effect . . . . .	49
3.7. A special class of stray light noise: the "ripples" . . . . .	52
3.8. Summary . . . . .	56
<b>4. Photon pressure calibration</b>	<b>59</b>
4.1. Introduction . . . . .	59
4.2. Experimental setup of the photon pressure calibrator . . . . .	60
4.2.1. Measurement of the modulated light power . . . . .	62
4.3. Injections with different amplitudes . . . . .	64
4.4. Injections with different frequencies . . . . .	66
4.5. Validation of the official calibration . . . . .	69
4.5.1. Transfer function from ESD to $H$ . . . . .	70
4.5.2. ESD injections up to high frequencies . . . . .	70
4.6. The phase picture . . . . .	73
4.7. Non-rigidity of the test mass . . . . .	74
4.7.1. Rough estimation of photon pressure calibrator induced test mass deformation . . . . .	75

4.7.2. Finite element analysis of photon pressure calibrator induced test mass deformation . . . . .	76
4.7.3. Effective test mass displacement . . . . .	76
4.7.4. Comparison of pendulum response and mirror deformation . . .	79
4.7.5. High frequency injections using the photon pressure calibrator .	81
4.7.6. Influence of beam jitter to the photon pressure calibration . . . .	83
4.7.7. Conclusion and consequences . . . . .	85
4.8. Effects from test mass rotation . . . . .	86
4.8.1. Method to determine the off centering of the photon pressure calibrator . . . . .	90
4.9. Determining the sign of $H$ . . . . .	91
4.10. Summary . . . . .	94
<b>5. A statistical veto method employing an amplitude consistency check</b>	<b>95</b>
5.1. Introduction . . . . .	95
5.2. Motivation for a standard statistical veto for GEO 600: Hourly mains glitches . . . . .	97
5.3. Motivation for a statistical veto with amplitude consistency check: Dust falling through laser beams . . . . .	101
5.4. Description of the event trigger generator used: mHACR . . . . .	104
5.4.1. Estimation of burst parameter with mHACR . . . . .	105
5.5. The standard statistical veto . . . . .	107
5.5.1. The method in general . . . . .	107
5.5.2. Application of a standard statistical veto to GEO S5 data . . . .	109
5.6. A statistical veto for channels containing GW information . . . . .	112
5.6.1. The method in general . . . . .	113
5.6.2. A ‘real-world’ scenario . . . . .	114
5.7. Application of a statistical veto with a amplitude consistency-check to GEO 600 data . . . . .	114
5.7.1. Data set 1: Full September 2006 with low dust concentration . .	116
5.7.2. Data set 2: 8 hours from May 2006 with high dust concentration	120
5.7.3. Performance of the veto analysis . . . . .	120
5.8. Summary . . . . .	122
<b>6. Towards DC-readout for GEO 600</b>	<b>123</b>

6.1. Introduction . . . . .	123
6.2. Motivation . . . . .	125
6.2.1. Shot noise . . . . .	127
6.2.2. Oscillator phase noise . . . . .	128
6.2.3. Electronic noise of the main photo diode . . . . .	128
6.3. Determination of the optimal dark fringe offset . . . . .	128
6.4. Technical realization . . . . .	133
6.5. Summary and outlook . . . . .	135
<b>A. The suspended output telescope of GEO 600</b>	<b>137</b>
<b>B. Light fields at the output port for detuned signal recycling</b>	<b>143</b>
<b>C. Design for an AR coated window for quadrant diodes</b>	<b>147</b>
<b>D. Optical layout of GEO 600</b>	<b>149</b>
<b>E. Matlab script: Photon pressure calibration</b>	<b>151</b>
<b>F. A gravity calibrator for GEO 600</b>	<b>159</b>
<b>G. Matlab script: Statistical veto with amplitude consistency-check</b>	<b>163</b>
<b>H. FINESSE input file of GEO 600 for DC-readout</b>	<b>169</b>
<b>I. Measurement of the bulk-absorption of the GEO 600 beam splitter</b>	<b>177</b>
I.1. Introduction . . . . .	177
I.2. A new method for measuring bulk absorption . . . . .	178
I.3. Setting an upper limit for the bulk absorption in the GEO 600 beam splitter	182
I.4. Conclusion . . . . .	183
<b>Bibliography</b>	<b>185</b>
<b>Acknowledgement</b>	<b>193</b>
<b>Curriculum vitae</b>	<b>195</b>
<b>Publications</b>	<b>197</b>

# List of Figures

1.1. Sensitivities of the large-scale GW detectors . . . . .	2
1.2. Simplified optical layout of GEO 600. . . . .	4
1.3. Sensitivity improvement of GEO 600 over the last few years. . . . .	5
2.1. Shot noise limit of GEO 600 for different transmittances of the signal recycling mirror. . . . .	8
2.2. Shot noise limit of GEO 600 for different tunings of the signal recycling cavity. . . . .	9
2.3. Sideband picture for tuned and detuned SR . . . . .	10
2.4. Simplified control scheme for two longitudinal degrees of freedom of GEO 600	12
2.5. Signal recycling error signals versus microscopic position of MSR for various modulation frequencies . . . . .	14
2.6. Simulations of longitudinal error signals for MI and SR loop for detuned and tuned SR . . . . .	17
2.7. Simplified diagram of the loop controlling the differential arm length of the Michelson . . . . .	19
2.8. Measurement of the optical gains for tuned and detuned signal recycling for the two orthogonal quadratures P and Q. For the tuned case the demodulation phase was not optimized. Therefore the the differential armlength signal is still clearly present in the optical gain of the Q-signal.	20
2.9. Measurements of the transfer functions from oscillator phase noise (OPN) and oscillator amplitude noise (OAN) to the error signal of the differential arm length servo . . . . .	22
2.10. Measurements of the transfer functions from laser frequency noise and laser power noise to the error signal of the differential arm length servo	23

2.11. Comparison of the sensitivity of GEO 600 for tuned and detuned signal recycling operation . . . . .	26
2.12. Comparison of the sensitivity of GEO 600 for two different operating points of detuned signal recycling . . . . .	28
3.1. Stray light shoulders showing up in various interferometer configurations.	32
3.2. Controlled forced scattering: driving the stray light source with 1 Hz and amplitudes in the millimeter range. . . . .	35
3.3. Controlled forced scattering: driving the stray light source with 810 Hz and an amplitude of less than an laser wavelength. . . . .	36
3.4. Controlled forced scattered light generation for a medium frequency and amplitude . . . . .	38
3.5. Spectrograms of the detector sensitivity for enhanced scattering and no scattering. . . . .	40
3.6. Spectra of the detector sensitivity for times of clean data and times of enhanced scattering. . . . .	41
3.7. Time series of the mean ASD in the band from 904 to 1005 Hz of the uncalibrated detector sensitivity with and without enhanced scattering.	42
3.8. Sketch of the filter experiment . . . . .	44
3.9. Progression of the optical layout of the signal recycling bench in order to reduce stray light. . . . .	47
3.10. Sensitivity progress of GEO 600 from autumn 2004 . . . . .	48
3.11. Schematic of the cat's eye effect . . . . .	50
3.12. Spectrum of the ripple noise . . . . .	52
3.13. Spectrograms of $H$ and the seismometer in the north end station for a time when the $n*45$ Hz ripple noise is present. . . . .	54
3.14. Slight frequency drift of the $n*45$ Hz ripple noise seen in $H$ and the north seismometer. . . . .	55
4.1. Response function of the lowest stage of a GEO 600 main pendulum. . .	61
4.2. OPTOCAD layout of the optics in the north end station of the GEO 600 detector, including the setup of the photon pressure calibrator. . . . .	63
4.3. photon pressure calibrator injections with different amplitudes. . . . .	65
4.4. Photon pressure calibrator injections for various frequencies. . . . .	67
4.5. Ratio and phase of official and photon pressure calibration. . . . .	68



4.6. Transfer function ESD to $H$ . . . . .	71
4.7. Measurement of the relative calibration accuracy of the official calibration for high frequencies . . . . .	72
4.8. Calibration discrepancy: The phase picture. . . . .	73
4.9. Finite element model (FEM) of the deformation of a GEO test mass caused by a the beam of the photon pressure calibrator. . . . .	77
4.10. Overlap of photon pressure calibrator induced test mass deformation and the main interferometer beam. . . . .	78
4.11. Radial contribution to the effective displacement for photon pressure cal- ibrator induced test mass deformation. . . . .	78
4.12. Simple model for the photon pressure calibrator taking into account the responses from the pendulum and from the mirror deformation effect. .	80
4.13. Measurement of the photon pressure calibrator response at high frequencies.	82
4.14. Effective displacement for different spatial overlaps of the beams from photon pressure calibrator and the main interferometer. . . . .	84
4.15. Effective longitudinal mirror displacement from mirror rotation . . . . .	87
4.16. Phase picture for photon pressure calibrator induced test mass rotation.	88
4.17. Magnitude of the transfer function from PCALmon to $H$ versus the po- sition of the main interferometer beam at MFn. . . . .	90
4.18. Time series of the photon pressure calibrator signal (PCALmon) . . . . .	92
4.19. Transfer function from photon pressure calibrator monitor diode (PCAL- mon) to $H$ . . . . .	93
5.1. Time series of the ripple control signals. . . . .	97
5.2. Spectra of the ripples control signals. . . . .	98
5.3. Time coincidence analysis for the GW channel and the mains monitor. .	100
5.4. Time coincidence analysis for the GW channel ( $H$ ) and $\mathcal{P}_{DC}$ for times of high and low dust concentration at the GEO output bench. . . . .	102
5.5. Coherence between $\mathcal{P}_{DC}$ and sinusoidal differential arm length injections	103
5.6. Schematic of mHACR pipeline . . . . .	106
5.7. Exemplary application of a statistical veto to a 24 hour stretch of GEO data using a GW-free channel as veto channel. . . . .	110
5.8. Exemplary application of a statistical veto including an additional coin- cidence condition for the central frequency of the events. . . . .	111

5.9. A schematic view of two different scenarios in which coincident transient events can appear in both the main GW channel, $H$ , and an auxilliary channel, $X$ . . . . .	112
5.10. Efficiency, background and significance of a veto using $\mathcal{P}_{\text{DC}}$ as veto channel for various sizes of the time and frequency coincidence window. . . . .	115
5.11. Standard deviation of the distribution of the mHACR errors plotted as a function of the snr of the triggers. . . . .	117
5.12. Application of a statistical veto with a amplitude consistency check to GEO 600 data for the entire month of September 2006. . . . .	118
5.13. The application of a statistical veto with a amplitude consistency check to 8 hours of GEO data from May . . . . .	119
5.14. Schematic of the veto pipeline used for the analysis of Data Set 1 (full September 2006). . . . .	121
6.1. Operating points for heterodyne and DC readout. . . . .	124
6.2. Noise projections from a time of S5 . . . . .	126
6.3. Comparison of shot noise limited sensitivities of heterodyne and DC readout of GEO 600 in S5 configuration. . . . .	129
6.4. Simulated displacement sensitivity of GEO 600 with DC-readout versus the offset from the dark fringe. . . . .	130
6.5. Sensitivity achievable with DC-readout versus the modelled shot noise of S5 . . . . .	132
6.6. Optical layout of the detection bench. . . . .	134
A.1. Optical layout of the GEO 600 output telescope. . . . .	138
A.2. Suspension of BDO2 . . . . .	139
A.3. Suspension of BDO1 and BDO3. . . . .	140
A.4. Drawing of a BDO mirror. . . . .	141
B.1. Power measurement of the light fields present at the output port of GEO 600. . . . .	144
C.1. Front plate of the new quadrant diode encapsulation. . . . .	148
C.2. Back plate of the new quadrant diode encapsulation. . . . .	148
D.1. Optical layout of GEO 600 . . . . .	150

F.1. Geometry of a 3-mass gravity calibrator. . . . .	160
I.1. Simplified optical layout with and without thermal lensing. . . . .	179
I.2. Influence of thermal lensing to the output mode . . . . .	180



# List of Tables

2.1. A summary of the resonance condition of the important light fields at the dark-port for a positive and negative detuning of the signal recycling cavity. The given values indicate the distance of the light field from the center of the nearest resonance peak. . . . .	27
3.1. Summary of the normalized backscattering efficiencies for the three scenarios depicted in Figure 3.11 . . . . .	52
5.1. A summary of the results of applying a statistical veto with a amplitude consistency check to two different data sets from GEO 600. . . . .	120
A.1. Optical and mechanical parameters of the mirrors used for the output telescope. . . . .	142



# Abbreviations and Symbols

AR	anti reflective
AS	amplitude spectrum
ASD	amplitude spectral density
BLRMS	band limited rms
DAQS	data acquisition system
DC	originally: "direct current". In this work also used for frequencies very close to 0 Hz.
DER_DATA_H	official channel name of the main gravitational wave channel of GEO 600
<i>diff-CAL</i>	signal injected into the differential arm length servo for calibration
DW	dewhitenning filter
ESD	electro static drives
ETG	event trigger generator
FEA	finite element analysis
FEM	finite element method
FFT	fast Fourier transform or discrete Fourier transform (DFT)
FWHM	full width at half maximum
FSR	free spectral range
GPS	global positioning system
GW	gravitational wave
$H$	main gravitational wave channel, $h(t)$
HR	high reflective
HVA	high voltage amplifier
IFO	interferometer
LCGT	large-scale cryogenic gravitational wave telescope
LIGO	laser interferometric gravitational wave observatory

LPN	laser power noise
LSC	LIGO scientific collaboration
MCe	end mirror of east arm
MCn	end mirror of north arm
MFe	folding mirror in the east building
MFn	folding mirror in the north building
MI	Michelson interferometer
MPR	power recycling mirror
MSR	signal recycling mirror
NS	neutron star
OAN	oscillator amplitude noise
OMC	output mode cleaner
OP	operational amplifier
OPN	oscillator phase noise
PCALmon	Record of the monitor of the photon pressure calibrator
$\mathcal{P}_{\text{DC}}$	DC light power hitting the main photodiode
PEM_CBCTR_PWRGRID	official channel name of the mains monitor
PS	power spectrum
PSD	power spectral density
PR	power recycling
PRC	power recycling cavity
PTB	Physikalisch technische Bundesanstalt (equivalent to NIST in the US)
RF	radio frequency
rms	root mean square
rot	misalignment in horizontal direction (rotation, yaw)
S4	S4 LSC science run
S5	S5 LSC science run
snr	signal to noise ratio
SR	signal recycling
SRC	signal recycling cavity
std	standard deviation
UTC	coordinated universal time
tilt	misalignment in vertical direction (tilt, pitch)



# Chapter 1.

## Introduction

### 1.1. Detection of Gravitational waves

The existence of gravitational waves (GW) is a consequence of the General Theory of Relativity, which was discovered and published by Albert Einstein in 1916. Supernovae, coalescing compact binary systems and pulsars are only a few representatives of astrophysical source, which can emit gravitational waves. Gravitational waves are expected to cover a wide frequency range, starting at the lower end at about  $10^{-17}$  Hz and going up to frequencies as high as a few kHz. The strength of even the strongest signals, for instance a supernova in our own galaxy, will be very small at the earth and only cause a relative length change of about  $10^{-21}$ . A good overview of gravitational wave sources can be found in [\[Cutler/Thorne\]](#).

The first efforts towards detecting gravitational waves were carried out by Joseph Weber in the 1960s. He used large metal cylinders, so called bar detectors or resonant detectors, as antennas [\[Weber\]](#). While Weber and his first followers used the bar detectors at room temperature, later experimenters cooled their bar detectors down to liquid Helium temperatures to suppress the intrinsic thermal noise. An overview of the present status of the resonant detectors can be found in [\[Astone02\]](#).

Indirect evidence of the existence of gravitational waves was supplied by R. A. Hulse and J. H. Taylor [\[Hulse\]](#), [\[Taylor\]](#). They observed a pulsar, in the binary star system PSR 1913+16 over years, and found a continuous increase of its rotation frequency. The observed increase exactly matched the increase predicted from emission of gravitational waves. For this work, Hulse and Taylor were awarded the Nobel price in 1993.

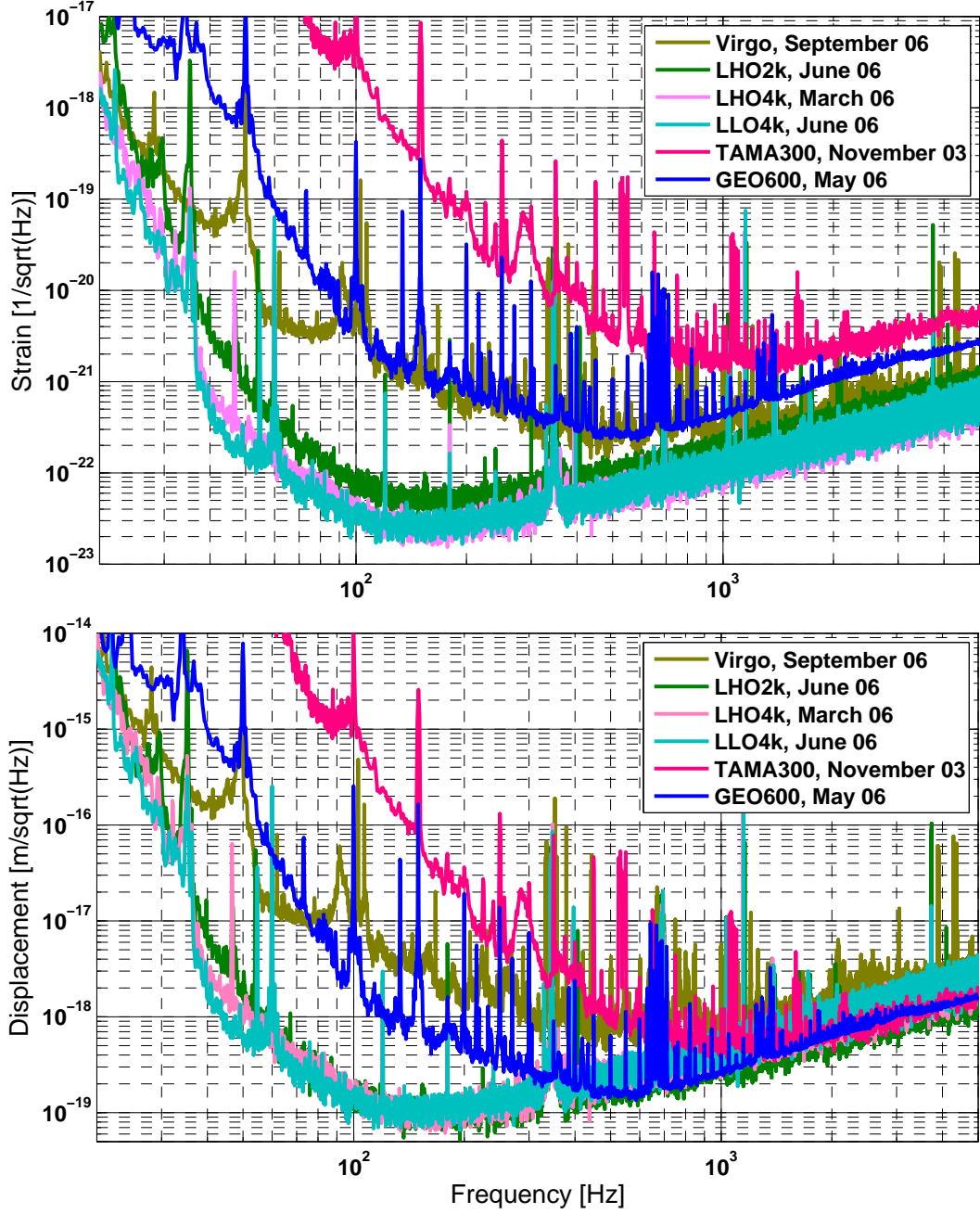


**Figure 1.1.:** Overview of the achieved sensitivities of the 6 large-scale laser-interferometric gravitational wave detectors. The upper subplot shows the strain sensitivities, while the lower plot depicts the corresponding displacement sensitivities, which are the sensitivities of the detectors to an absolute length change of the interferometer arms.

Today the direct search for gravitational waves concentrates on using large-scale laser interferometers, such as GEO 600. These extremely sensitive machines are based on kilometer long Michelson interferometers. Detailed descriptions of the measuring principle can be found [Rowan/Hough], [Saulson] and [Blair]. The currently operating generation of laser-interferometric GW detectors achieves sensitivities of the order  $10^{-22}/\sqrt{\text{Hz}}$  and therefore it seems only to be a question of time until the first gravitational wave signal will be detected.

## 1.2. A world wide network of large-scale gravitational wave detectors

Currently six large-scale gravitational wave detectors are in operation. In the USA there are the three LIGO detectors [Waldman06]: One 4 km interferometer in Livingston (LLO), Louisiana and two detectors with arm lengths of 2 and 4 km in Hanford (LHO), Washington. An Italian-French Collaboration operates the 3 km long VIRGO detector [Acernese06]. The 300 m long Japanese detector TAMA300 is located in Tokio [Ando05]. Finally there is the 600 m long GEO 600 detector near Hannover, operated by a team of British and German scientists [Hild06c]. The sensitivities achieved by the detectors are shown in Figure 1.1.

Within the frame of LIGO Scientific Collaboration (LSC) GEO 600 and the three LIGO detectors have taken a huge amount of coincident data. These periods of simultaneous data taking are called *science runs*. The data of these 4 detectors are searched for gravitational wave signals by scientists of the LSC. Probably soon a memorandum of understanding (MOU) will be signed between the LSC and VIRGO collaboration. Then people will be able to analyze simultaneous data streams from the five most sensitive gravitational wave detectors built so far.

## 1.3. A brief description of the GEO 600 GW detector

The GEO 600 gravitational wave detector is a very complicated device, consisting of about 300 partly coupled control loops. The core of the detector comprises of about 30 optics, suspended by multi-stage vibration isolations and enclosed by an ultra high

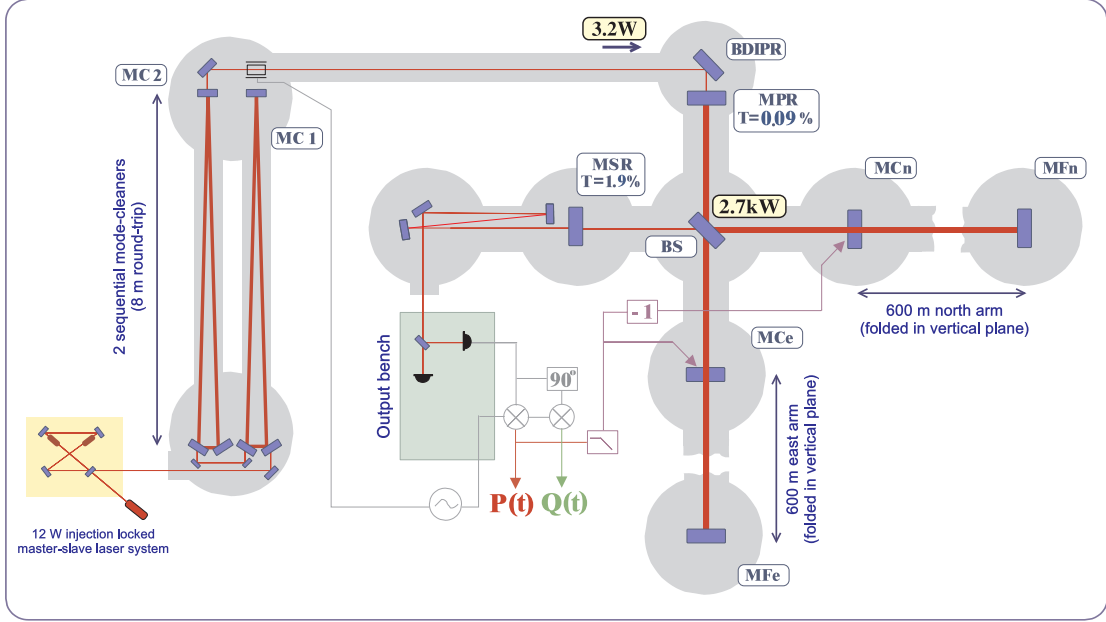


**Figure 1.2.:** The light of a 12 Watt master-slave laser system is injected into two sequential mode-cleaners, MC1 and MC2 of 8 and 8.1 meters round-trip length, and a finesse of 2700 and 1700, respectively. The stabilized and filtered light enters the main Michelson interferometer through the power-recycling mirror (MPR). The main interferometer consists of five optical components: the beam splitter (BS), the two end mirrors (MCe and MCn) and the two folding mirrors (MFe and MFn). In contrast to most of the other large scale interferometric gravitational-wave detectors GEO600 does not use Fabry-Perot resonators in the arms, but instead the simplest case of an optical delay line including one folding mirror per arm. The light containing potential gravitational-wave information leaves the Michelson interferometer at the antisymmetric port and the signal gets enhanced by usage of a second recycling mirror, the signal recycling mirror (MSR). The light passing the signal-recycling mirror is detected at the output bench, and the gravitational-wave information is derived from a RF-heterodyne method.

vacuum system of a volume of about 400 cubic meters. A simplified optical layout of the detector is shown in Figure 1.2. The alignment systems of GEO 600 automatically controls 38 angular degrees of freedom. At a frequency of 450 Hz a displacement sensitivity of  $1.5 \cdot 10^{-19} \text{m}/\sqrt{\text{Hz}}$  and a strain sensitivity of better than  $3 \cdot 10^{-22}/\sqrt{\text{Hz}}$  are achieved. Figure 1.3 shows the improvement of the sensitivity from GEO 600 over the last few years. About 100 gigabytes of science data are collected and processed per day.

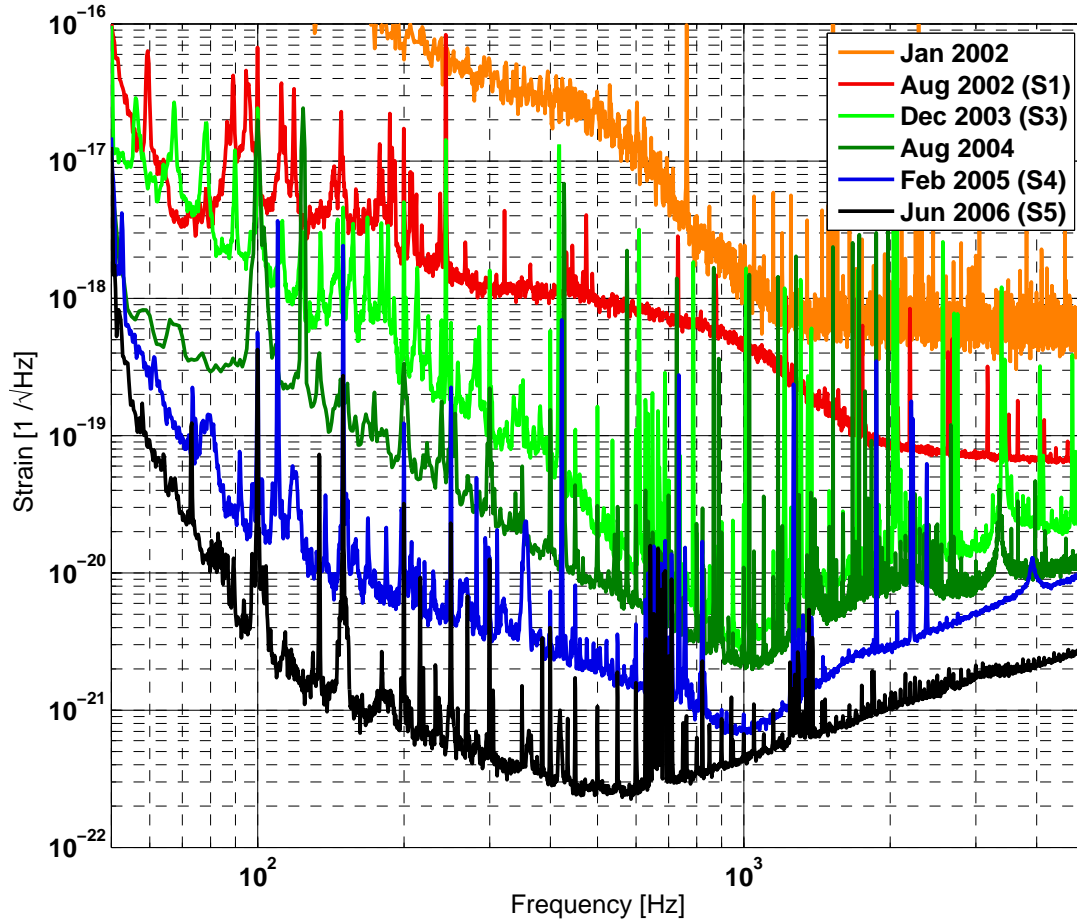


**Figure 1.3.:** Sensitivity improvement of GEO 600 over the last few years.

The preceding gives an impression of the complexity of GEO 600. A full description of GEO 600 would not fit into the frame of a single dissertation. Therefore the curious reader is asked to refer to the latest papers giving the status of GEO 600 [Willke04], [Grote05], [Lück06], [Hild06c] for a quick overview. More detailed descriptions of the most important subsystems of the GEO 600 detector can be found in the following five

dissertations: [Freise03], [Grote03], [Hewitson04a], [Gossler04] and [Smith06].

## Chapter 2.

# Demonstration and comparison of tuned and detuned signal recycling in a large-scale gravitational wave detector

### 2.1. Introduction

Placing a mirror (MSR in Figure 2.4) in the dark port of an interferometric gravitational wave detector can significantly increase its sensitivity in a certain frequency band. This technique, called signal recycling (SR), was proposed by Brian Meers [Meers] and first demonstrated in a table top experiment by Strain and Meers [Strain91]. The combination of power and signal recycling, called dual recycling, was realized 1998 in a fully suspended interferometer at the Garching prototype [Heinzel98]. The GEO 600 interferometer is the first and so far only large scale gravitational wave detector using signal recycling. However, nearly all projects plan to use signal recycling in their next generation of instruments, like for example Advanced LIGO [Giaime] or the Japanese LCGT project [Kuroda06].

The use of signal recycling allows a frequency dependent shaping of the detector response function, which is defined as the transfer function from to differential arm length changes to the output of the detector. The bandwidth of the signal recycling resonance is determined by the reflectivity of the signal recycling mirror. A high reflectivity gives a large increase of the response function in a narrow band (narrow-band operation), while a moderate reflectivity yields a medium improvement of the response function over a broader frequency range (broadband operation). Figure 2.1 shows exemplary the

shot noise limit of the GEO 600 detector for three different transmittances of the signal recycling mirror.

The frequency of maximum response, also called tuning frequency, is determined by the length of the signal recycling cavity and can be chosen by a change of the microscopic position of the signal recycling mirror. In this thesis we will refer to *tuned* signal recycling as the case when one of the resonances of the signal recycling cavity is centered at the frequency of the carrier, in contrast to *detuned* signal recycling where the signal recycling resonance is shifted to a frequency different from the carrier. The difference between the frequency of the signal recycling resonance and the carrier frequency is referred to as the detuning frequency. In Figure 2.2 the shot noise limit of GEO 600 is shown for various tuning frequencies.

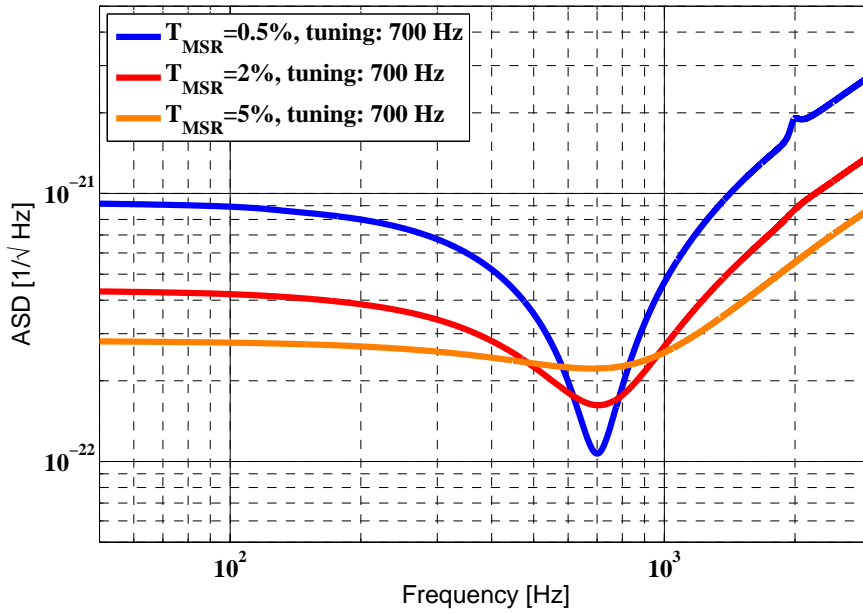


**Figure 2.1.:** Shot noise limit of GEO 600 for different transmittances of the signal recycling mirror.

Until recently, the GEO 600 detector has been operated with detuned signal recycling in order to shift the peak sensitivity to frequencies between 350 and 1000 Hz [Hild06c]. This was done to optimize the science contribution of the GEO 600 detector to the LSC (LIGO Scientific Collaboration) detector network. However, the use of detuned signal recycling brings some disadvantages. In contrast to a Michelson interferometer having



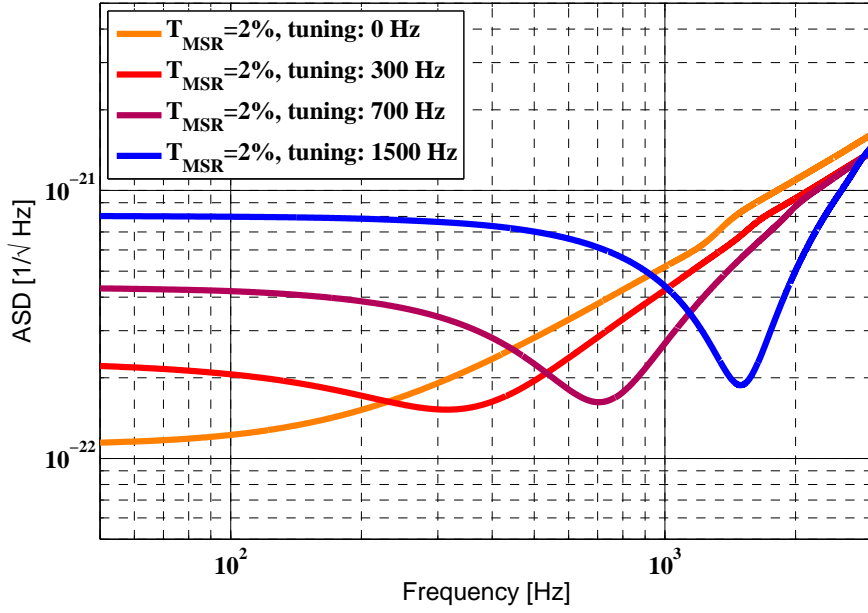


**Figure 2.2.:** Shot noise limit of GEO 600 for different tunings of the signal recycling cavity.

only power recycling, the signal recycling cavity changes amplitude and phase of almost any light component present at the dark port, for instance the gravitational wave signal sidebands or the radio frequency (RF) sidebands used for detector control.

Figure 2.3 gives a qualitative overview of the light fields in the signal recycling cavity for tuned and detuned operation. In the tuned case, the differential arm length information can be derived completely from demodulation of the photo current detected at the dark port in the in-phase quadrature (in the following referred to as P quadrature). In the detuned signal recycling case this information is in a frequency-dependent way spread over both quadratures, P and Q (out-of-phase quadrature) and both have to be analyzed to obtain the best signal-to-shotnoise ratio. A detailed description of this effect and its consequences for the calibration of the instrument can be found in [Hewitson04] and [Hewitson05].

Furthermore, the asymmetry of the RF control sidebands at the dark port causes a strong amplitude modulation of the light on the main photo detector, containing no gravitational wave signal. However, this strong RF amplitude modulation was found to

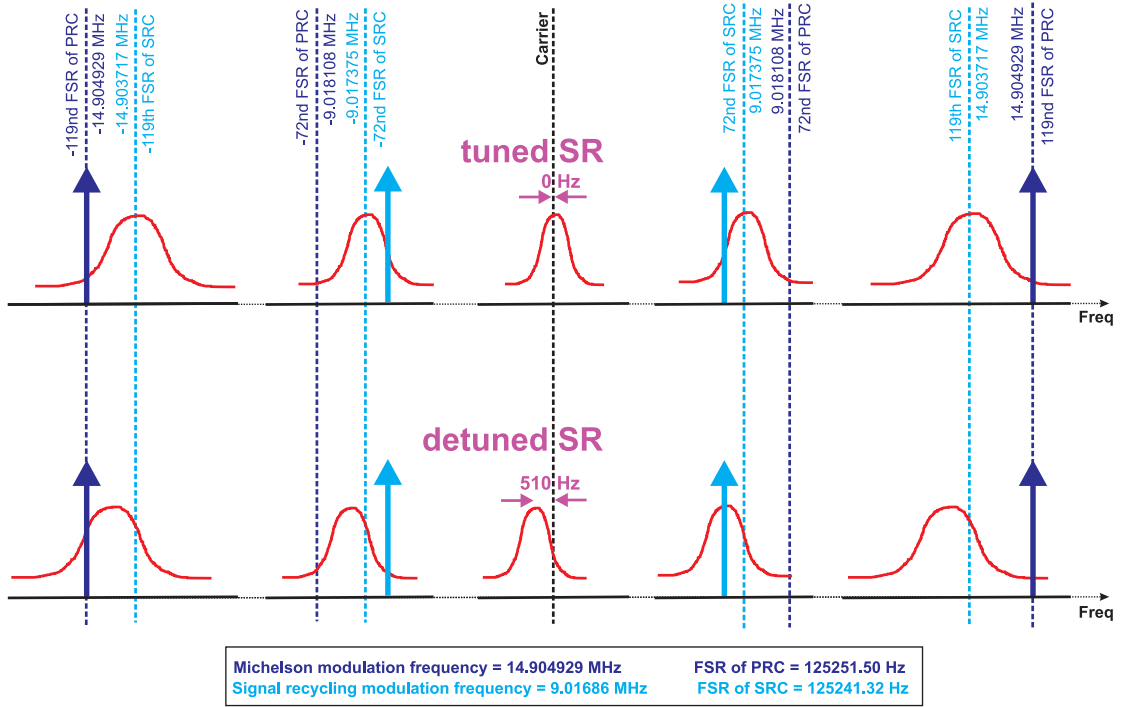


**Figure 2.3.:** Overview of the resonance conditions for the carrier (black dashed line), Michelson control sidebands (dark blue arrows) and signal recycling control sidebands (light blue arrows) inside the signal recycling cavity. The resonance conditions are shown for tuned and detuned (510 Hz) signal recycling in the upper and lower subplot, respectively. The comb of equidistant resonances of the signal recycling cavity (SRC) is indicated by the red Airy peaks. Due to the Schnupp asymmetry the shape of the resonance gets wider for frequencies far off the carrier. The gravitational wave signal is located around the carrier. The frequency of the Michelson modulation was chosen to be close to resonant in the 119th free spectral range (FSR) of the power recycling cavity (PRC). In detuned signal recycling the two Michelson sidebands see different resonance conditions inside the SRC: The lower sideband is nearly resonant, while the upper one is nearly off resonance. When going from detuned to tuned signal recycling using the method described in this thesis the frequency of all sidebands stays the same, but the comb of signal recycling resonances (red curves) is shifted by 510 Hz towards higher frequencies. In the tuned case the sidebands used for the Michelson control are balanced as well as the ones used for signal recycling control.

be a potential source of saturation of the main photo detector [Grote].<sup>1</sup>

It was also observed in the detuned case that various noise sources, for instance oscillator phase noise and laser power noise, couple to the gravitational wave channel in a more complex way than one would expect from simple models. A suspected cause for this are the imbalances of the sidebands in the interferometer and at the dark port.

An illustrative example of the complexity of the noise couplings in an interferometer with detuned signal recycling can be found on the CD-ROM (Multimedia Appendix) at the end of this thesis. The time lapse video shows the evolution of the sensitivity of GEO 600 during an experiment in which a single parameter of the detector, namely the radius of curvature of MFE, was changed by about 1 %. The black trace indicates a reference sensitivity, while the blue trace represents the actual sensitivity.

The facts given above made it highly desirable for us to directly compare tuned and detuned signal recycling operation in GEO 600. In section 2.2 we describe the GEO control scheme implemented for detuned signal recycling, while in section 2.3 we introduce a new technique, which allows the operation of tuned signal recycling. In Sections 2.4-2.6 important aspects of tuned and detuned signal recycling (510 Hz) are compared: Section 2.4 shows measurements of the optical gain, in Section 2.5 a comparison of the size of the amplitude modulation at the main photodiode is given. In section 2.6 exemplary measurements of some noise coupling transfer functions to the gravitational wave channel are shown. Finally the sensitivity is compared for detuned and tuned signal recycling in Section 2.7 as well as for positive and negative detunings in Section 2.8.

## 2.2. Control scheme for signal recycling in GEO 600

The signal used to control the microscopic position of the signal recycling mirror (MSR) is derived from a radio frequency modulation/demodulation technique. Figure 2.4 shows a simplified diagram of the control of two degrees of freedom, the Michelson differential arm length and the length of the signal recycling cavity in blue and green respectively.

---

<sup>1</sup>At the LIGO detectors an additional feedback loop (called *I-servo*) is used which reduces the part of the RF signal that is not suppressed by the interferometer control loop. This is done by adding an appropriate RF-signal, essentially a sine wave at the modulation frequency, with correct amplitude and phase, directly to the PD-resonant circuit, thereby cancelling the RF-signal (at this frequency) in one quadrature [Sigg04].

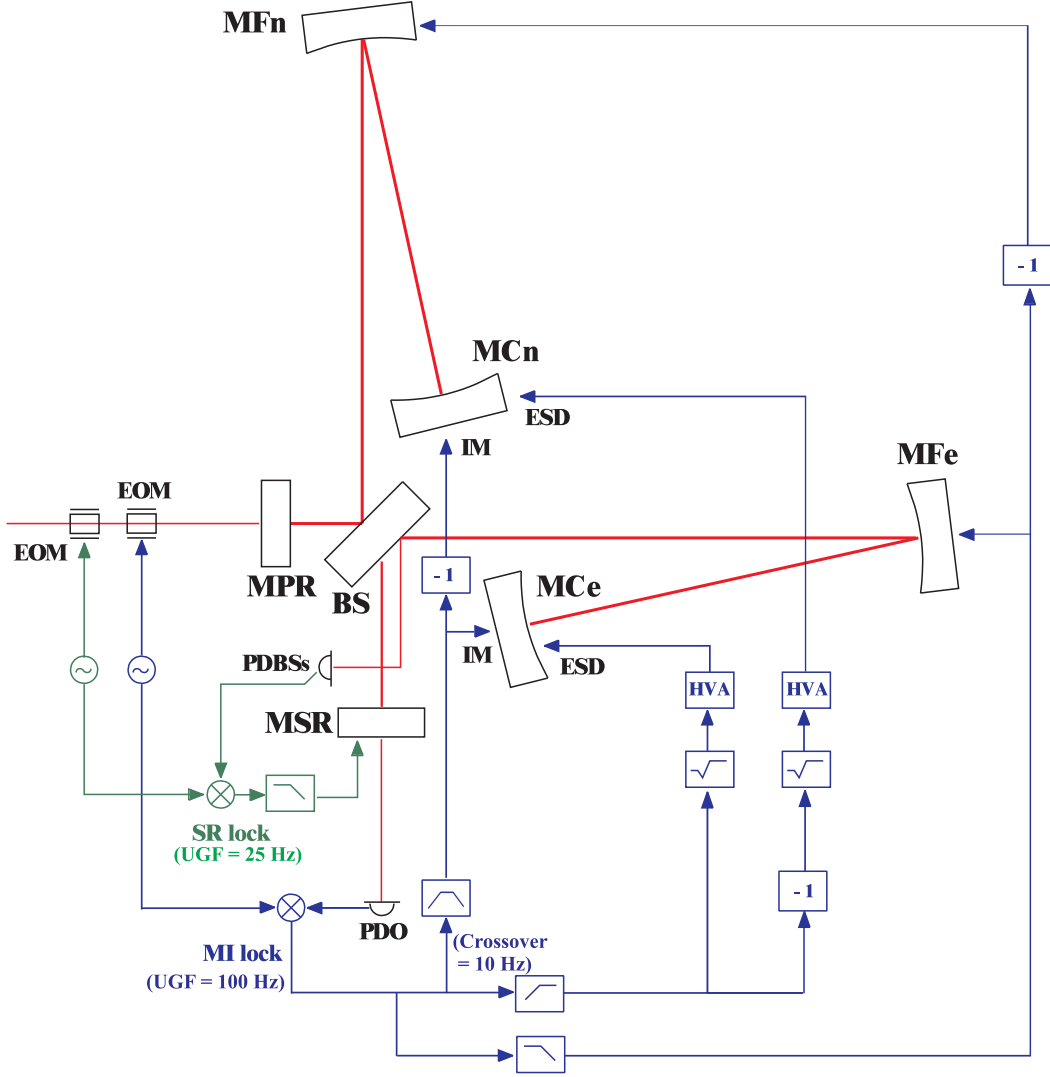


**Figure 2.4.:** Simplified control scheme for two longitudinal degrees of freedom of GEO 600. Shown are the Michelson differential loop and the signal recycling loop in blue and green, respectively. The control signals used for lock acquisition are not shown in the diagram.

Two sets of phase modulation sidebands are created in front of the power recycling mirror (MPR in Figure 2.4). Due to an asymmetry in interferometer arms of several cm (Schnupp asymmetry), a fraction of these sidebands leaves the interferometer at the dark port [Schnupp]. The error signal for controlling the differential arm length of the Michelson interferometer is derived from the photodiode PDO placed at the dark port of the interferometer. For the sensing of the signal recycling loop a pick-off beam from one of the interferometer arms is used (photodiode PDBSs, sensing the beam reflected at the beam splitter AR coated side).

For various reasons (described in detail in [Grote03]) it was so far not possible to realize lock acquisition for the tuned configuration of GEO 600. Therefore a procedure was developed to acquire lock at a high detuning (a few kHz) and then gradually tune the signal recycling cavity to lower frequencies. This so-called tuning process is done by changing the radio frequency of the signal recycling modulation and other relevant parameters [Grote05].

Figure 2.5 shows the error signal of the signal recycling loop for different modulation frequencies versus the position of the signal recycling mirror. These simulations were done using the FINESSE software [Freise04]. In the case of detuned signal recycling, the error signal structure shows three zero crossings. The two outer ones are referred to as the lower and upper sidebands corresponding to a negative or positive detuning, while the zero crossing in the center corresponds to the tuned case. So far the zero crossing corresponding to the upper sideband was chosen to be the nominal operating point. If the modulation frequency is increased, the zero crossings from the lower and upper signal recycling sideband are shifted towards the zero crossing corresponding to tuned signal recycling, i.e. the whole error signal structure gets squeezed, but keeps roughly its shape. As the signal recycling mirror is locked to the position at which the upper sideband crosses zero, the position of the mirror is shifted corresponding to the change of the modulation frequency of the SR control sideband. This tuning technique works for tunings as low as about 300 Hz.

As indicated in the second subplot of Figure 2.5, for tunings below 300 Hz the error signal structure is not only squeezed, but also changes its shape significantly. The slopes of the error signals of the upper and lower sideband become asymmetric around their zero crossings. For the extreme condition of a modulation frequency corresponding to the tuned case the zero crossings of the sidebands vanish completely. For frequencies

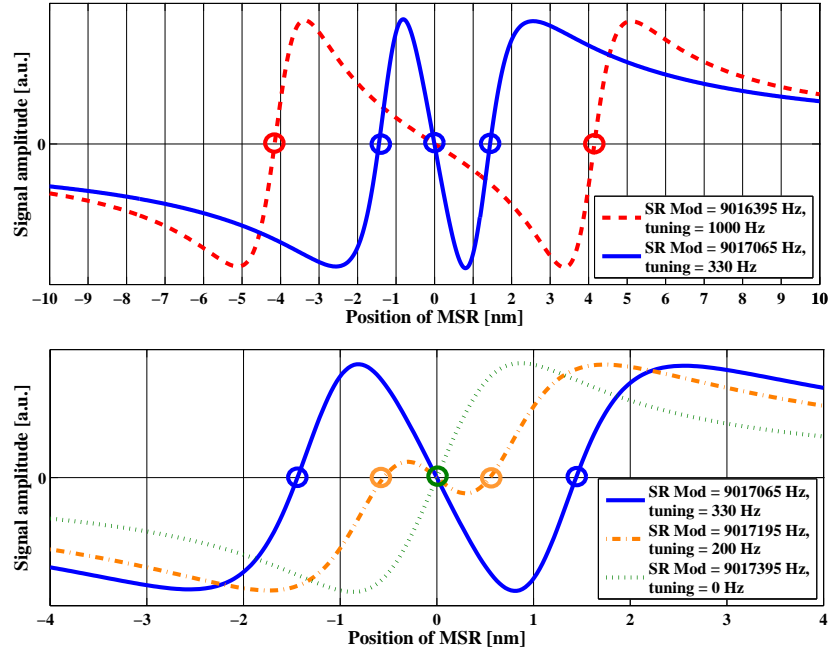


**Figure 2.5.:** Signal recycling error signals derived from an RF modulation demodulation technique versus microscopic position of the signal recycling mirror. The error signal is plotted for various modulation frequencies corresponding to detunings of the signal recycling cavity between 1000 Hz and 0 Hz. By increasing the modulation frequency the structure gets more and more narrow.

corresponding to tunings between 300 and 0 Hz in the presence of electronic or seismic noise, the error signals cannot be used for a stable control of the signal recycling mirror. Their range with a constant slope is too small to hold the mirror in a defined position, given that the control bandwidth of the signal recycling loop is limited. Therefore reaching the tuned case in small steps seems not a promising technique here.

### 2.3. A new method for locking tuned signal recycling

One possible way to reach the tuned case is to start from the lowest stable tuning, then make the microscopic position of the signal recycling mirror 'jump' over the region where the control signals are not valid, and 'catch' it again at the tuned state, where reasonable control signals can be derived. This can be done without changing the signal recycling modulation frequency by jumping from the zero crossing corresponding to the upper sideband to the zero crossing corresponding to the tuned case.

We realized this jumping by pushing the signal recycling mirror in the direction corresponding to a smaller detuning frequency and stopping it near the zero crossing of the tuned case. In order to not disturb the other control loops, for example the loop controlling the differential arm length of the Michelson interferometer, the signal recycling mirror has to be pushed over the region of non-valid error signals quickly.

In detail the procedure works as follows: We start from a modulation frequency corresponding to a tuning of about 350 Hz where the signal recycling mirror is locked at the position corresponding to the zero crossing of the error signal around the upper sideband. Then we switch off the signal recycling control loop to be able to push the signal recycling mirror away from its operating point. At the same time we start pushing the signal recycling mirror as hard as the coil-magnet actuators allow. After 4 milliseconds of pushing, the mirror has covered half the distance between the zero crossing of the upper sideband and the one from tuned case which is in this case a distance of 0.7 nm. Then the sign of the force applied to mirror is inverted to decelerate the mirror in 4 milliseconds from maximum speed to a velocity near zero when the mirror finally reaches the tuned position. After these 8 milliseconds the signal recycling feedback loop is closed again, but with opposite polarity, to account for the different sign of the slope around the zero crossing of tuned signal recycling.<sup>2</sup> The duration of this procedure is short

---

<sup>2</sup>Another possibility would be to change the modulation frequency while the mirror is being pushed,

enough, to not significantly disturb other control loops.

Using this technique it was also possible to jump twice the distance (about 3 nm) with the signal recycling mirror, and thereby go from the zero crossing of the upper sideband to that of the lower sideband, which turns out to be an equally stable operating point.

### 2.3.1. Simulation of the control parameters for tuned signal recycling

When jumping from detuned to tuned signal recycling a few control parameters need to be adjusted to account for the different operating point of the signal recycling mirror. The gain of the signal recycling loop needs to be adjusted for the different slope of the error signal. Furthermore in the case of tuned signal recycling the pole of the signal recycling cavity for carrier light is shifted towards lower frequencies, thus all signals generated from the dark port need to be adapted.

Figure 2.6 shows the results of simulations, done using the Finesse software [Freise04], for the longitudinal gains of the Michelson (upper set of subplots) and signal recycling (lower set of subplots) longitudinal error signals. In tuned signal recycling operation the Michelson error signal has at low frequencies about 9.5 dB and around the unity gain frequency (100 Hz) about 7.8 dB higher gain. Due to the shifted signal recycling cavity pole around the unity gain frequency about 30 degrees of phase are lost in tuned signal recycling operation compared to detuned operation. For tuned signal recycling operation this is compensated by switching an additional differentiator into the loop controlling the Michelson differential arm length and adjusting the overall gain of the loop.

The gain of the signal recycling error signal is about 2 dB higher in tuned case for all frequencies within the control bandwidth of 50 Hz. The phase is for all frequencies of interest 180 degrees different between tuned and detuned operation, i.e. the sign is swapped as indicated in Figure 2.5. A simple change of the overall loop gain of 2 dB is sufficient for stable operation of tuned signal recycling.

---

and then to keep the sign of the control loop.



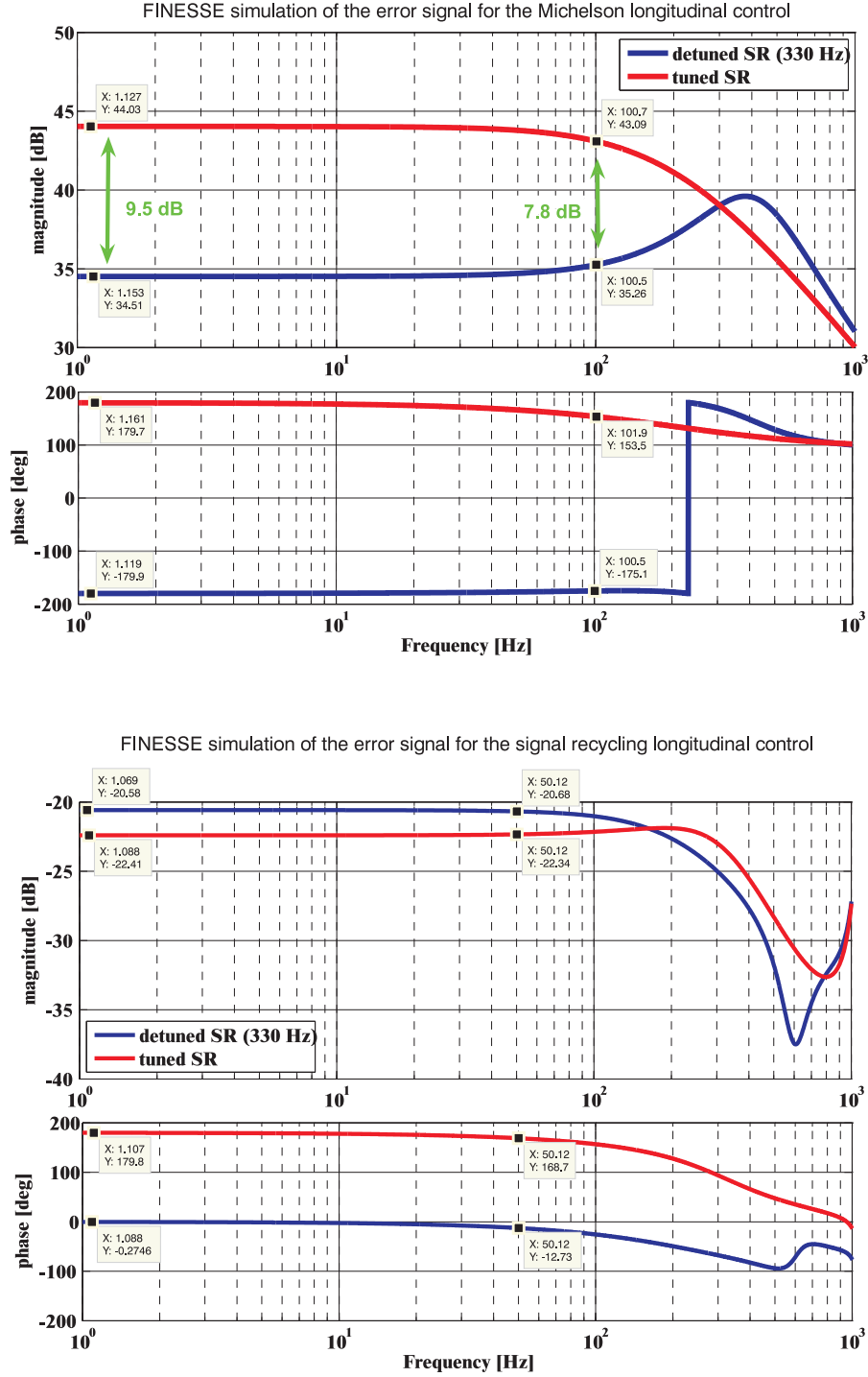


**Figure 2.6.:** Simulations of the error signal gain for the longitudinal control of the Michelson differential armlength (upper pair of plots) and the longitudinal control loop of the signal recycling mirror (lower pair of plots). The Michelson control loop has an unity gain frequency of about 100 Hz. The signal recycling control loop has unity gain frequencies of about 50 Hz in acquisition mode and 25 Hz in low-noise run mode.

### 2.3.2. Calibration of the actuator strength

In order to increase the accuracy of the jumping process it is desirable to calibrate the applied force to the signal recycling mirror in order to be able push the mirror as accurate as possible to its new operating point.

The idea of the calibration process is to use the known distance of the two positions of the signal recycling mirror for detuned and tuned operation. Starting from position  $P_{\text{start}}$  corresponding to detuned operation the mirror is pushed for  $\Delta t$  milliseconds with a force  $F_p$  towards the tuned operation point. Afterwards the mirror is decelerated by again  $\Delta t$  milliseconds, but with opposite force  $-F_p$ . At the end of this process the mirror reaches the position  $P_{\text{end}}$  and should, in absence of any disturbance, hang still again. We now vary  $\Delta t$  and  $F_p$  in order to stop the exactly at the position corresponding to tuned operating point. This position is in particular suitable as it corresponds to a zero crossing of the error signal.

Using the maximum force that can be driven by the coil driver electronics we get the following calibration of the actuator. The maximal acceleration  $a_{\text{push}}$  amounts to:

$$a_{\text{push}} = 1.53 \cdot 10^{-4} \frac{\text{m}}{\text{sec}^2} \quad (2.1)$$

## 2.4. Measurements of optical gain

The response function of the Michelson differential error signal to differential arm length fluctuations, the so called optical gain  $G_{\text{opt}}$ , is frequency dependent. In the case of detuned signal recycling the signal is also inherently spread between the two orthogonally demodulated signal quadratures, P and Q.

Figure 2.7 shows a simplified diagram of the loop controlling the differential arm length of the Michelson. The optical gain of the P quadrature can be described by the following expression

$$G_{\text{opt}}(P) = \frac{\text{EP-P} \cdot \text{P-dw}}{\text{FB} \cdot \text{FB-dw}} \cdot \frac{1}{\text{ESD}} \cdot \frac{1}{\text{HVA-dw}} \quad (2.2)$$

where EP-P (LSC\_MID\_EP-P\_HP) is the error signal from the P quadrature recorded in the data acquisition system (DAQS) and FB (LSC\_MID\_FB-MCEMCN) is the record of

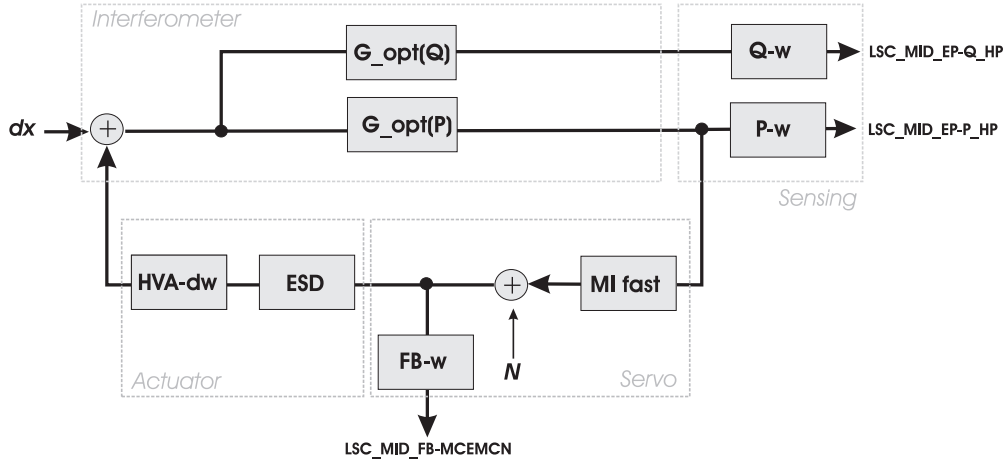


**Figure 2.7.:** A simplified diagram of the loop controlling the differential arm length of the Michelson. The diagram contains only components important for calibration and measuring the optical gains  $G_{opt}$  from the two orthogonal signal quadratures P and Q. Abbreviations used: MI fast = electronics of the servo, FB-w = whitening filter of feedback signal, ESD = high voltage amplifier (HVA) and electro static drives, HVA-dw = HVA dewhitening filter, P-w = whitening filter for P signal, P-w = whitening filter for Q signal,  $N$  = noise injected (for optical gain and loop transfer function measurements),  $dx$  = mirror displacement.

the feedback. ESD and HVA-dw represent the responses of the actuators, FB-dw is the response of the feedback whitening filter and P-dw is the inverse of the P error signal whitening filter.

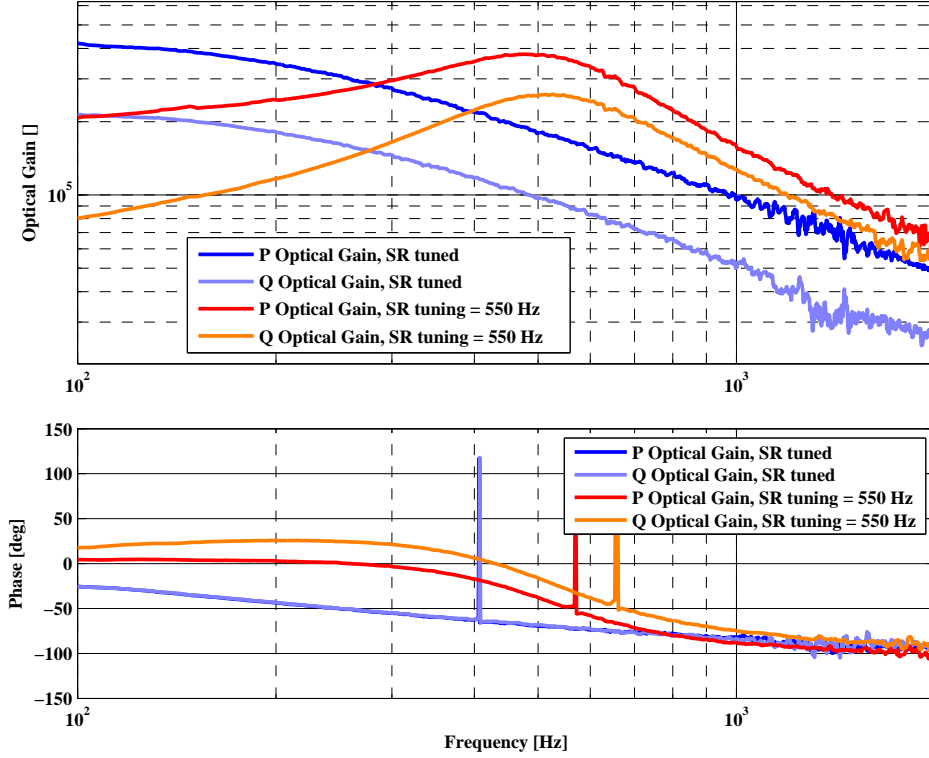


**Figure 2.8.:** Measurement of the optical gains for tuned and detuned signal recycling for the two orthogonal quadratures P and Q. For the tuned case the demodulation phase was not optimized. Therefore the the differential armlength signal is still clearly present in the optical gain of the Q-signal.

Figure 2.8 shows measurements of the optical gains for detuned and tuned signal recycling for the two quadratures. In the detuned case the optical gain shows a maximum at the frequency of the signal recycling detuning. The width of the maximum is given by the bandwidth of the signal recycling cavity, which is about 700 Hz for the currently installed signal recycling mirror with a transmission of about 2%. In the tuned case the maximum of the optical gain is centered around 0 Hz and the bandwidth of the response function is decreased to 350 Hz.

## 2.5. Reduction of the RF amplitude modulation

In detuned signal recycling the RF sidebands from the Schnupp modulation which originally represented a pure phase modulation get partly converted to amplitude modulation inside the signal recycling cavity. The light hitting the main photo diode at the dark port shows strong amplitude modulation at the frequency of the Michelson control sidebands, which are in case of GEO 600 at a frequency of about 15 MHz.

Some of our observations indicated that the strong amplitude modulation (in detuned SR) together with a high averaged photo current might cause saturation effects and nonlinearities in the photodiode. A detailed description of these problems can be found in [Grote]. However, it is important to mention that most of the spurious effects depend on the size of the RF amplitude modulation. Therefore it would be desirable to reduce the size of the amplitude modulation.

In the case of tuned signal recycling we have been able to reduce the rms of the signal in the Q quadrature, which is a good measure of the size of the amplitude modulation, by a factor of 12 compared to detuned operation.

## 2.6. Comparison of noise transfer functions for tuned and detuned signal recycling

Measurements of the transfer functions from various technical noise sources to the error signal of the differential arm length servo (and hence the gravitational wave channel) during detuned operation indicate complex couplings [Smith06]. Many of the measured transfer functions contain resonances and notch structures that could not be explained completely even by a complex frequency domain model of the interferometer [Malec06].

Asymmetry of the radio frequency sidebands in the detuned case was suspected to be the origin for some of the complexity observed in the noise couplings. To investigate this we performed measurements for four important technical noise sources for tuned and detuned signal recycling in order to check whether the couplings get simpler and perhaps less significant for tuned signal recycling.

- *Oscillator phase noise (OPN)*: The two sets of upper plots in Figure 2.9 show the measurements of the coupling from oscillator phase noise (of the modulation

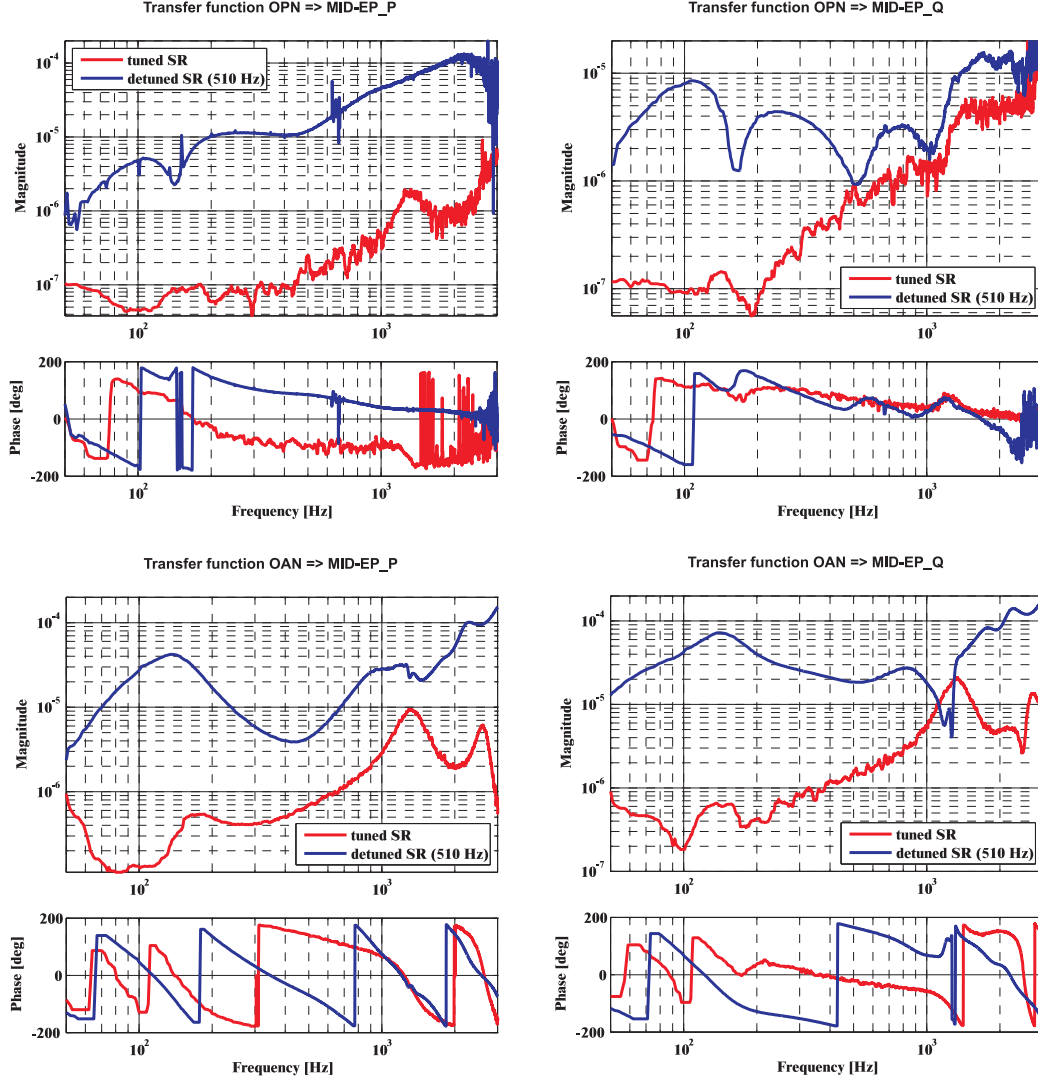


**Figure 2.9.:** Measurements of the transfer functions from oscillator phase noise (OPN) and oscillator amplitude noise (OAN) to the error signal of the differential arm length servo. The red trace represents tuned signal recycling, while blue indicates a detuning of 510 Hz. The magnitudes of transfer functions are normalized by magnitudes of the optical gains from Figure 2.8, which allows for a direct comparison of the transfer functions regarding the strain sensitivity of the detector.

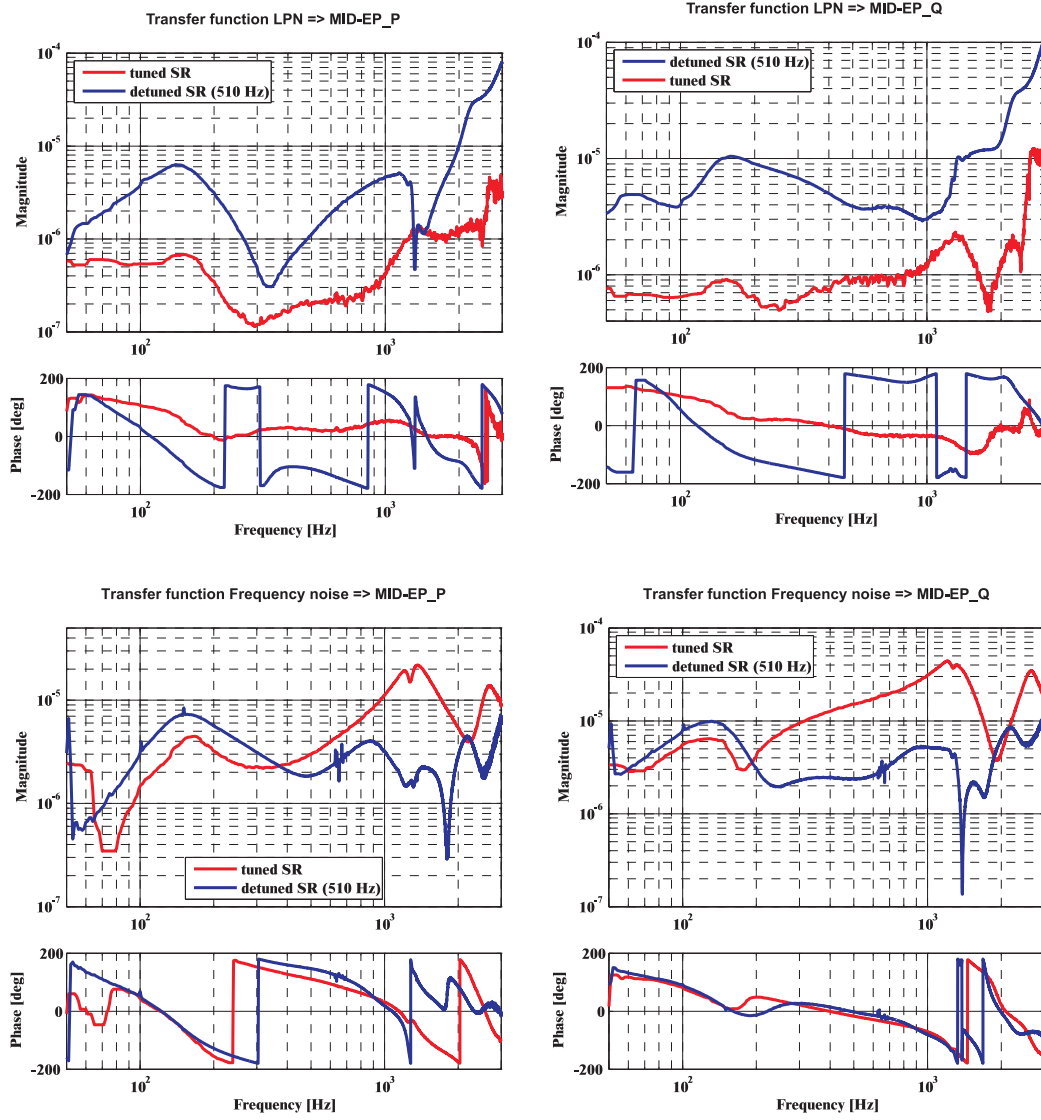


**Figure 2.10.:** Measurements of the transfer functions from laser frequency noise and laser power noise to the error signal of the differential arm length servo. The red trace represents tuned signal recycling, while blue indicates a detuning of 510 Hz. The magnitudes of transfer functions are normalized by magnitudes of the optical gains from Figure 2.8, which allows for a direct comparison of the transfer functions regarding the strain sensitivity of the detector.

used for creating control signals for the differential arm length of the Michelson interferometer and the local oscillator signal) to differential arm length. In the P quadrature the coupling in the tuned case is dramatically reduced over a wide frequency range by about two orders of magnitude. This can be explained by the reduction of the rms of the signal in the Q quadrature, (see section 2.5). The coupling of OPN to the Q quadrature is for frequencies below 500 Hz significantly decreased by up to a factor of 100 at 100 Hz. A detailed description of potential coupling mechanisms can be found in [Smith06].

- *Oscillator amplitude noise (OAN)*: The two sets of lower plots in Figure 2.9 show the measurements of the coupling from oscillator amplitude noise (of the modulator used for creating control signals for the differential arm length of the Michelson interferometer) to differential arm length. The amplitude noise in the EOM path is eventually imparted on the carrier and control sidebands and couples to the detector output via asymmetries in the interferometer, as explained in [Malec06]. Again the coupling into both quadratures is strongly suppressed in tuned signal recycling due to more balanced sideband conditions at the dark-port.
- *Laser power noise (LPN)*: The two sets of upper plots in Figure 2.10 show the measurements of the coupling from laser power noise to differential arm length. The coupling to both quadratures is decreased on average by about a factor of 5 to 10 over the frequencies of interest. In addition at least in the P quadrature the structure of the coupling got slightly simpler. The strongly pronounced notch structure around 1.5 kHz vanishes for tuned signal recycling.
- *Laser frequency noise*: The two sets of lower plots in Figure 2.10 show the measurements of the coupling from laser frequency noise to differential arm length. At low frequencies we observed a moderate reduction of the coupling in the tuned case, while for higher frequencies the coupling is significantly increased. On the other hand the very distinct notch structures between 1 and 2 kHz seem to vanish completely.

## 2.7. Calibrated detector sensitivity for tuned signal recycling

Even though the performed investigations on comparing tuned and detuned signal recycling focus on the different propagation of optical sidebands through the interferometer,



the curious reader should get a chance to look at the GW sensitivity for tuned and detuned signal recycling, too.

The calibration of the detuned detector is done continuously using a time-domain method. A detailed description can be found in [Hewitson04] and [Hewitson05]. In order to calibrate the new case of tuned signal recycling operation we used a frequency domain method. With the aid of the closed loop transfer function (*CLTF*) the differential displacement  $dx$  (see Figure 2.7) can be expressed by:

$$dx = \frac{EP \cdot P \cdot dw}{G_{opt}(P) \cdot CLTF}. \quad (2.3)$$

To convert the displacement  $dx$  to strain sensitivity we have to divide  $dx$  by the optical arm length of GEO 600:

$$HP = \frac{dx}{1200 \text{ m}} \quad (2.4)$$

The calibration of the orthogonal quadrature Q is done analogous.

Figure 2.11 shows the calibrated sensitivities of the two output quadrature signals. By going to tuned signal recycling no improvement in the calibrated P signal is observed. As shot noise is the main contribution to the noise level of GEO 600 for frequencies above 500 Hz, the sensitivity got worse in that frequency range when going to tuned signal recycling. At low frequencies we observed no increase in sensitivity because in that frequency range the shot noise is masked by the noise contributions of several technical noise sources.

For the sensitivity derived from the Q signal the situation is different: Between 90 and 200 Hz an improvement is achieved for tuned signal recycling operation. On the other hand, above 300 Hz the sensitivity is worse by about a factor of 2.

This is only a preliminary result as not much time during the science run could be spend to optimize the detector for tuned signal recycling operation yet.

## 2.8. Comparison of detuned signal recycling for upper and lower operating point

From the sensitivity point of view it might also be interesting to compare the sensitivities of the detector for locking the signal recycling mirror either at the position corresponding

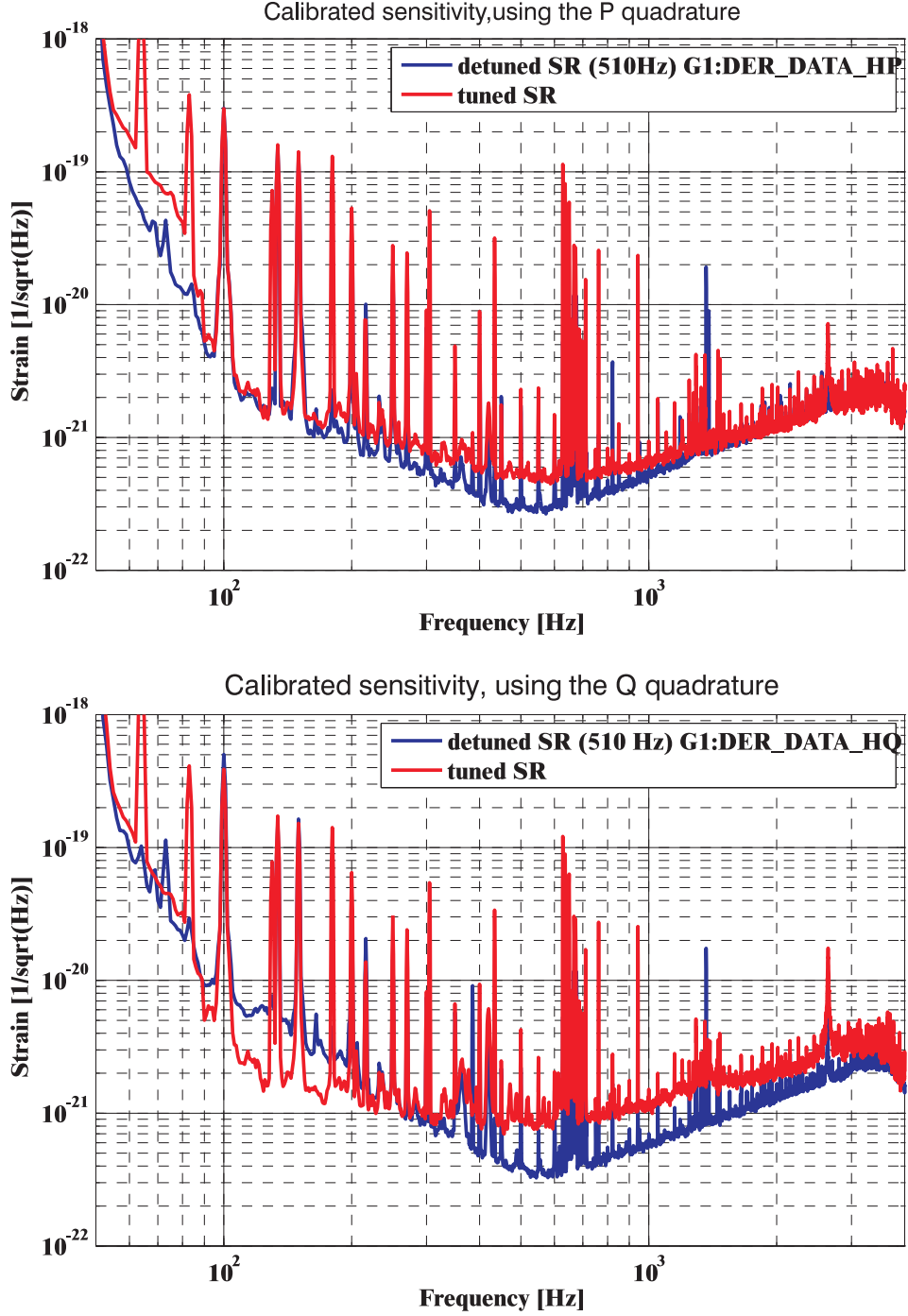


**Figure 2.11.:** Comparison of the sensitivity of GEO 600 for tuned and detuned signal recycling operation. The upper plot shows the calibration derived from using the in-phase signal (P), while the lower plot is derived from using the out-of-phase signal (Q).

## 2.8. Comparison of detuned signal recycling for upper and lower operating point

to the lower sideband crossing or the position corresponding to the upper sideband crossing. In principle there should be no difference between the two cases: By going from the upper sideband lock to the lower sideband lock all the imbalances of the light fields in the dark-port are preserved. In the lower subplot of Figure 2.3 the resonance condition is plotted for a positive signal recycling detuning of 510 Hz. How does this picture change when going to the opposite detuning of -510 Hz. As the signal recycling mirror is locked in that case to the zero crossing of the lower signal recycling sideband, the comb of signal recycling resonances is shifted by 1020 Hz to the right, thus the -72nd signal recycling resonance is centered around lower signal recycling sideband. Consequently the complete picture in the lower plot of Figure 2.3 is just mirrored at the carrier frequency.

Light field	lower MI SB	lower SR SB	carrier	upper SR	sideband
SR tuning = +510 Hz	-702 Hz	+1020 Hz	+510 Hz	0 Hz	+1722 Hz
SR tuning = -510 Hz	-1722 Hz	0 Hz	-510 Hz	-1020 Hz	+702 Hz

**Table 2.1.:** A summary of the resonance condition of the important light fields at the dark-port for a positive and negative detuning of the signal recycling cavity. The given values indicate the distance of the light field from the center of the nearest resonance peak.

Table 2.1 gives an overview of the resonance condition of the light fields of interest inside the dual recycled interferometer. Provided that any kind of technical noise is impressed equally onto the lower and the upper sideband of each, MI and SR modulation, the detected signals at the dark-port, which originate from the beat of the two sidebands with the carrier field, should be equivalent for positive and negative detuning. That is also the reason why all the gains of the control loops can stay the same for both cases and no adjustments of any control system is required.

Figure 2.12 shows a measurement of the sensitivity for a positive (blue trace) and a negative (red trace) detuning of the signal recycling cavity of 510 Hz. Apart from a few line features an astoundingly agreement is found.

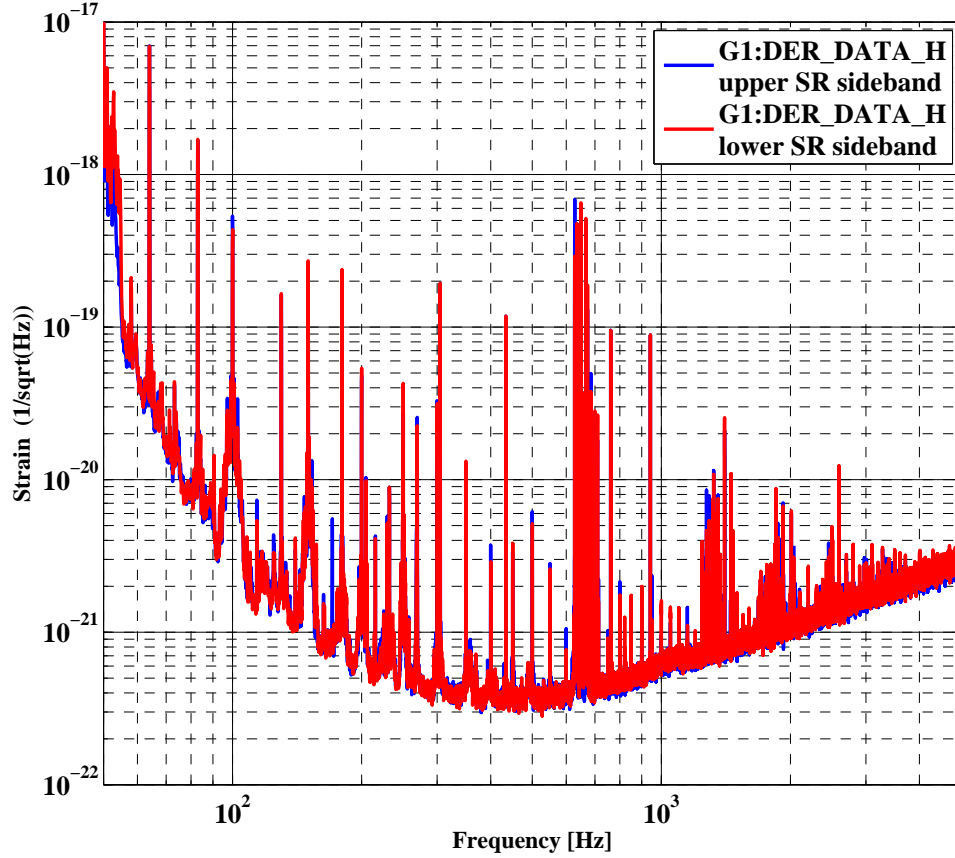


**Figure 2.12.:** Comparison of the sensitivity of GEO 600 for two different operating points of detuned signal recycling. The blue trace corresponds to a nominal tuning frequency of +510 Hz, while the red trace represents a negative detuning frequency of -510 Hz.

## 2.9. Summary

We developed and demonstrated a new technique for rapidly changing the signal recycled GEO 600 gravitational wave detector from the detuned to the tuned operating state. With this method, the signal recycling mirror is shifted accurately between two positions within milliseconds. This allowed for jumping with the signal recycling mirror from a position corresponding to a positive detuning of 510 Hz to a position corresponding to the tuned case and also from a positive detuning of 510 Hz to the corresponding negative detuning of  $-510$  Hz. The method is generally applicable and only limited by the strength of the actuators used for longitudinal control of the signal recycling mirror.

A comparison of tuned and detuned (510 Hz) signal recycling was given. The measurements of the optical gain for the tuned case show that the maximum in the signal response is shifted to DC. In the tuned case the rms of the signal in the Q quadrature is reduced by a factor of 12. The measurement of various noise couplings to the gravitational wave channels were performed for tuned and detuned signal recycling. The transfer functions are shown to be significantly different. For most of the noise sources (except laser frequency noise) we found the magnitude of couplings being strongly decreased in tuned signal recycling. Furthermore in the tuned case the complexity of transfer functions seems to be, at least for some couplings, slightly reduced.

In the future we will try to improve the simulations of the noise couplings in order to reproduce the measured results. A deeper understanding of the complex noise couplings, originating from imbalanced sidebands, is not only important for commissioning of the current interferometers, but also essential for the design of next generation gravitational wave detectors.



## Chapter 3.

# Scattered light problems in interferometric gravitational wave detectors

### 3.1. Introduction

Stray light problems have been encountered during the commissioning of all currently operating large scale gravitational wave detectors. The underlying principle of all these interferometers is to make an extremely sensitive phase measurement. Therefore even tiny stray light contributions with a different or varying phase will harm the measurement. The currently achieved sensitivity of GEO 600 can already be spoiled by stray light of the order  $10^{-20}$  W (!).<sup>1</sup>

A well-known manifestation of stray light noise is the so called *scattering shoulder* which has been observed in many detectors independent of their topology, as shown in Figure 3.1. A shoulder was observed in the VIRGO and LIGO instruments, which are power recycled Michelson interferometers with arm cavities, as well as in the folded arm GEO 600 configuration with and without signal recycling.

Stray light problems have already been observed in former interferometers like the 30 m-prototype in Garching. However, there the scattering was caused by the core optics of

---

<sup>1</sup>GEO 600 currently reaches a displacement sensitivity of  $3 \cdot 10^{-19}$  m/ $\sqrt{\text{Hz}}$  for an end mirror (MCe, MCn), which corresponds to an accuracy of the phase readout of,  $\phi = 4\pi \cdot 3 \cdot 10^{-19}$  m/ $\sqrt{\text{Hz}}/\lambda \approx 3.5 \cdot 10^{-12}$  rad/ $\sqrt{\text{Hz}}$ . If we now assume the carrier light inside the Michelson interferometer to be represented by  $E_C$  with the amplitude  $A_C$ , we can calculate which minimal amplitude,  $A_S$ , of a potential stray light field  $E_S$  is required in order to shift the phase of the total field  $E_T = E_C + E_S$  by  $\phi$ . Assuming  $E_C$  and  $E_S$  to be 90 degrees out of phase we get  $A_S = A_C \cdot \tan(\phi)$ . With the actual intra cavity power  $A_C = 2.7$  kW we get minimal stray light power of  $A_S^2 \approx 3 \cdot 10^{-20}$  W.

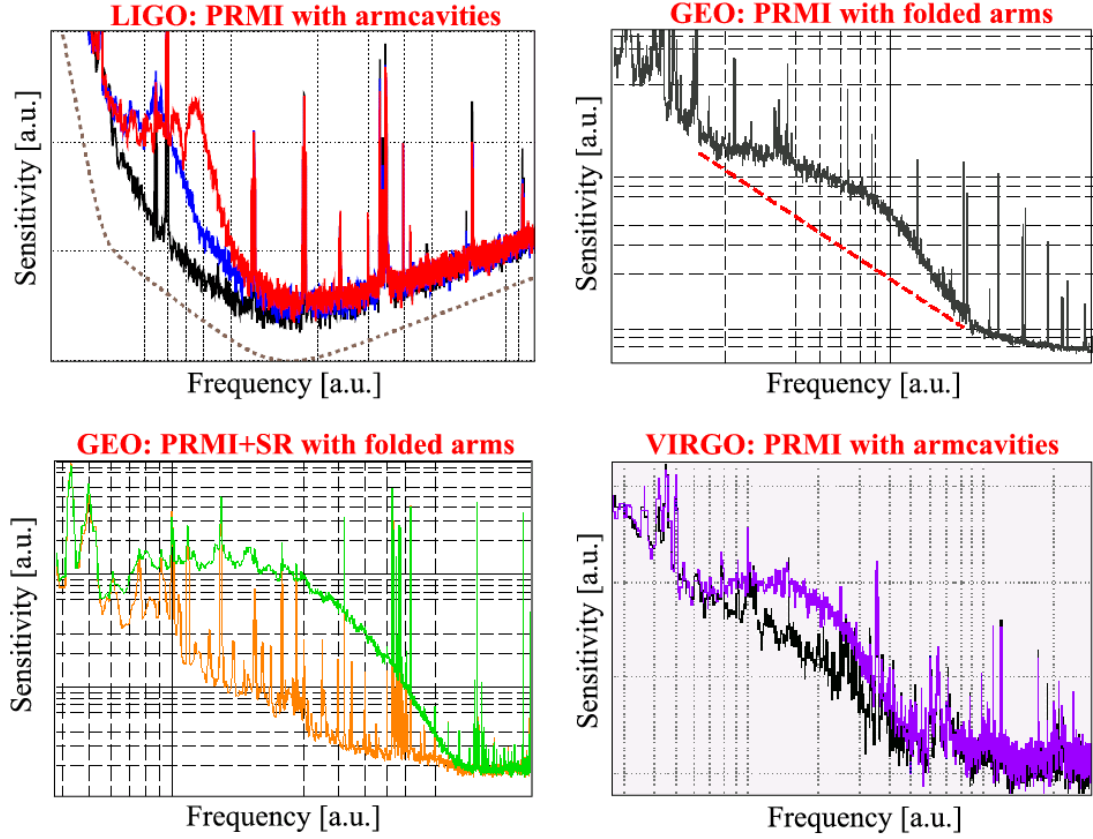


**Figure 3.1.:** In all interferometric gravitational wave detectors stray light is showing up in shape of a scattering shoulder. *UPPER LEFT PLOT:* Stray light shoulder in the LIGO Livingston detector, which is a power recycled Michelson interferometer of 4km arm length using arm cavities [LIGO05]. *UPPER RIGHT PLOT:* Stray light shoulder in the GEO 600 detector, which was at the time shown here a power recycled Michelson interferometer using single folded arms of 600 m length. *LOWER LEFT PLOT:* Stray light shoulder in the dual recycled GEO 600 detector, which is a power and signal recycled Michelson interferometer with 600 m long folded arms. *LOWER RIGHT PLOT:* Stray light shoulder in the VIRGO detector, which is a power recycled Michelson interferometer of 3km arm length using arm cavities [ILIAS06]. All four subplots have logarithmic x and y-axis.



the interferometer, i.e. the Herriot delay lines [Winkler]. The effect scattered light interacting with the walls of the vacuum vessel is theoretical described in [Vinet96]. In more recent times in the Japanese Tama300 detector stray light reflecting from the vacuum tubes was experimentally observed and characterized [Takahaschi04].

Learned from the experience collected in the prototypes, both the core optics and the beam tube of GEO 600 have been designed with great care with respect to stray light. So far there was no indication for stray light problems related to either the tube or the main optics.

The scattered light contributions observed in GEO 600 seem to originate from auxiliary beam paths where light is intentionally coupled out of the main interferometer for the purpose of sensing of the angular and longitudinal degrees of freedom. If some light from these paths is scattered back towards the interferometer it can reenter the main interferometer beam path. This light has, depending on the optical path length outside the interferometer, a shifted phase that varies in time with respect to the original light and is detected as noise in the output.

This chapter describes the experience with scattered light in the GEO 600 detector from the last two years. Powerful tools for observation, identification and elimination of stray light limiting the sensitivity of the GEO 600 detector have been developed and will be presented in this chapter.

## 3.2. Controlled stray light injections

This section describes experiments done with the goal to verify the general understanding of the stray lights effects observed in GEO 600. This is done by controlled generation of stray light in auxiliary beam pathes outside the vacuum system. For the experiments shown in this section the auxiliary path behind MFn and the one on the SR bench (a beam originating from a reflection on the AR coated side of the beam splitter) are used (see Appendix D for an optical layout of GEO 600).

### 3.2.1. How to produce stray light sowing up in $H$ at 1 kHz

The scattering noise shoulders observed in GEO 600 extend to high frequencies of up to about 1 kHz (see for example Figure 3.6). In order to generate stray light effects inside

the GW detector at a frequency of 1 kHz one can image two ways:

- **The "high frequency small amplitude" scenario:** An optical component moving with a frequency of 1 kHz only needs to move by a fraction of the laser wavelength, in our case a micron. In presence of acoustical and seismic excitation most optical components, mounted in a standard way onto any optical table, show some movement at high frequencies, i.e. their resonance frequencies.
- **The "low frequency large amplitude" scenario:** An optical component moving with a very low frequency but with an large amplitude. Even though all suspension in GEO 600 are damped at their resonance frequencies they show a significant movement at low frequencies. Suppose a suspended optic with a resonance frequency of 1 Hz moves with an amplitude of 0.25 mm, then this will, as it will be shown in Equation 3.2.3, generate stray light with a phase shift of  $2000 \cdot \pi$  showing up at 1 kHz in the sensitivity.

These two scenarios are extremes and of course an intermediate state, for example an component moving with an amplitude of 10 microns and a frequency of 25 Hz, would also be able to produce a stray light component showing up at a frequency of 1 kHz in the sensitivity. Often the stray light noise originates from number different vibrations at different frequencies. If for example the excess stray light is originating from a beam director on an optical table the surface of the mirror will at least to some amount vibrate with all kind of frequencies corresponding to the resonance frequencies of the optical table, the mirror mount and the mirror itself. Since the movement of the beam director has to be measured with respect to the main interferometer, which is moving up to several tens of microns at frequencies around 1 Hz in addition to the small amplitude high frequency movement we get also a low frequency large amplitude component.<sup>2</sup>

### 3.2.2. A device for controlled stray light generation

It is desirable to prove whether the scattered light we find in the GEO 600 detector can really be described fully by the picture of a moving optical component. This can be done by placing a scattering surface in an auxiliary beam path and moving the surface of the

---

<sup>2</sup>A third mechanism for stray light noise generation is known, but was so far not observed in GEO 600: Laser frequency noise in combination with stray light that travels a different path length with respect to the main beam can create stray light noise even without any moving component.

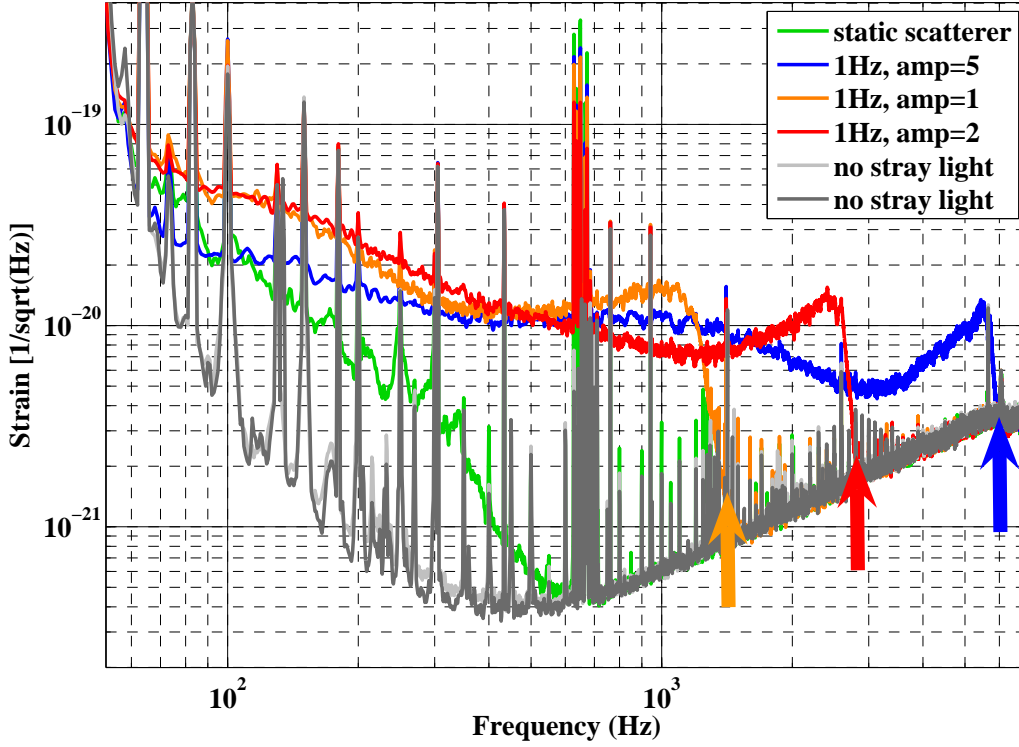


**Figure 3.2.:** Controlled forced scattering at the signal recycling bench: driving the stray light source with a triangular voltage of 1 Hz and amplitudes in the millimeter range. The two gray traces show the reference sensitivity for no stray light present. The green curve represents the scattered light contribution to the sensitivity for the speaker being installed but not driven with any signal. We see the usual scattering shoulder originating from the relative movement of the interferometer and the acoustically excited speaker diaphragm. The traces in orange, red and blue indicate the speaker driven with 1 Hz and different amplitudes. The cutoff frequency of the orange shoulder is around 1.3 kHz which corresponds to an amplitude of the movement of about 0.35 mm of the cone surface. When the amplitude of the triangular is increased by a factor of 2 (red trace) the cutoff frequency is doubled to 2.6 kHz as well. When the amplitude is further increased to a factor of 5 a cutoff frequency of about 5.5 kHz is observed which corresponds to a peak to peak movement of the scattering source of nearly 1.5 mm. This is already quite a large amplitude for the speaker and is probably the reason for the non-linearity of the observed cutoff frequency. Overall this experiment confirms our present understanding of the low frequency large amplitude scenario.

stray light source in a controlled way. We realized such a controllable scattering source

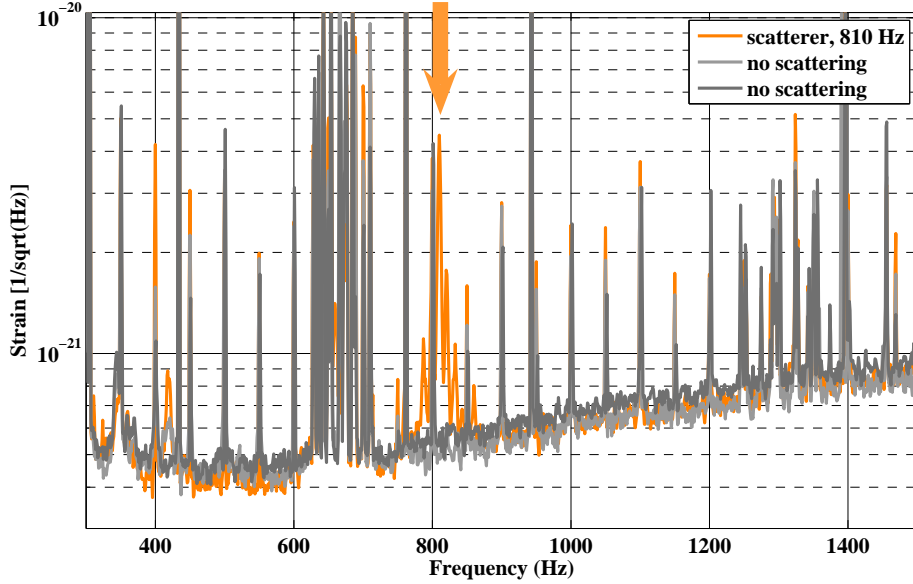


**Figure 3.3.:** Controlled forced scattering from the beam path transmitted through MFn: The two gray traces show reference spectra without any scattered light contribution. The orange curve represents a time when the stray light source (speaker) was driven with 810 Hz and an amplitude of less than a laser wavelength. A noise peak at 810 Hz surrounded by a strong sideband structure is observed.

by using an commercial low-cost loudspeaker driven by a commercial audio amplifier. In order to increase the backscattering amplitude on the one hand and to reduce the risk of thermal damage of the speaker caused by absorption of the laser light on the other hand we chose a speaker with a rough and silvery metal diaphragm (anodised aluminium). In addition we used the bare speaker without any housing to reduce the sound emission of the speaker. A speaker with high compliance was chosen to allow a total travel of several millimeters. The scattering efficiency was maximized by positioning the surface of the speaker close to a beam waist (see Section 3.6). The speaker was fixed into a strong metal frame with a mount to allow a rigid connection to the optical table.

### 3.2.3. Low frequency large amplitude scenario

First we want to verify that a low frequency movement of the speaker cone with a large amplitude produces a smooth scattering shoulder. Figure 3.2 shows the corresponding measurement, where the speaker was driven with triangular voltage of a frequency of 1 Hz. Shown are calibrated strain sensitivities for two reference times without any stray light contribution (gray), a reference for the static scattering source, where the speaker was installed but not driven (green) and three times when the speaker was driven in a controlled way with amplitudes in the mm-range. The static speaker already produces a strong scattering shoulder originating from the relative movement of the speaker surface and the suspended main interferometer. The cutoff frequency,  $f_{\text{cutoff}}$ , can roughly be estimated by the following relation

$$f_{\text{cutoff}} \approx 4 \cdot f_{\text{sp}} \cdot \frac{A_{\text{sp}}}{\lambda_{\text{laser}}}, \quad (3.1)$$

where  $f_{\text{sp}}$  is the frequency of the signal the speaker is driven by,  $A_{\text{sp}}$  is the peak to peak amplitude of the diaphragm and  $\lambda_{\text{laser}}$  is the wavelength of the laser. The factor 4 originates from a factor of 2, accounting for the fact that the light hitting the speaker and being reflected travels twice the distance the diaphragm moves, and a second factor of 2, originating from the fact that during a single period of the triangular signal 2 times the peak-peak movement is covered. For the measurement corresponding to the red trace of Figure 3.2 an amplitude twice as large as for the measurement corresponding to the orange trace was chosen. In good agreement the cutoff frequency of the red trace, 2.6 kHz, is found to be twice as large as the cutoff frequency of the orange curve, 1.3 kHz. However, caused by the non linear response of the speaker for large amplitudes, we find for the blue trace instead of the expected cutoff frequency of 6.5 kHz only 5.5 kHz. However, overall it can be stated that our understanding of the low frequency large amplitude scenario is confirmed by this measurement.

### 3.2.4. High frequency low amplitude scenario

The next measurement was done to prove the high frequency low amplitude scenario. The speaker was driven by a triangular signal with a frequency of 810 Hz and an amplitude much smaller than one laser wavelength<sup>3</sup>. Figure 3.3 shows this measurement

<sup>3</sup>That the amplitude was much smaller than the laser wavelength could be determined by the fact that no additional line in sensitivity was observed at 1620 Hz.

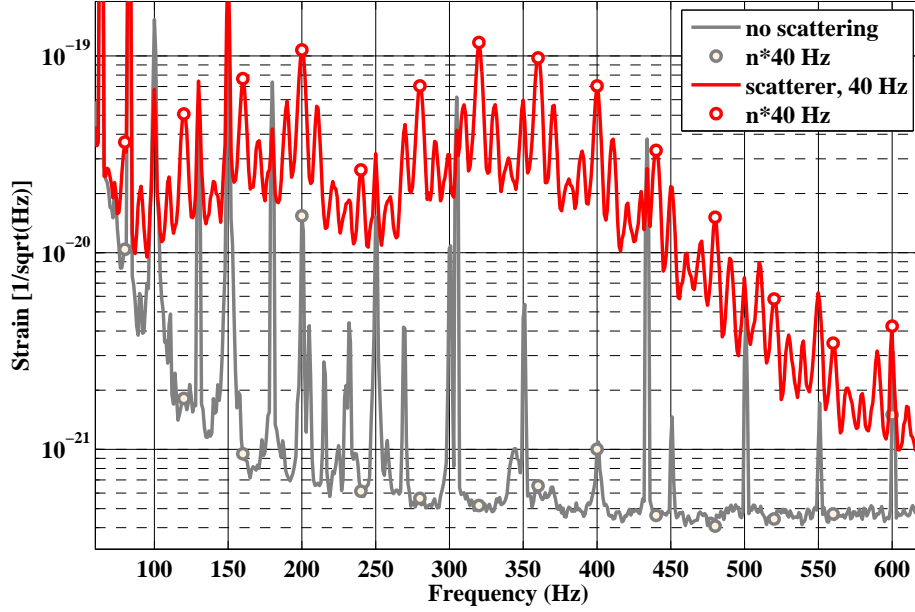


**Figure 3.4.:** Scattered light injection by controlled movement of the speaker surfaces. A triangle with a frequency of 40 Hz and an amplitude of a few ten microns.

in detail. The two gray traces represent reference spectra in the absence of any stray light contribution. The orange curve represents the time of the stray light injection. A large noise peak is generated with a strong sideband structure around it. The dominant sideband frequencies are 10 and 23 Hz with amplitudes of 50 and 25 % of the center peak, respectively. The sideband structure represents the up-converted low frequency movement of the speaker relative to the main interferometer. Comparisons of measurements for stray light injections at different frequency have shown identical sideband structures for all frequencies. The same is also true for measurements of injections with amplitudes of a few laser wavelengths, thus the first few harmonic frequencies with their sideband structures could be observed.

### 3.2.5. Combination of the two scenarios

Figure 3.4 shows a measurement where the speaker was driven with a frequency of 40 Hz and an amplitude of several tens of microns. As expected we find a comb of harmonics of 40 Hz (red circles). Each line of a frequency  $n \cdot 40$  Hz is surrounded by the same

sideband structure that was already observed in Figure 3.3. That is why each line is accompanied by 10 Hz sidebands. Altogether this excitation of the speaker diaphragm gives a scattering shoulder containing strong peaks at all harmonic frequencies of 40 Hz. As we will see later (Section 3.7) this stray light injection shows some similarities to an observed stray light phenomenon called *ripple noise*.

### 3.2.6. Summary of the stray light injections

We found a simple and very efficient way to generate stray light in an controlled way by using the cone of a loudspeaker as scattering surface. By carrying out stray light injections with various amplitudes and frequencies we found the excess noise in the sensitivity originating from stray light to qualitatively match our expectations. This means that we understand the basic principle of scattered light problems and there seems no "magic" about them.

## 3.3. Indications for a stray light limited sensitivity

During the commissioning of a gravitational wave detector one of the main problems regarding stray light is to find out whether the current detector sensitivity is in any frequency band limited by stray light effects. The tiny amounts of stray light that can already limit the sensitivity of GEO 600 are hardly detectable by independent sensors.

Therefore the most promising method to identify whether there is any stray light contribution is to use the specific signature of the stray light in the sensitivity of the GW detector. In GEO we found stray light always to show up in the sensitivity with three specific characteristics:

- **Non-stationarity on short time scales:** The noise originating from stray light is in many cases found to be highly non-stationary on second's time scales. In contrast to most of the technical noise, for instance feedback or electrical noises, and most of the fundamental noise, for instance thermal noise or shot noise, which are rather stationary. Figure 3.5 shows spectrograms of the uncalibrated error signal of the differential arm length servo for a time without any contribution from stray light and a time of intentionally increased scattered light contribution. The stray light shows up as strongly varying broadband excess noise. Not only the size of



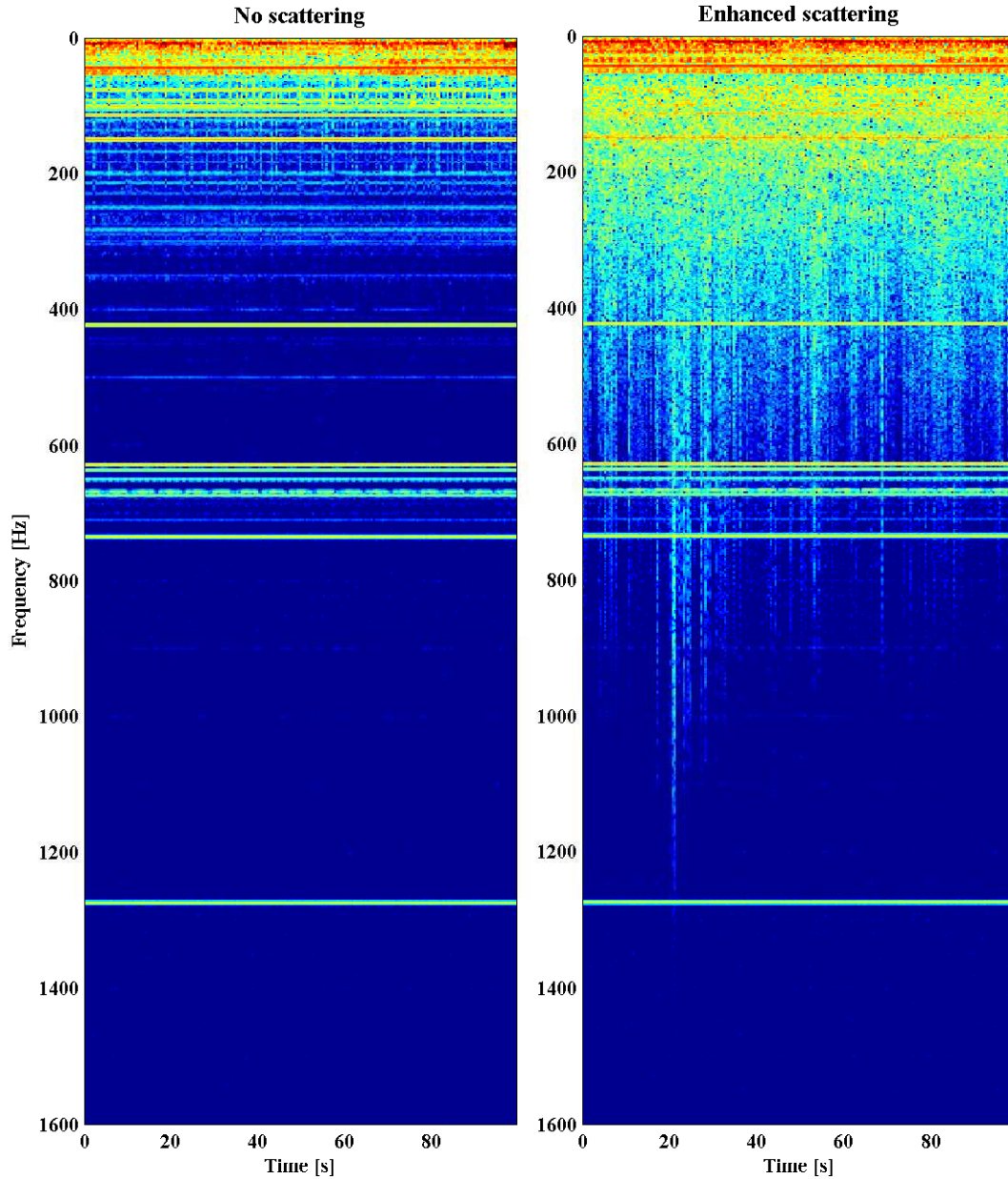


**Figure 3.5.:** Spectrograms of the uncalibrated error signal (P quadrature) of the differential arm length servo. The left hand plot shows 100 seconds of "clean" data without enhanced scattered light limiting the sensitivity. For frequencies above a few hundred the sensitivity is reasonably stationary. The right plot shows 100 seconds of data from a time when the scattering was intentionally enhanced. Over most of the detection band the sensitivity varies strongly on the time scale of a second.



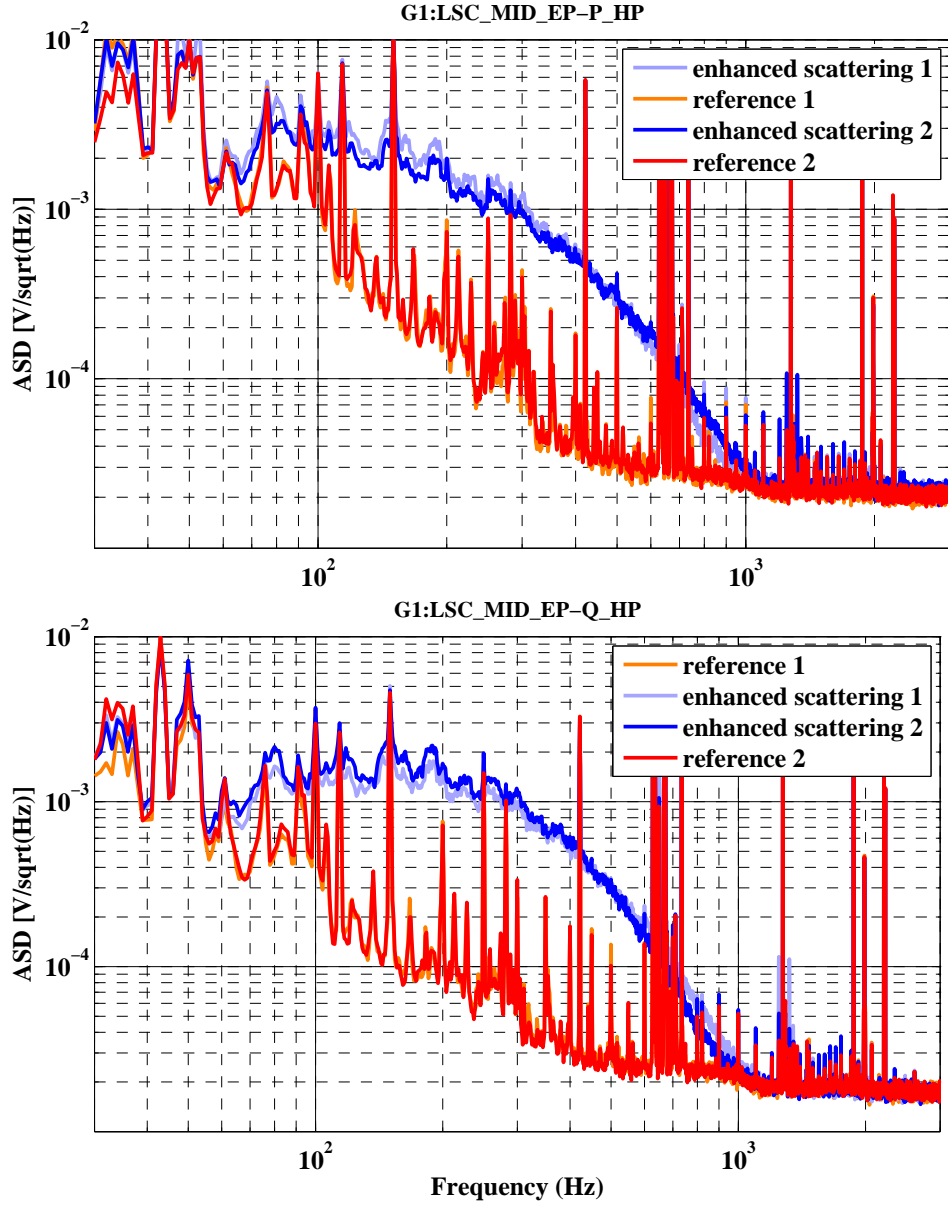


**Figure 3.6.:** Spectra of the uncalibrated error signal of the differential arm length servo. Shown are both output quadratures, P and Q, for each two times of "clean" data (minimal noise contribution from scattering) in red and orange and two times of enhanced scattering limiting the sensitivity from 60 to 1000 Hz (blue and light blue). The stray light causes excess noise in the typical shoulder shape. Below 100 Hz the stray light is suppressed by the loop gain of the servo controlling the differential arm length of the Michelson interferometer.

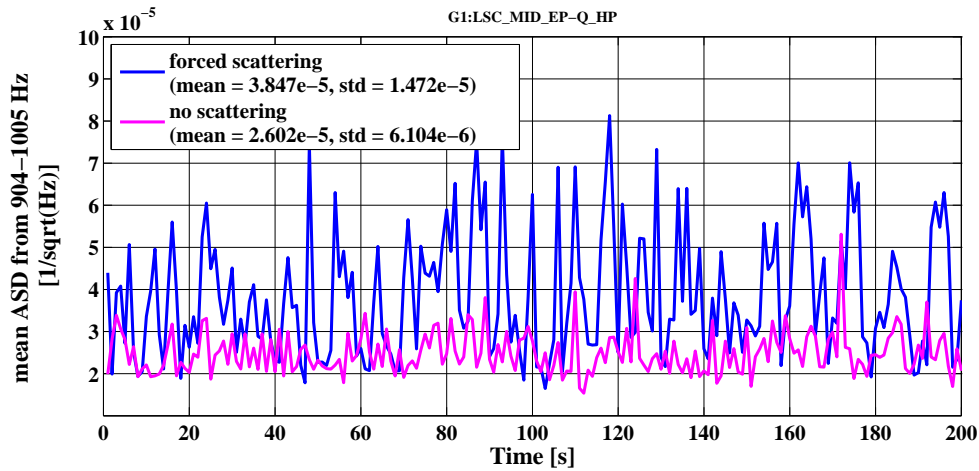


**Figure 3.7.:** Time series of the mean ASD of the uncalibrated detector sensitivity in the band from 904 to 1005 Hz. The pink trace represents a time when the frequency band was not limited by stray light, while the blue trace indicates a time of enhanced scattering. If stray light is present not only the mean of the time series is larger but also the standard deviation,  $\sigma$ , is strongly increased.

the scattered light noise changes but also the maximal effected frequency. Another way to look at the stationarity of the noise is plotted in Figure 3.7. Depicted are the time series of the mean ASD of the uncalibrated detector sensitivity in the band from 904 to 1005 Hz for two different times. The pink trace represents a time when the frequency band was not limited by stray light, while the blue trace indicates a time of enhanced scattering. If stray light is present not only the mean of the time series is larger but also the standard deviation,  $\sigma$ , is strongly increased.

- **The specific sound of stray light:** An excellent tool to judge the stationarity of a signal on short time scales is the human ear. Listening to a whitened signal representing the sensitivity was found to be the most powerful tool for identifying scattered light noise. At least in GEO stray light had a very specific sound. Two audio examples, of the sound of the sensitivity of GEO 600 for a time of clean data and a time when excess noise from stray light was present, can be found on the CD-ROM (Multimedia Appendix) at the end of this thesis.<sup>4</sup>

<sup>4</sup>The unique sound of stray light is hard to describe in words. Probably everybody of the GEO commissioning team would describe it in a different way. Some call it "wooshing", others compare it

- **The typical scattering shoulder:** As already mentioned in Section 3.1 noise from stray light is often found to show up as a shoulder of excess noise. As Figure 3.6 indicates the shoulder starts at low frequency and then extends to a certain frequencies called the *cutoff frequency*. In many cases the cutoff frequency scales with the size of the shoulder at low frequencies as one can see in the righthand spectrogram of Figure 3.5.

Even though none of these three points alone can give a reliable indication, all three together give a pretty strong indication for stray light limiting the sensitivity of the GW detector. If all three indicators suggest the presence of stray light, the next step is to find the source and coupling path of the stray light.

### 3.4. The filter experiment: A reliable method to identify the source of stray light

In the commissioning of the GEO 600 detector the so called *filter experiment* was found to be the best method to identify and locate limiting scattering paths [Hild06a]. Many potential scattering sources such as the auxiliary beam paths used for control and diagnosis of the detector are located outside the vacuum system. Auxiliary beam paths used for longitudinal and angular control of the interferometer usually contain many optical components like for instance lenses, telescopes or photodiodes, each of these a potential source of scattering.

Let us consider a simplified setup as it is depicted in Figure 3.8 to explain how the filter experiment works. A fraction,  $A_0$ , of the light circulating in the main interferometer is entering the auxiliary beam path of interest. A potential source of stray light scatters the light amplitude  $A_0 \cdot k_1$  back towards the main interferometer, where  $k_1$  is the scattering coefficient. Usually only a small fraction of  $A_0 \cdot k_1 \cdot k_2$  then re-enters the main interferometer mode and is detected. If now an optical attenuator with the amplitude transmission of  $T_f$  is positioned between the main interferometer and the scattering source, first of all, the light incident on the scattering source is decreased and afterwards the scattered light going back into the interferometer is also attenuated. Overall the light amplitude re-entering the detection path is reduced from  $A_0 \cdot k_1 \cdot k_2$  to  $A_0 \cdot T_f^2 \cdot k_1 \cdot k_2$  by inserting the optical attenuator.

---

to an avalanche or a storm. I think the best way is to listen yourself.

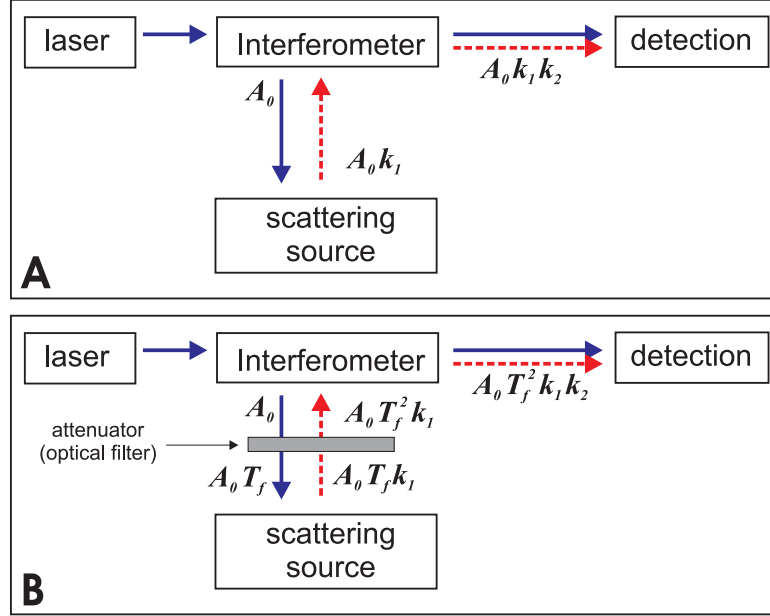


**Figure 3.8.:** Sketch of the filter experiment which provides an easy and reliable method to identify stray light limiting the sensitivity of the interferometer. **Figure A:** A fraction,  $A_0$ , of the light circulating in the interferometer leaves the main interferometer and enters an auxiliary beam path (for example used for alignment control). A scattering source in this auxiliary path would scatter  $A_0 \cdot k_1$  back towards the interferometer, where  $k_1$  is the scattering coefficient. Assuming the coefficient for the coupling back into the main interferometer to be  $k_2$  a total light amplitude of the scattered light of  $A_0 \cdot k_1 \cdot k_2$  is detected. **Figure B:** If an optical attenuator with the amplitude transmission of  $T_f$  is inserted between the main interferometer and the source of stray light the detected stray light amplitude is decreased by  $T_f^2$ .

If, for example, a neutral density filter is used as an attenuator, which has a power transmission of about 60 % at  $\lambda = 1064 \text{ nm}$  we expect the sensitivity limiting stray light contribution to go down by 60 % as well. Now by putting in the filter at different positions in the auxiliary path we can identify component by component their contribution to the detected scattering. However, as the inserted filter is an additional potential source for scattering it is necessary to take great care of the quality and cleanliness of the filter in order to not spoil the measurements. To decrease the chance of added scattering the filter must not be installed under normal incidence. In addition, as it is shown in Section 3.6 it is essential to avoid placing the filter near a beam waist.

Of course in the case the light in the auxiliary beam is used for automatic control of the interferometer it is necessary to adjust the gain of the servo in order to compensate for less light power hitting the photo detector.

#### 3.4.1. Limitations of the filter experiment

Obviously it is not easily possible to insert an attenuator to any beam path inside the vacuum system. Therefore the filter experiment is limited to the parts of the auxiliary beams that are located outside the vacuum system. Another restriction can be given for scattering sources in the main detection path: For many conditions the potential benefit from reducing stray light in this case is compensated by less signal on the main photo detector. If we take for example a sensitivity which is at the frequencies of interest limited to equal shares by stray light and shot noise the stray light contribution<sup>5</sup> will decrease by  $T_f$  as well as the shot noise level will increase by  $T_f$ .

Finally the strongest limitation of the method is that only stray light contributions that actually limit the total detector noise can be identified. As long as the stray light does not contribute significantly to the detector noise we have no measure whether the stray light was reduced or not. This method does not allow for projecting the stray light noise.

---

<sup>5</sup>In opposite to the scenario described in Figure 3.8, when the attenuator is placed in the detection path the scattered light is only attenuated once.

### 3.5. Experience of stray light problems in GEO

In fall 2004 the sensitivity of GEO 600 was found to be limited by stray light induced noise over a wide range of the detection band. A typical scattering shoulder with a cutoff frequency of about 1.2 kHz was traced back to backscattering on the signal recycling bench. The steps involved in reducing the stray light on this optical table are a good example how to eliminate stray light problems in the optical setup of an auxiliary path.

On the signal recycling bench a pick-off beam, originating from the beam splitter AR coating in the east arm, is detected and used for longitudinal control and auto alignment of the signal recycling mirror (see Figure D.1). Figure 3.9A shows the original layout of the bench as it was present in late summer 2004. The beam leaves the vacuum system through an AR coated window and passes an AR coated focusing lens L1. Afterwards a set of two beam steering mirrors (bd1, bd2) is used to align the beam onto the second AR coated lens L2 of the beam telescope and a 2-axis galvo-scanner. Finally the beam is detected by a quadrant diode. With the aid of the filter experiment we identified L2 and the galvo scanner as sources of limiting stray light noise. A reduction of the stray light was achieved by replacing L2 and the galvo scanner by a high quality beam director<sup>6</sup>. In a next step we found bd3 still causing a measurable amount of stray light coupling to the GW channel. This was mainly caused by the fact that bd3 was located close to a beam waist, which is in terms of stray light in a very critical position for any kind of optical elements, regardless of their quality (see Section 3.6). Therefore the quadrant diode was moved in a next step closer towards L1 in order to avoid the presence of any beam waist on the SR bench. The corresponding layout which was used during the S4 science run is depicted in Figure 3.9C. Figure 3.10 shows the sensitivity improvements from autumn 2004 achieved by minimizing stray light from the signal recycling bench.

The curious reader might ask, why the optical layout of the bench was reorganized, instead of simply attenuating the stray light by installing several optical attenuators (permanent filter experiment). In general such an approach should have worked out, even though it always feels better to eliminate the source of a problem instead of suppressing the consequences. However, in the special case of the GEO SR bench any attenuation of the light level would have caused an increased feedback noise of the signal recycling

---

<sup>6</sup>In GEO galvo scanners are commonly used in front of all quadrant diodes in order to make sure the beams are well centered on the diodes all the time. However, after taking out the scanner from the signal recycling bench no excess noise was found in any of the related control loops.

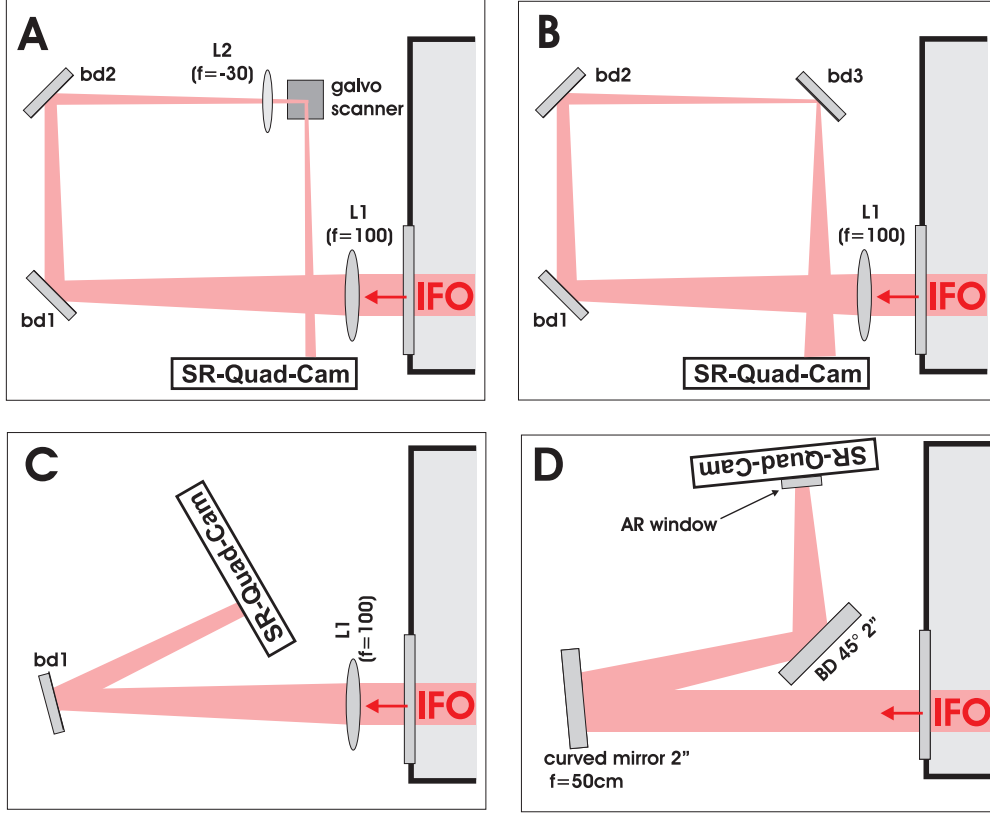


**Figure 3.9.:** Progression of the optical layout of the signal recycling bench in order to reduce stray light. **A:** Original layout of the bench from summer 2004. The beam leaves the vacuum system through a window, passes a focusing lens L1 and two steering mirrors (bd1, bd2) which are used to align the beam to the second lens L2 of the beam telescope and 2 axis galvo-scanner. Finally the beam is detected by a quadrant diode. **B:** With the aid of the filter experiment we identified L2 and the galvo scanner as sources of limiting stray light noise. Both components were taken out and replaced by a single high quality mirror (bd3). **C:** S4 configuration. In a next step we found bd3 still causing a measurable amount of stray light. This was mainly caused by the fact that bd3 was located close to a beam waist, which is in terms of stray light in a very critical position for any kind of optical elements, regardless of their quality (see Sec.3.6). Therefore the quadrant diode was moved in a next step closer towards L1 in order to avoid the presence of a beam waist on the SR bench. **D:** S5 configuration. At the start of 2006 we found again stray light limiting the improved sensitivity of GEO 600. The un-coated window of the quadrad photodiode was replaced by an AR coated fused silica window. In a second step L1 was replaced by a curved 2" diameter mirror.

longitudinal loop which is limited by shot noise for frequencies of our interest. As the feedback noise of this loop is already close to limiting the overall sensitivity of GEO 600 in the few hundred Hz region, any reduction of the stray light noise by attenuating the beam path would have been compensated by larger feedback noise in the attenuated setup.

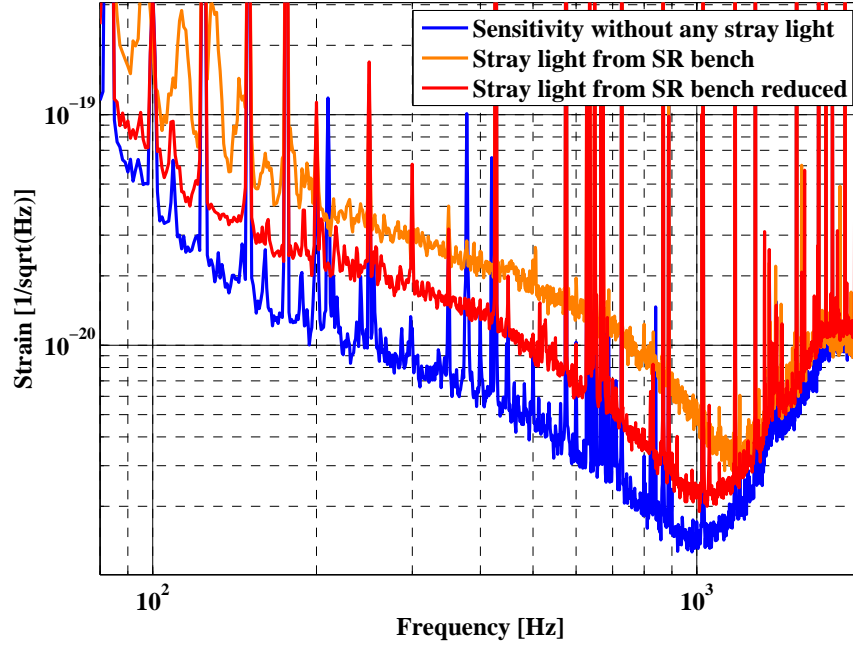


**Figure 3.10.:** Sensitivity progress of GEO 600 from autumn 2004. By eliminating stray light from the signal recycling bench the sensitivity of the GEO 600 detector was improved by about a factor of 3 for frequencies between 100 and 1000 Hz.

After S4 GEO's sensitivity was improved by about a factor of 10 in the few hundred Hz region at the beginning of 2006 again scattered light originating from the SR bench was found to limit the sensitivity. The dominating source of stray light was the low quality window of the quadrant photo detector. The original window was cut off and the diode was clamped in between two copper plates of which one was holding a 1" AR coated fused silica window. The AUTOCAD drawing of this diode holder can be found in Appendix C. The major difficulty of realizing this setup is to cleanly cut off the window of the quadrant diode. In contrast to small single element diodes where the window can easily be taken off, removing the window of a large quadrant diode poses difficulties. Due to the much larger ratio of diameter to thickness of the housing it turns



out to be nearly impossible to cut off the window without partly cracking it and spilling many small splinters over the active area of the diode. The only reliable way to get rid of the splinters was found to be repeated rinsing the whole diode with a few milliliters of ethanol and immediately afterwards drying it with compressed nitrogen.

In a second step of improvement the lens (L1) was replaced by a high quality 2" curved mirror. There was no strong indication that L1 was causing any additional stray light noise. However, in contrast to a curved mirror lenses always have the disadvantage that a fraction of their surface is always perpendicular with respect to the incidence beam. Finally it has to be mentioned that all secondary beams, such as the reflected beam from the photodiode itself, have to be properly dumped.

### 3.6. The cat's eye effect

As already stated in the previous section one important experimental finding of our stray light investigations was that stray light sources positioned close to a beam waist caused the largest stray light contributions to the GEO 600 sensitivity. Analogous to the cat's eye effect the light scattered directly at a beam waist has exactly the right geometrical mode to reenter the main interferometer.

Figure 3.11 shows an illustrative example of an optical configuration which is similar to the signal recycling bench described in the previous section. The subplot 1 shows the setup with no stray light present. Inside the central cluster the main interferometer beam has an radius of  $\omega_{cc} \approx 1$  cm. A fraction of the beam leaves the interferometer at the beam splitter AR coating and is then focused down on the SR bench. With the drawn lens of 50 cm focal length an beam waist of  $\omega_0 \approx 17 \mu\text{m}$  is generated. For the following analysis we assume the light amplitude incident to the lens is  $A_0$  and all beams have an gaussian profile at all positions. For all scenarios described below we will use the same source of scattering which is a square area of  $5 \times 5 \mu\text{m}$  which is assumed to scatter proportional to  $\cos(\varphi)$  into the solid angle, where  $\varphi = 0$  corresponds to normal incidence.

Figure 3.11.2 shows the situation for the scattering square directly located in the waist. Since the beam is so small at the waist,  $A_2$  which is the fraction of  $A_0$  incident to the

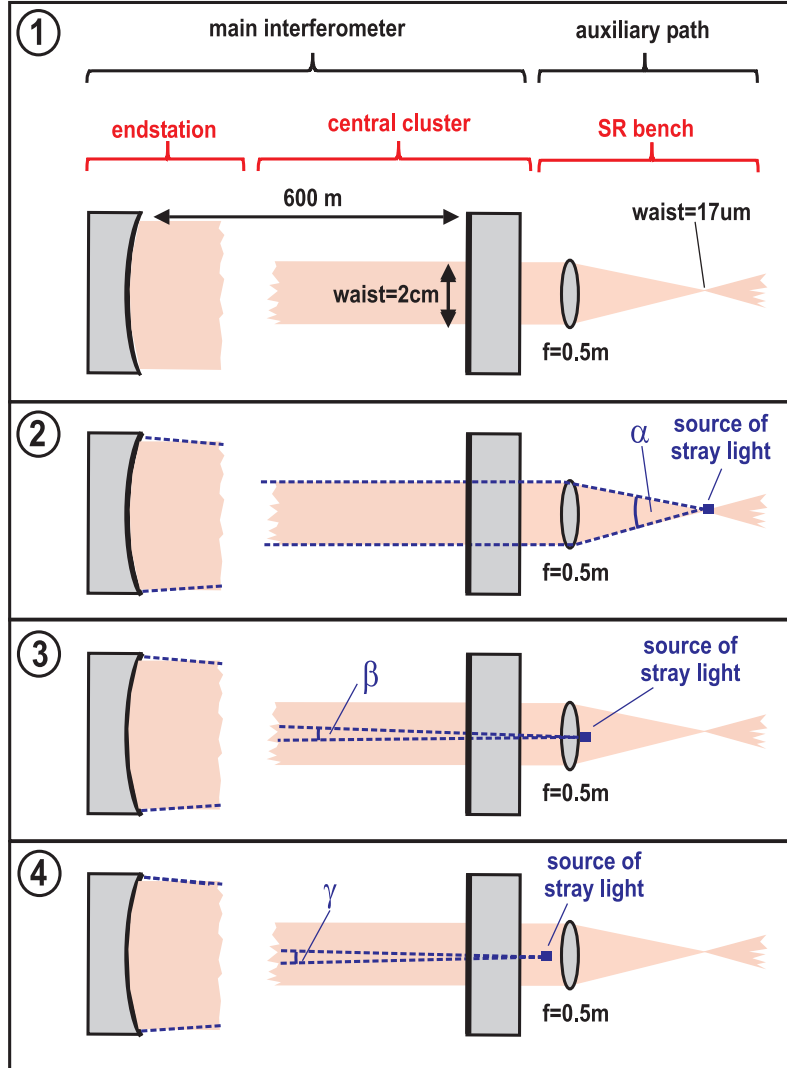


**Figure 3.11.:** Illustrating schematic of the cat's eye effect: The scattering efficiency of a scattering source strongly depends on its position in the auxiliary path. An extremely large back scattering efficiency is found for a stray light source sitting directly in the beam waist, because in that case first of all a large light power is reflected and secondly all light scattered back towards the lens reenters the main interferometer in the correct mode. A scattering source located right in the beam waist (panel 2) is found to have a  $1.6 \cdot 10^9$  larger backscattering efficiency than the same scattering source sitting in the non diverging beam in front of the lens (panel 4). A detailed description of the depicted scenarios can be found in the text.

scattering square, is quite large:

$$A_2 = 0.2 \cdot A_0. \quad (3.2)$$

All of  $A_2$  scattered back into  $\alpha$ , which is  $2.3^\circ$ , reenters the main interferometer and is transferred to the output.

The situation when the same scattering source is placed right behind the lens is shown in Figure 3.11.3. In this scenario  $A_3$  which is the fraction of  $A_0$  incident to the scattering square is much smaller than before due to the larger beam radius.

$$A_3 = 1.6 \cdot 10^{-7} \cdot A_0 \quad (3.3)$$

Furthermore, the light scattered back is to a large fraction not in the correct interferometer mode. An upper limit for the amount of light that can in principle<sup>7</sup> reenter the interferometer and being transferred to the output is given by  $\beta = 0.017$  which originates from the requirement that the stray light has at least to hit the far mirror (diameter = 18 cm) at a distance of 600 m. This means that the scattering efficiency will be very small in this case due to the small accepted angle  $\beta$ .

Finally in Figure 3.11.4 a scenario is depicted where the scattering square is placed on the left hand side of the lens in the parallel beam. The light amplitude  $A_4$  incident onto the square is, due to equal beam sizes, identical to  $A_3$ .

$$A_4 = 1.6 \cdot 10^{-7} \cdot A_0 \quad (3.4)$$

Also the angle of acceptance  $\gamma$  is equal to  $\beta$ .

The overall amount of light backscattered into  $\gamma$ ,  $A_{4\text{back}}$ , can be described by the following expression:

$$A_{4\text{back}} \propto A_4 \int_0^{\gamma/2} \cos(\varphi) d\varphi. \quad (3.5)$$

Analogously  $A_{3\text{back}}$  and  $A_{2\text{back}}$  can be calculated. If we normalize the results by  $A_{4\text{back}}$  we get the following normalized backscattering efficiencies.

Exactly at the beam waist the backscattering efficiency is 1.6 billion times larger than for a scattering surface at the lens. From this result we can derive the rule that we have

---

<sup>7</sup>Assuming all light is converted by mode healing from the signal recycling back into the ground mode.

Scenario	Efficiency of backscattering
2	$1.6 \cdot 10^9$
3, 4	1

**Table 3.1.:** Summary of the normalized backscattering efficiencies for the three scenarios depicted in Figure 3.11

to avoid placing optics exactly in the beam waist of any auxiliary beam path directly connected to the main interferometer, or even better to avoid the presence of any waist at all if possible.

### 3.7. A special class of stray light noise: the "ripples"

In this section a class of stray light noise is described, the so called "*ripples*". For two reasons these ripples are very interesting: First of all they have a noteworthy shape in the frequency domain and secondly this kind of stray light noise was limiting the sensitivity of the GEO 600 detector in the few hundred Hz range at least part time of S5.

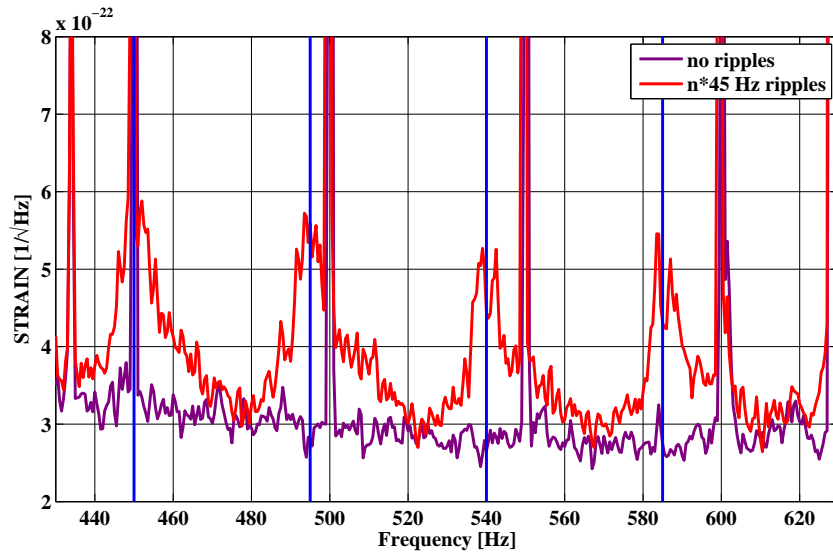


**Figure 3.12.:** Strain sensitivity of GEO 600 for a time when the  $n \cdot 45$  Hz ripple noise is present (red) and reference time (purple). The vertical blue lines indicate harmonic frequencies of 45 Hz.

During S5 excess noise was frequently observed that showed up in the few hundred Hz region of the sensitivity as a series of equidistant bumps. Figure 3.12 shows spectra of a reference time (purple) when no ripples were present and a time with ripple noise (red). As indicated by the blue vertical lines which are drawn at harmonic frequencies of 45 Hz the ripples show up in this case at  $n \cdot 45$  Hz. At the center frequency of the bumps the sensitivity is decreased by up to 80 %. The bumps have a FWHM of about 10 Hz and from the presence of their wings even in the middle between two bumps the sensitivity seems to be slightly decreased.

The  $n \cdot 45$  Hz ripples showed up during S5 in irregular intervals of several hours and were then present for about 20 minutes. Figure 3.13 depicts how the  $n \cdot 45$  Hz ripples shows up in the sensitivity. Plotted are spectrograms of  $H$  and the seismometer in the north end station. Both spectrograms are normalized by the overall average in each frequency bin. Reddish pixels indicate values larger than the average. Between hour 3 and 3.5 an excess noise is present at 45 Hz in the seismic. At the same time we see strong ripples at  $n \cdot 45$  Hz in the sensitivity of GEO 600. This observation led to the suspicion that stray light is generated at a seismically driven component in the north end building. This suspicion was further confirmed by the observation of a slight drift in the frequency of the ripples, which was also seen in the frequency of the seismic excitation, as shown in Figure 3.14.

The excess noise in the seismic was tracked down to a cooling fan of a turbo-pump. The fan was automatically controlled and switched on only when a certain threshold of the turbo-pump temperature was crossed. For further experiments the cooling fan was set to continuous operation in order to continuously generate ripples. In that condition a filter experiment was carried out on the optical table in the north endstation. Even with the beam leaving the vacuum completely blocked the ripples stayed constant in size. This for the first time in GEO 600 gives strong evidence for a stray light problem originating from inside the vacuum system.

Potential stray light sources inside TF<sub>n</sub> are the catcher of MF<sub>n</sub>, the tank walls and the curved and partly un-coated rim of the view port behind MF<sub>n</sub>. A series of experiments where the beam position on MF<sub>n</sub> was changed gave the result that the  $n \cdot 45$  Hz ripples are smallest when the beam is not centered on the mirror, but centered on the view port. This makes the view port to be the strongest suspect for being the stray light source. As shown in Figure 4.2 a significant fraction of the beam transmitted through

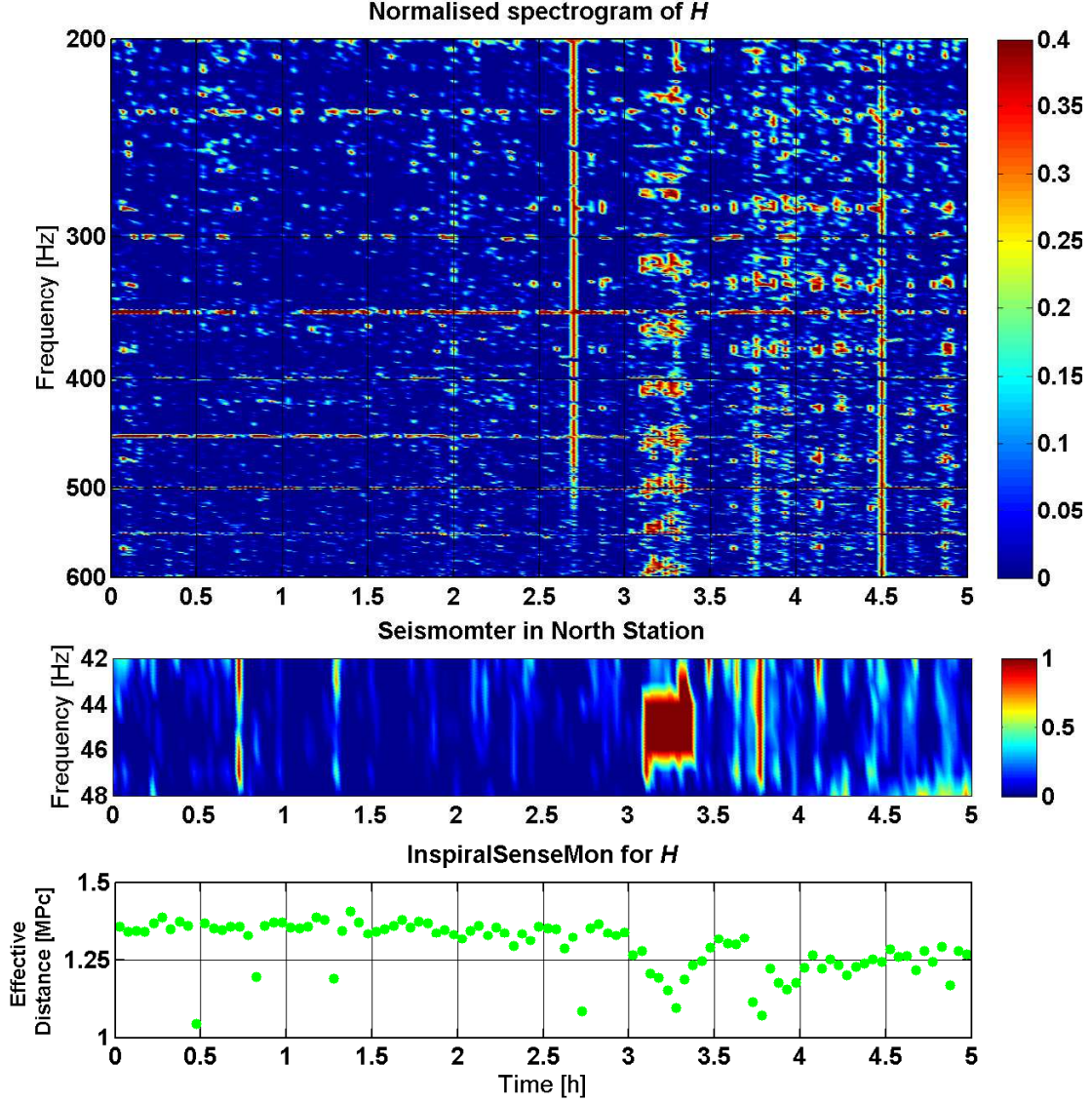


**Figure 3.13.:** Spectrograms of  $H$  and the seismometer in the north end station. Both spectrograms are normalized by the overall average in each frequency bin, thus the varying features are highlighted. Reddish pixels indicate values larger than the average. Between hour 3 and 3.5 an excess noise is present at 45 Hz in the seismic. At the same time we see strong ripples at  $n \cdot 45$  Hz in the sensitivity of GEO 600. The decrease in sensitivity can also be seen in the neutron-star-neutron-star (NSNS) inspiral horizon which is decreased by about 10% in the presence of the ripples. The NSNS inspiral horizon is calculated for neutron stars of 1.4 solar masses and optimal orientation for GEO 600.



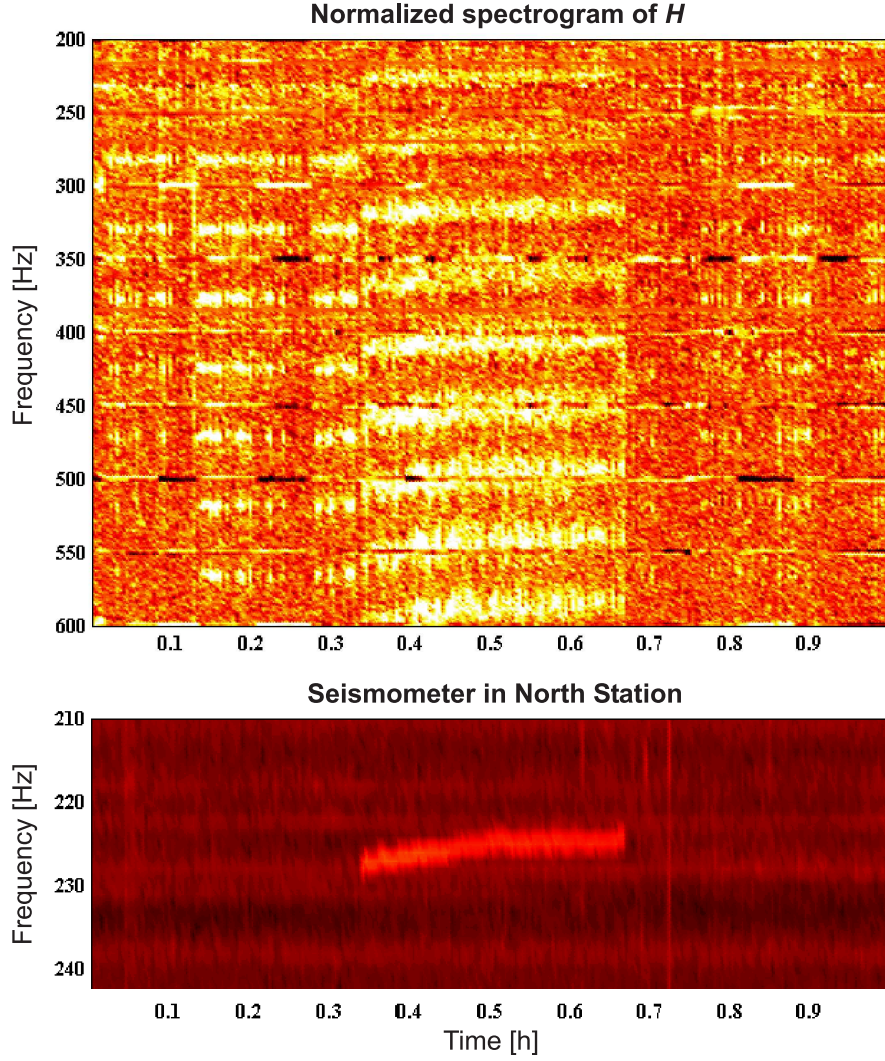


**Figure 3.14.:** Normalized spectrograms of  $H$  and the seismometer in the north end station. Orange pixels indicate the average value, black pixels show values below the average and white pixels indicate values above the average, i.e. excess noise. In  $H$  we find two different sets of ripple noise. The first class are weak ripples with frequencies corresponding to  $n*47$  Hz, present for example at hour 0.2, 0.3 and 0.9. The second class of ripple noises are the strong  $n*45$  Hz ripples, present in the period from hour 0.35 to 0.65. The frequency of this class changes slightly between hour 0.35 and hour 0.5. The same drift is observed in the fifth harmonic of 45 Hz in the seismometer signal from the north station. This gives a very strong indication for the  $n*45$  Hz ripples be generated by seismically driven stray light generation in the north end station.

MF<sub>n</sub> is clipped at the too small view port.

In order to eliminate the  $n \cdot 45$  Hz ripples we plan in a first step to reduce the seismic excitation in the north station. If that does not give enough reduction of the ripples we plan in a second step to open the vacuum system and exchange the view port by a larger one.

So far I only described the class of  $n \cdot 45$  Hz ripples. As can be seen in Figure 3.14 we also observed a second class of ripples with a fundamental frequency of 47.2 Hz. The origin of these ripples is still under investigation.

### 3.8. Summary

Stray light is one of the main noise sources in gravitational wave detectors. Tiny amounts of phase shifted stray light can cause sensitivity limiting excess noise. A well known class of stray light noise is the scattering shoulder which was observed in all currently operating gravitational wave detectors (see Figure 3.1). The stray light problem might even become more important in the next generation of gravitational wave detectors operating with up to 1000 times larger light powers.

In order to widen the understanding of stray light generation and propagation through the interferometers, in this work a device was developed able to generate stray light with a controllable phase shift. With the aid of this device stray light injections have been carried out and it was proven that the stray light behavior and transfer can be explained in a purely linear coupling scheme.

Furthermore in Section 3.3 a rough guide is given which indicators point to stray light problems. A powerful tool to identify the origin of the scattered light in auxiliary beam paths, the so called filter experiment, was presented in Section 3.4.

In order to avoid stray light problems some simple rules have to be observed:

- Avoid the presence of a beam waist in auxiliary beam paths in air.
- If you cannot avoid the presence of a beam waist, do not place a optical component close to it.
- Only use low scatter optics, preferably with sub-angstrom surface finish and ion-beam-sputtered dielectric coatings.



- Always properly dump any secondary beams.
- Reduce movement of optical components by using stiffer mounts.
- Less seismic and acoustic excitation helps.

After two years of nearly continuous work on stray light problems in GEO 600 we now have a good understanding of scattering and know which aspects have to be taken into account for the design of next generation detectors.



## Chapter 4.

# Photon pressure calibration

### 4.1. Introduction

The production of a precisely calibrated output stream of a gravitational wave detector is one of the most challenging detector characterization tasks. An accurate calibration is essential for any multi-detector analysis. A lot of research effort is currently focussing on the use of null-stream construction [Wen05]. Null-streams combine the outputs of multiple detectors in order to produce a data stream containing no GW information, which can be used for veto analysis. However, it is clear that if the strain signals from the individual detectors are subject to systematic calibration errors then the resulting null-stream will not be truly null and could contain residual traces from any detected GW signal. Another class of multi-detector analysis, requiring high calibration accuracy are coherent analysis (for example, when searching for pulsar signals [Dupuis05]) where phase inaccuracies could potentially destroy a signal.

For the official calibration of the GEO 600 detector, we use an on-line time-domain technique to produce two calibrated signals, each potentially containing gravitational wave information, one for each output quadrature, P and Q [Hewitson04]. These two calibrated data streams are then optimally combined, using a maximum likelihood method, in order to give a single signal with the best snr at all frequencies,  $H$  [Hewitson05].

The calibration of a gravitational wave detector can in general be split into two parts. The *absolute* calibration is given by a single overall factor, while the *relative* calibration represents a frequency dependent contribution. The absolute calibration of GEO 600 is a rather complicated procedure. In order to obtain a calibration for the ESD, the main actuator for the differential arm length of the interferometer, the ESD is first calibrated

back to the common mode error point of the frequency stabilization loop, which is then calibrated back through the mode cleaners to the frequency of the master laser, which is finally calibrated by using the well known free spectral range of the first mode-cleaner. Besides accumulating errors due to the many steps involved, this procedure implicates some drawbacks: some of the measurements can only be performed with low SNR and others are limited to be carried out in a certain frequency range. Furthermore, the procedure, which takes about on day on the whole, needs to be done partly with an unlocked interferometer, which means that the detector is not taking science data for the duration of the measurements.

Given the facts stated above, it is highly desirable to find new methods for providing an independent calibration of the gravitational wave detector. One approach is to use intentionally induced gravity gradients to apply a well known force to one of the test masses [Mantone06], [Hild04]. One proposal for such a "gravity calibrator" employing 3 masses rotating in a commercial spin dryer can be found in Appendix F. Another method is to use the photon pressure of a power modulated laser beam in order to apply a force to the test mass [Weiland04], [Mossavi06]. The mayor advantage of this method is that the displacement of the test mass,  $x(\omega)$ , is given in the ideal case by the simple relation:

$$x(\omega) = \frac{2 \cdot P}{M \cdot c \cdot \omega^2} \quad (4.1)$$

where  $P$  is the modulated light power,  $M$  is the mass of the test mass,  $c$  represents the speed of light and  $\omega$  is the modulation frequency of the calibration signal. All values going into Equation 4.1 are, in principle easily measurable to a high precision. Figure 4.1 shows the corresponding (idealized) pendulum response of the lowest stage of a GEO main suspension. For frequencies much larger than the resonance frequency the magnitude of the response is analogous to Equation 4.1 proportional to  $1/f^2$ , and the pendulum follows the excitation with a phase shift of  $\phi = -180$  deg.

## 4.2. Experimental setup of the photon pressure calibrator

An optical layout of the north end station of GEO 600 where the photon pressure calibrator is currently installed is shown in Figure 4.2. The beams from the main interferometer are drawn in red color. A small fraction of the light hitting MFn from the south is transmitted through the test mass. It then leaves the vacuum system via a view port,

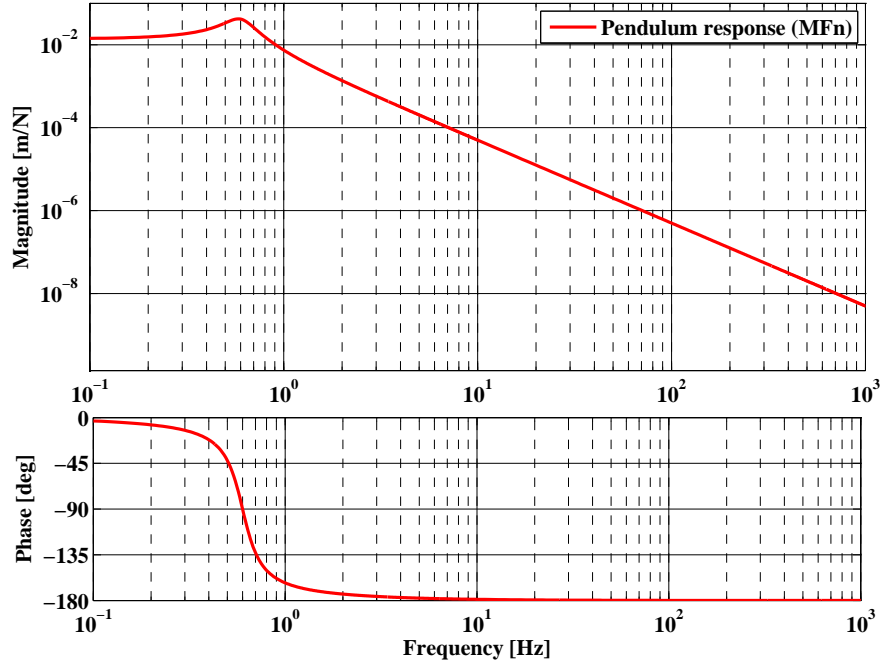


**Figure 4.1.:** Response function of the lowest stage of a GEO 600 main pendulum. For frequencies much larger than the resonance frequency the pendulum follows with a phase shift of  $\phi = -180$  deg.

is focused down by a lens (LNB) and is finally detected on the north bench by a spot position detector (PSDNB) and a CCD (CCDNB), both used for alignment control. As this auxiliary beam is essential for the alignment control of the main interferometer we cannot allow for any disturbance in its beam path, which sets some restrictions for the setup of the photon pressure calibrator.

The GEO photon pressure calibrator uses a fiber-coupled laser-diode with a wavelength of 1035 nm as a light source. After the light leaves the fiber it is collimated by a lens (collimator) of 60 mm focal length. The converging beam enters the vacuum via the view port and has a waist of about 5 mm diameter at the front surface of MF<sub>n</sub>. The PCAL beam (green in Figure 4.2) first passes the AR coating at the back surface of MF<sub>n</sub> and travels through the test mass substrate, made of fused silica, before it gets reflected at the HR coating. Then the PCAL beam passes the substrate and the AR coating a second time, leaves the vacuum system again via the view port and is finally dumped at the north bench. Some problems are connected to the setup described above. The beam profile provided by the laser diode is not a TEM<sub>00</sub> and quickly diverges after being reflected at the test mass. Therefore, clipping of the outgoing beam at the small view port (radius = 4 cm) cannot be ruled out, thus a reliable measurement of the reflected light power is not accessible. Furthermore, the PCAL beam does not pass the view port and the mirror under normal incidence. Even though the angle is only about 2 degrees, effects depending on the polarization of the light may occur.

#### 4.2.1. Measurement of the modulated light power

As described in the previous section the main disadvantage of the actual photon pressure calibrator setup is the fact that the light power reflected from the test mass is not accessible via any easy measurement. Therefore the light power is measured by an internal monitor photodiode connected to the laser diode. This signal is recorded in the DAQS and will be referred to as PCALmon in the following. PCALmon was calibrated at DC using a calibrated power meter. The measurement of the light power is then propagated through the collimator lens ( $T_{\text{lens}} = 0.9988$ ) and the view port ( $T_{\text{vp}} = 0.9986$ )<sup>1</sup>. The reflection of the AR coating and the transmission of the HR coating can be neglected since both are, according to their specifications, clearly below a tenth of a

---

<sup>1</sup>As the transmission of the currently used view port cannot be measured in situ, the given value was measured at a spare view port with identically specified properties.

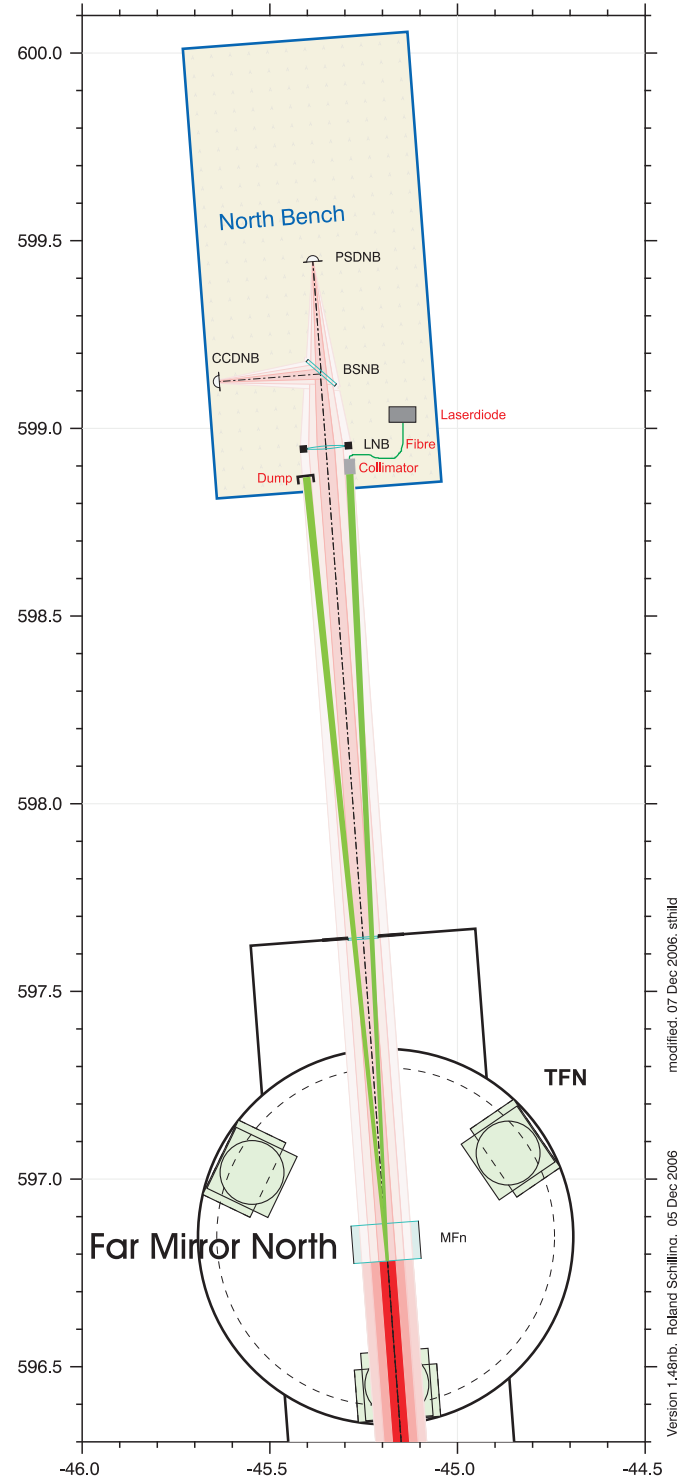


**Figure 4.2.:** OPTOCAD layout of the optics in the north end station of the GEO 600 detector, including the setup of the photon pressure calibrator.

percent. Again a direct in situ measurement of these two coatings is not possible.

However, a reliable measurement of the reflected DC light using a large lens (LNB on Figure 4.2) to collect all the light leaving the vacuum, showed that only 77 % of the light power entering the vacuum are leaving it afterwards. This strong power loss can only be explain by absorbtion due to dirty optics. Again an in situ measurement of the losses is not possible without opening the vacuum system. Venting the vacuum system was not possible due to the high risks involved, such as breaking a fused silica fibre of the quasi-monolith mirror suspension.

The unexplained loss of 23 % is the largest limitation of absolute accuracy of this setup. Depending on the position of the losses, any calibration derived from this photon pressure calibrator may be wrong by 23 % !! For all investigations in this chapter we will assume symmetrically distributed losses, meaning that 11.5 % of the light power are lost in front of the HR coating and 11.5 % are lost after the HR coating.

Altogether, the effective light power is estimated in the followin way

$$P[\text{W}] = \text{PCALmon}[\text{V}] \cdot T_{\text{lens}} \cdot T_{\text{vp}} \cdot K_{\text{pm}} \cdot (0.885 \pm 0.115) \quad (4.2)$$

where  $K_{\text{pm}}$  includes the calibration of the power meter and the calibration from PCALmon to the power meter.

### 4.3. Injections with different amplitudes

Injections using the photon pressure calibrator have been performed with different amplitudes in order to check that the response of the system is linear with respect to the amplitude of the modulated light power. A sine wave of 134 Hz has been injected with four different amplitudes, between 50 and 500 mW.

Figure 4.3 shows the analysis of this measurement. In the upper figure the magnitude of the transfer coefficient from PCALmon to  $H$  is plotted over the amplitude of the modulated light. The mean is indicated by red dashed line. The lower figure shows the deviation of each measurement point from the mean. We observe that the response function of the photon pressure calibrator is linear within  $\pm 4\%$  for different amplitudes of the modulated light power.



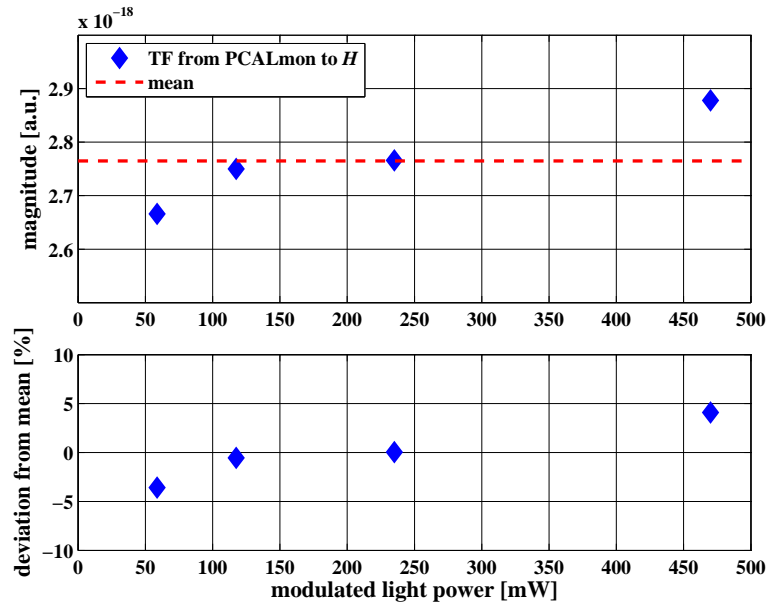


**Figure 4.3.:** Measurement of the transfer coefficient from PCALmon to  $H$  for various amplitudes of the modulated light. The upper plot shows the magnitude of the transfer coefficient (blue diamonds) and the mean (red dashed line). In the lower plot the deviation of each measurement from the mean is plotted. All measurements agree within  $\pm 4\%$  with the mean.

#### 4.4. Injections with different frequencies

One of the main goals of the experiments using the photon pressure calibrator is to check the relative accuracy (frequency dependence) of the official calibration. Therefore injections over the full detection band have been performed. Due to the strongly decreasing response ( $1/f^2$ ) of the system it is not possible to get identical SNR at all frequencies. Especially towards high frequencies only small SNR could be achieved and the uncertainties of the measured value originating due the noise floor needs to be taken into account. Analogous to measuring the amplitude of an ESD line, described in [Koetter03], the amplitude of a photon pressure calibrator injection,  $A_{\text{pcal}}$ , can be approximated by

$$A_{\text{pcal}} = \sqrt{V_{\text{pcal}}^2 - \eta^2}, \quad (4.3)$$

where  $V_{\text{pcal}}^2$  is the power measured in the frequency bin containing the injection and  $\eta^2$  represents the averaged power of noise floor in the frequency bins around the injection.

Figure 4.4 shows the result of photon pressure calibrator injections at various frequencies. Each point is derived from a measurement that uses 2 minutes of data for computing a single FFT.<sup>2</sup> The blue diamonds are the amplitudes of the injections,  $A_{\text{pcal}}$ , as seen from the GW channel, which represent the official calibration. The red circles show the amplitude of the PCAL injection predicted from PCALmon,  $A_{\text{pcal}}^{\text{theo}}$ , using Equation 4.1 and represent the photon pressure calibration. Above 3 kHz the measurements are not accurate due to too low SNR as indicated by the measurement of the noise floor (green stars). At all frequencies the injections show up smaller in the official calibration than expected from the photon pressure calibration. Furthermore the discrepancy between the two calibration methods is observed to vary with frequency. Especially towards higher frequencies the deviation seems to increase strongly. The ratio of the calibration derived from the photon pressure calibrator and the official calibration is plotted over frequency in the upper subplot of Figure 4.5. The red circles are calculated assuming the observed power loss of 23 % (see Section 4.2.1) is caused half on the way in and half on the way out of the vacuum system. The two blue dashed lines indicate the extremes, i.e. all 23 % lost on the way in and all 23 % lost on the way out. The observed

---

<sup>2</sup>In order to get best SNR in this measurement we have to choose a high frequency resolution. The frequency bin to be analysed is determined automatically by the used MATLAB script by finding the frequency bin of maximum power in the amplitude spectrum of PCALmon. The full MATLAB code used for these investigations can be found in Appendix E.

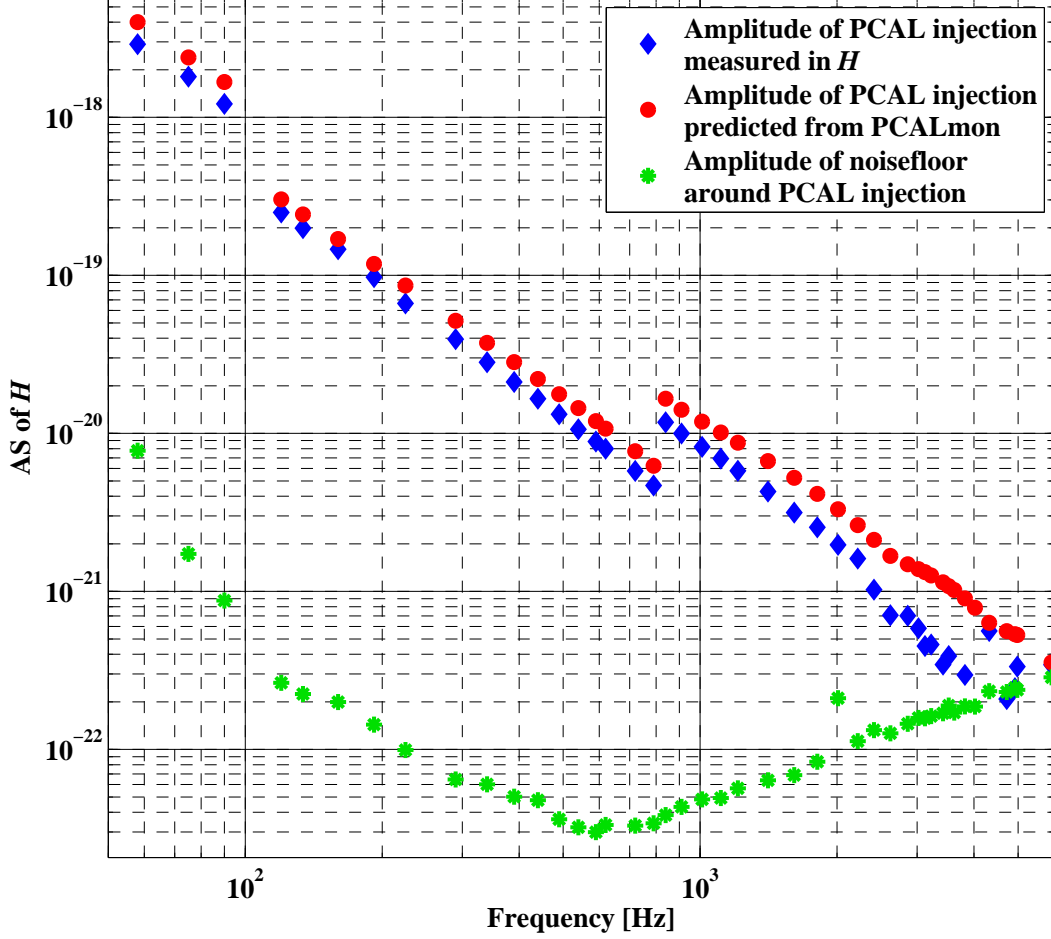


**Figure 4.4.:** Photon pressure calibrator injections for various frequencies. The blue diamonds represent the amplitude of the injections,  $A_{\text{pcal}}$ , already corrected for the noise floor using Equation 4.3. The red circles show the amplitude of the PCAL injection predicted from PCALmon,  $A_{\text{pcal}}^{\text{theo}}$ , using Equation 4.1. A discrepancy between the official calibration (blue diamonds) and the calibration derived from PCAL (red circles) is observed. Above 1 kHz the discrepancy seems to quickly increase. For frequencies higher than 3 kHz the measurements are not accurate due to too low SNR as indicated by the measurement of the noise floor (green stars). The injections in the frequency band from 100 to 800 Hz were performed using a smaller amplitude.

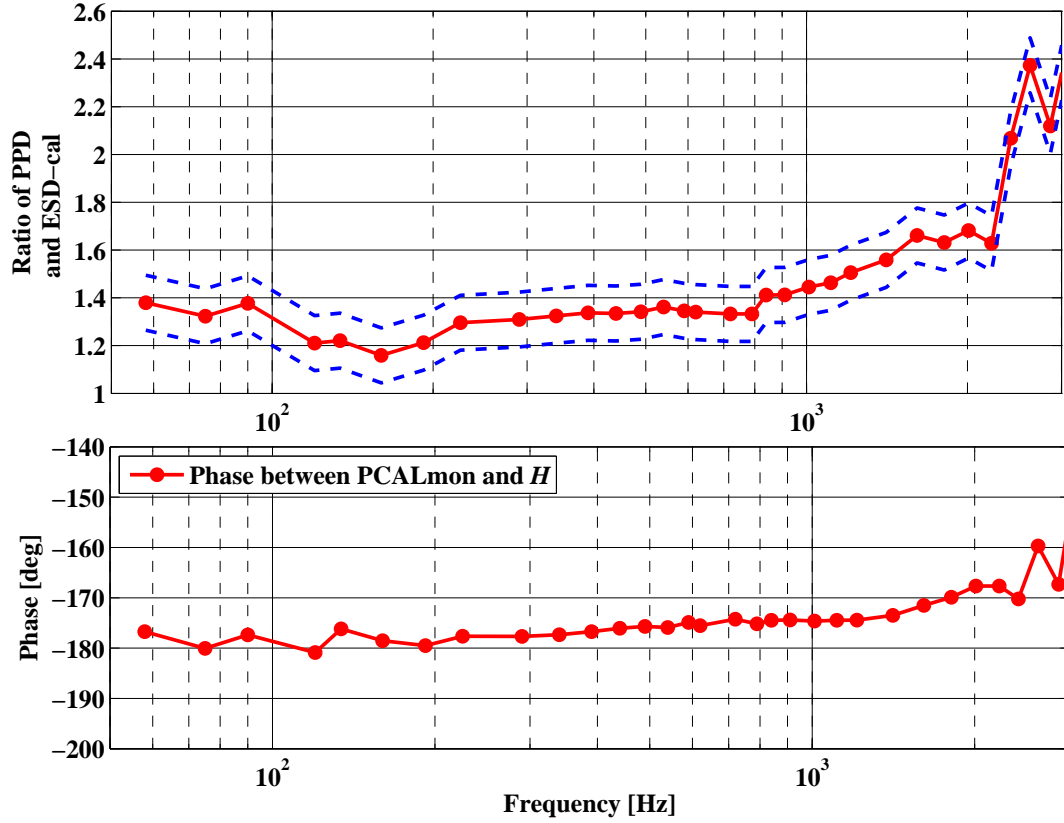


**Figure 4.5.:** *Upper plot:* Ratio of the photon pressure calibration and the official calibration versus frequency. The blue dashed lines indicate an uncertainty of  $\pm 11.5\%$ , caused by the observed power loss of 23 % (see Section 4.2.1). The observed discrepancy between the two calibration methods is on average about 20 to 40 % for frequencies below 1 kHz. Above 1 kHz the discrepancy quickly increases to about 120 % at 3 kHz. *Lower plot:* Phase relation between injected light power (PCALmon) and  $H$ . For all frequencies below 1 kHz the phase is -180 degrees within 5 degrees. Above 1 kHz the phase starts slowly to go off and reaches about -160 degrees at 3 kHz.

discrepancy between the two calibration methods is on average about 20 to 40 % for frequencies below 1 kHz. Above 1 kHz the discrepancy quickly increases to about 120 % at 3 kHz. The lower subplot of Figure 4.5 shows the phase relation between injected light monitored by PCALmon and  $H$  at the frequency of the injection. As we would expect from the pendulum response the phase is about -180 degrees. For all frequencies below 1 kHz the phase is -180 degrees within 5 degrees. Above 1 kHz the phase starts slowly to go off and reaches about -160 degrees at 3 kHz.

The discrepancy between the two calibration methods is surprisingly large, especially considering that the official calibration is, as we will see in Section 4.5, strongly believed to be correct. The observed deviation can roughly be separated into two phenomena: First of all there seems to be an absolute discrepancy of 20 to 40 % showing up equally at all frequencies. Secondly, at high frequencies the relative deviation increases strongly; the response of the photon pressure calibrator does not follow the  $1/f^2$  expected from the pendulum response.

One effect that could explain the absolute mismatch is photon pressure calibrator induced test mass misalignment, which will be described in detail in Section 4.8. To find a mechanism that can explain the frequency dependent discrepancy seems to be harder. Any kind of potential beam clipping should occur frequency independent. Also the above mentioned photon pressure calibrator induced test mass misalignment or polarization related problems can only explain a frequency independent error. As will be shown in Section 4.7 the behavior of the photon pressure calibrator at high frequencies might be explainable by photon-pressure-induced non-rigidity of the test mass.

## 4.5. Validation of the official calibration

So far we compared the official calibration with the calibration derived from the photon pressure calibrator. The observed discrepancy can of course originate from either the official calibration being wrong, the photon pressure calibrator being wrong or both being wrong. There is no easy way to distinguish these three possibilities. However, the official calibration of GEO 600 was repeated and evaluated several times by several people over the last few years. Therefore the official calibration is strongly believed to be correct within 10 % in magnitude and 20 degrees in phase for frequencies between 50 and 2000 Hz. This statement includes the absolute calibration accuracy as well as the

relative calibration accuracy. Two validation measurements important for the context of this work are presented in the following.

#### 4.5.1. Transfer function from ESD to $H$

The frequency dependent discrepancy between the official calibration observed in Section 4.4 could also be explained by a potential relative error of the official calibration. In order to rule out any relative inaccuracy in the official calibration we performed noise injections into the electro static drives (ESD) and measured the transfer function from the input of the ESD to  $H$ .

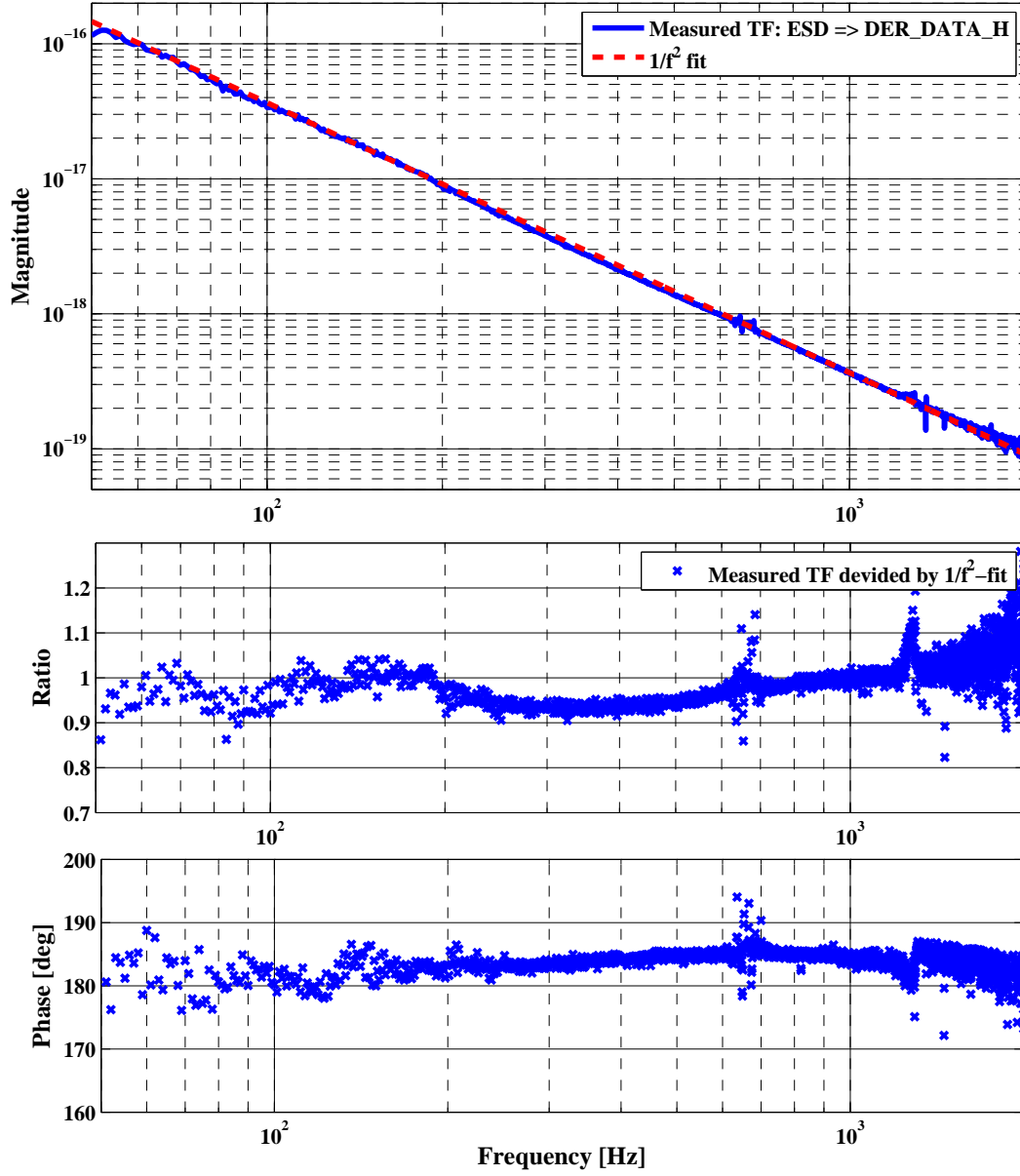
The electro static drives are believed to have a flat frequency response for all frequencies of interest. We would therefore expect to find the transfer function from the ESD to  $H$  to follow a  $1/f^2$ -law, originating from the pure pendulum response. The correctness of the ESD model was checked by white-noise injections in the power-recycled Michelson mode, where the optical response is known to be flat.

Figure 4.6 shows the measurement of the corresponding transfer function for frequencies between 50 and 2000 Hz. The signal was injected at the last OP of the electronics controlling the Michelson differential arm length. Then the transfer function from the feedback monitor of high voltage amplifiers (HVA) to  $H$  was computed and corrected for the responses of the dewhitening filters installed behind the high voltage amplifiers. As the upper subplot of Figure 4.6 indicates the transfer function is very close to an  $1/f^2$ -behavior. In center plot Figure 4.6 the deviation from an  $1/f^2$ -fit is shown. In the lower plot of Figure 4.6 the phase of the transfer function is plotted versus frequency.

Overall we can state that this measurement confirms a relative calibration accuracy of  $\pm 10\%$  in magnitude and  $\pm 5$  degree in phase is achieved for frequencies between 50 and 2000 Hz.

#### 4.5.2. ESD injections up to high frequencies

As already stated at the beginning of this chapter the main purpose of a calibration based on the photon pressure calibrator is to get an absolute and relative comparison to the official calibration. To get a measure to compare the photon pressure calibration to we have to make sure that we compare it to a meaningful measure. Therefore we have



**Figure 4.6.:** Measurement of the transfer function from the input of the ESD to the calibrated output of GEO 600,  $H$ . *Upper plot:* Measurement of the transfer function (solid, blue line) and a corresponding  $1/f^2$ -fit (dashed, red line). Above 1.5 kHz the accuracy of the measurement goes slightly down due to low SNR of the measurement. *Center plot:* Ratio of the measured transfer function and the  $1/f^2$ -fit. *Lower plot:* Phase between the injected signal and  $H$ . Overall a relative calibration accuracy of  $\pm 10\%$  in magnitude and  $\pm 5$  degree in phase is achieved for frequencies between 50 and 2000 Hz.

to validate the official calibration to the best of our knowledge before we can use it as an 'absolute standard'.

Most of the astrophysical analysis using data from GEO 600 consider only frequencies up to 2 kHz. That is why so far the calibration was examined only up to this frequency. However, some of the measurements presented in this chapter are performed at frequencies as high as 6 kHz. Therefore we have to make sure that a reasonable relative calibration accuracy is given also at higher frequency. The method we can use for this investigation is similar to the one described in Section 4.5.1, but at high frequencies we have to inject single discrete lines instead of broadband noise in order to get a sufficient SNR in the measurement.

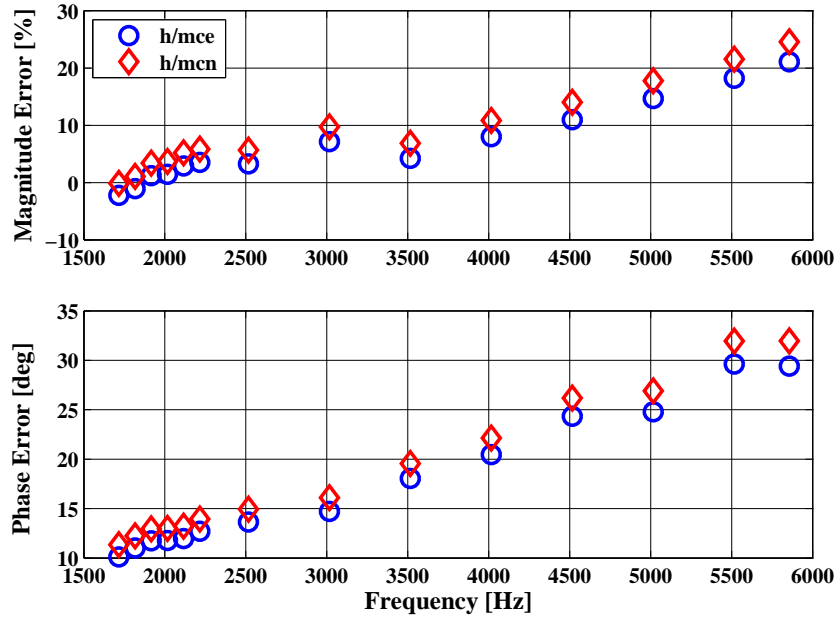


**Figure 4.7.:** Measurement of the relative calibration accuracy of the official calibration for high frequencies. Plotted are the differences between the official calibration ( $H$ ) and the propagation of the injections through the loop model for two individual ESD at MCE and MCN. The analysis of this injections was provided by J.R.Smith.

Figure 4.7 shows the analysis of the high frequency ESD injections. The magnitude and phase of the injections measured in the officially calibrated data are compared to the expected values from propagating the injections through the loop model for each for the



two ESD, MCE and MCn. Compared to the measurements at 2 kHz for frequencies up to 6 kHz the relative error in the official calibration increases by 20 % in magnitude and 20 degrees in phase.

The relative errors of the official calibration are in summary:

- For frequencies below 2 kHz: 10 % in magnitude and 5 degree in phase.
- For frequencies between 2 and 6 kHz: 20 % in magnitude and 30 degree in phase.

## 4.6. The phase picture

The observed discrepancy of the official calibration and the photon pressure calibration can only be explained in the presence of an additional unknown effect, I will call "mystery effect" in this section, that adds to the pendulum response. As I will show in this section

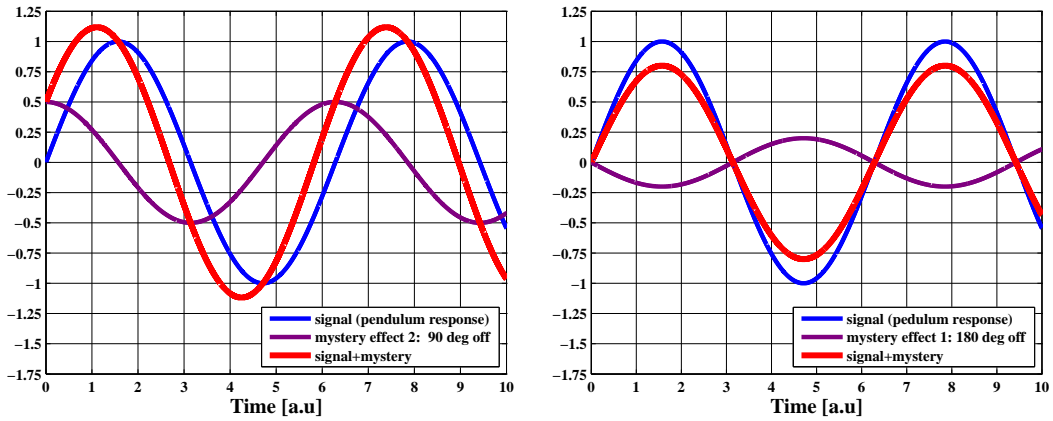


**Figure 4.8.:** The observed discrepancy of the official calibration and the photon pressure calibration might be explainable by an additional "mystery" effects adding to the pendulum response. *Left plot:* If the mystery effect is 90 deg off phase with the pendulum response the overall response would be increased (and the phase shifted). Therefore such a "mystery" effect cannot explain the observations of smaller overall response (and a constant phase of -180 degree). *Right plot:* Only a mystery effect 180 degrees off phase from the pendulum response can explain the observation of a reduced overall response (and a constant phase of -180 degrees).

the measurements shown in Figure 4.5 already contain very strong boundaries for the

behavior of the unknown "mystery" effect. In order to explain the absolute and the relative discrepancy of the two calibration methods, the "mystery" effect has to add to the pendulum response in a way that, first of all the overall response gets smaller in amplitude, and secondly the phase of the overall response still stays at -180 degrees. As indicated by Figure 4.8 these two conditions can be satisfied by an effect that is 180 degrees out of phase from the pendulum response, or in other words, an effect that is in phase with the modulated light of the photon pressure calibrator.

## 4.7. Non-rigidity of the test mass

The widely held assumption within the GW-community so far has been that a test mass acts like a rigid body for frequencies below the first internal resonance. However, no quotable reference could be found that documents or proves this hypothesis.

In fact, in this section I will present some investigations disproving the theory of test masses being rigid bodies at low frequencies.

The idea of this traditional model is that a mirror for all frequencies below its first internal mode, which is for the GEO test masses around 11 kHz [Smith04], behaves equivalent to any other oscillator:

- It just follows the excitation without any phase lag (phase difference = 0 degree)
- The response is flat in frequency and equals the response at a frequency of 0 Hz (DC).

However, obviously at DC we can (to a tiny amount) compress any piece of glass by pushing from both sides, or stretch it by pulling on both ends. In a linear setup the amount of the compression (or elongation)  $\Delta L$  only depends on the Young's module  $E_{\text{young}}$  of the material and the geometry of the test body

$$\Delta L = \frac{1}{E_{\text{young}}} \frac{L \cdot F}{A}, \quad (4.4)$$

where  $L$  is the length and  $A$  the cross section of the test body and  $F$  is the applied force.

The beam of the photon pressure calibrator hits the high reflective coating of the test mass and pushes at the surface of the mirror. Due to the inertia of the test mass the

force applied to the surface causes a deformation of the test mass. In order to find out whether this effect can be responsible for the strong discrepancy between the official and photon pressure calibration observed at frequencies around a few kHz, the main question we have to answer first is if the effect from force-induced mirror-deformation is roughly of the same size as the center of mass movement of the test mass induced by the photon pressure calibrator. In Section 4.7.1 a rough estimation is given using a very simple model, while in Section 4.7.2 a finite element analysis of the problem is presented.

#### 4.7.1. Rough estimation of photon pressure calibrator induced test mass deformation

As we first just want to get an estimation of the order of magnitude of any effect related to photon pressure calibrator-induced mirror-deformation, we can use a simplified model using the following assumptions:

- The beam of the photon pressure calibrator has a flattop profile and illuminates the full mirror.
- The backplane of the test mass is fixed in position.

In this case we can simply apply Equation 4.7. With the parameters of the GEO test masses  $L = 0.1 \text{ m}$  and  $A = \pi \cdot 90^2 \text{ mm}^2$ , Young's module for Suprasil of  $E_{\text{young}} = 7 \cdot 10^4 \text{ N/mm}^2$  [Heraeus] and a photon pressure induced force  $F = 2.25 \cdot 10^{-9} \text{ N}$  (750 mW light power) we obtain a homogenous elongation of the test mass of:

$$\Delta L = 1.26 \cdot 10^{-19} \text{ m} \quad (4.5)$$

This corresponds to an apparent strain  $H_{\text{def}}$  of

$$H_{\text{def}} = 2.1 \cdot 10^{-22}. \quad (4.6)$$

If we now compare this result with the measurement shown in Figure 4.4 we find that for high frequencies (a few kHz) this effect might have some non negligible influence. In conclusion that means that we have to evaluate this effect with a more realistic model, which is presented in the next section.

#### 4.7.2. Finite element analysis of photon pressure calibrator induced test mass deformation

The finite element method (FEM) is a numerical technique to simulate complex mechanical and thermal setups. This type of analysis is widely used in engineering and has proven its reliability. One of the most powerful tools for finite element analysis (FEA) is the software ANSYS [[Ansys](#)], which was used for the analysis described below. The FEM simulation presented here was done by our colleagues from Glasgow: I.Martin, S.Reid and J.Hough.

The test mass (diameter = 18 cm, thickness = 10 cm, bulk material = suprasil) is represented by 87000 discrete nodes. A total force of 2.77 N (diameter = 5 mm, gaussian profile) is applied to the center of the front surface of the test mass.<sup>3</sup>

Figure 4.9 shows the setup and the result of the analysis. In the simulation the force is applied from the outside to the front surface of the test mass while in the photon pressure calibrator setup the test mass surface is pushed from inside. Since the deformation depends on the intermolecular forces, which can, for small deformations, be assumed to be linear, the simulated setup is equivalent to the photon pressure calibrator setup. The lower subplot of Figure 4.9 shows the resulting displacement in  $z$ -direction (along the axis of the main interferometer beam). The simulation and the corresponding result are rotationally symmetrical. The area of the front surfaces, illuminated by the photon pressure calibrator beam, is locally squeezed. The maximum displacement of  $5 \cdot 10^{-9}$  m occurs in the center of the front surface.

#### 4.7.3. Effective test mass displacement

The displacement measured by the interferometer is determined by the overlap of the photon pressure calibrator beam and the main interferometer beam, which can be described by a gaussian beam. The radial intensity,  $I(r)$  is given by

$$I(r) = \exp\left(\frac{-2r^2}{\omega^2}\right) \quad (4.7)$$

where  $\omega$  is the radius of the beam. At the north end mirror the radius of the main interferometer beam is about 2.4 cm. Each point of the mirror surfaces contribution

---

<sup>3</sup>The test mass is held in place using an inertial relief function.

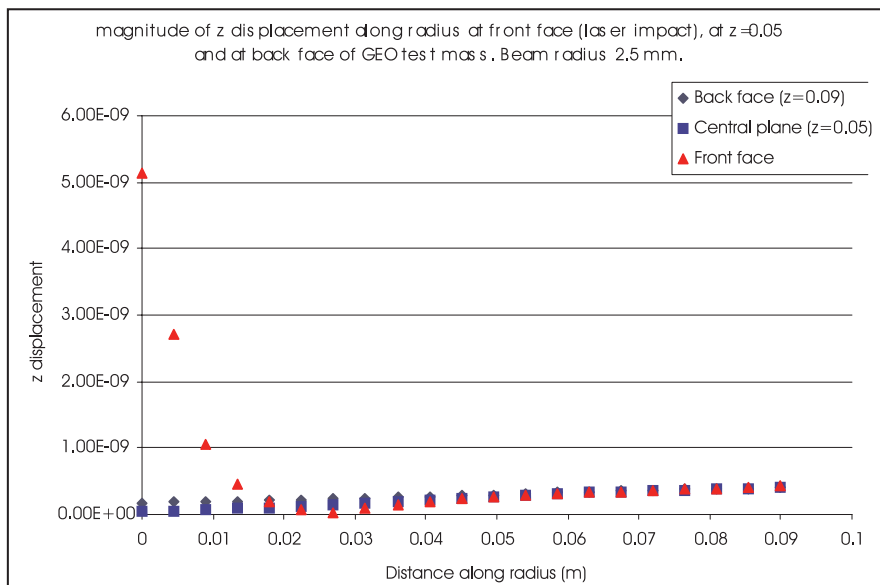
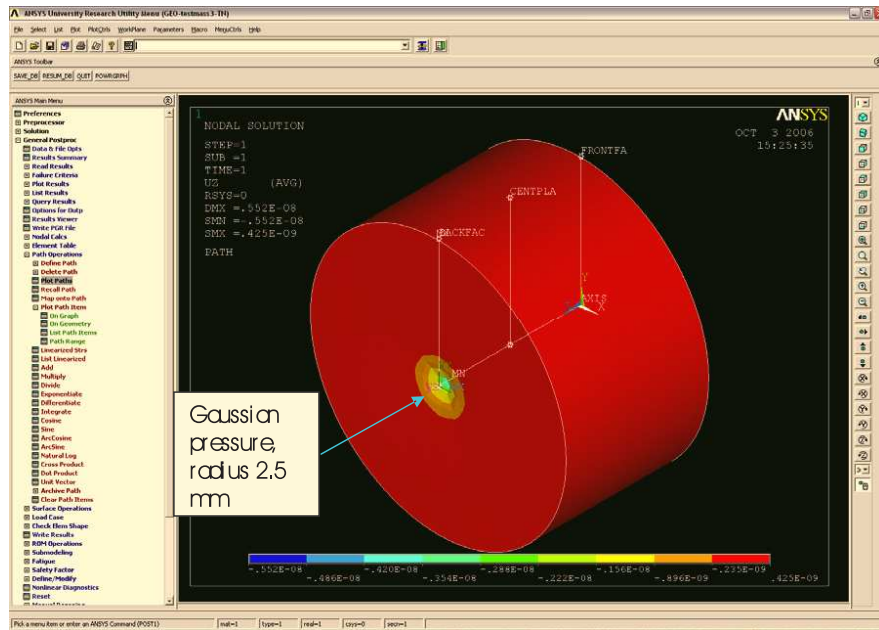


**Figure 4.9.:** *Upper plot:* Finite element model (FEM) of the deformation of a GEO test mass caused by the beam of the photon pressure calibrator. A total force of 2.77 N (diameter = 5 mm, gaussian profile) is applied to the center of the front surface of the test mass. The test mass is held in place using a inertial relief function. The analysis was done using the ANSYS software [Ansys]. The mirror was modelled by 87000 nodes. *Lower plot:* Result of this analysis. Plotted is the displacement over the radius of the test mass. The whole FEM analysis was provided by our colleagues from Glasgow: I.Martin, S.Reid and J.Hugh.

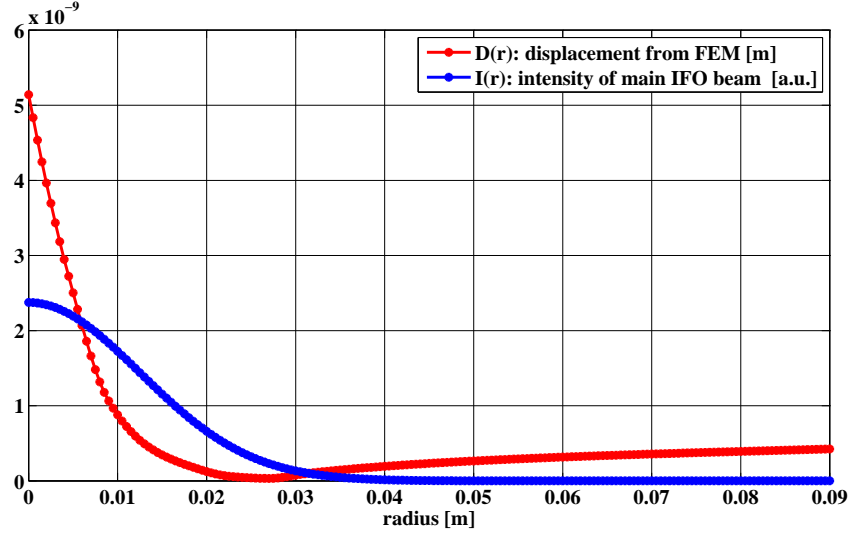


**Figure 4.10.:** Radial profile of the photon pressure calibrator induced test mass deformation,  $D(r)$ , and the intensity of the main interferometer beam,  $I(r)$ . The effective displacement of the test mass measured by the interferometer depends on the overlap of these two functions and is proportional to the  $I(r) \cdot D(r)$ .

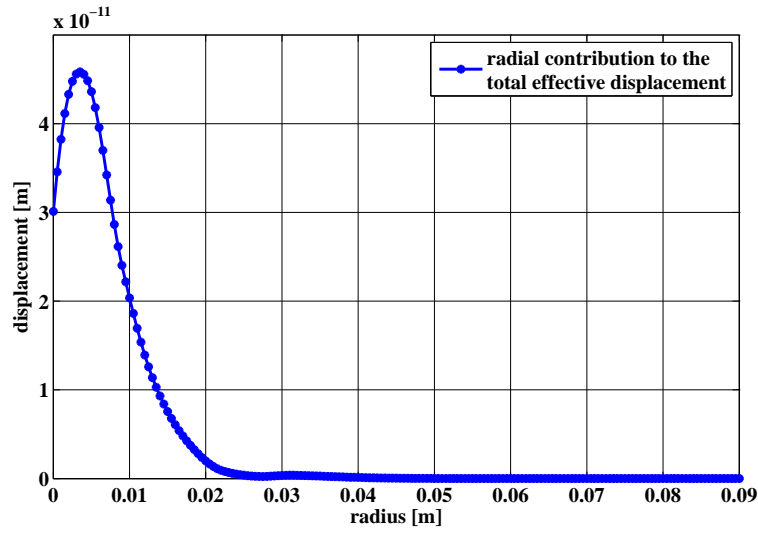


**Figure 4.11.:** Radial contribution to the effective displacement for photon pressure calibrator induced test mass deformation computed using Equation 4.8. The total effective displacement amounts to  $7.57 \cdot 10^{-10}$  m.

to the total effective displacement,  $D_{\text{total}}$ , weighted by the product of the power of the main interferometer beam,  $I(r)$ , and the corresponding displacement  $D(r)$ . For a radially symmetric setup, as described above, the total effective displacement can be expressed by a single integral:

$$D_{\text{total}} = \int_0^{0.09\text{m}} \int_0^{2\pi} D_{\text{eff}} \cdot dr \cdot d\varphi = \int_0^{0.09\text{m}} 2\pi \cdot r \cdot k_I \cdot I(r) \cdot D(r) \cdot dr. \quad (4.8)$$

The factor  $k_I$  is a normalization factor for  $I(r)$  in order to give

$$\int_0^{0.09\text{m}} 2\pi \cdot r \cdot k_I \cdot I(r) \cdot dr = 1. \quad (4.9)$$

Using Equation 4.8 the total effective displacement amounts to  $7.57 \cdot 10^{-10}$  m. Figure 4.11 shows the radial contribution to the effective displacement for photon pressure calibrator induced test mass deformation.

#### 4.7.4. Comparison of pendulum response and mirror deformation

The last section showed that the test masses are not completely rigid and that the photon pressure calibrator beam really causes a non-negligible deformation. Next we have to evaluate how strong the displacement originating from the non-rigidity of the test mass is, compared to the displacement of the center of mass (originating from the pendulum response). Since both responses are linear for the applied light power of the photon pressure calibrator we can simply compare their responses.

The pendulum response,  $\alpha_{\text{pen}}$ , follows a  $1/f^2$ -law for frequencies above 100 Hz, has a magnitude of  $5 \cdot 10^{-7}$  m/N at 100 Hz and is 180 degrees out of phase with the power modulation (see Figure 4.1). The response of the mirror deformation,  $\alpha_{\text{def}}$ , is assumed to be flat in frequency and in phase with the modulated light power for frequencies below the first internal resonances of the test mass. In Section 4.7.3 an effective displacement of  $7.57 \cdot 10^{-10}$  m was found for an applied force of 2.77 N, which leads to a response of  $2.73 \cdot 10^{-10}$  m/N. The magnitude and phase of  $\alpha_{\text{pen}}$  and  $\alpha_{\text{def}}$  are shown in Figure 4.12, in blue (dashed) and red (dashed-dotted), respectively. The total response,  $\alpha_{\text{total}}$ , plotted in green (solid) is the sum of the two individual responses:

$$\alpha_{\text{total}} = \alpha_{\text{pen}} + \alpha_{\text{def}}. \quad (4.10)$$

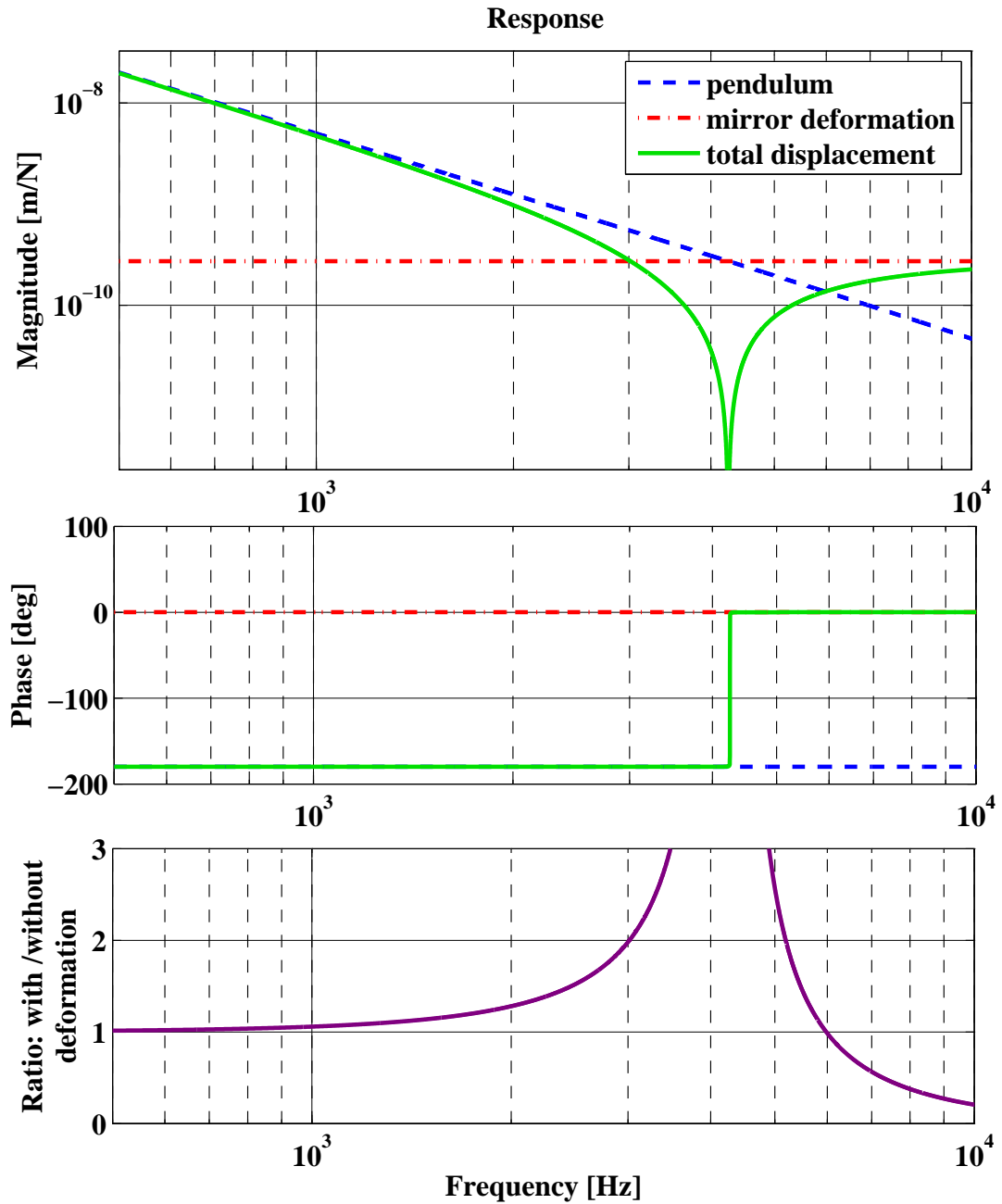


**Figure 4.12.:** Simple model for the photon pressure calibrator taking into account the responses from the pendulum and from the mirror deformation effect. The pendulum response follows a  $1/f^2$ -law and is 180 degrees out of phase from PCAL. The mirror deformation has a flat response and is in phase with PCAL. If both responses are added a notch appears at the frequency where both responses have equal size. The purple trace shows the expected discrepancy between the official calibration and photon pressure calibrator.



The total response shows a steep notch at the frequency where both individual responses have the same size and compensate each other completely due to having opposite phase. At the frequency of the notch the phase of  $\alpha_{\text{total}}$  jumps from -180 to 0 degrees. The resulting discrepancy between the official calibration and the calibration derived from the photon pressure calibrator, including the effect from mirror deformation, is shown in lowest subplot of Figure 4.12.

In order to prove this model we have to do photon pressure calibrator injections up to higher frequencies. It will be difficult to find the notch in the magnitude of the response because at these frequencies the snr of any injected line is going to be very small, even for measurements of very long duration. However, the distinct change in phase should be measurable with reasonable effort.

#### 4.7.5. High frequency injections using the photon pressure calibrator

Long duration injections using the photon pressure calibrator have been performed for frequencies in the range from 3 to 6 kHz. The snr of a periodic signal increases with the length of data used for a single FFT. This is due to the fact that by decreasing the width of the frequency bins, the noise contained in the signal-bin is decreased, while the signal stays constant. For the measurement presented in this section FFT containing between 2 and 10 hours of data were used. Such amounts of data<sup>4</sup> are difficult to handle with standard computers. This problem can be avoided by using a heterodyning technique. The time series of the data containing the signal of interest,  $E_{\text{sig}} \cdot \sin(\omega_{\text{sig}}t)$ , is multiplied by a sine wave with a slightly lower frequency,  $\omega_{\text{het}}$ :

$$E_{\text{sig}} \cdot \sin(\omega_{\text{sig}}t) \cdot \sin(\omega_{\text{het}}t) = \frac{1}{2}E_{\text{sig}}[\cos(\omega_{\text{sig}} - \omega_{\text{het}})t - \cos(\omega_{\text{sig}} + \omega_{\text{het}})t] \quad (4.11)$$

The second term of the right hand side of Equation 4.11 still contains the signal, but shifted towards even higher frequencies. The signal component we are interested in is shifted to a very low frequency,  $(\omega_{\text{sig}} - \omega_{\text{het}})$ , which for our investigations was chosen to be 9 Hz. After heterodyning, the data stream is strongly low passed and down sampled to give a data stream that can be handled by desktop computers.

In order to compute the transfer function from PCALmon to  $H$ , both data streams are processed with the same heterodyning algorithm. Afterwards, the transfer function is calculated using the *tfe* function of MATLAB.

---

<sup>4</sup>10 hours of data sampled with 16384 Hz consist of about 600 000 000 data points.

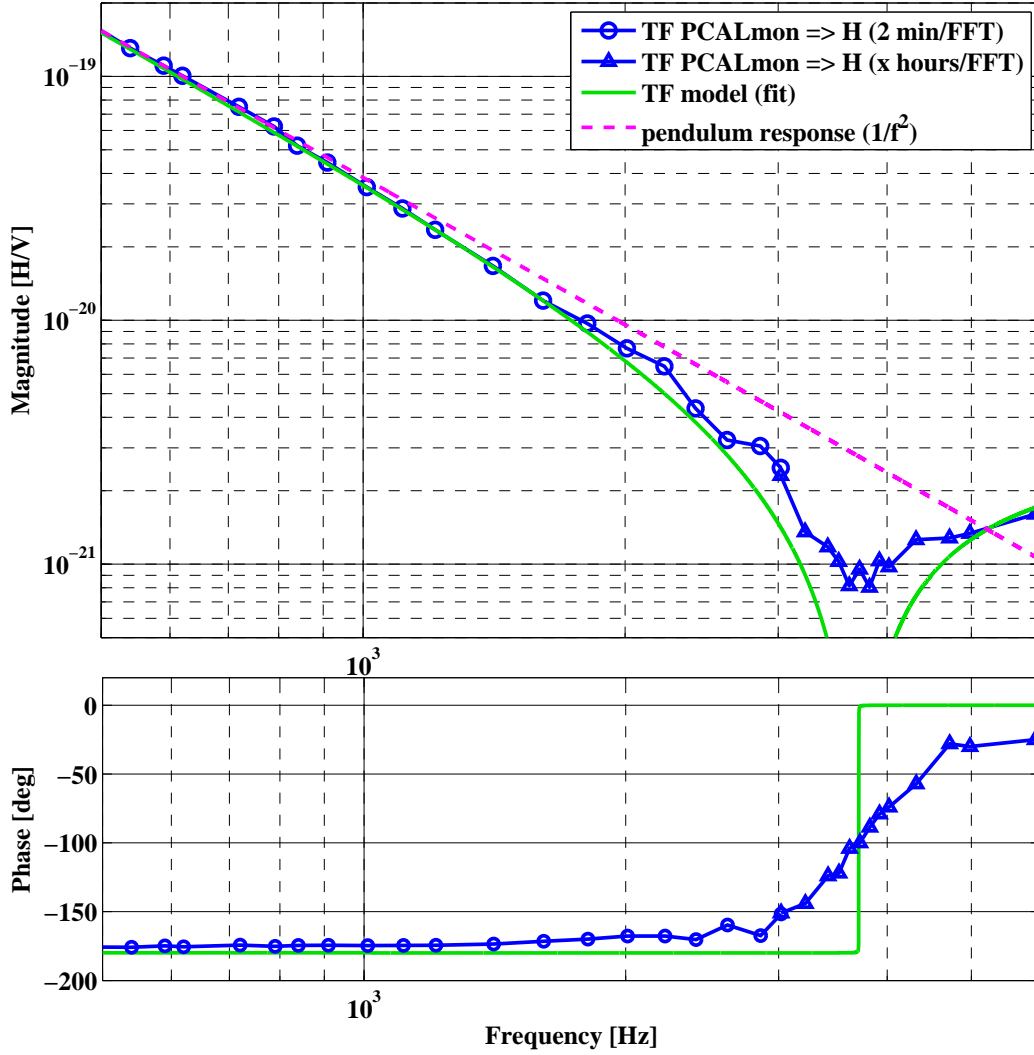


**Figure 4.13.:** Measurement of the photon pressure calibrator response at high frequencies. The measurements at frequencies below 3 kHz (blue circles) are the same as presented in Section 4.4. The measurement points above 3 kHz (blue triangles) are derived from long data stretches and contain up to 10 hours of data in a single FFT. The green line represents the model described in Section 4.7.4. The model was fitted in order to shift the notch frequency from 4.25 to 3.8 kHz. The  $1/f^2$  response from the pendulum is indicated by the pink dashed line. The presence of the expected notch structure is clearly confirmed by the measurement. However, the notch seems to be smeared out which might be explainable by beam jitter of the main interferometer beam (see Section 4.7.6).

Figure 4.13 shows the result of the photon pressure calibrator injections at high frequencies. The presence of the expected notch structure is clearly confirmed by the measurement. However, the notch seems to be smeared out. The magnitude of the response is about a factor of 3 below the pendulum response for frequencies between 3 to 4 kHz. At 5 kHz the measurement matches the pendulum response and finally at 6 kHz the measured response clearly exceeds the  $1/f^2$  behavior of the pendulum response. The green line in Figure 4.13 represents the model including the photon pressure calibrator induced mirror deformation, described in Section 4.7.4. The model was fitted in order to shift the notch frequency from 4.25 to 3.8 kHz; this required an increase in the response,  $\alpha_{\text{def}}$ , by about 25 %, from the originally estimated value of  $2.73 \cdot 10^{-10}$  m/N to  $3.41 \cdot 10^{-10}$  m/N. Around the notch frequency, the phase of the photon pressure calibrator response also changes significantly from about -165 degree at 2.8 kHz to about -30 degree at 4.8 kHz. A phase of nearly 0 degree at high frequencies clearly indicates that the response is no longer dominated by the pendulum response.

All together this result clearly confirms the hypothesis that the observed relative discrepancy between official and photon pressure calibration at high frequencies is caused by the influence of an additional effect with flat response and 0 degree phase lag compared to the modulated light power. The mirror deformation described above is obviously a strong suspect for this additional effect. However, we have to find a mechanism that can cause the smearing out of the notch structure. A candidate for such an effect is given in the next section.

#### 4.7.6. Influence of beam jitter to the photon pressure calibration

So far we assumed a perfect spatial overlap of the beams from the photon pressure calibrator and the main interferometer. The beam of the photon pressure calibrator is expected to show no significant beam jitter because the whole setup is rigidly mounted on an optical table and the lever of the beam is only a few meters (see Figure 4.2). However, the main interferometer is known to have some beam jitter. On long time scales its position on MFn is controlled by a low bandwidth servo. For frequencies above the unity gain frequency of this servo, which is around 0.01 Hz, the beam jitter is not suppressed.

If the two beams from the photon pressure calibrator and the interferometer move relative to each other, the effective displacement seen by the interferometer changes. A

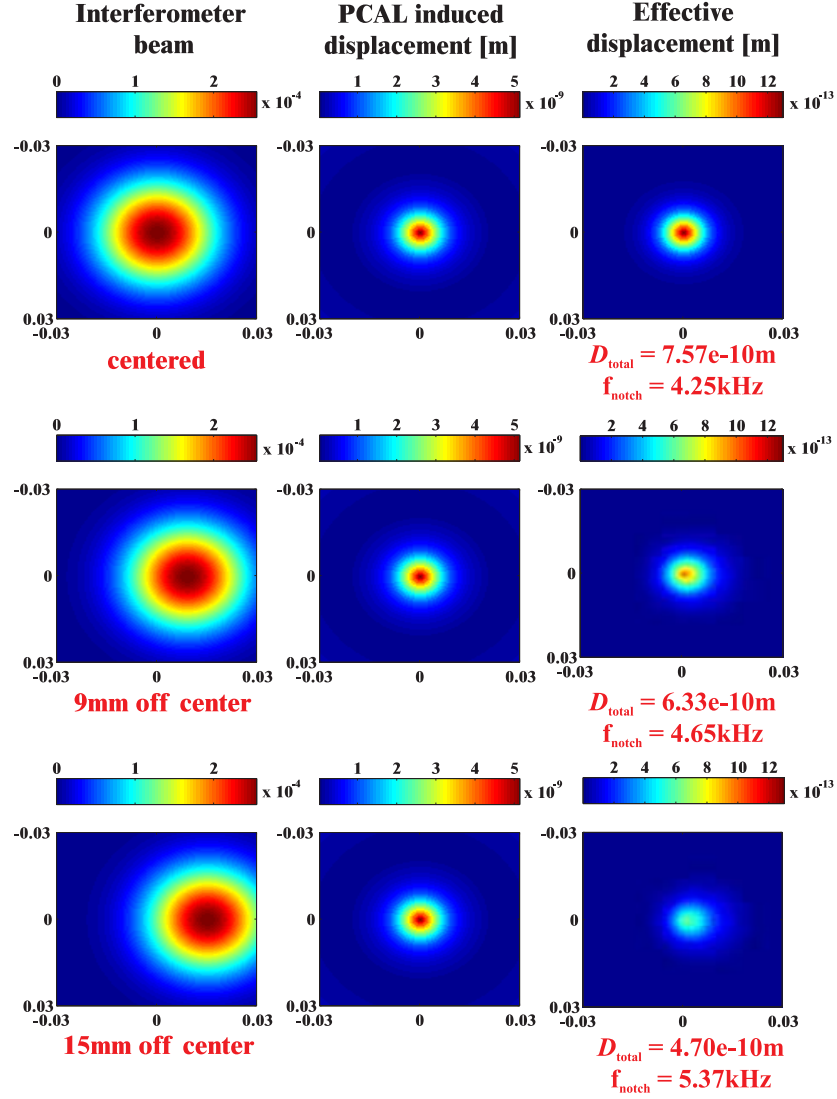


**Figure 4.14.:** The total effective displacement  $D_{\text{total}}$  caused by the photon pressure calibrator induced mirror deformation depends on the spatial overlap of the beams from the main interferometer and the photon pressure calibrator. The three plots in the left column show the main interferometer beam ( $\text{TEM}_{00}$ ,  $\omega = 2.4\text{ cm}$ ). The plots in the center column display the test mass deformation derived from the FEM simulation (see Section 4.7.2). The right hand column shows the contribution to the effective displacement. All plots show an area of  $6 \times 6\text{ cm}$ . A relative drift of the two beams of 15 mm would decrease the  $D_{\text{total}}$  by about 40 % from  $7.57 \cdot 10^{-10}\text{ m}$  to  $4.7 \cdot 10^{-10}\text{ m}$ , corresponding to a change of more than 1 kHz of the notch frequency.

change in the relative size of the two displacement components would lead to a different cross over frequency of the responses from the pendulum and the mirror deformation and thus a shift in the notch frequency. The measurements, shown in Figure 4.13, are averaging over hours and thereby also averaging over different notch frequencies. This would lead to a smearing out of the notch as observed in the measurement.

The question we have to answer now is how much the main interferometer beam moves in reality and whether this movement gives a large enough shift of the notch frequency. Over a period of 10 hours a maximum variation of the position of 9 mm was observed in vertical direction. Analogous to Equation 4.8 we can now calculate the overall measured displacement,  $D_{\text{total}}$ . As this problem is not any longer rotationally symmetric we have to modify Equation 4.8 slightly by introducing a double integration.

$$D_{\text{total}} = k_I \int_0^{0.09\text{m}} \int_0^{360\text{deg}} \cdot I(r, \varphi) \cdot D(r, \varphi) \cdot dr \cdot d\varphi. \quad (4.12)$$

In Figure 4.14 the total effective displacement,  $D_{\text{total}}$ , caused by the photon pressure calibrator induced mirror deformation is shown for different spatial overlaps of the beams from the main interferometer and the photon pressure calibrator. The three plots in the left column show the amplitude of the main interferometer beam ( $\text{TEM}_{00}, \omega = 2.4\text{ cm}$ ). The plots in the center column display the test mass deformation derived from the FEM simulation (see Section 4.7.2). The right hand column shows the contribution to the effective displacement derived using Equation 4.12. A relative drift of the two beams of 15 mm would decrease  $D_{\text{total}}$  by about 40 % from  $7.57 \cdot 10^{-10}\text{ m}$  to  $4.7 \cdot 10^{-10}\text{ m}$ , corresponding to a change of 600 Hz of the notch frequency.

Overall the influence of beam jittering of the main interferometer beam seems to be sufficient to explain that the measured notch in Figure 4.13 is smeared out.

#### 4.7.7. Conclusion and consequences

In the previous section a new idea was presented that can, at least to a large extent, explain the strong discrepancy between the official and the photon pressure calibration observed at high frequencies. In contrary to general belief, a test mass made of fused silica seems to show non rigidity also at frequencies below its first internal resonance.

The achievable accuracy of a calibration derived from a photon pressure actuator is at least to some extent limited by the non-rigidity of the test mass for frequencies in

the kHz range. However, careful design and the implementation of new ideas, like for instance minimizing the overlap of the PCAL beam and the interferometer beam by the use of two off center PCAL beams [Savage06], may help to improve the calibration accuracy. However, it needs to be taken into account that even off center PCAL beams can excite eigenmodes of the test mass.

Finally it has also to be stated that the above described deformation of a test mass can not only be induced by strong modulated light beams, but also by any other kind of inhomogeneous actuation, such as for example coil magnet actuators.

## 4.8. Effects from test mass rotation

The photon pressure calibrator might cause a non-negligible rotation or tilt of the test mass. One potential mechanism for that would be if the photon pressure calibrator is hitting the test mass off center. The frequencies of our interest are far above the resonance frequencies of the suspension, thus we consider the test mass as being a free mass for rotation or tilt. The rotation corresponding to an angle  $\theta$  can be described by using the moment of inertia  $I$

$$\theta(\omega) = \frac{2 \cdot P \cdot d_{PPD}}{c \cdot I \cdot \omega^2} \quad (4.13)$$

where  $P$  is the modulated light power,  $\omega$  is modulation frequency and  $d_{PPD}$  the distance of the PPD beam center from the center of the testmass.

Figure 4.15 depicts the longitudinal effects from mirror rotation. If the beam from the main interferometer is centered on the testmass the longitudinal displacement is given by

$$x_d \approx \frac{d}{4} \theta^2 \quad \text{for } \theta \ll 1. \quad (4.14)$$

In the case that the beam of the main interferometer is off center, then the effective displacement,  $x_d$  also contains a factor linearly depending on  $\theta$  [Weiland04]:

$$x_r \approx d_c \theta + \frac{d}{4} \theta^2 \quad \text{for } \theta \ll 1. \quad (4.15)$$

For very small angles,  $\theta$ , as the ones we are interested in we can neglect the second part of Equation 4.15 and take only the first term. Together with Equation 4.13 this gives

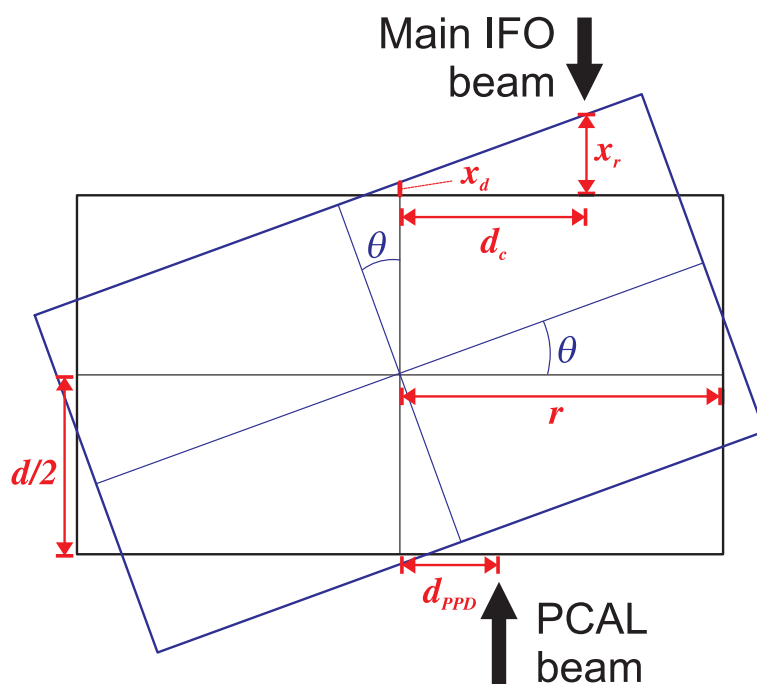


**Figure 4.15.:** Rotation of the mirror induced by the photon pressure drive will yield a longitudinal displacement of  $x_d$  in the case that the main interferometer beam is centered on the test mass. If the main interferometer beam is off center the longitudinal displacement is given by  $x_r$ .

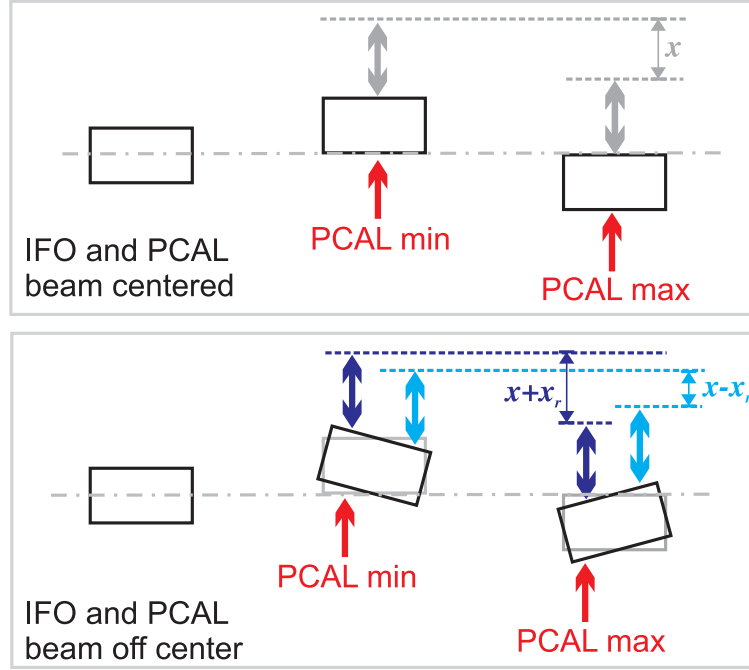


**Figure 4.16.:** *Upper plot:* When the PCAL beam (red) and the main interferometer beam (grey) are centered the amplitude of the photon pressure calibrator injection is  $x$ . *Lower plot:* When both beams are off center to the same side the measured amplitude of the injection will be increased to  $x + x_r$  (blue). If both beams are offset to opposite sides the measured signal amplitude is decreased to  $x - x_r$  (cyan).



an angle-independent displacement

$$x_r(\omega) \approx \frac{2P \cdot d_c \cdot d_{PPD}}{I \cdot c \cdot \omega^2} \quad (4.16)$$

which only depends on the modulation frequency and the distances of the laser beams from the center of the testmass.

If we want to check the influence of the rotational induced displacement we have to compare this with the longitudinal displacement from the pure pendulum transfer function

$$x(\omega) = \frac{2 \cdot P}{M \cdot c \cdot \omega^2}. \quad (4.17)$$

The ratio is

$$\frac{x_r(\omega)}{x(\omega)} = \frac{M d_c d_{PPD}}{I} \quad (4.18)$$

and does not depend on  $\omega$ . Hence the rotation of the photon pressure calibrator induced test mass rotation results in a frequency independent error, i.e. an absolute error. Using  $M = 5.3 \text{ kg}$  and  $I = 0.01601 \text{ kgm}^2$  we can calculate how far the beams have to be off center to explain the observed error of 30 % in Figure 4.5:

$$d_r d_{PPD} = 0.3 \frac{I}{M} = 9.075 \cdot 10^{-4} \text{ m}^2 \quad (4.19)$$

Assuming both beams to be misaligned by the same distance we would have to take the square root which would give  $d_r = d_{PPD} = 3.0 \text{ cm}$ .

If we were aiming for an 1 % accuracy we would have to make sure that both beams, the one from the photon pressure calibrator and the one from the interferometer are well centered on the test mass to within 0.5 cm.

Unfortunately with the currently installed setup of the photon pressure calibrator it is not possible to get an estimate better than a few centimeters of the position where the PCAL beam hits the mirror. This is mainly due the fact that the position of MFn in respect to the view port used for the PCAL beam is not accurately known. Furthermore the positions of the view ports available at MFn do not allow for a more accurate optical estimation of the spot positions. However, in the following section a method will be presented to accurately determine the spot position of the photon pressure calibrator beam by scanning the test mass with the position of the main interferometer beam.

#### 4.8.1. Method to determine the off centering of the photon pressure calibrator

As given by Equation 4.15 the effective displacement  $x_r$  depends on one hand on the photon pressure calibrator induced misalignment of the test mass and on the other hand on the spot position of the main interferometer beam. If the beam from PCAL is exactly centered on MFn, no test mass misalignment is induced, and changing the spot position of the main interferometer beam should not change  $x_r$ . However, in the case the beam from PCAL is off center,  $x_r$  is a function of the spot position of the main interferometer beam,  $d_c$ . This relation can be used to accurately determine the position of the PCAL beam hitting MFn,  $d_{PPD}$ . Figure 4.17 shows the corresponding

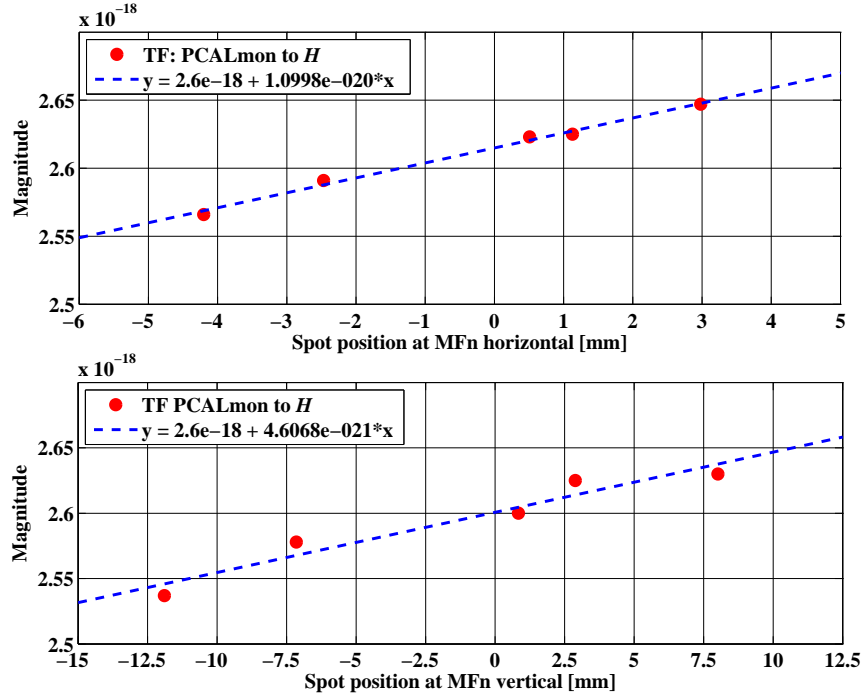


**Figure 4.17.:** Magnitude of the transfer function from PCALmon to  $H$  versus the position of the main interferometer beam at MFn. *Upper plot:* Changing the position of the main interferometer beam on MFn in horizontal direction changes the photon pressure calibration by 4.23 % / cm. *Lower plot:* Changing the position of the main interferometer beam on MFn in vertical direction changes the photon pressure calibration by 1.71 % / cm.

measurements. The position of the main interferometer beam was shifted on MFn and

the transfer function from PCALmon to  $H$  was measured. Changing the position of the main interferometer beam on MFn in horizontal direction changes the photon pressure calibration by 4.23 %/cm, while in vertical direction a change of 1.71 %/cm is found. Using Equation 4.18 these values can be used to calculate the horizontal and vertical off centering of the PCAL beam,  $d_{PPD}^{\text{rot}}$  and  $d_{PPD}^{\text{tilt}}$  respectively.

$$d_{PPD}^{\text{rot}} = 12.8 \text{ mm} \quad \wedge \quad d_{PPD}^{\text{tilt}} = 5.2 \text{ mm} \quad (4.20)$$

Assuming that the main interferometer beam and the beam from the photon pressure calibrator are off center in the same direction, the interferometer beam would have to be 44 mm off center to explain the smallest observed discrepancy of 20 % (see Figure 4.5) between the official and the photon pressure calibration. Such a large off centering cannot be completely excluded but seems fairly unlikely. Using the method described here  $d_{PPD}$  can iteratively be minimized. However, in order to keep the duty cycle of GEO 600 in S5 as high as possible, this work was postponed so far.

## 4.9. Determining the sign of $H$

For all kinds of network analysis that use data from two or more gravitational wave detectors (see, for example, [Ajith06a, Wen05, Candonati04, Rakhmanov05, Heng03]) it is indispensable to get well calibrated detector outputs. First of all a correct strain amplitude output is needed and secondly the sign of  $H$  must be determined.

In principle this information is easily accessible from the polarity of the fast actuators used for longitudinal control of the Michelson differential arm length which are in case of GEO 600 the ESDs. However, in reality the injected signals pass a complex system of electronics containing many stages with potential swaps of sign, like for instance inverted OPs and differential senders and receivers. Thus, one needs to very carefully measure the polarity of many pieces of electronics to find the correct sign of  $H$ .

A much less vulnerable procedure to determine the sign of  $H$  is provided by the photon pressure calibrator which only involves a very simple and clearly laid out system. The monitor photodiode built in the photon pressure calibrator laser diode and recorded in the DAQS (PCALmon) provides a measurement of the light hitting the suspended mirror. As shown in Figure 4.18 the amplifier of the photodiode gives a positive voltage

proportional to the detected light. The force  $F_{\text{PCAL}}$  acting on MFn is proportional to the voltage recorded in PCALmon.

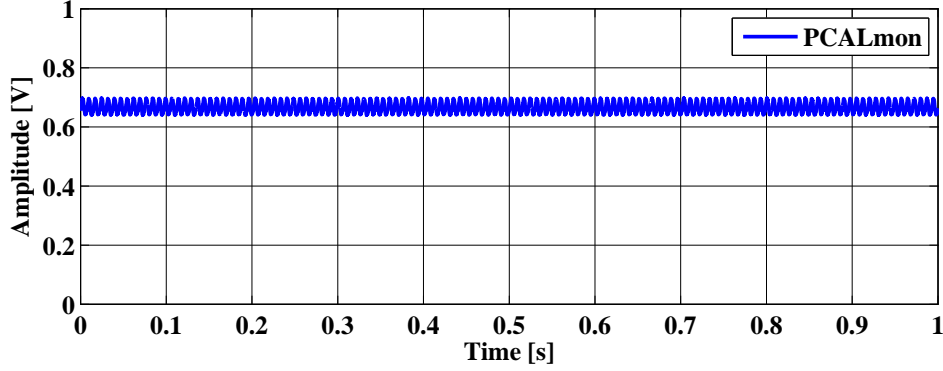


**Figure 4.18.:** Time series of the signal PCALmon, derived from the internal monitor photo diode of the photon pressure calibrator. The time series consists of a DC voltage of 0.67 V and an AC peak-peak voltage of  $\pm 25$  mV corresponding to the injected calibration signal.

Next it is necessary to measure the phase relation between PCALmon and  $H$  by means of computing the transfer function at the frequency of the photon pressure calibration line  $f_{\text{PCAL}} = 134$  Hz. Figure 4.19 shows this transfer function for a time during S5. The two signals have opposite phase,  $\phi_{F_{\text{PCAL}} \rightarrow H} = -180$  deg out of phase. Finally we need to take the pendulum response of the MFn suspension into account. As indicated by Figure 4.1 the phase of the pendulum response is  $\phi_{F_{\text{PCAL}} \rightarrow x_{\text{MFn}}} = -180$  deg for a frequency  $f \gg f_0$  where  $f_0$  the resonance frequency of the pendulum and  $x_{\text{MFn}}$  the movement of MFn is.

Putting both relations together we get:

$$\phi_{x_{\text{MFn}} \rightarrow H} = \phi_{F_{\text{PCAL}} \rightarrow H} + \phi_{F_{\text{PCAL}} \rightarrow x_{\text{MFn}}} = -360 \text{ deg} \quad (4.21)$$

Due to the fact that the photon pressure calibrator shines onto the back of MFn  $x_{\text{MFn}} > 0$  corresponds to a shortening of the north arm. Hence, all together we determine the sign of  $H$  as follows:

$$H > 0 \quad \text{for} \quad \delta l_{\text{north}} < \delta l_{\text{east}} \quad (4.22)$$

$$H < 0 \quad \text{for} \quad \delta l_{\text{north}} > \delta l_{\text{east}} \quad (4.23)$$

where  $l_{\text{north}}$  and  $l_{\text{east}}$  are the lengths of the north and the east arms, respectively.

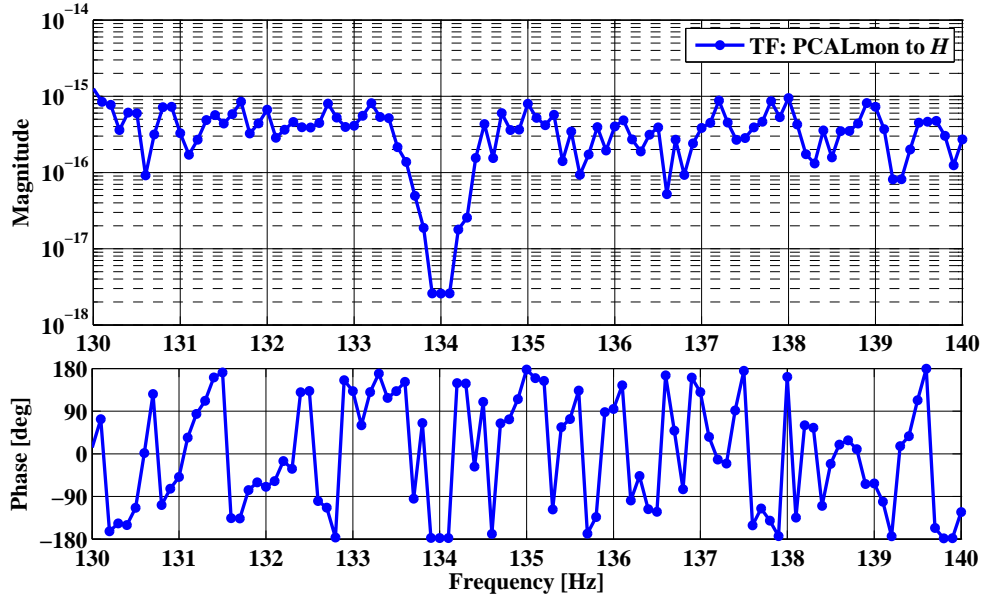


**Figure 4.19.:** Transfer function from the photon pressure calibrator monitor diode (PCALmon) to  $H$ . The photon pressure calibrator is used to apply a calibration line at  $f_{\text{PCAL}} = 134$  Hz. Only at this frequency is the transfer function is physically meaningful. The phase difference between both signals was measured to be  $\phi_{F_{\text{PCAL}} \rightarrow H} = -180$  deg.

## 4.10. Summary

In this section experiments and investigations related to establishing a photon pressure calibration for GEO 600 are presented. The experimental setup and potential imperfections are described in detail in Section 4.2. A direct comparison of the relative and absolute values of the official GEO calibration and the calibration derived from the photon pressure calibrator is given in Section 4.4. The discrepancy between the two calibration methods was found to be unexpectedly large. The two resulting absolute calibrations seem to be different by about 20 to 40 %, which might be explained by effects from photon pressure induced test mass rotation as described in Section 4.8. The Section 4.7 focuses on the strong discrepancy of the relative calibration found at high frequencies, which can be explained by photon-pressure-induced deformation of the test mass. A finite element analysis is presented which predicts the presence of a notch structure in the response of the photon pressure calibrator. In long-duration measurements of the photon pressure calibrator at very high frequencies this notch structure was found. The The effect of non-rigidity of the test mass limits the accuracy of the photon pressure calibrator for frequencies above 1 kHz. Finally in Section 4.9 it is shown that a photon pressure calibrator can be used to reliably determine the polarity of  $H$  which is important for any kind of astrophysical analysis using data from more than one GW detector.

## Chapter 5.

# A statistical veto method employing an amplitude consistency check

### 5.1. Introduction

One of the most promising class of gravitational wave (GW) signatures that may be detected by the current array of ground-based laser interferometric GW detectors [Hild06c, Waldman06, Acernese06, Ando05] is un-modelled transient (burst) signals arising from short-duration, violent astronomical events. The search for such signals typically focusses on time-scales of the order of a few (or few tens of) milliseconds.

Due to their extremely complicated nature, GW detectors are themselves usually potent sources of transient signals. A subset of such signals arising from many different sub-systems within the detectors can (and do) couple to the main detector output, and hence appear as false GW triggers in any search effort. While a great amount of effort is afforded in the reduction of these instrumental and environmental glitches and/or their coupling to the main detector output (also termed the  $H$  channel), there is still a residual number that remain.

Once the glitch population of a particular sub-system (and its coupling to the GW channel), is (physically) reduced to a minimum, the residual must be identified and characterised so as to exclude those glitches from the search for GWs. The rate of false glitches in the GW channel ultimately sets a limit on the confidence with which a particular trigger can be identified as a GW. It is therefore important to try to reduce the number of glitches in the GW channel that are to be considered in a search for GWs. This is traditionally done by *vetoing* those events detected in  $H$  using events and

knowledge of events detected in auxiliary channels. Once an auxiliary channel has been identified as being a source of transient events which couple to  $H$ , it is termed a veto channel and is then studied and used to reduce the event list of  $H$ .

The application of a veto is done by identifying those events in the auxiliary channel which are, in some way, coincident with events detected in  $H$ . Detected glitches are typically characterised by a few parameters (time of occurrence, amplitude, central frequency, *etc*), such that saying that two events are coincident can be as simple as saying that they occur at the same time (within some error window) or as complicated as saying that many of the characteristics of the glitches are (within some defined windows) the same. When a parameterisation of glitch events is used to compare events between data-streams, we refer to the resulting veto as a *statistical* veto since its performance is based on the statistical properties of the distributions of glitches in the two data-streams and does not rely on any knowledge of the physical coupling mechanisms involved. Examples of the application of statistical veto methods to GW detector data can be found in [DiCredico05, Akutsu, Beauville05]. Another class of veto methods which relies on detailed knowledge of the coupling mechanism involved in transferring glitches from an auxiliary channel to the  $H$  channel, is not discussed here, but an example is given in [Ajith06]. There are also interferometer channels which, by definition, contain negligible GW information but can nevertheless remain highly correlated to the main GW channel. These ‘null-stream’ channels can also be used as effective veto channels (see [Hanna06, Koetter03, Hewitson05a] for examples). In addition to these single-detector veto methods, there is active research in the use of multiple detector outputs as a means of vetoing the events in a detector network (see, for example, [Ajith06a, Wen05, Candonati04, Rakhmanov05, Heng03]).

The approach of using a pure statistical correlation (such as time of occurrence) can, of course, lead to *false vetoes*, that is, events in the auxiliary channel which are only accidentally coincident with events in the  $H$  channel. Requiring that more glitch characteristics be ‘similar’ when performing the coincident test can reduce the false-veto rate (usually at the cost of a reduced veto efficiency). The usefulness of a particular veto channel can be characterised according to the number of  $H$  events it can veto (its efficiency) for a given number of false-vetoes (false/accidental-veto rate).

This chapter investigates many aspects of the identification, characterisation and use of veto channels for data recorded from GEO 600, in particular for the case when



the simple coupling described above is further complicated by the presence of GW signal traces in the auxiliary channel. To motivate the application of statistical veto methods to data from GEO 600, in the Sections 5.2 and 5.3 two examples are given where events from the auxiliary channel  $X$  and the GW channel  $H$  are found to show a significant correlation. Section 5.4 describes the burst detection algorithm used in these studies. Section 5.5 goes on to discuss the *standard* statistical veto and shows an example application (with single and multiple coincidence windows) to data from GEO 600. Section 5.6 shows a possible extension to the classical statistical veto method for the case where the auxiliary channel can contain traces of GW signals, *i.e.*, the channel's sensitivity to GW signals is non-negligible. Section 5.7 shows the application of the extended classical statistical veto method to GEO 600 data. For a month of data the full GEO veto pipeline is applied, also including a statistical veto employing a amplitude consistency check.

## 5.2. Motivation for a standard statistical veto for GEO 600: Hourly mains glitches

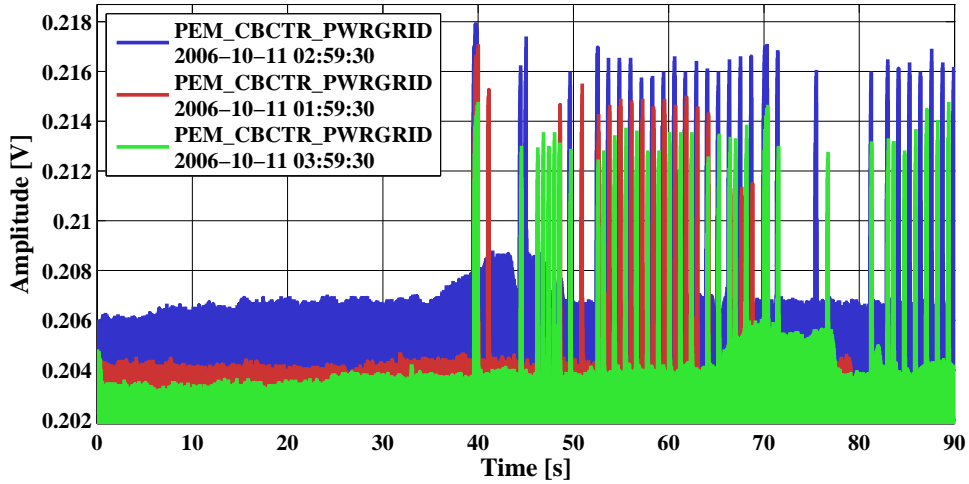


**Figure 5.1.:** Stacked time series of the mains monitor at the GEO site. Ripple control signals repeatedly show up 10 seconds after the beginning of a UTC-hour.

The power supply companies in Germany use a technique called *ripple control* to trans-

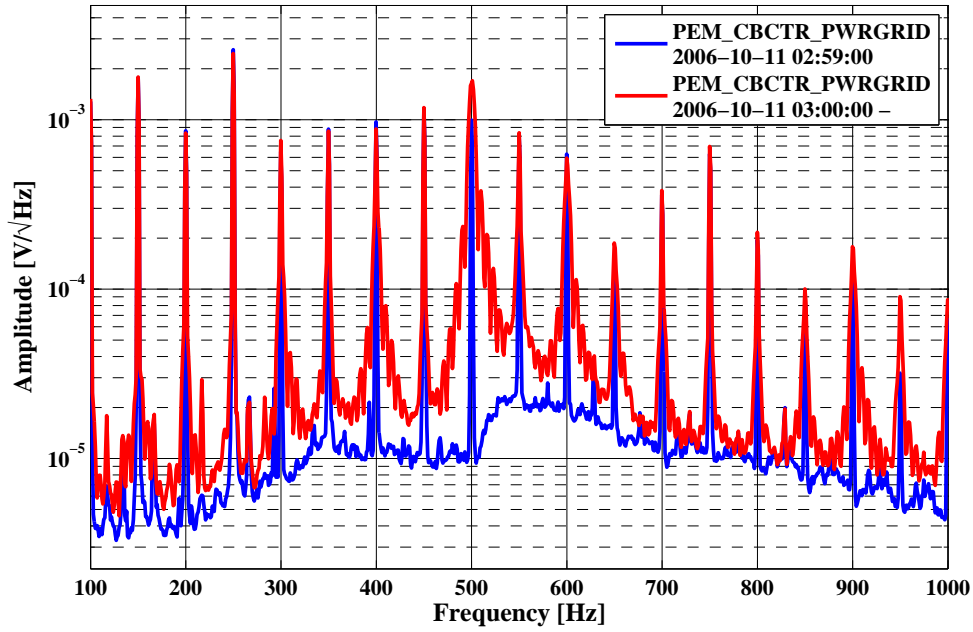


**Figure 5.2.:** Spectra of the mains monitor for the last (blue) and the first (red) minute of a UTC-hour. The ripple control signal has a nominal frequency of 500 Hz, but it is also strongly visible as sidebands around all harmonics of 50 Hz.

fer information via the mains from the power plant to the consumers. An amplitude modulation with a certain frequency (in our case 500 Hz) is superimposed on the usual 50 Hz power grid in order to remotely control lanterns and night storage heaters.

Figure 5.1 shows overlayed time series from a monitor of the main site power supply (mains). The ripple control signals repeatedly show up 10 seconds after the beginning of an UTC-hour. They consist of an up to 90 seconds long series of on-off-states with a maximum amplitude increase of about 6 %.

Spectra of a time when ripple control signals were present, compared to a time of their absence are shown in Figure 5.2. The ripple control signals have a nominal frequency of 500 Hz, but they are also strongly visible as sidebands around all other harmonics of 50 Hz, especially 400, 600 and 900 Hz.

It was found that, as indicated in Figure 5.3, some of the glitches in the mains monitor are time coincident with glitches in the main gravitational wave channel. A large fraction of the coincident events shows up shortly after the start of an hour. Furthermore nearly all of them are identified to have central frequencies of about 400, 500, 600 and 900 Hz, the same frequencies, where we found most of the excess power in the mains monitor caused by the ripple control (see Figure 5.2).

The coupling mechanism is not completely understood yet. Glitches in the mains can potentially couple in various ways to the GW channel. A glitch in the mains causes a glitch in the magnetic field surrounding the power line which can then interact with magnets glued onto the mirror [Gossler02]. Or the magnetic glitch can directly induce a voltage glitch in a piece of electronics used for control or readout of the detector.

However, as the coupling path for the ripple control signals to the gravitational wave channel is not known and therefore not accessible via measurements, no other veto method than a statistical veto can be applied. In Section 5.5.2 we will show some investigations done in order to find out whether a reasonably performing veto analysis can be based on the mains monitor.

In the long term we plan to filter the ripple control signals out of the local power grid by using some resonant LC-filter stages<sup>1</sup>. The installation of such a filter requires powering down of the full GEO 600 site which needs to be well prepared and is not free of risk.

---

<sup>1</sup>More detailed information about available filters can be found in <http://www.eskap.de/tonfrequenzsperren.pdf>.

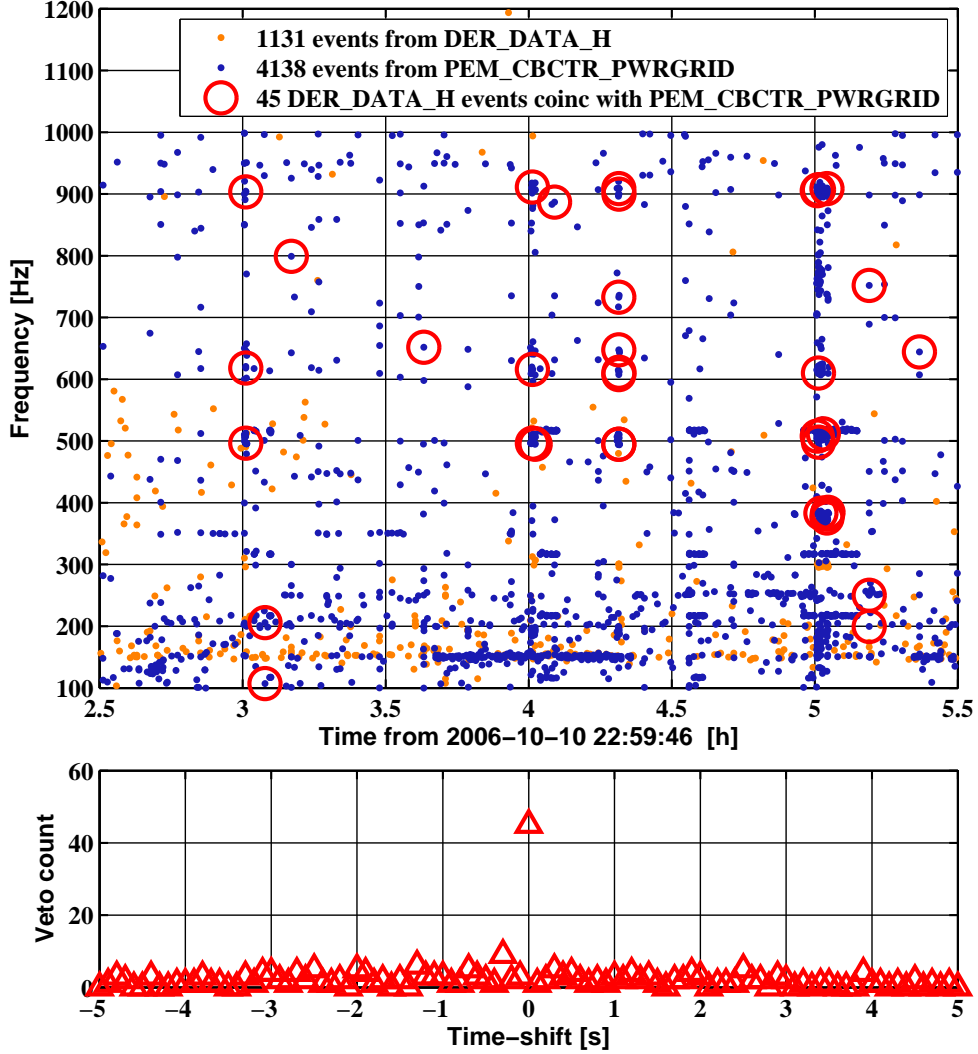


**Figure 5.3.:** *Upper plot:* Time frequency map of burst triggers in the mains monitor (blue dots) and the main gravitational wave channel (orange dots). The events in the mains monitor that are time coincident with an event in the GW channel are marked with a red circle. A time coincidence window of 10 milliseconds was used. No further coincident condition was imposed. *Lower plot:* Time shift analysis of the coincidence analysis from the plot above. A significant statistical correlation between the events from the mains monitor and the events from the GW channel is confirmed.

### 5.3. Motivation for a statistical veto with amplitude consistency check: Dust falling through laser beams

In May 2006, a significant increase in the glitch rate of the main GW channel ( $H$ ) of GEO 600 was observed. A broken air conditioning system blew unfiltered air into the main clean room and increased the dust particle concentration by more than one order of magnitude. It turned out that the increase in the glitch rate of  $H$  originated from dust particles falling through the main output beam of the interferometer.

Many glitches in the recorded DC light power hitting the main photodiode (referred to as  $\mathcal{P}_{\text{DC}}$ ), were observed to be coincident with glitches in  $H$ . Figure 5.4 shows a time coincidence analysis of the two channels for two different times of the S5 LSC science run. The upper plot shows an 8 hour data stretch from May 2006, when the air conditioning system was broken. 1245 of the 1719 detected events in  $H$  (72 %) are time coincident with an event in  $\mathcal{P}_{\text{DC}}$ . For this analysis a time coincidence window of 10 milliseconds was used. The lower subplot of Figure 5.4 shows the same analysis (with identical parameters) for a data segment from June 2006, when the air conditioning system was fixed again. Compared to the time of high dust concentration, in the low dust condition the total number of events from both signals is significantly reduced. Only about 5 % of the events in  $H$  are time coincident with an event from  $\mathcal{P}_{\text{DC}}$ .

However, tests involving injecting signals (noise, sinusoidal, burst events) into the differential length control actuator for the Michelson Interferometer (to mimic the effect of a GW), showed that  $\mathcal{P}_{\text{DC}}$  can contain, to a non-negligible degree, some GW signal. Figure 5.5 shows sinusoidal GW-like hardware injections (calibration lines) using the electro static drives. Spectra of the injected signal (*diff-CAL*) and  $\mathcal{P}_{\text{DC}}$  are plotted in the two upper figures. The frequencies of the injected sine waves are indicated by the circled markers. The lower figure shows the coherence of the two signals, which is nearly one for all frequencies of the hardware injections.

Hence, using a standard statistical veto could, undesirably, also veto potential GW events. That is why we developed a method, described in the Sections 5.6–5.7, that extends the standard statistical veto methods by an additional amplitude consistency check.

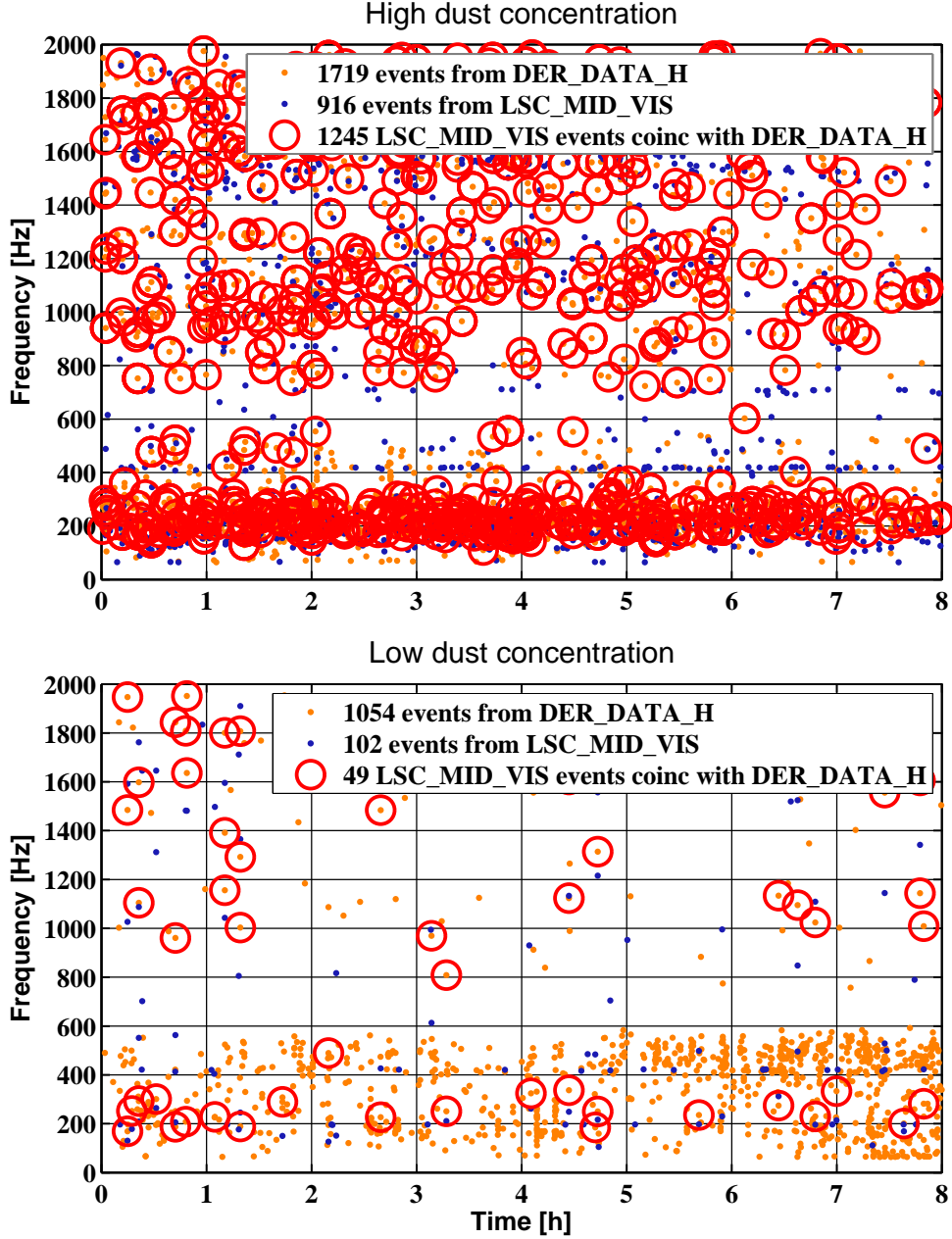


**Figure 5.4.:** *Upper Subplot:* Time coincidence analysis for the GW channel ( $H$ ) and  $\mathcal{P}_{DC}$  for a time of high dust concentration at the detection bench, corresponding to a time when the air conditioning system was broken. *Lower Subplot:* The same analysis, but for a time of low dust concentration at the detection bench, corresponding to a time of nominal operation of the air conditioning system. For both analysis a time coincidence window of 10 milliseconds was applied.

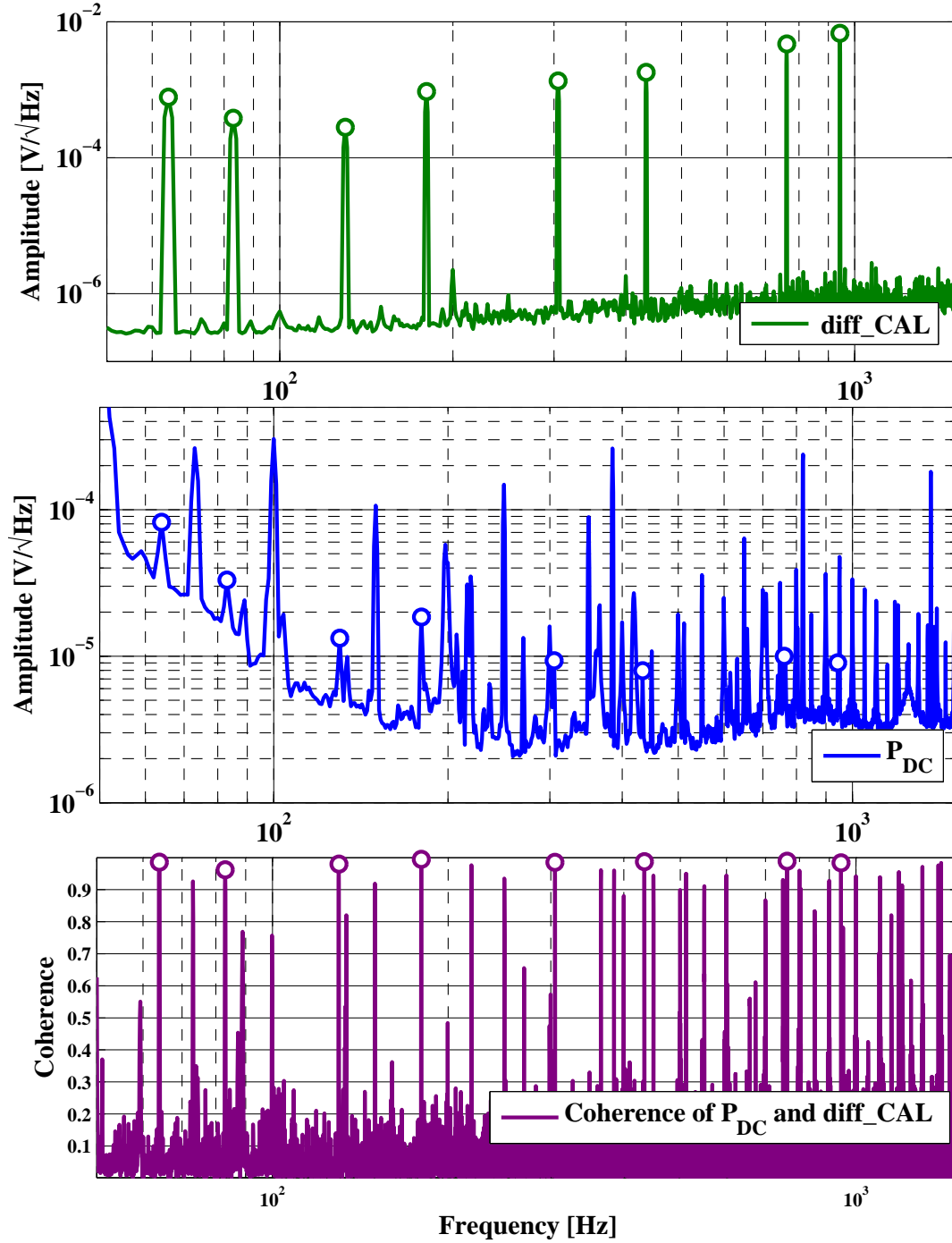


**Figure 5.5.:** Sinusoidal gravitational wave like hardware injections: The upper plot is a spectrum of the injected signal. The frequencies of the injections are marked with circles. The plot in the middle shows a spectrum of  $P_{\text{DC}}$ . The lower plot shows the coherence of the two signals. For all frequencies of the injections the coherence is found to be nearly one. This confirms that a non neglectabel amount of differential arm length signal couples to  $P_{\text{DC}}$ .

## 5.4. Description of the event trigger generator used: mHACR

Any potential *burst* gravitational wave signal is expected to be very weak and of very short duration, barely visible and hard to separate from the intrinsic noise of the instrument. Therefore sensitive detection algorithms have been developed in order to identify and parameterize any excess power in the main gravitational wave output. Examples of these event trigger generators (ETG) used for astrophysical searches are *Kleine Welle* [Chatterji04], *Excess Power* [Anderson01] and *Waveburst* [Klimenko04]. For the commissioning of the GEO 600 detector we use an ETG called *mHACR*, which is described in detail in [Balasubramanian05] [Heng03] and [Hild07a].

For the understanding of the following sections it is important to know how mHACR roughly works. That is why in this section I give a brief and simplified description of mHACR.

32 seconds of data from the channel to be analyzed are divided into short segments of 32 milliseconds length with an overlap of 28 milliseconds. From each of the 32 milliseconds-long subsegments a FFT is computed. Afterwards, all of the FFTs are joined together to give a time-frequency map, also known as spectrogram, with a very high time resolution of 4 milliseconds and a (poor) frequency resolution of 32 Hz. A normalization of the spectrogram is performed, such that the spectrogram has units of power spectral density.

This normalized spectrogram will be called  $\rho$  and each pixel  $\rho_{kl}$  can be identified by two indexes  $k$  and  $l$ , representing frequency bin and time, respectively. The main task of the ETG is to identify pixels which are statistically different from the background noise. This is done by computing the significance,  $s_{kl}$  of each pixel, given by

$$s_{kl} = \frac{\rho_{kl} - \mu_k}{\sigma_k}, \quad (5.1)$$

where  $\mu_k$  is the mean and  $\sigma_k$  is the standard deviation of the  $k^{th}$  row of  $\rho$ . The significance is now used to sort the pixels into three groups of color, according to the following criteria:

$$\text{colour}(\rho_{kl}) = \begin{cases} \text{black,} & \text{if } s_{kl} \geq T_{\text{upp}} \\ \text{grey,} & \text{if } T_{\text{upp}} > s_{kl} \geq T_{\text{low}} \\ \text{white,} & \text{if } s_{kl} < T_{\text{low}}, \end{cases}$$



where  $T_{\text{low}}$  and  $T_{\text{upp}}$  are the chosen lower and the upper threshold. For the analysis described in the following the thresholds were chosen to be 5 and 25. In the next step mHACR identifies clusters of neighboring grey and black pixels. If a cluster consists of at least two pixels (black, grey) of which at least one is black, this cluster is identified as a burst event.

#### 5.4.1. Estimation of burst parameter with mHACR

After the burst event is identified by mHACR we need to parameterize this event. Amplitude, time of occurrence, central frequency and duration are, amongst others, the most important parameters for the understanding of the following sections. The signal power of a single pixel,  $S_{kl}$ , is given by the power of the pixel minus the mean noise-power of the frequency bin:

$$S_{kl} = \rho_{kl} - \mu_k. \quad (5.2)$$

With this, the amplitude,  $a$ , of an event can be computed as

$$a = \sqrt{\frac{\sum_{k,l} S_{kl}}{r}}, \quad (5.3)$$

where  $r$  is the redundancy factor accounting for the 28 milliseconds overlap of each FFT. The estimation of the *central frequency*,  $f_0$ , and *central time*,  $t_0$ , is analogous to the calculation of the centre-of-mass of an extended body. Here, the *signal power*,  $S_{kl}$ , in each time-frequency pixel serves as the ‘mass’ term and the time/frequency associated with each pixel serves as the ‘position’ term. That is,

$$f_0 = \sum_{k,l} S_{kl} f_k / \sum_{k,l} S_{kl} \quad (5.4)$$

$$t_0 = \sum_{k,l} S_{kl} t_l / \sum_{k,l} S_{kl}. \quad (5.5)$$

Finally, the duration,  $d$ , of an event can be estimated by from the extend of the event in the time axis as

$$d = \max(t_l) - \min(t_l). \quad (5.6)$$

Usually there are more parameters available from mHACR, for instance bandwidth, peak power and SNR, but these are not used for any analysis presented in this work. In Figure 5.6 the whole algorithm of mHACR is briefly illustrated.

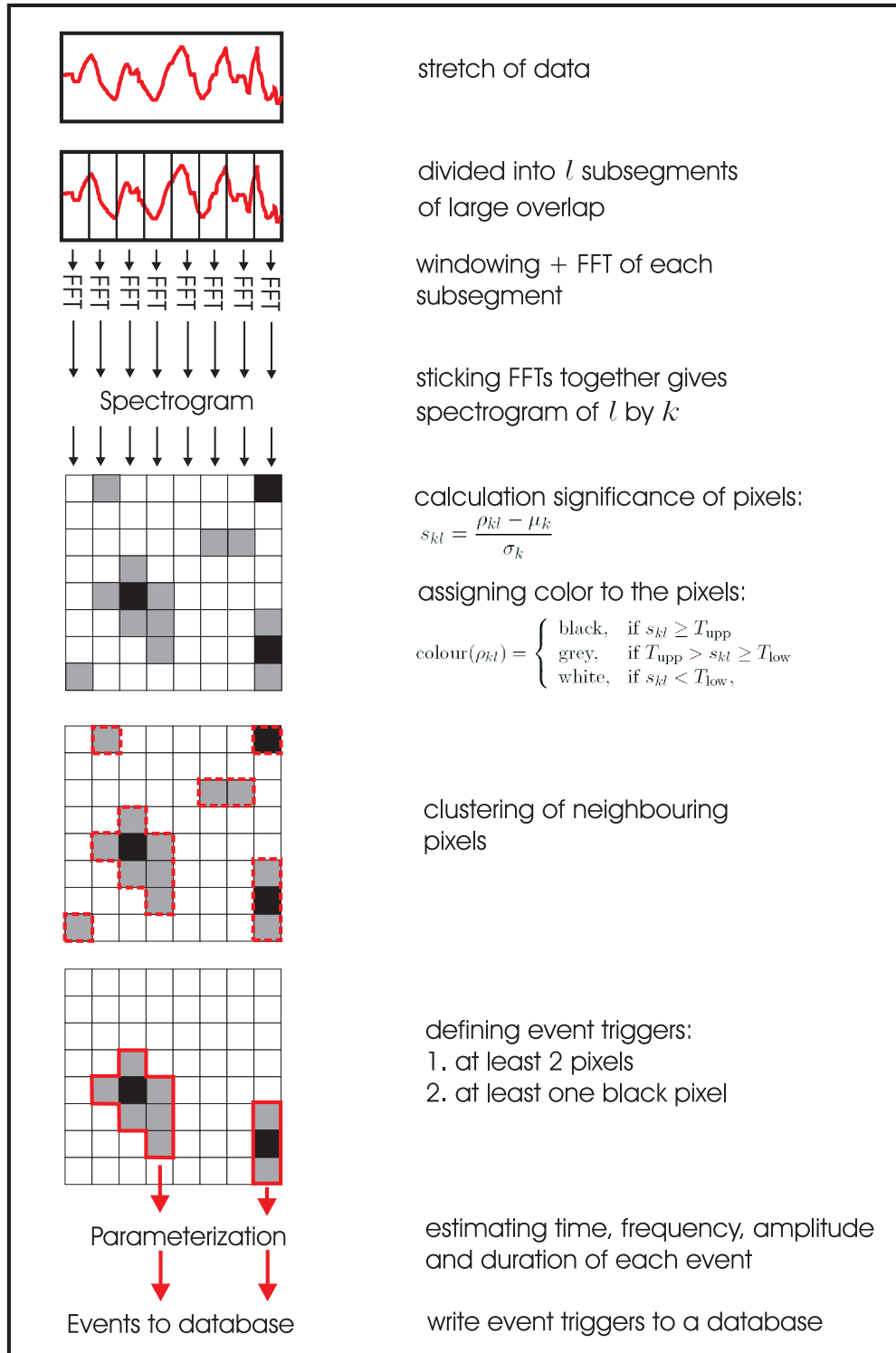


**Figure 5.6.:** Simplified illustration of the mHACR burst pipeline. A detailed description is given in the text.

## 5.5. The standard statistical veto

All currently operating GW detectors face the problem that several instrumental and environmental noises can couple to the GW channel. Therefore, it is desirable to identify in the GW stream, those events which can be shown to have a local instrumental or environmental source, and exclude them from any astrophysical analysis.

At each GW detector a multitude of sensors is installed to monitor instrumental noise sources (for instance, laser power noise) and environmental noise sources (such as magnetic fields). In the following, we will refer to both instrumental and environmental noise as technical noise sources.

If detected events in the GW channel are caused by a technical noise source, there will be a significant statistical correlation between the events of the GW channel and those detected in the recording of any device which monitors the noise source. (This assumes that both the main detector output and the auxiliary channel are properly recorded, and that the ETG does a good job of detecting and parameterising any glitch events in the data streams.) Even in the case when the coupling mechanism from the technical noise source to GW channel cannot be measured, we can use the statistical correlation to veto the coincident events.

In order that we end up with a sufficiently low false-veto rate, we must restrict ourselves (for the time-being) to auxiliary channels which cannot contain any GW information.

### 5.5.1. The method in general

Usually a simple statistical veto is based on the comparison of the time,  $t_0^H$ , of the event in the GW channel and the time,  $t_0^X$ , of the event in an auxiliary channel. Two events,  $H[i]$  and  $X[j]$ , are defined as being coincident when they are separated in time by less than a chosen time window,  $t_{\text{win}}$ :

$$| t_0^H[i] - t_0^X[j] | < t_{\text{win}}. \quad (5.7)$$

Every event,  $H[i]$ , that is time-coincident with at least one event from the auxiliary channel is vetoed.

The performance of a veto depends on many parameters (such as the event rates in the individual channels), and needs to be evaluated. The following measures can be useful

to judge the performance of a veto:

- The **Efficiency**,  $E_X$ , is the percentage of triggers in the GW channel that are vetoed by the use of the events of the auxiliary channel,  $X$ .
- The **Background**,  $B_X$ , is the percentage of triggers in the GW channel that are *accidentally* vetoed by the use of the events of the auxiliary channel,  $X$ . In general there are two possible groups of coincident events:
  1. The event  $H[i]$  is either caused by, or originates from the same source as, the event  $X[j]$ .
  2. The event  $H[i]$  is not caused by any event recorded in the auxiliary channel, but by accident there happens to be an independent event  $X[j]$  that is time coincident with the event  $H[i]$ .

By time-shifting the events in the GW channel with respect to the events in the auxiliary channel, it is possible to destroy the causal relationship between the events of the two channels and by that, to determine the accidental rate. Sometimes it is useful not to measure the background in percentage, but in units of accidentally-vetoed events per unit time, in order to determine how many potentially real GW events would be missed when applying the veto.

- The **Significance**,  $S_X$ , is defined as the ratio of efficiency and background and can be seen as the main figure of merit of a veto analysis. This can be illustrated by some examples. A veto that has a high efficiency of 50 % might also have a high background of, for example, 5 %, which would mean that we would falsely veto a large number of potential GW signals. On the other hand a very low background of 0.01 % does not necessarily guarantee a good veto performance, as it can still have a low efficiency of, say, 0.03 %. That is why we choose here the ratio of efficiency and background as a good way of judging the trade-off between efficiency and background. (When changing the width of a coincidence window, both the efficiency and the background are changed as well, but in general with different slopes.)
- The **Use-percentage**,  $U_X$ , is another means of the measuring the veto performance. It is defined as the percentage of the events in the auxiliary channel that can veto an event in the GW channel.

### Additional coincident windows

In order to improve the significance of a veto, it might often be useful to demand that, not only are two events coincident in time, but also that other parameters of the events are similar. Assuming the event,  $X[j]$ , to be the origin of the event  $H[i]$ , for instance, also the central frequency of the two events, or their duration, might show a correlation. Of course, the strength of the correlation depends strongly on the coupling from channel  $X$  to the GW channel,  $H$ , and also on the noise level and the stationarity of noise in the two channels. In the worst case, the correlation might be completely destroyed. However, in GEO 600 we found some cases where the application of a second coincidence condition clearly improves the significance of a statistical veto.

In the following sections we will also apply an additional coincidence window,  $f_{\text{win}}$ , for the central frequency of the events. In that case an event,  $H[i]$ , in the GW channel is vetoed by the event,  $X[j]$ , from the auxiliary channel only when the following equation is satisfied,

$$|t_0^H[i] - t_0^X[j]| < t_{\text{win}} \wedge |f_0^H[i] - f_0^X[j]| < f_{\text{win}}, \quad (5.8)$$

where  $f_0^H[i]$  and  $f_0^X[j]$  are the central frequencies of the two events.

#### 5.5.2. Application of a standard statistical veto to GEO S5 data

In this section, we will show some investigations done in order to find out whether it is reasonable to use a monitor of the main site power supply (mains) as a veto channel.

As described already in Section 5.2 glitches on the mains can easily couple to  $H$ , while on the other hand it is hard to imagine any way in which a GW could couple back to the mains monitor. This was confirmed by performing GW-like hardware injections. There we inject sine-Gaussian type waveforms into the electrostatic actuators used for the differential length control of the Michelson interferometer and no back coupling to the mains monitor was observed.

Figure 5.7 shows the application of a standard statistical veto to the GW channel using a mains monitor as veto channel. The efficiency and background rate are plotted for time windows between 0 and 20 ms. The shapes of both curves are roughly the same, *i.e.*, the significance stays roughly constant around a value of 20 for different sizes of the time coincidence window.

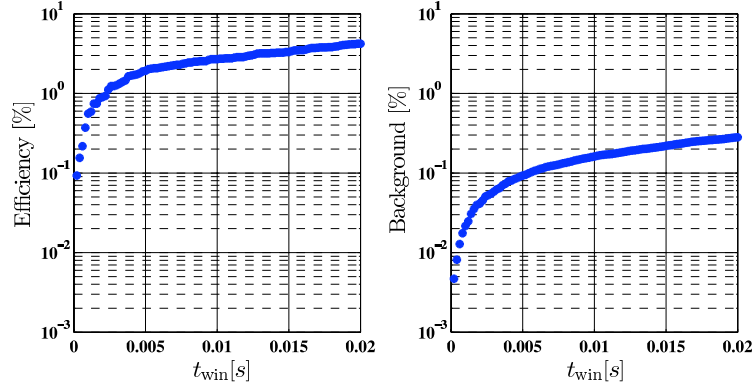


**Figure 5.7.:** Exemplary application of a statistical veto to a 24 hour stretch of GEO data using a GW-free channel (in this case a mains monitor), as veto channel. Efficiency and background are given as a function of the size of the coincidence time window. The data set used consisted of 3228 and 7725 events in the GW channel and the mains monitor, respectively.

If we choose a time-window of 6 milliseconds in order to get a background of 0.1 %, we achieve an efficiency of about 2 %. Figure 5.8 shows (for the same set of data and a fixed time-window of 6 milliseconds), the effect of including an additional coincidence window for the central frequency of the events.

The right-hand plot of Figure 5.8 shows the improvement in the significance for different sizes of the frequency coincidence window, compared to the case where only a coincidence window for the time of the events is applied. In this case, for all sizes of the frequency coincidence window, the significance is improved. A maximal improvement of about 50 % is achieved for a frequency window of 200 Hz.

If we choose windows,  $t_{\text{win}} = 6$  msec and  $f_{\text{win}} = 200$  Hz, we get an efficiency of 1.5 %, a background of 0.05 %, a use-percentage of 0.6 % and a significance of 30. This example demonstrates the usefulness of additional coincidence windows. However, as the actual performance of this veto is not very impressive in itself, the veto should rather be viewed as an illustrative example.

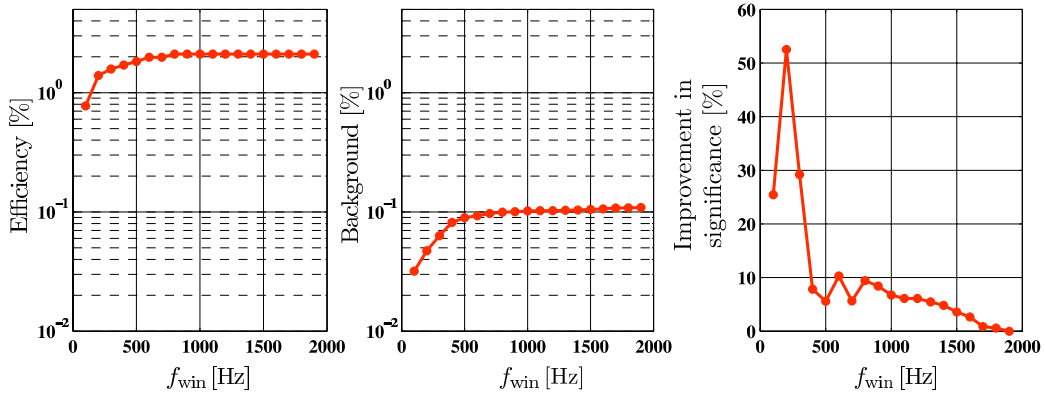


**Figure 5.8.:** Exemplary application of a statistical veto including an additional coincidence condition for the central frequency of the events. The same data set as for Figure 5.7 is used. A time coincidence window of 6 milliseconds is applied. The background and efficiency are plotted versus the size of the coincidence window for the central frequency. In addition, the right hand plot shows the improvement in significance versus the size of the frequency window. The improvement of significance is the relative improvement compared to the case where no frequency coincidence window is applied.

## 5.6. A statistical veto for channels containing GW information

In the previous section, we described the statistical veto method using an auxiliary channel containing no gravitational wave information. In this section we will show that, under certain conditions, and when handled with care, a reliable statistical veto can also be based on a veto channel which can contain gravitational wave information.

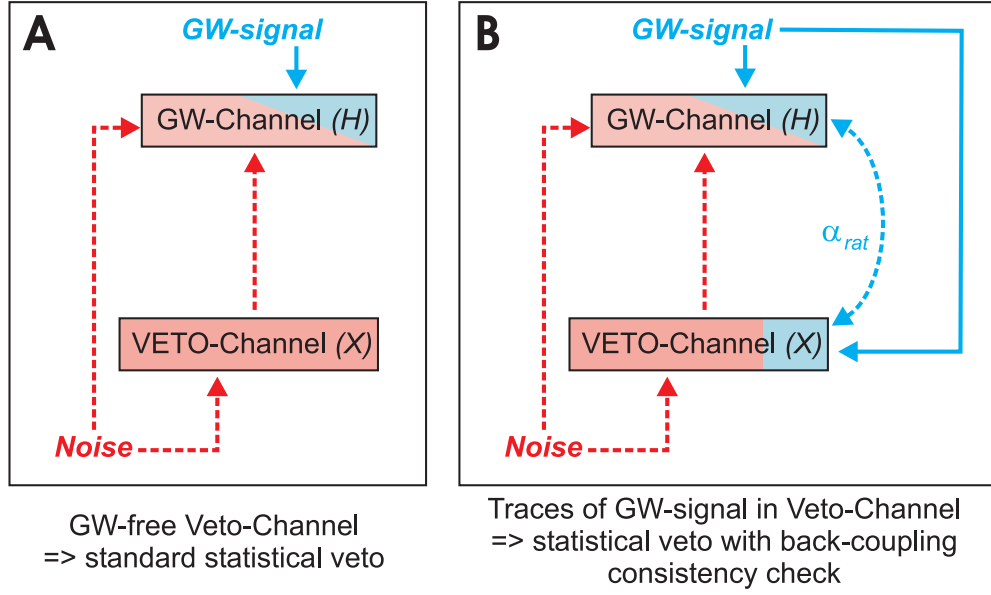


**Figure 5.9.:** A schematic view of two different scenarios in which coincident transient events can appear in both the main GW channel,  $H$ , and an auxiliary channel,  $X$ . The first scenario (Panel A) shows coincident events arising from a single noise source, which couples events to  $H$  either directly, or via subsystem  $X$ , or both. The second scenario (Panel B) shows the case where the events in  $X$  can originate, not only from the noise source, but also from the GW signal. The frequency dependent amplitude ratio of a GW-like event measured in both channels,  $\alpha_{rat}$ , can be determined by injecting differential arm length noise (to mimic the effect of an GW signal) and measuring the transfer function from  $H$  to  $X$ .

Figure 5.9 shows two scenarios. Panel A describes the case where there is an (unknown) coupling of a noise source,  $N$ , into both the main GW channel, and an auxiliary channel,  $X$ ; for this case, the standard statistical veto described in Section 5.5 can be applied. Panel B shows the case where the events in  $X$  can originate, not only from the



noise source, but also from the GW signal. In order to apply a statistical veto (with a sufficiently low false-veto rate), in such a situation, we have to introduce further coincidence conditions, such as a frequency-dependent amplitude cut. The application of this method requires a rough knowledge of the amplitude ratio,  $\alpha_{\text{rat}}$ , and its stability.

### 5.6.1. The method in general

In the presence of gravitational wave signal in the veto channel, we will have two classes of coincidence events to consider when applying a standard statistical veto:

- Noise events that couple via the (red) dashed lines of Figure 5.9. These are the events we would like to veto.
- Gravitational-wave-like events that are showing up in the GW channel as well as in the veto channel.

It is essential to discriminate these two populations and exclude events from the latter class from being vetoed.

A possible way to do this is to compare the amplitudes  $a^H[i]$  and  $a^X[j]$  of the two coincident triggers  $H[i]$  and  $X[j]$ . In the case that the event  $X[j]$  originates from the same GW-like event as the event,  $H[i]$ , the following (ideal) amplitude ratio can be computed:

$$\frac{a^X[j]}{a^H[i]} = |\alpha_{\text{rat}}[i]|, \quad (5.9)$$

where  $|\alpha_{\text{rat}}[i]|$  is amplitude ratio of the GW signal in  $H$  and  $\mathcal{P}_{\text{DC}}$ ,  $\alpha_{\text{rat}}$ , evaluated at the central frequency of the event,  $H[i]$ , in the gravitational wave channel.

If all quantities in Equation 5.9 are known, the application of the statistical veto is rather simple. First of all, the coincident events need to be determined in the same way as for the standard statistical veto. Secondly, for each pair of events, the ratio of the two amplitudes is compared. If this ratio equals the magnitude of the amplitude ratio,  $\alpha_{\text{rat}}$ , at the central frequency of the event, the event in the gravitational wave channel is not vetoed. If the amplitude ratio is not consistent with the  $\alpha_{\text{rat}}$ , the event  $H[i]$  is vetoed.

It is also possible that more than one event in the veto channel is coincident with the event  $H[i]$ . In this case, the  $H$  event is excluded from being vetoed if at least one of the

coincident pairs satisfies Equation 5.9.

### 5.6.2. A ‘real-world’ scenario

In reality, Equation 5.9 needs to be extended to account for several systematic and statistical errors. Probably the largest contribution to the error originates from the amplitude estimation of the burst events. The errors associated with the amplitude estimation of the events  $H[i]$  and  $X[j]$  are referred to as  $\Delta a^H[i]$  and  $\Delta a^X[j]$ , respectively. Also, the measurement of the amplitude,  $\alpha_{\text{rat}}$ , can be a source of error. More over, the amplitude ratio can also be non-stationary over time. We represent the cumulative errors due to these two effects by  $\Delta\alpha_{\text{rat}}$ .

Considering these errors, we make a simple generalisation of Equation 5.9 into the ‘real-life’ situation. In order to veto an event,  $H[i]$ , in the gravitational wave channel, we first require that it be coincident with the another event,  $X[j]$ , in the veto channel in the sense of a standard statistical veto (in time and frequency), and secondly that it satisfy either of the following conditions:

$$\frac{a^X[j]}{a^H[i]} < \frac{|\alpha_{\text{rat}}[i]|}{(1 + \Delta a_{\text{tot}})}, \quad (5.10)$$

or

$$\frac{a^X[j]}{a^H[i]} > |\alpha_{\text{rat}}[i]| (1 + \Delta a_{\text{tot}}) \quad (5.11)$$

where  $\Delta a_{\text{tot}}$  is an upper-limit of the cumulative error from the amplitude estimation and the amplitude ratio measurement (also due to the non-stationarity of the amplitude ratio over time).

We will call the veto method based on the condition described above, a *frequency-dependent amplitude cut*, because we cut the events with a certain amplitude ratio out of the list of coincident vetoed events.

## 5.7. Application of a statistical veto with a amplitude consistency-check to GEO 600 data

In the following three subsections we will present the results of applying a statistical veto with a amplitude consistency check to GEO 600 data using  $\mathcal{P}_{\text{DC}}$  as the veto channel.

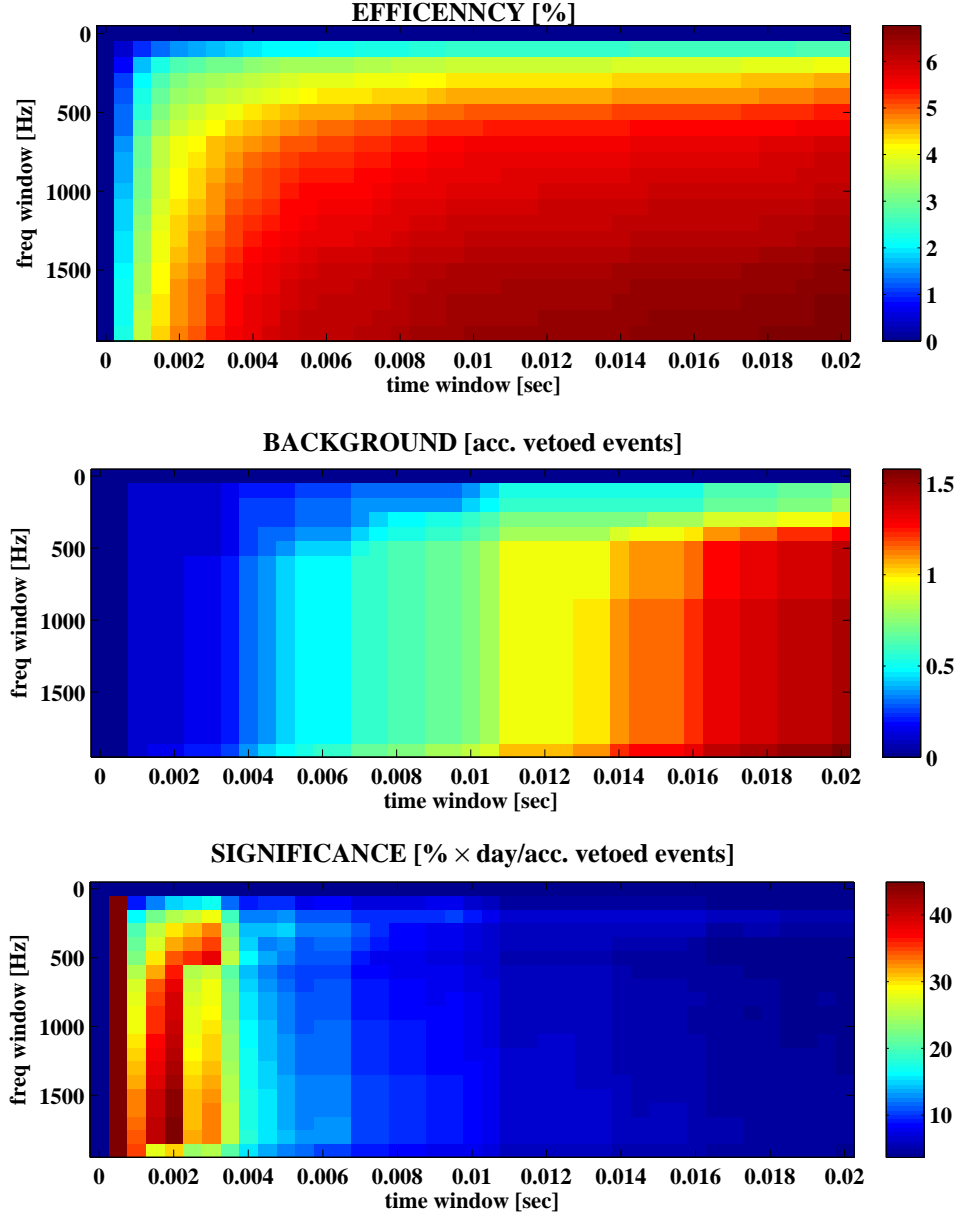


**Figure 5.10.:** Efficiency, background and Significance of a veto using  $\mathcal{P}_{DC}$  as veto channel for various sizes of the time and frequency coincidence window. To reduce computational resources required for this analysis a data stretch of 24 hours from September 2006 was used instead of the full month. This analysis is done to find good sizes for the coincidence windows. At this stage of the analysis no amplitude consistency-check is applied.

Two different periods of time are analysed. The analysis of a long stretch of data covering the entire month of September 2006 (where the dust concentration in the clean-room was nominal), is presented in subsection 5.7.1. An 8 hour stretch of science data from May 2006 (where a high dust concentration in the clean room was observed), is analysed in subsection 5.7.2. There are only short data stretches available for this period because the broken air conditioning system was fixed within a few days. However, even with the nominal dust concentration restored, still, dust glitches contribute to the glitch rate of  $H$ . Finally, the performance of the veto for both periods is compared in subsection 5.7.3.

### 5.7.1. Data set 1: Full September 2006 with low dust concentration

First we have to determine reasonable sizes for the time and frequency coincidence windows. This was done by computing efficiency, background and significance of the veto for various window sizes for a subset of 24 hours of data from September 2006. The result of this analysis is shown in Figure 5.10. The best significance can be achieved for very small time windows. However for these small time windows the efficiency is very small. That is why we have to trade off significance and efficiency. For a time window of 8 milliseconds and a frequency window of 1000 Hz we achieve a best efficiency for an acceptable background rate of about 0.5 events per day.

For both data sets, and the hardware injections, firstly a coincidence analysis is performed using a time coincidence window of 8 milliseconds and a frequency coincidence window of 1 kHz determined by the analysis described above. The upper plot of Figure 5.12 shows the ratio of the amplitude of the coincident events from  $\mathcal{P}_{\text{DC}}$  and  $H$  versus the central frequency of the event in  $H$ . The (blue) diamonds, corresponding to the GW-like hardware injections, are close to the measured amplitude ratio,  $\alpha_{\text{rat}}$  (as expected); all the coincident events from the first data set (represented by the purple points), show either a similar amplitude ratio or a higher one. If the ratio is similar to the hardware injections, the points most probably correspond to GW-like events. If the amplitude ratio is higher, this means that  $\mathcal{P}_{\text{DC}}$  events show a higher amplitude than is consistent with events originating from a GW-like event. As we do not observe any pairs of events with an amplitude ratio much lower than from the hardware injections,

it is reasonable to simplify Equation 5.11 to the single condition,

$$\frac{a^X[j]}{a^H[i]} > |\alpha_{\text{rat}}[i]| (1 + \Delta a_{\text{tot}}). \quad (5.12)$$

Over one month,  $\alpha_{\text{rat}}$  was measured a few times and  $\Delta\alpha_{\text{rat}}$  was found to be less than 0.5.

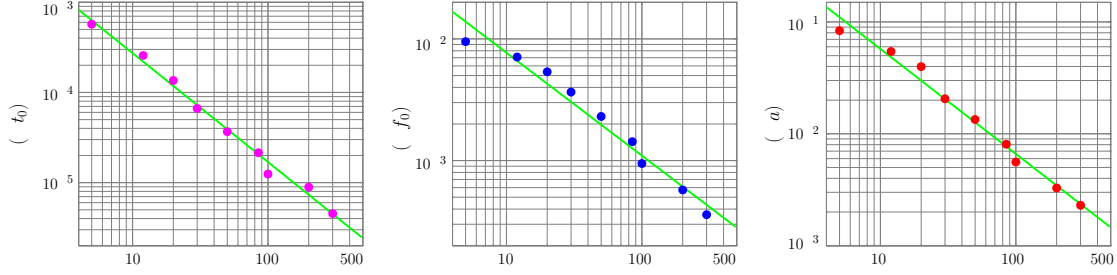


**Figure 5.11.:** Standard deviation of the distribution of the mHACR errors (in estimating the parameters of injected sine-Gaussian waveforms into gaussian noise) plotted as a function of the snr of the triggers. Also shown are linear-polynomial fits to the data. This plot is taken from [Hild07a] and was produced by P. Ajith.

The main error contribution of the amplitude estimation of the events can be described by three times the standard deviation ( $3\sigma$ ) given in the right hand plot of Figure 5.11. The lowest SNR of an event contained in this analysis is about 4, which means that the maximum error in estimating the amplitude of an event is about 60 % (see Figure 5.11). Since the values in Figure 5.11 are estimated from ideal conditions<sup>2</sup>, we will allow for a 200 % error in the amplitude estimation to get a safe upper limit of the error. All together,  $\Delta a_{\text{tot}}$  amounts to 2.

In the end we get the final set of three veto conditions:

$$|t_0^X[j] - t_0^H[i]| < 8 \text{ ms}, \quad (5.13)$$

$$|f_0^X[j] - f_0^H[i]| < 1 \text{ kHz}, \quad (5.14)$$

<sup>2</sup>The errors in parameter estimation given by a particular detection algorithm depend on many things, for example, the waveform of the transient signal and the characteristics of the underlying data-stream (noise, spectral lines, etc).

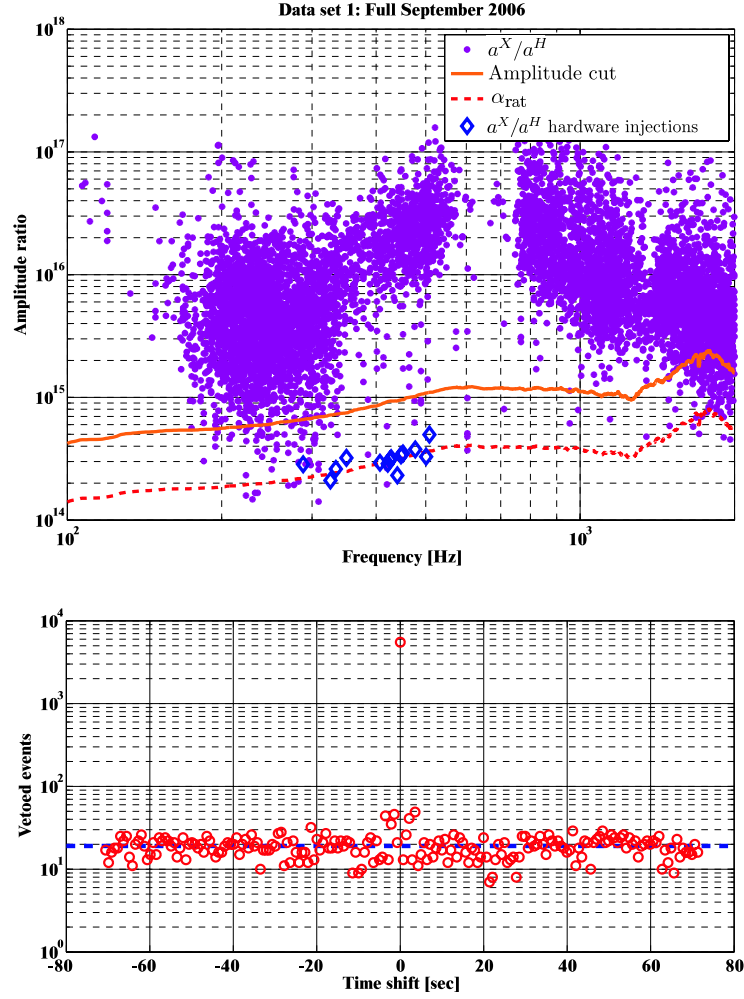


**Figure 5.12.:** *Upper plot:* Application of a statistical veto with a amplitude consistency check to GEO 600 data for the entire month of September 2006. The (red) dashed line is a measurement of the amplitude ratio,  $\alpha_{\text{rat}}$ . The (blue) diamonds are the amplitude ratios of the coincident events in  $\mathcal{P}_{\text{DC}}$  and  $H$  from GW-like burst hardware injections. The hardware injections are consistent with  $\alpha_{\text{rat}}$ . The solid (orange) line is the chosen amplitude cut, corresponding to  $\Delta a_{\text{tot}} = 2$ . The (purple) points indicate the amplitude ratio of the coincident events from  $\mathcal{P}_{\text{DC}}$  and  $H$  for September. Each  $H$  event corresponding to a point above the solid line is vetoed, while each point below the solid line is taken as being consistent with a GW signal and is excluded from being vetoed. *Lower plot:* A time-shift analysis of the statistical veto with a amplitude consistency check for data set 1. 5517 events in  $H$  are vetoed, while the background of accidentally-vetoed events amounts to 19.1 events per month.

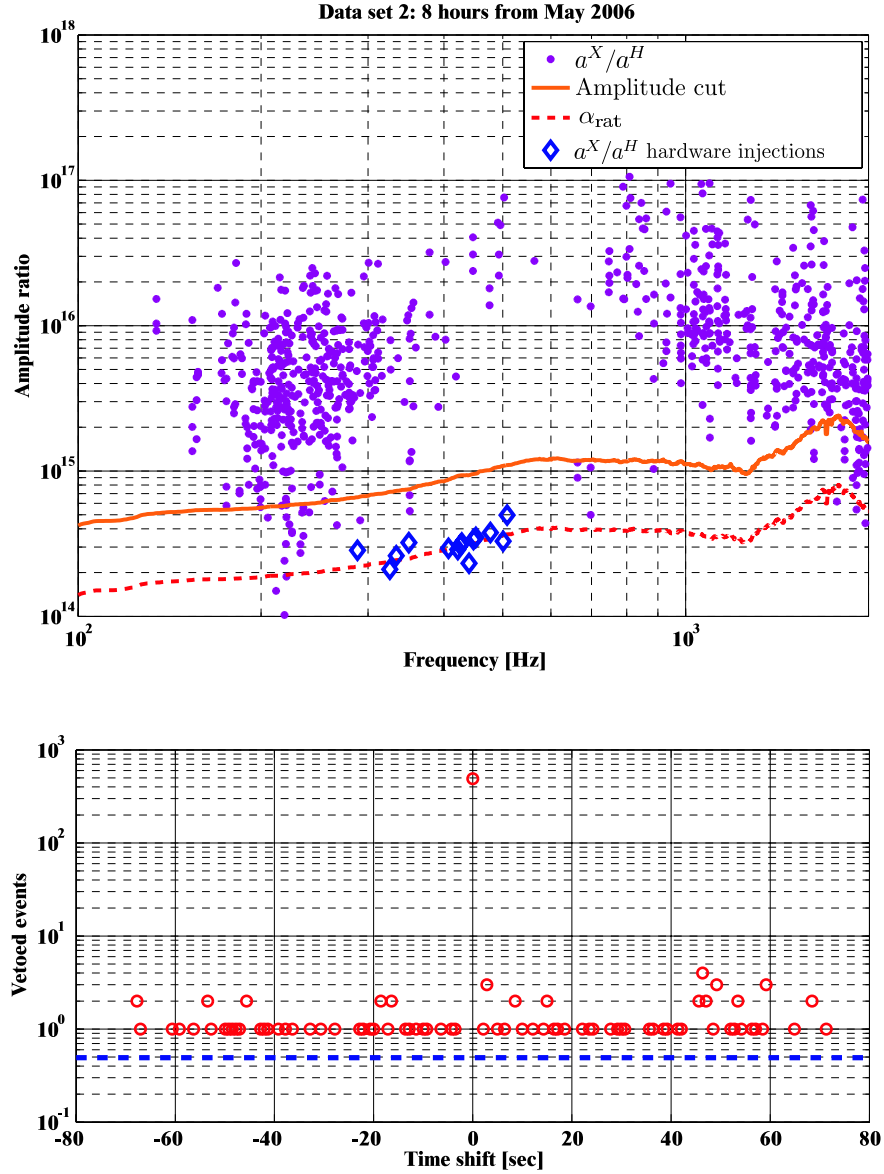


**Figure 5.13.:** *Upper plot:* The application of a statistical veto with a amplitude consistency check to 8 hours of GEO data from May. For further details, please see Figure 5.12. *Lower plot:* A time-shift analysis of the statistical veto with a amplitude consistency check for data set 2. 291 events in  $H$  are vetoed, while the background of accidentally vetoed events amounts to 0.49 events per 8 hours.

and

$$\frac{a^X[j]}{a^H[i]} > 3 \alpha_{\text{rat}}[i]. \quad (5.15)$$

The last condition can be seen as an amplitude cut. The solid (orange) line in Figure 5.12 indicates the level of this amplitude cut. Each  $H$  event corresponding to a (purple) point above the solid line is vetoed, while each point below the solid line is taken as being consistent with a potential GW signal and is excluded from being vetoed. By introducing the amplitude cut the veto efficiency is reduced from 5.94 to 5.72 %. The background rate of this veto is estimated by time-shifting the  $H$  events and is indicated by the (blue) dashed line in the lower plot of Figure 5.12.

### 5.7.2. Data set 2: 8 hours from May 2006 with high dust concentration

Data set 2 is from a time with a high dust concentration in the main clean room. For the analysis, identical veto conditions are applied as for data set 1. The result of the veto application is shown in Figure 5.13.

For this set of data, a high veto efficiency of greater than 20 % is obtained. The background rate of this veto, estimated from a time-shift analysis, is indicated by the (blue) dashed line in the lower subplot of Figure 5.13.

### 5.7.3. Performance of the veto analysis

The results of applying a statistical veto based on  $\mathcal{P}_{\text{DC}}$ , together with a amplitude consistency check, are summarised in Table 5.1.

Data Set	1	2
Efficiency [%]	5.72	21.5
Background [%]	0.02	0.02
Significance	286	1075
Use-percentage [%]	20.7	79.8

**Table 5.1.:** A summary of the results of applying a statistical veto with a amplitude consistency check to two different data sets from GEO 600.



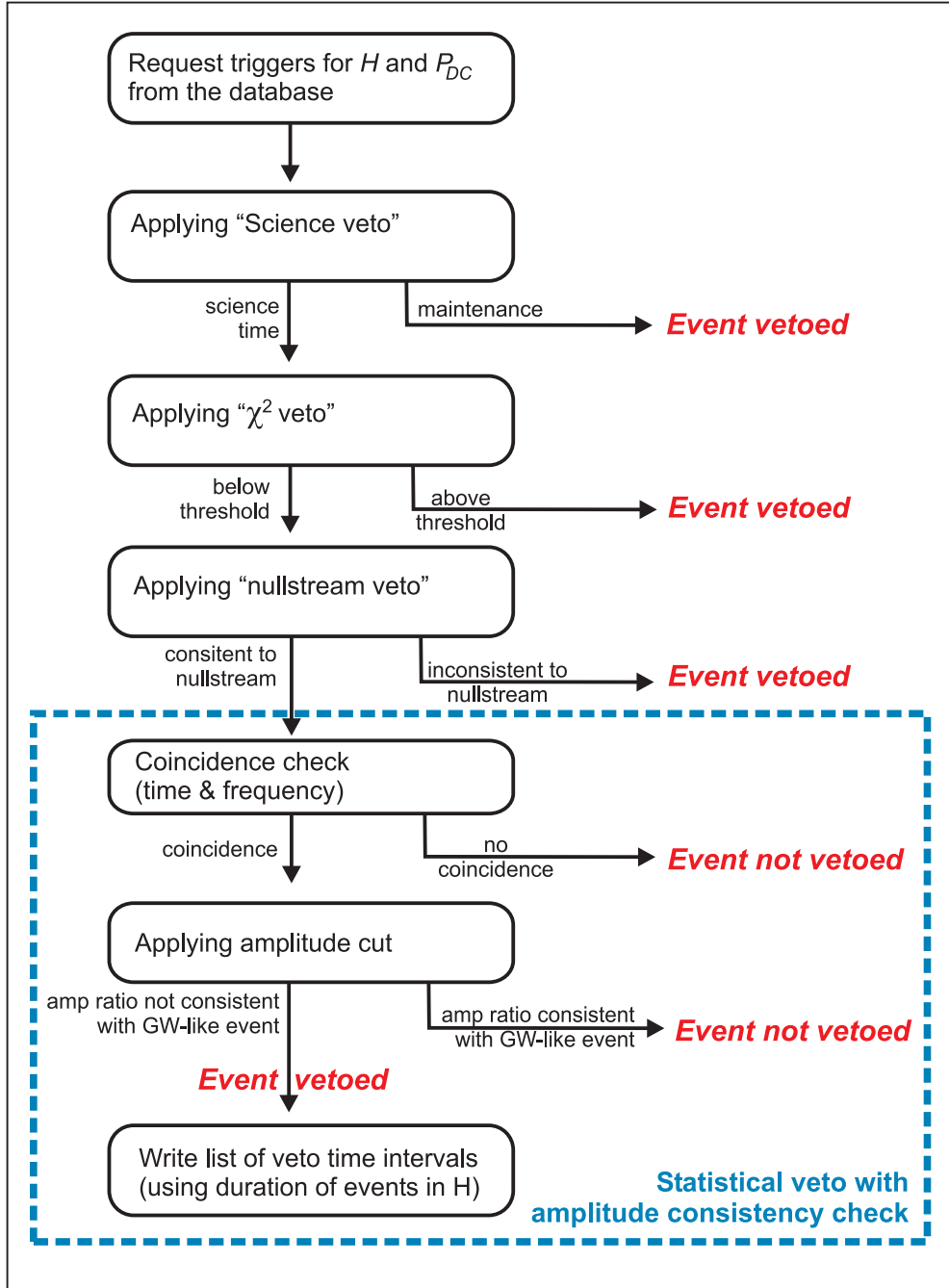


**Figure 5.14.:** Schematic of the veto pipeline used for the analysis of Data Set 1 (full September 2006). Before the statistical veto three other vetoes (science,  $\chi^2$  and null stream) are applied. The output of the whole pipeline is a list of veto intervals.

Figure 5.14 gives a schematic overview of veto analysis performed for the analysis of full September 2006. The corresponding Matlab script can be found in Appendix G.

## **5.8. Summary**

It was shown that the performance of a standard statistical veto can be improved by application of more than one coincidence window. Furthermore, a new veto method was developed which allows the use of veto channels which can contain GW signal. By introducing an amplitude consistency check, safe statistical vetoes can be derived from interferometer channels. GW-like hardware injections have been performed to demonstrate the robustness of this veto method. Application of a statistical veto with amplitude consistency check to data from the GEO 600 detector was shown to perform well, giving a veto efficiency of up to 20 % and a use-percentage of up to 80 %. This new method is generally applicable and can also be used on the data from other GW detectors.

## Chapter 6.

# Towards DC-readout for GEO 600

### 6.1. Introduction

All of the currently running large-scale gravitational wave detectors are operated at the dark fringe and use a heterodyne readout. For a Michelson interferometer without signal recycling the choice of this operating point has two predominant advantages: First of all, the couplings of some technical noise, for example laser power noise, are suppressed. Secondly, the power recycling technique can easily be implemented.

However, the experience in the currently running interferometers reveal several problems connected to a heterodyne readout:

- As it will be shown in Section 6.2 a heterodyne readout always implies an increased shot noise level with respect to a homodyne readout.
- Phase noise of the applied modulation would probably limit the sensitivity of advanced detectors.
- Since the Michelson RF sidebands propagate differently through the interferometer than the carrier light the spatial overlap of the GW signal (carrier) and the local oscillator (Michelson sideband) might be imperfect.
- In an interferometer with detuned signal recycling the presence of imbalanced RF sidebands at the output port increases and complicates the technical noise contributions [Hild07b].

A way to get around these problems is to choose an operating point slightly off the dark fringe and to use a DC-readout (homodyne) scheme.

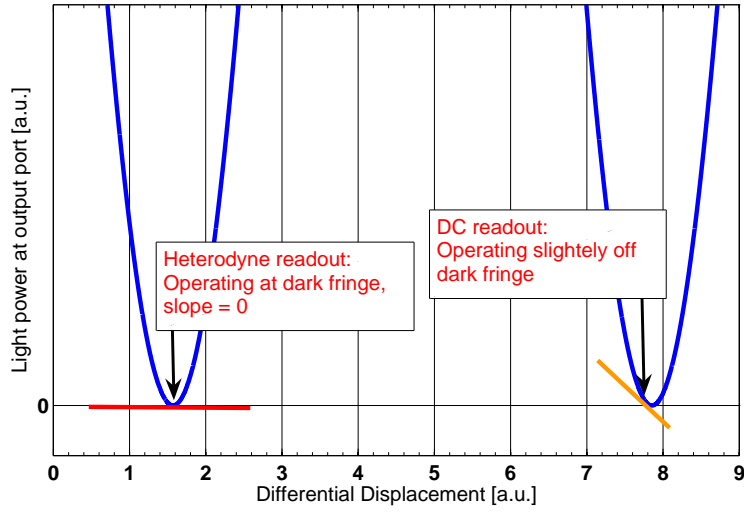


**Figure 6.1.:** Overview of the operating points of a heterodyne and DC-readout scheme. Currently GEO 600 uses heterodyne readout and is operated at the dark fringe. A DC-readout scheme uses an operating point slightly off the dark fringe. While in the heterodyne case RF sidebands are used as local oscillator, in the DC-readout scheme a fraction of the carrier light can leave the interferometer at the output port and serve as local oscillator.

Figure 6.1 schematically depicts the two different readout schemes. The currently in GEO 600 used heterodyne readout is shown on the left side: The Michelson interferometer is operated at the dark fringe, the slope of the light power is 0, and heterodyne sidebands at RF are used for the readout in order to produce a bipolar control signal. On the right side the situation used for DC-readout is shown. The operating point is slightly off the dark fringe, thus a fraction of the carrier light can leave the interferometer and serve, due to the large power recycling gain, as a highly stabilized local oscillator at the photodiode. Since the slope of the output light level versus differential arm length is not zero any more a bipolar control signal can be obtained from the level of DC light.

Due to the advantages of DC-readout with respect to heterodyne readout, for advanced LIGO [AdvLIGO] a DC-readout scheme will be used. Also for GEO 600 there are good reasons to change over to a DC-readout scheme as will be shown in the following sections.

## 6.2. Motivation

In the next few years LIGO as well as VIRGO are going to improve their detectors. Both plan for precursor projects, called enhanced LIGO [Adhikari06] and VIRGO+ with moderate sensitivity improvements before going to advanced LIGO [AdvLIGO], [Giaime] and advanced VIRGO [AdvVIRGO]. As shown in Figure 1.1 the current sensitivity of the only 600 m long GEO 600 detector is competitive to the much longer detectors only at frequencies above 500 Hz. Therefore in the near future any sensitivity improvement of GEO 600 at high frequencies is probably going to be more valuable than an improvement at low frequencies.<sup>1</sup>

Figure 6.2 shows the S5 noise projections of the GEO 600 detector [Smith06]. Above 400 Hz the uncorrelated sum of the individual noise contributions is mainly dominated by the modelled shot noise<sup>2</sup>. The first step in order to improve the sensitivity of GEO 600 at

<sup>1</sup>This statement is of course build on many assumptions, which might change in future. However, it bases on our currently best knowledge.

<sup>2</sup>Due to the asymmetric sidebands present at the output of a detuned signal recycled interferometer, the calculation of the shot noise limit of GEO 600 is more complicated than for a detector without signal recycling or tuned signal recycling and is therefore still a field of research. However, assuming completely unbalanced Michelson sidebands we can calculate an upper limit of the shot noise for the heterodyne readout. It was estimated by using the *pdS2*-command of FINESSE. The outcome of the FINESSE simulation was then multiplied by two correction factors: First a factor  $1/\sqrt{2}$ , accounting

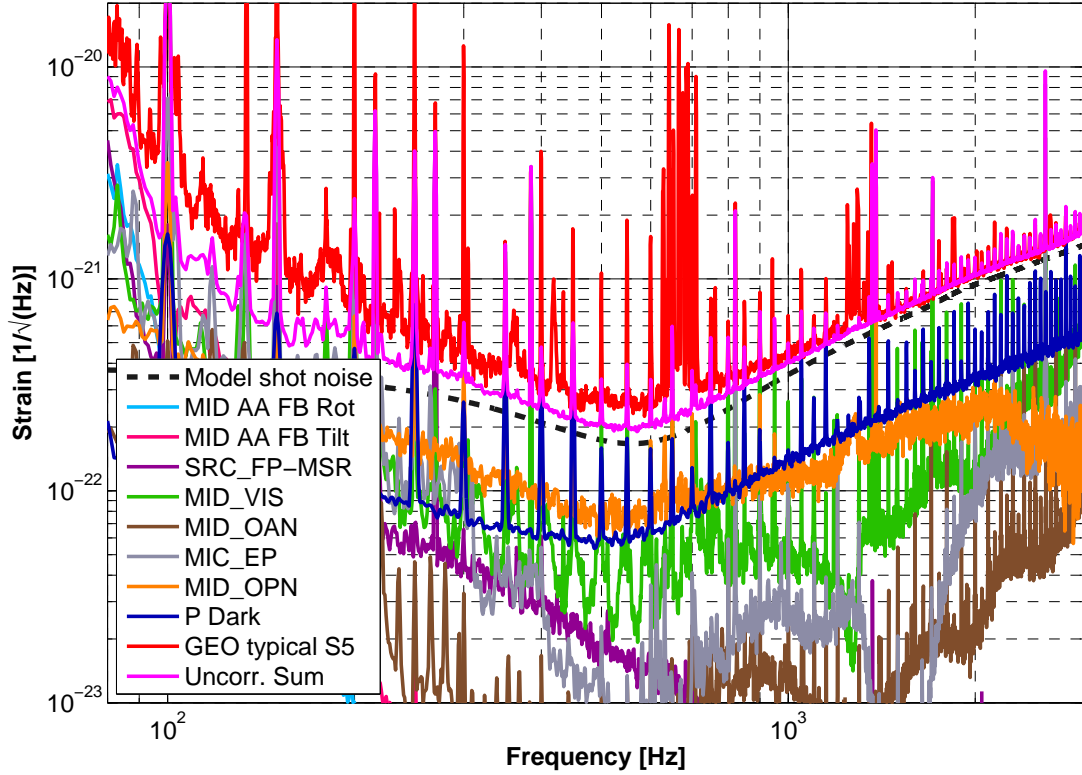


**Figure 6.2.:** Noise projections for a time of S5. The pink curve represents the uncorrelated sum of the individual noise contributions. The red trace shows a snapshot of the actual sensitivity. Above 400 Hz the uncorrelated sum is mainly dominated by the modelled shot noise (explanation is given in the text). The near-future plan is to increase the circulating light power by about a factor 4 in order to decrease shot noise by a factor of 2. Then the sensitivity between 500 and 2000 Hz would be limited to roughly equal shares by shot noise, oscillator phase noise (MID\_OPN) and electronic noise of the main photodiode (P Dark). All three of these noise contributions will potentially be decreased by changing over from a heterodyne to a DC-readout scheme.

frequencies above 500 Hz is to decrease the shot noise contribution by means of increasing the circulating light power. As soon as the light power is increased by a factor of 4, which would bring the shot noise (black dashed line in Figure 6.2) down by a factor of 2, the sensitivity of GEO 600 would be limited above 500 Hz by roughly equal shares of three noise sources:

- Shot noise
- Oscillator phase noise of the modulation used for creating control signals for the differential arm length of the Michelson interferometer and the gravitational wave readout (MID-OPN, orange trace in Figure 6.2).
- Electronic noise of the main photo diode (P Dark, blue trace in Figure 6.2).

If we want to increase the sensitivity of GEO 600 by more than a factor of two at frequencies above 500 Hz we have to attack all three of the noises listed above. The concept of DC-readout implies the wonderful chance to reduce all three of these noises at once.

### 6.2.1. Shot noise

When going from the currently used heterodyne read out scheme to a DC-readout scheme the signal to shot noise ratio will be increased by a factor between  $\sqrt{1.5}$  and  $\sqrt{2}$  [Buonanno03], [Harms06]. This depends on the balancing of the two Michelson sidebands at the dark-port. The sensitivity will be increased by between a factor of  $\sqrt{1.5}$  for balanced sidebands and a factor of  $\sqrt{2}$  for completely unbalanced sidebands. This can in an easy picture be understood by looking at the individual shot noise contributions at the dark-port. Amongst others we find in the heterodyne case shot noise contributions from frequencies,  $2\omega$ , corresponding to two times the heterodyne modulation frequencies (see Appendix B). It is worth noting that this improvement in sensitivity is achieved by only changing the readout scheme and does not require any increase of light power.

---

for the different propagation of signal and shot noise in a FINESSE-mixer (for a detailed description see [Finesse], page 61). The second factor,  $\sqrt{2}$ , accounts for additional shot noise in a heterodyne readout with respect to a homodyne readout [Buonanno03], [Harms06].

### 6.2.2. Oscillator phase noise

The oscillator phase noise is a serious problem for all heterodyne readout techniques. Even though this noise is usually classified as a technical noise source we are now already close to the limits, even though a low phase noise crystal oscillator is currently used in GEO 600. One way to reduce the oscillator phase contribution would be to reduce the coupling factor by going to tuned signal recycling (see Section 2.6). However, when going from a heterodyne to a DC-readout scheme it would be possible to derive the GW signal without an RF demodulation of the main output photodetector. By that we would completely eliminate any oscillator phase noise contribution.<sup>3</sup>

### 6.2.3. Electronic noise of the main photo diode

The electronic noise of the main photodiode can also be reduced by changing over to DC-readout. At the moment the diode is required to have a large dynamic range and to be capable of detecting large RF signals at the same time. This requirement restricts the maximal possible conversion factor for the photo current to voltage transformation [Grote]. However, as in a DC-readout scheme the photodiode does not have to detect RF signals, the electronic noise of the photodiode can be significantly reduced by increasing the photocurrent to voltage conversion factor and an additional gain increase of the first amplification stage.

## 6.3. Determination of the optimal dark fringe offset

The most important question we have to answer is, what is the optimal offset from the dark fringe for a DC-readout scheme for GEO 600? The dark fringe offset,  $\xi_{df}$ , is defined as:

$$\xi_{df} = \frac{|\Delta L_n| + |\Delta L_e|}{2}, \quad (6.1)$$

where  $\Delta L_e = -\Delta L_n$  are the intentionally added offsets in the distance between the beam splitter and the end mirrors MCE and MCN, respectively. In the following, FINESSE simulations [Freise04] are used to find the optimal dark fringe offset. The

---

<sup>3</sup>It is a noteworthy fact, that in recent times the relative stability of the light in the interferometer is better than the relative phase noise achievable with excellent RF technique.



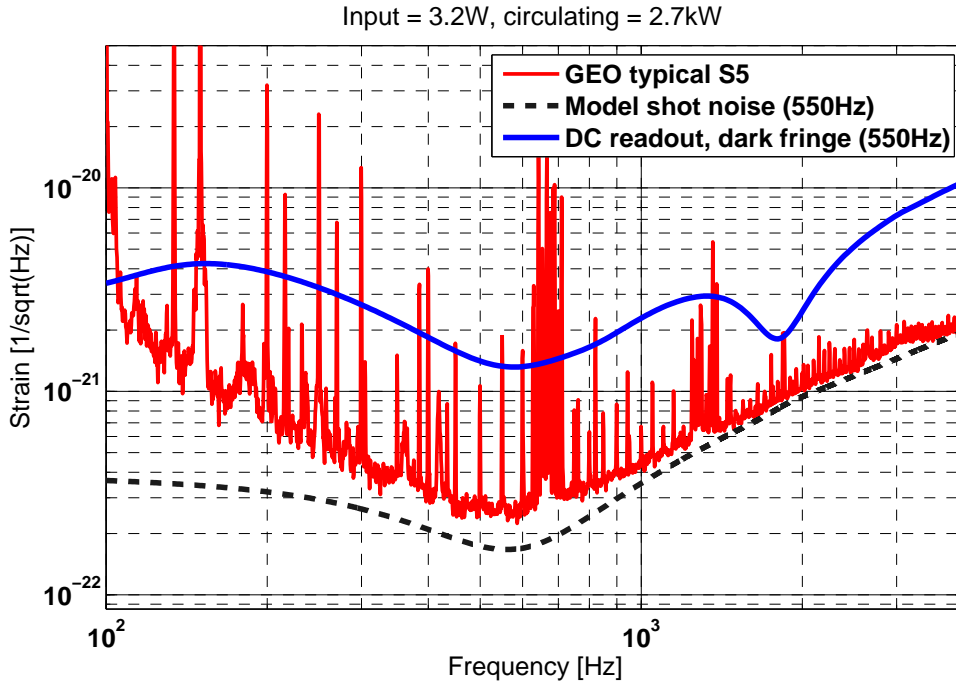


**Figure 6.3.:** Heterodyne versus DC-readout for GEO 600 in S5 configuration: The red trace shows the typical sensitivity of GEO 600 of S5. The blue trace corresponds to the shot noise limited sensitivity for using the DC light level of main photo detector,  $\mathcal{P}_{\text{DC}}$ . For this simulation the nominal modulation indices of S5 have been used and the operating point was chosen to be the dark fringe. The black dashed curve represents the modelled shot noise.

first simulation that was carried out is shown in Figure 6.3. The blue line represents the sensitivity that can in principle be obtained in the current configuration of GEO 600 (nominal S5 parameters) by using the DC light of the main photo detector. As already presented in Chapter 5.3 the DC light of the main photo detector,  $\mathcal{P}_{\text{DC}}$  is sensitive to gravitational wave signal as well. This originates from the fact that for the Michelson modulation sidebands the Michelson interferometer is not at the dark fringe, i.e. the sideband strength at the output port is to some extent proportional to the differential arm length of the interferometer. With respect to the actual sensitivity of GEO 600 (red trace in Figure 6.3), the blue trace shows a maximal sensitivity around 1.8 kHz. The bump around 1.8 kHz can also be found in the measurement of the transfer function from differential arm length to  $\mathcal{P}_{\text{DC}}$  shown in Figure 5.12.

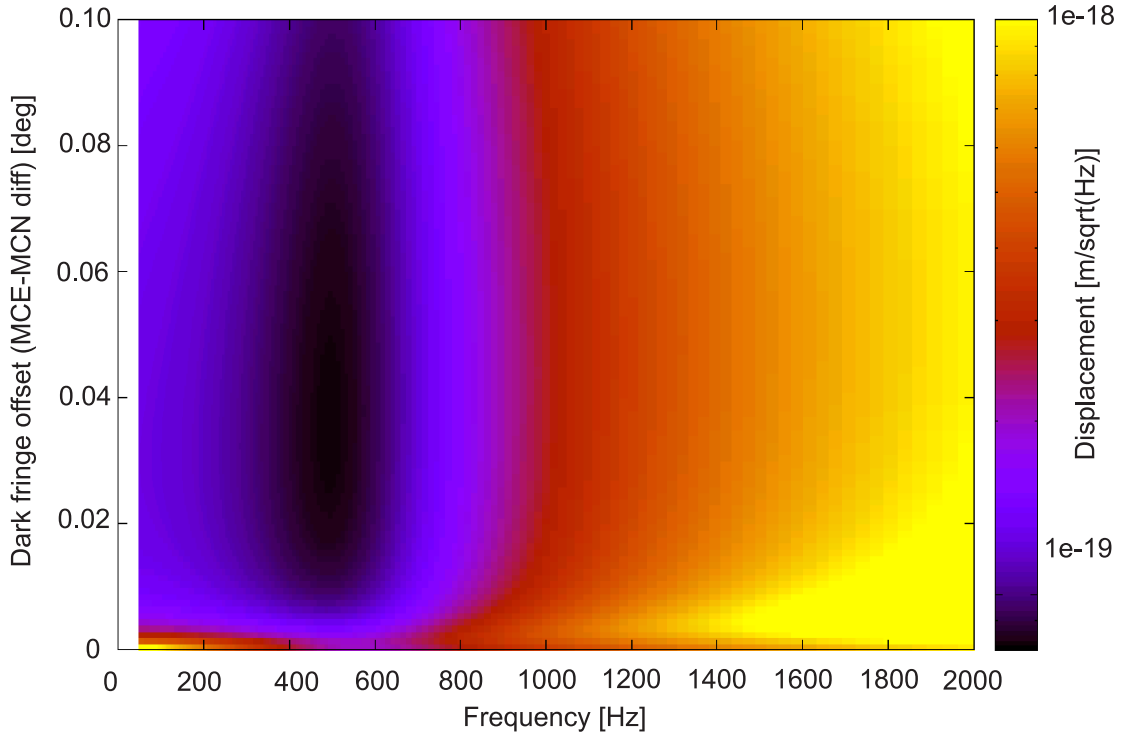


**Figure 6.4.:** Simulated displacement sensitivity of GEO 600 with DC-readout versus the offset from the dark fringe,  $\xi_{\text{df}}$ . The offset from the dark fringe was realized in this simulation by adding a differential phase offset to MCE and MCN. The modulation index of the Michelson sidebands was set to 5 % of the nominal S5 value. The best peak sensitivity is found for  $\xi_{\text{df}} = 0.036$  deg.

Currently a modulation index for the Michelson modulation of 0.38 is used. For the DC-readout scheme it is desirable to get rid of all RF contributions at the output port light field in order to not spoil the measurement. The strength of the sidebands at the dark port is planned to be decreased in two steps. First it seems reasonable to decrease the applied modulation by a factor of two and still get reasonable control signals. In a second step it is planned to insert an output mode cleaner (OMC) into the main detection path which is assumed to suppress the Michelson sidebands by another factor of ten. Overall this would give a reduction by a factor of 20 of the Michelson sidebands at the main photo detector. In the following simulations this sideband suppression is realized by turning down the modulation in front of the interferometer from the nominal S5 value of 0.38 to 0.019<sup>4</sup>.

With the reduced Michelson sideband strength we can now find the optimal offset from the dark fringe. Figure 6.4 shows the simulated displacement sensitivity versus the dark fringe offset,  $\xi_{df}$ . The offset from the dark fringe was implemented in this simulation by adding a differential phase offset (given in degree) to the end mirrors of the Michelson interferometer, MCE and MCN.  $\xi_{df}$  given in degrees can be converted into  $\xi_{df}$  given in meters by

$$\xi_{df} [\text{m}] = \frac{\lambda}{360 \text{ deg}} \xi_{df} [\text{deg}], \quad (6.2)$$

where  $\lambda = 1064 \text{ nm}$  is the wavelength of the laser. The optimal dark fringe offset giving the best peak sensitivity is found for a  $\xi_{df}$  of 0.036 degrees, which is equivalent to  $\xi_{df} = 1.06 \cdot 10^{-10} \text{ m}$ . The slope of the sensitivity improvement is found to be very steep for small offsets from the dark fringe,  $\xi_{df} < 0.01 \text{ deg}$ , and is nearly flat for larger offsets. That is why already for half the optimal dark fringe offset,  $\xi_{df} = 0.018 \text{ degrees}$ , which is equivalent to a dark fringe offset of about 50 pm, the achieved sensitivity is nearly optimal<sup>5</sup>. The FINESSE input file used for this simulation can be found in Appendix H.

Since many potential problems connected to a DC-readout scheme, such as noise couplings, increase with the dark fringe offset, a smaller offset, giving nearly the same sensitivity, is actually preferable. Figure 6.5 shows the spectra of the shot noise limit

---

<sup>4</sup>In contrast to an output mode cleaner this scenario gives a slightly increased circulating light power inside the interferometer, as now ratio of carrier and Michelson sidebands is increased. However, this effect influences the following simulations only on a scale of a few percent.

<sup>5</sup>This relation is also illustrated in a more obvious way in Figure 6.5.

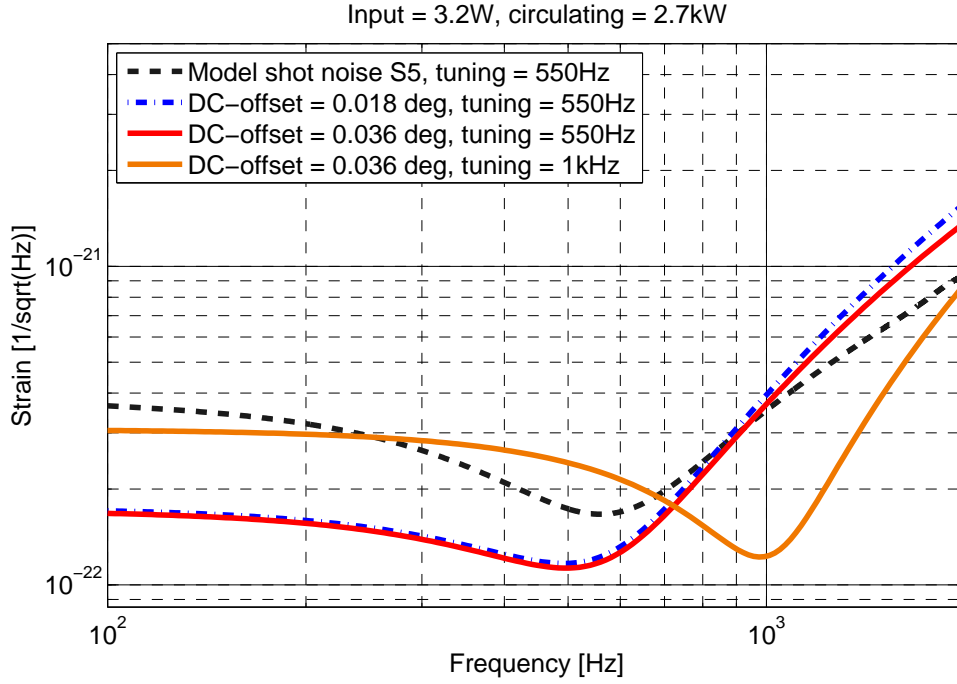


**Figure 6.5.:** Shot noise limited sensitivity achievable with DC-readout versus the modelled shot noise of S5: The red and the blue dashed-dotted trace represent the sensitivity with a DC-readout scheme for two different  $\xi_{df}$ . Even though an optimal  $\xi_{df} = 0.036$  deg was determined from Figure 6.4, half of that dark fringe offset ( $\xi_{df} = 0.018$  deg) already gives a sensitivity only marginally worse. An improvement of the peak sensitivity by about a factor 1.5 is achievable with respect to the modelled shot noise of S5. For the currently used input power of 3.2 W a peak sensitivity of about  $1.1 \cdot 10^{-22}/\sqrt{\text{Hz}}$  is obtained. The orange trace shows the sensitivity for a signal recycling tuning frequency of 1 kHz.

achievable with DC-readout versus the modelled shot noise of S5. The red and the blue dashed-dotted trace represent the sensitivity with a DC-readout scheme for two different  $\xi_{df}$ . Even though an optimal  $\xi_{df}=0.036$  deg was determined from Figure 6.4, half of that dark fringe offset ( $\xi_{df}=0.018$  deg) already gives a sensitivity only marginally worse. An improvement of the peak sensitivity by about a factor 1.5 is achievable with respect to the modelled shot noise of S5. For the currently used input power of 3.2 W a peak sensitivity of about  $1.1 \cdot 10^{-22}/\sqrt{\text{Hz}}$  is obtained.

The orange trace shows the simulated shot noise limited sensitivity with DC-readout for a signal recycling tuning frequency of 1 kHz. Again a peak sensitivity of about  $1.2 \cdot 10^{-22}/\sqrt{\text{Hz}}$  is obtained. At a frequency of 1 kHz this sensitivity is a factor of roughly 3 better than the S5 sensitivity of GEO 600 with the currently used signal recycling tuning of 550 Hz.

## 6.4. Technical realization

The technical implementation of a pure DC-readout scheme for GEO 600 would require some major changes, such as finding a new locking procedure or developing good in-vacuum photodiodes. Before the implementation of DC-readout into a running gravitational wave detector can be considered, a challenging R&D project needs to be carried out, which can probably be best done at a small prototype interferometer.

Nevertheless, a mix-scenario of a heterodyne and a DC-readout scheme for GEO 600 might be easy to implement and would give the chance get a sensitivity improvement at least at high frequencies. The idea is to keep the GEO detector as it is and only implement two changes: The first change would be to introduce an offset from the dark fringe of 50 pm. The second change would be to install an output mode cleaner (OMC) in front of the main photo detector (HPD), see Figure 6.6. Since in GEO 600 the Michelson sideband frequency is about 15 MHz, an OMC with a pole frequency of 1.5 MHz is required in order to give a suppression factor of 10 for the MI sidebands. The locking procedure and the full angular and longitudinal control of the interferometer would stay the same as it is now, except that the signal for the Michelson differential arm length is no longer derived from the main photo detector, but from an auxiliary detector (PDOQ) that is currently only used for lock acquisition and during the down-tuning procedure. For the DC-readout of the GW wave signal still the main photo

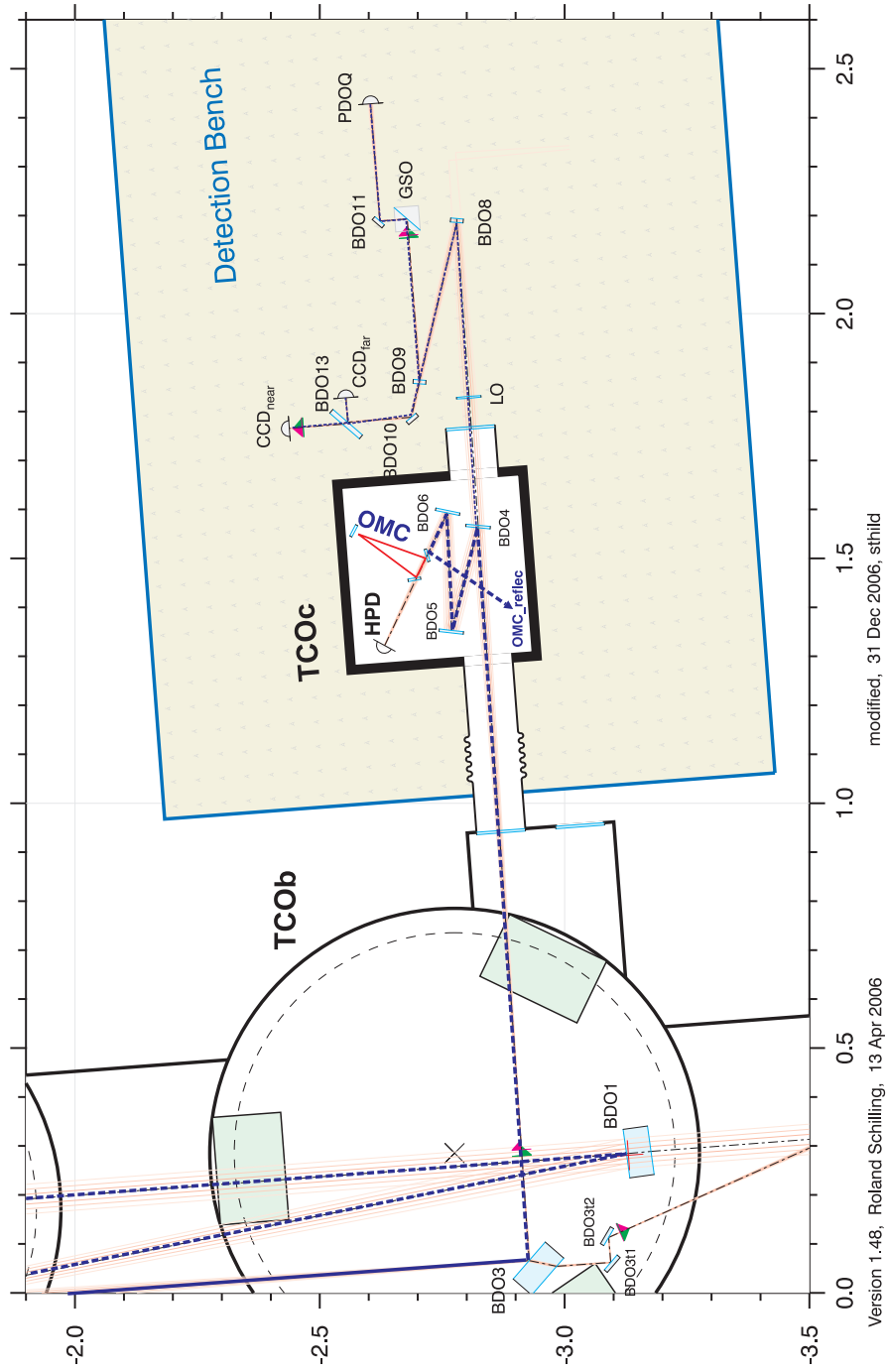


**Figure 6.6.:** Optical layout of the main detection bench of GEO 600. In front of the main photodiode (HPD) an output mode cleaner (OMC) needs to be added in order to suppress the Michelson sidebands (blue dashed lines) at the HPD. A more detailed explanation of a first realization of a DC-readout scheme can be found in the text.

detector would be used.

Figure 6.6 shows an optical layout of the detection bench. The output beam from the interferometer leaves TCOb and enters the small output vacuum chamber, TCOc, which is currently used at atmospheric pressure and only serves as acoustical enclosure. The beam is split by BDO4 (reflectivity = 0.98) into the so called *high power path* going to HPD and the so called *quadrant path* going to PDOQ. In the high power path an output mode cleaner is added. This filter cavity needs to be designed in a way that the carrier light can be transmitted, while the Michelson RF sidebands are reflected. The 2% of the light in the quadrant path still contain the MI sidebands and can therefore be used for deriving control signals.

With the setup described above, at least at frequencies above 500 Hz, there is a chance to see the improvement in shot noise with respect to the heterodyne readout. Below 500 Hz the sensitivity will probably be limited by feedback noise introduced by the electronic noise of the quadrant diode. Hence in a next step it would be desirable to use the homodyne signal derived from the HPD for differential arm length control. In a DC-readout scheme a multitude of low frequency noise is expected to originate from acoustical and seismic excitation. That is why in a following step this setup could further be improved by putting the output mode cleaner into vacuum (TCOc is already installed) and suspending the OMC.

## 6.5. Summary and outlook

In this chapter a possible new readout scheme of GEO 600 was introduced, combining a heterodyne scheme for control of the detector with a DC-readout scheme. With the aid of simulations a dark fringe offset of about 50 pm was found to be optimal. Without any change of the circulating light power a shot noise limited peak sensitivity can be obtained that is a factor of 1.5 improved with respect to currently modelled shot noise. However, the simulations shown in this chapter are not comprehensive and should be seen as an example of what we may find with GEO 600.

In case it will be decided to change the GEO 600 readout to the here described DC-readout scheme, further investigations have to be carried out in order to successfully enter this new and challenging field of GW detector design.





## Appendix A.

# The suspended output telescope of GEO 600

The output beam of GEO 600 transmitted through the signal recycling mirror has a diameter of about 2 cm. Such a large beam cannot easily be handled in the complex detection paths (see Figure 6.6 for example). Therefore it is desirable to convert the large interferometer beam to a smaller beam by the use of an output telescope. Up to May 2004 the GEO 600 output telescope consisted of 3 mirrors rigidly connected to optical tables, with most of the beam path being in air.

In May 2004 a new output telescope, shown in Figure A.1, was installed. It consists of three suspended mirrors, BDO1, BDO2 and BDO3, of which the first one is curved in order to focus the beam. Each suspension consists of a vertical isolation stage, realized by cantilever springs, passively damped by eddy currents, and a horizontal stage, realized by a single pendulum stage. The mirrors are suspended in steel wire loops (127 microns) and the length of the pendulums was chosen to be 460 mm. The position of the mirror is read out by shadow sensors and feedback is applied via four coil magnet actuators each.

The new output telescope provides for the following benefits:

- **In-vacuum beam path:** Since the beam is inside the vacuum, the chance of stray light originating from dust is significantly reduced (see Section 5.3). In addition air induced beam distortion is avoided as well as acoustical excitation of the telescope mirrors.
- **Seismic isolation:** The seismic isolation of the three mirrors reduces the beam

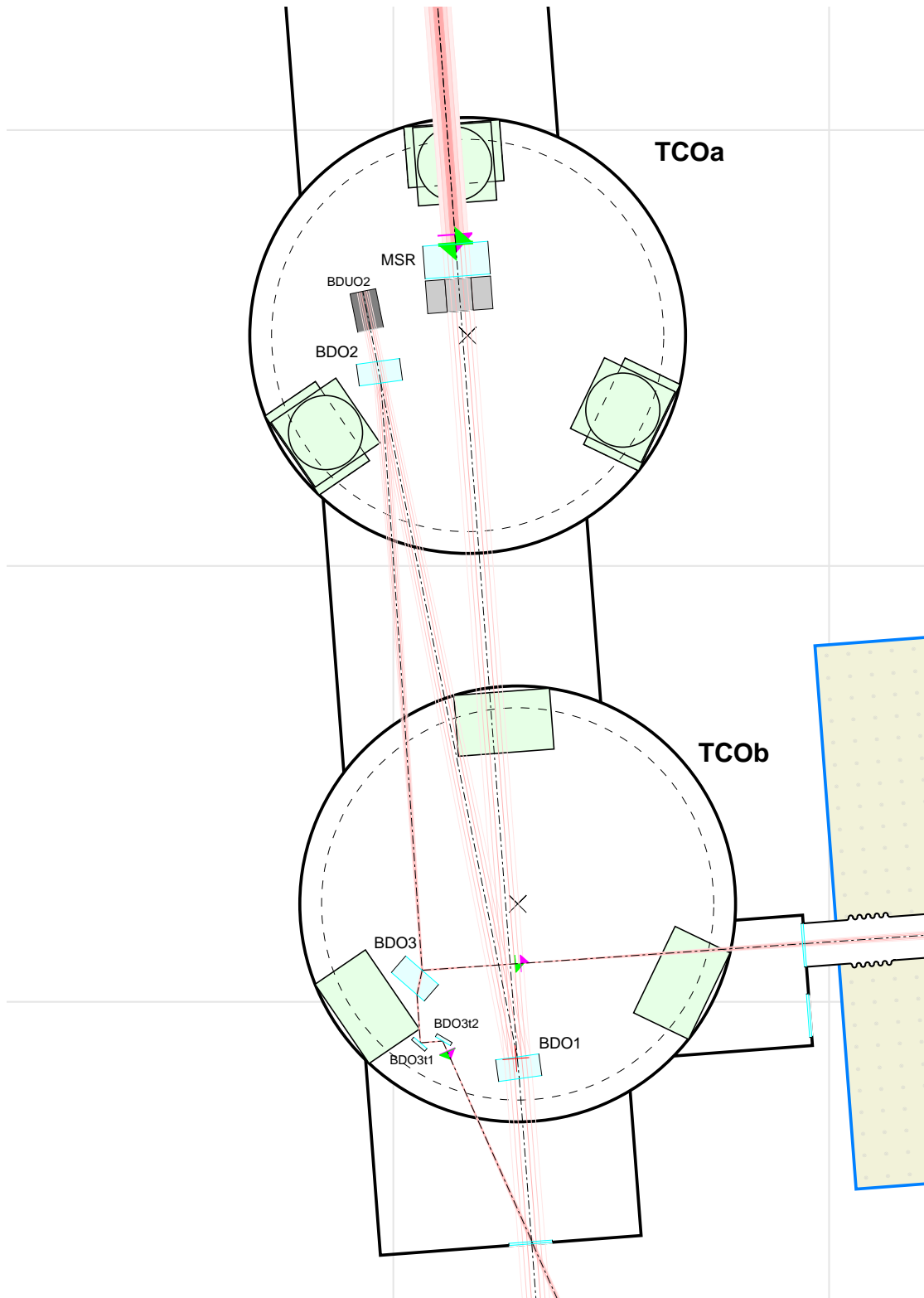


**Figure A.1.:** OPTOCAD layout of the GEO 600 output telescope, consisting of the three suspended mirrors BDO1, BDO2 and BDO3.

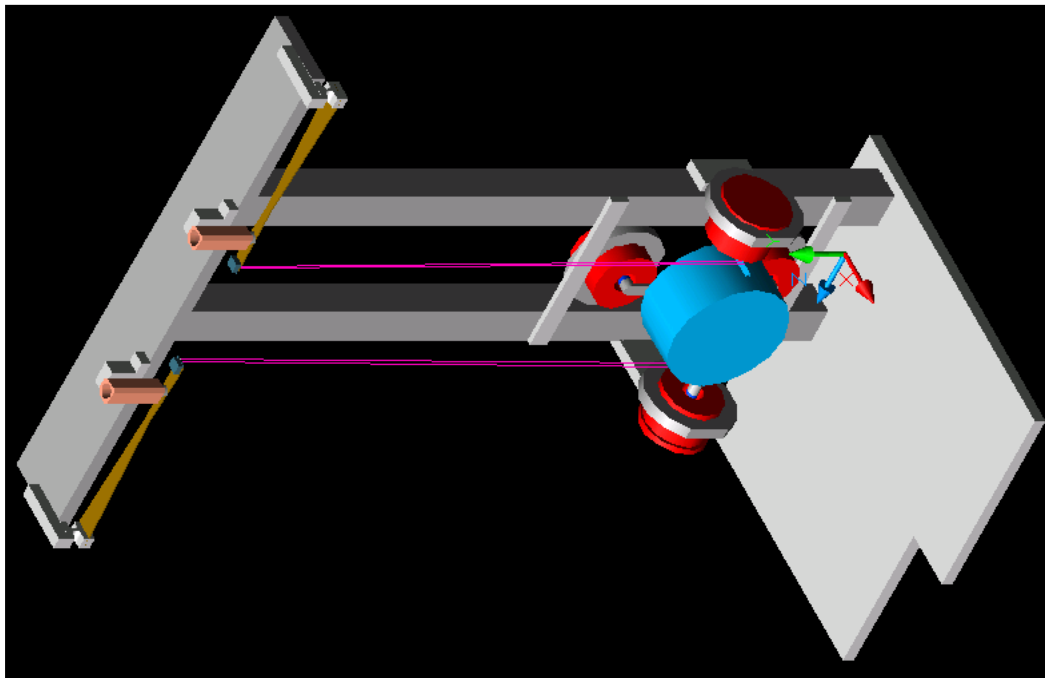


**Figure A.2.:** Suspension of BDO2. For BDO2 a stand alone Suspension is used which is clamped onto the bottom plate of TCOa.

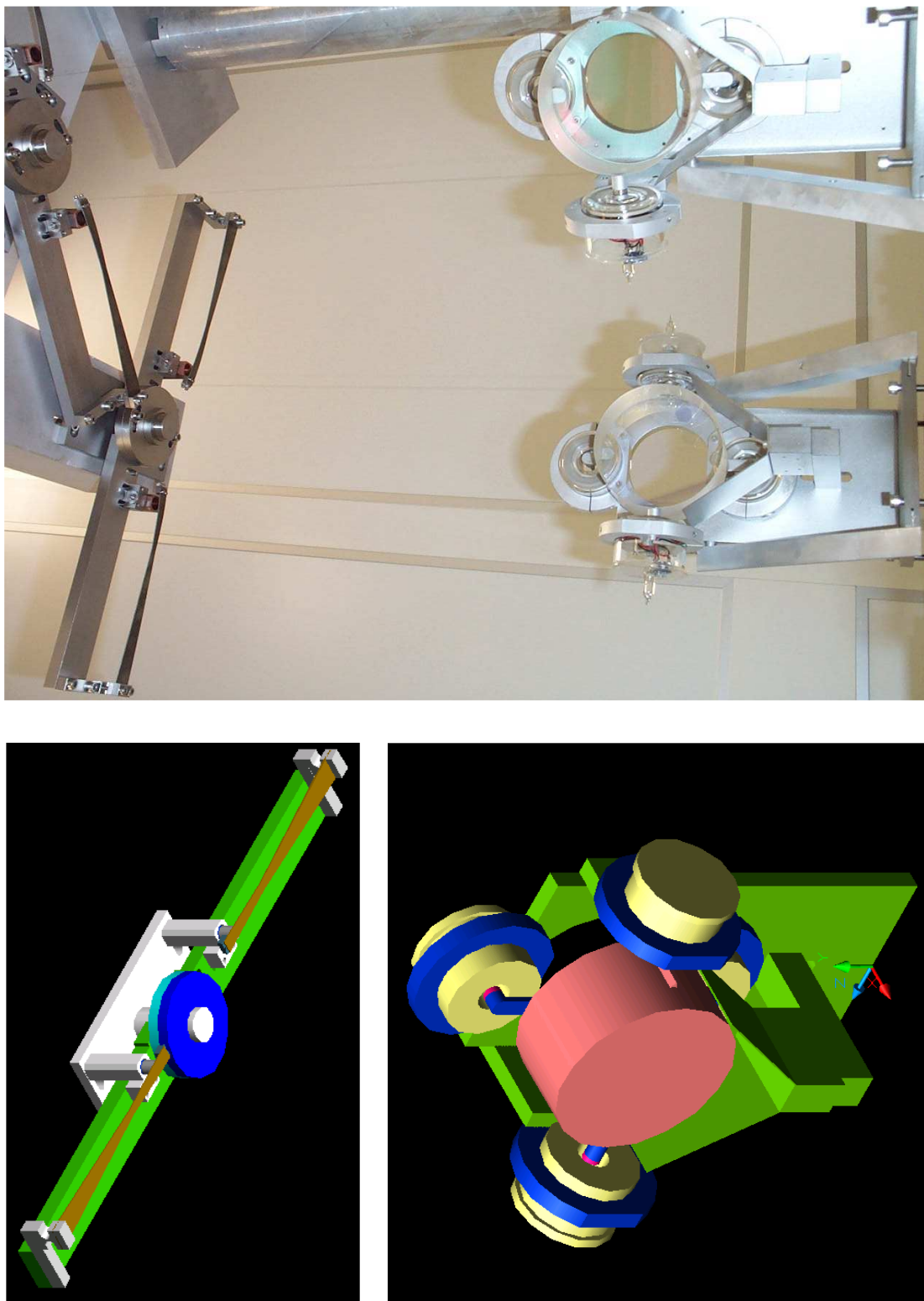


**Figure A.3.:** The suspensions for BDO1 and BDO3

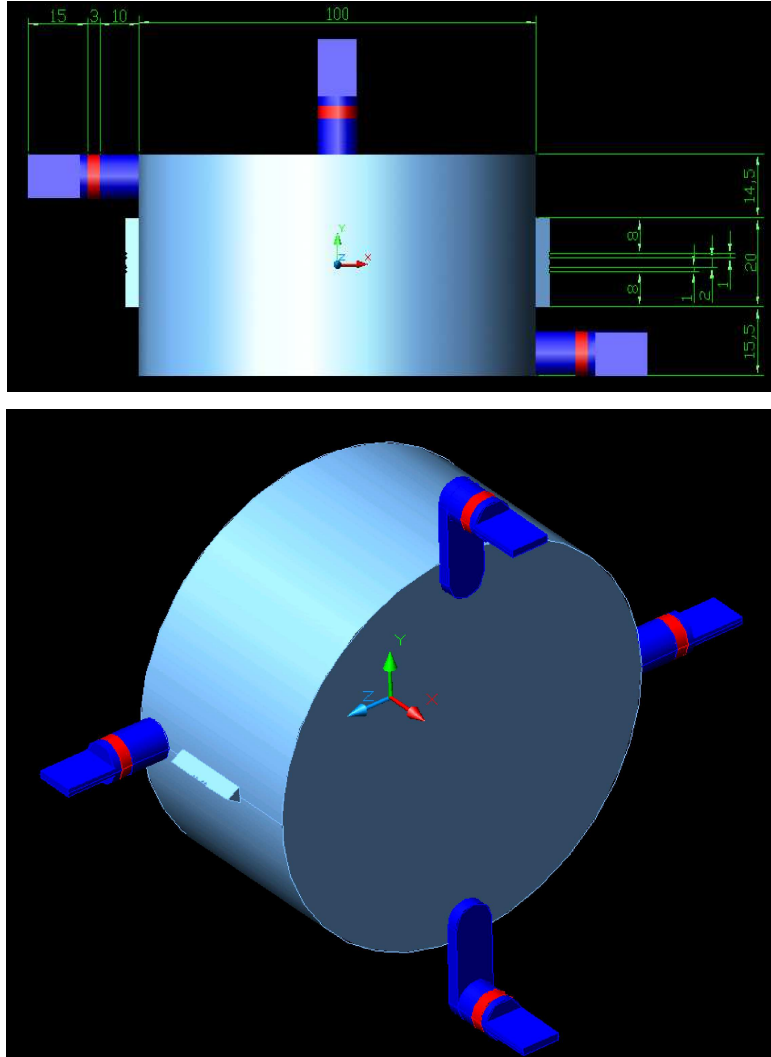


**Figure A.4.:** AutoCAD drawing of a BDO mirror with glued on break-off-bars, magnets (red) and flags, used for the local controls.

jittering at the main photo detector.

- **Auto-alignment of the output beam:** The suspended telescope mirrors can be used for auto-alignment of the main output beam. The position of the beam transmitted through BDO3 and the position of the beam close to the main photo detector are sensed with quadrant diodes and stabilized by feeding back to the local controls of the output telescope mirrors.

The following table gives an overview of the most important optical and mechanical parameters of the three telescope mirrors.

	BDO1	BDO2	BDO3
Transmission of HR coating (normal incidence)	<b>1.0 %</b>	<b>0.1 %</b>	14 %
Transmission of HR coating (45°)	7 %	1.3 %	<b>0.1 %</b>
Focal length	3.35 m	planar	planar
Thickness	49.8 mm	49.6 mm	49.7 mm
Diameter	99.7 mm	99.9 mm	99.8 mm
Separation of wire loops	2 mm	2 mm	3 mm

**Table A.1.:** Optical and mechanical parameters of the mirrors used for the output telescope.

## Appendix B.

### Light fields at the output port for detuned signal recycling

Figure B.1 shows the optical power of the different light fields present at the output of GEO 600, derived from measurements done with a scanning Fabry Perot cavity. Only three light fields are observed in this measurement: The two Michelson sidebands (MI+, MI-) and the carrier (C). As already shown in Figure 2.3 the two Michelson sidebands show a significant asymmetry, which contributes to the complex noise couplings described in Chapter 2.

For the reconstruction of the the total output field,  $E$ , we have to take three individual light fields into account, namely the lower Michelson sideband ( $E_-$ ), the carrier ( $E_c$ ) and the upper Michelson sideband ( $E_+$ ). In general we can describe these fields in the following way,

$$E_- = a_- e^{i\omega_- t} \quad \text{with} \quad a_- = A_- e^{i\phi_-} \quad (\text{B.1})$$

$$E_c = a_c e^{i\omega_c t} \quad \text{with} \quad a_c = A_c e^{i\phi_c} \quad (\text{B.2})$$

$$E_+ = a_+ e^{i\omega_+ t} \quad \text{with} \quad a_+ = A_+ e^{i\phi_+} \quad (\text{B.3})$$

where  $\omega_i$  is the frequency of the light and  $a_i$  is complex and contains the amplitude  $A_i$  and the phase  $\phi_i$  of the corresponding field. The total output field is just the sum of the three fields

$$E = E_- + E_c + E_+. \quad (\text{B.4})$$

The actual by the photodiode detected property is the power,  $P$  of the output field

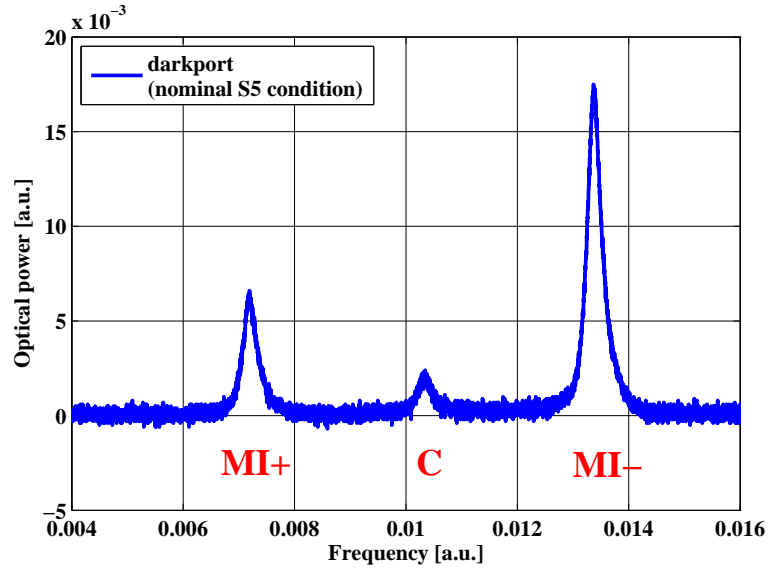


**Figure B.1.:** Power measurement of the light fields present at the output port of GEO 600. A strong asymmetry of the Schnupp modulation sidebands (MI+, MI-) used for the control of the differential arm length of the Michelson interferometer is observed. The measurement was done using a scanning Fabry Perot cavity.



---

given by

$$\begin{aligned}
P &= EE^* \\
&= a_- a_-^* + a_- a_c^* e^{i(\omega_- - \omega_c)t} + a_- a_+^* e^{i(\omega_- - \omega_+)t} + a_c a_-^* e^{i(\omega_c - \omega_-)t} + a_c a_c^* \\
&\quad + a_c a_+^* e^{i(\omega_c - \omega_+)t} + a_+ a_-^* e^{i(\omega_+ - \omega_-)t} + a_+ a_c^* e^{i(\omega_+ - \omega_c)t} + a_+ a_+^*
\end{aligned}$$

Now we can try to simplify this expression by introducing the following definitions. We use the frequency of the carrier light as reference which we define as zero,  $\omega_c = 0$  and now redefine the frequencies of the sidebands to be:

$$\omega_- = -\omega \quad \text{and} \quad \omega_+ = +\omega \quad (\text{B.5})$$

In addition we also use the phase of the carrier field as reference and define it to be zero,  $\phi_c = 0$ . With this the whole expression forms to

$$\begin{aligned}
P &= A_-^2 + A_- A_c e^{i(-\omega t + \phi_-)} + A_- A_+ e^{i(-2\omega t + \phi_- - \phi_+)} + A_c A_- e^{i(\omega t - \phi_-)} \\
&\quad + A_c^2 + A_c A_+ e^{i(-\omega t - \phi_+)} + A_+ A_- e^{i(2\omega t + \phi_+ - \phi_-)} + A_+ A_c e^{i(\omega t + \phi_+)} + A_+^2
\end{aligned}$$

Now we group the terms by frequency. The DC component,  $P_{\text{DC}}$  is given by

$$P_{\text{DC}} = A_-^2 + A_c^2 + A_+^2. \quad (\text{B.6})$$

Second we get a contribution at the modulation frequency  $\omega$

$$P_f = A_- A_c e^{i(-\omega t + \phi_-)} + A_c A_- e^{i(\omega t - \phi_-)} + A_c A_+ e^{i(-\omega t - \phi_+)} + A_+ A_c e^{i(\omega t + \phi_+)} \quad (\text{B.7})$$

$$= 2A_- A_c \cos(\omega t - \phi_-) + 2A_c A_+ \cos(\omega t + \phi_+) \quad (\text{B.8})$$

And finally from the beat of the lower and the upper Michelson sideband we also get a contribution at twice the modulation frequency:

$$P_{2f} = A_- A_+ e^{i(-2\omega t + \phi_- - \phi_+)} + A_+ A_- e^{i(2\omega t + \phi_+ - \phi_-)} \quad (\text{B.9})$$

$$= 2A_- A_+ \cos(2\omega t - \phi_- + \phi_+) \quad (\text{B.10})$$



## **Appendix C.**

### **Design for an AR coated window for quadrant diodes**

The standard windows of the quadrant diodes used in GEO 600 have been found to be of poor quality and a source of stray light (see Section 3.5). Therefore the housing of the diodes was cut and the window removed. A new encapsulation for the diodes was designed: The diode is clamped in between two copper plates (see Figures C.1 and C.2). In order to encapsulate the diode surface from dust an AR coated 1" window is glued onto the front-plate.

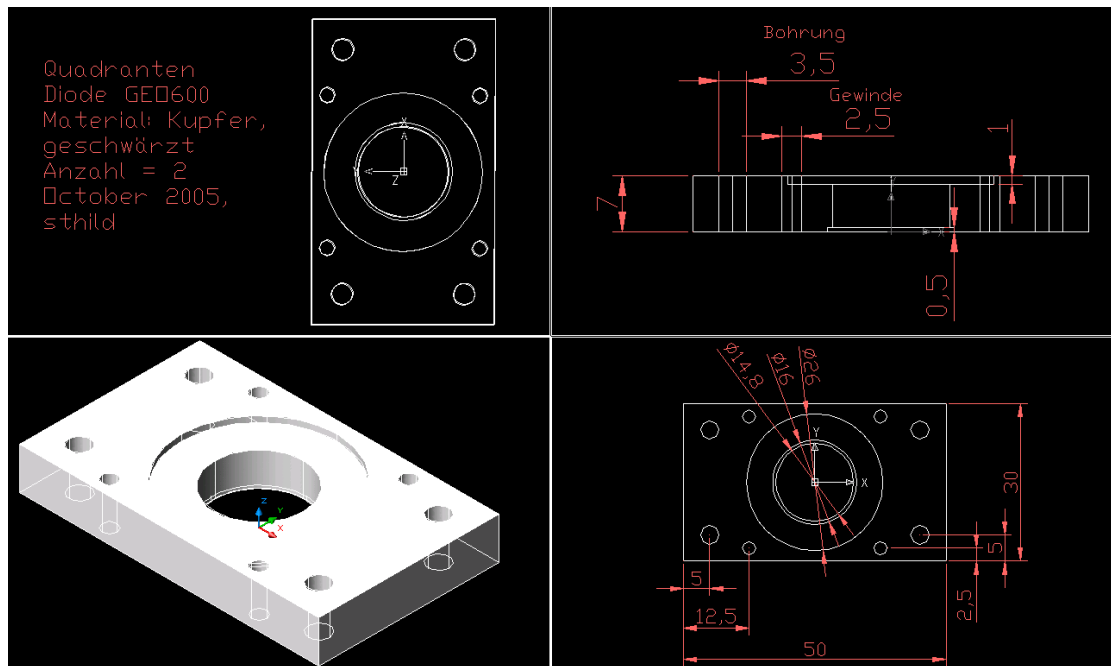


Figure C.1.: Front plate of the new quadrant diode encapsulation.

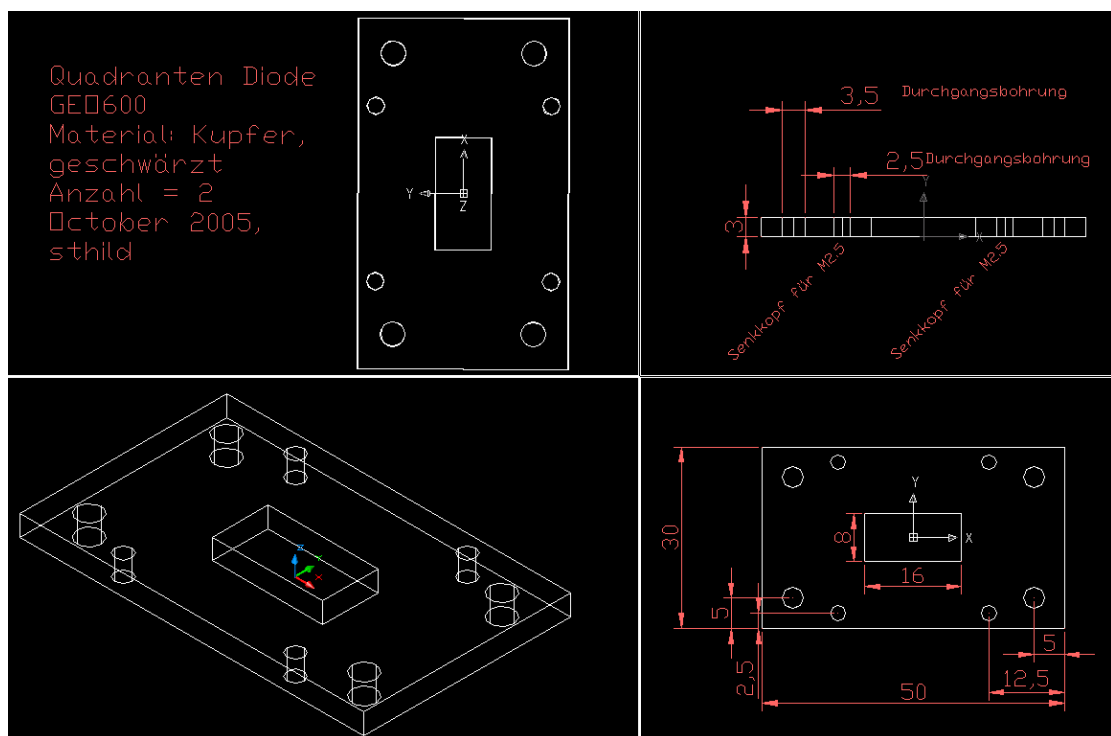


Figure C.2.: Back plate of the new quadrant diode encapsulation.

## **Appendix D.**

### **Optical layout of GEO 600**

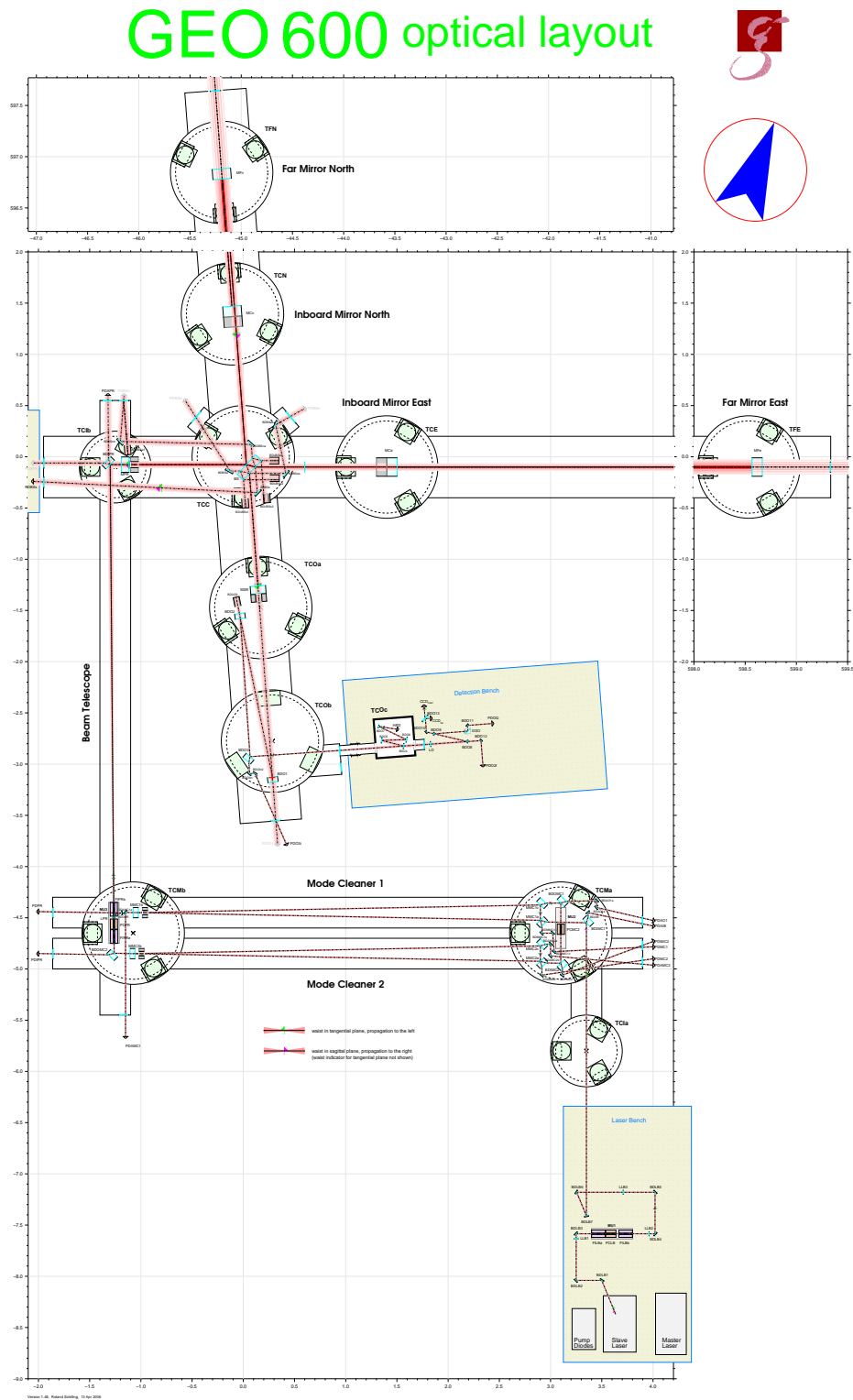


Figure D.1.: Optical layout of GEO 600.

## Appendix E.

### Matlab script: Photon pressure calibration

```
% Script for photon pressure calibration
% The script does the following steps
% - requesting data from H and PCALmon from the server
% - computation of the photon pressure calibration
% - comparing photon calibration with official calibration
% - computing the transfer function from PCAL to H (mag+phase)

clear;

savedir = ['disse\unsorted\PPD\final2006\nov_3rdrun\100sec_100secin\cal\'];
mkdir('D:\',savedir)%'GPS2UTC(start_time)')

savedir2 = ['disse\unsorted\PPD\final2006\nov_3rdrun\100sec_100secin\photon\'];
mkdir('D:\',savedir2)%'GPS2UTC(start_time)')

savedir3 = ['disse\unsorted\PPD\final2006\nov_3rdrun\100sec_100secin\TF\'];
mkdir('D:\',savedir3)%'GPS2UTC(start_time)')

time1 = UTC2GPS('2006-11-08 14:51:00');
f1 = 58;
time2 = UTC2GPS('2006-11-08 14:48:00');
f2 = 75;
time3 = UTC2GPS('2006-11-08 14:45:00');
f3 = 90;
time4 = UTC2GPS('2006-11-08 14:41:00');
f4 = 120;
```

```
time5 = UTC2GPS('2006-11-08 14:38:00');
f5 = 134;

times = [time1, time2, time3, time4, time5];
f_phot = [f1, f2, f3,f4, f5];

nsecs = 120;    % total number of seconds
n_sec_in =120;  % number of seconds in per FFT
loop_num = length(times);
%loop_num = 1;

convers = 1.078;          %conversion factor from V of PD to light power
                           % in W
c_light = 3e8;            % speed of light
m = 5.32 ;               % mass of testmass

error_array = [];
esd_array = [];
photon_array = [];
noise_array = [];
noise_array_HP = [];
HP_array = [];
HP_array_unwh = [];
phase_ar = [];
phase_ar2 = [];
tf = [];
f_real = [];

for loopcounter = 1:1:length(times)
f = f_phot(loopcounter)
start_time = times(loopcounter);

%%%%%% Getting data from photon_calibrator

server = '130.75.117.73';
port = 9000;
channel(2).name = 'G1:MISC_PHOTON_CAL';
c=2;
    [channel(c).t,channel(c).x,channel(c).fs] = m2fserv(server, port, start_time,
```



---

```

start_time+nsecs-1, channel(c).name);

nfft = n_sec_in*channel(c).fs
S1 = sum(hann(nfft));
S2 = sum(hann(nfft).^2);
[channel(c).pxx,channel(c).f] = pwelch(channel(c).x, hann(nfft), 0, nfft,
                                     channel(c).fs);

channel(c).info.enbw = channel(c).fs * S2 / (S1*S1);
channel(c).info.nfft = nfft;
channel(c).info.nsecs = nsecs;
channel(c).info.type = 'AS';
channel(c).info.ndata = nsecs * channel(c).fs;
channel(c).pxx = sqrt(channel(c).pxx) * sqrt(channel(c).info.enbw);
% channel(c).pxx2 = channel(c).pxx2/(sqrt(enbw));

pho_t=channel(2).t;
pho_x=channel(2).x;
pho_fs=channel(2).fs;
phot_data = channel(2).pxx;
[indexmax, valuemax] = getmax(phot_data(10:length(channel(2).f)))
indexmax = indexmax+9;

figure; semilogy(channel(2).f, phot_data, channel(2).f(indexmax),
phot_data(indexmax), 'or'); xaxis(f-1,f+4); legend('used AS of
photon', 'max value'); photon', 'max value'); grid on
xlabel('frequency [Hz]'); title('G1: MISC\_PHOTON\_CAL');

filename = ['D:\',savedir2, num2str(f)];
print(filename, '-dtiff');
delete(gcf)

%%%%%%%%%%%% Getting h(t) data
server = '130.75.117.164';
port = 9008;
rds_level = 9;
cal_version =1;

% Set the channel names
channel(1).name = 'G1:DER_DATA_H';
c = 1;

```

```
% Get the data
[channel(c).t,channel(c).x,channel(c).fs] = m2fserv(server, port, start_time,
    start_time+nsecs-1, channel(c).name, cal_version, rds_level);;
nfft = n_sec_in*channel(c).fs
S1 = sum(hann(nfft));
S2 = sum(hann(nfft).^2);
[channel(c).pxx,channel(c).f] = pwelch(channel(c).x, hann(nfft), 0, nfft,
    channel(c).fs);

channel(c).info.enbw = channel(c).fs * S2 / (S1*S1);
channel(c).info.nfft = nfft;
channel(c).info.nsecs = nsecs;
channel(c).info.type = 'AS';
channel(c).info.ndata = nsecs * channel(c).fs;
channel(c).pxx = sqrt(channel(c).pxx)* sqrt(channel(c).info.enbw);
enbw = channel(c).info.enbw;

h_t=channel(1).t;
h_x=channel(1).x;
h_fs=channel(1).fs;

h_data = channel(1).pxx;
photon_esd_uncor = h_data(indexmax)           %height of line in DER_DATA_H

noise = h_data((f+1)*n_sec_in+1:(f+3)*n_sec_in+1); %estimating the noisefloor
                                                %around the line

noisefloor = mean(noise);

photon_esd = sqrt((photon_esd_uncor^2)-(noisefloor^2)); % height of the ppd
                                                % line minus noisefloor

noisefloor_f = [(f+1) (f+3)]; % needed for plotting
                                                % the noisefloor

noisefloor_2 = [noisefloor noisefloor]; % needed for plotting
                                                % the noisefloor

figure;
semilogy(channel(1).f, h_data, noisefloor_f, noisefloor_2,channel(1).f(indexmax) ,
```

---

```

                                                                    photon_esd,'o');

axis(f-1,f+4);
legend('used AS of h(t)', 'used noise floor', 'PPD-line minus noisefloor');
grid on
xlabel('frequency [Hz]');
title('G1:DER\DATA\H');

filename = ['D:\',savedir, num2str(f)];
print(filename, '-dtiff');
delete(gcf)

photon_rms = phot_data(indexmax); %AS 1 Hz frequency resolution from DAQS

photo_pp = photon_rms *2*sqrt(2); %Gives modulation in Volts

mod_pwr = (photo_pp*converters)*1.029*0.9988*0.9986*0.885;
% photo_pp*converters = 1.078 // PD => PWR-meter
% 1.029 // PWR-meter => PTB
% 0.9988 // Collimator-lens loss
% 0.9986 // Viewport loss
% 0.885 // power loss

F = 2*mod_pwr /c_light ; % Force to mirror [N]

x = F / (m * channel(1).f(indexmax)^2 * 4 * pi^2); % actual displacement
% of MFN

h_photon = 2*x / 1200
h_photon_rms = h_photon / (2*sqrt(2)); %prc peak height from photon calib
h_esd = photon_esd %prc peak height from esd calib

error = (h_photon_rms-h_esd)*100/h_esd %error of h_photon to h_esd in percent

loopcounter

error_array(loopcounter) = error;
esd_array(loopcounter) = h_esd;
photon_array(loopcounter) = h_photon_rms;
noise_array(loopcounter) = noisefloor;

```

```

f_real(loopcounter) = channel(2).f(indexmax)

%%%%%%%%% making the TF %%%%%%%%%%%%%%%

[TF_cxy, TF_f] = tfe(pho_x, h_x, nfft, h_fs, hann(nfft), 0);

phas = angle(TF_cxy)*180/pi;

phase_ar(loopcounter)= phas(indexmax);
tf(loopcounter) = abs(TF_cxy(indexmax))
testphase=phase_ar(loopcounter);

figure;
subplot(2,1,1);
title('TF from MISC\_PHOTON\_CAL to DER\_DATA\_H');
semilogy(TF_f, abs(TF_cxy), TF_f(indexmax), abs(TF_cxy(indexmax)),'r*' );
ylabel('magnitude');
grid on;
subplot(2,1,2);
plot(TF_f, phas, TF_f(indexmax), phas(indexmax),'r*');
grid on;
ylabel('phase [deg]');
allxaxis(f-1,f+1);

filename = ['D:\',savedir3, num2str(f)];
print(filename, '-dtiff');
delete(gcf)

end

figure
subplot(3,1,2);
semilogx(f_real,error_array, '*r');
legend('error');
ylabel('relative error [%]');
xlabel('Time (hours)');
grid on;
subplot(3,1,1);
loglog(f_real,esd_array, '*b', f_phot,photon_array, '*m');

```

---

```

legend('height measured in h(t)', 'predicted for h(t)');
ylabel('AS of h(t)');
grid on;
subplot(3,1,3);
loglog(f_real, noise_array, '*g');
legend('noise floor around PPD-line');
ylabel('AS of h(t)');
xlabel('frequency of PPD [Hz]');
grid on;
%allxaxis(60,1100);

starttime = start_time-(nsecs*loopcounter);
msuptitle(sprintf('Time from %s (%d), freq = %d Hz', GPS2UTC(starttime),
                    starttime,f));

phase_ar2 = phase_ar;

for pz=1:length(phase_ar)
    if phase_ar(pz)>160
        phase_ar2(pz)= phase_ar(pz)-360
    end
end

ra_cal = photon_array./esd_array;
figure;
subplot(2,1,1);
plot(f_real, ra_cal, 'r*-')
xlabel('Frequency [Hz]')
ylabel('ratio of phot-cal/ead-cal')
grid on;
subplot(2,1,2)
plot(f_real, phase_ar2, 'r*-')
xlabel('frequency [Hz]');
ylabel('phase [deg]');
legend('Phase between PPD and G1:DER\_DATA\_H');
grid on;
allxaxis(0,2500);

```

```
figure;
subplot(2,1,1);
loglog(f_real, tf, 'r*-')
xlabel('Frequency [Hz]')
ylabel('TF from Phototn to H')
grid on;
subplot(2,1,2)
semilogx(f_real, phase_ar2, 'r*-')
xlabel('frequency [Hz]');
ylabel('phase [deg]');
legend('Phase between PPD and G1:DER\_DATA\_H');
grid on;
allxaxis(0,6000);
```

## Appendix F.

### A gravity calibrator for GEO 600

The gravity calibrator is a concept that could provide a calibration that is independent from any subsystem involved in the official calibration. The idea is to use a rotating system of masses, installed closely behind one of the test masses. This will yield, at the position of the testmass, a varying gravity gradient, which can be used as an independent actuator.

Figure F.1 shows the geometry of a possible 3-mass gravity calibrator. In order to find out which force can be applied to the testmass, we have to compare two different states of the gravity calibrator, which represent the two extreme cases of gravity force to the mirror. The first case is shown in the left part of the figure. We can simply calculate the force to the mirror by adding up three forces, one for each calibrator mass. The mirror is assumed to move only perpendicular to its surface.

The gravitational force  $F_G$  between two masses  $m_1$  and  $m_2$  separated by a distance of  $r$  is known as

$$F_G = G \frac{m_1 m_2}{r^2}, \quad (\text{F.1})$$

where  $G = 6,672 \cdot 10^{-11} \text{m}^3/\text{kg s}^2$  is the Gravity constant. Therefore the force  $F_1$  on the test mass  $m_{tm}$  caused by calibration mass 1 ( $m_{cal}$ ) is given by

$$F_1 = G \frac{m_{tm} m_{cal}}{(r - R)^2}. \quad (\text{F.2})$$

Due to the off axis position of calibration mass 2 and 3, their forces look slightly more complicated:

$$F_{2,3} = \cos(\beta) G \frac{m_{tm} m_{cal}}{(r + R \sin(\alpha))^2 + (R \cos(\alpha))^2}. \quad (\text{F.3})$$

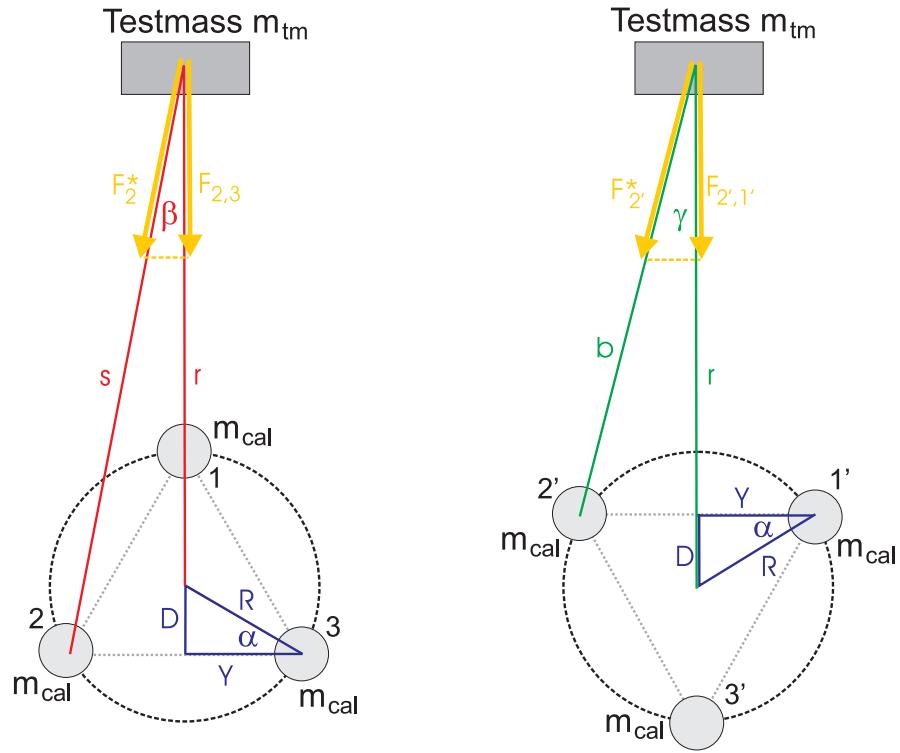


**Figure F.1.:** Geometry of a 3-mass gravity calibrator.



---

The cosine is present because we only allow the mirror to move perpendicular to its surface, leading to  $F_2 \cdot \cos \beta = F_{2,3}$ . The sum of these three forces gives

$$F_A = G \cdot m_{tm} m_{cal} \left( \frac{1}{(r - R)^2} + \frac{2 \cos(\beta)}{(r + R \sin(\alpha))^2 + (R \cos(\alpha))^2} \right) \quad (\text{F.4})$$

Now we consider that the calibrator is rotated 60 degrees. Now the calibration masses 1 and 2 are off axis and mass 3 is placed behind the testmass. This configuration is shown in the right part of Figure F.1.

The force caused by the calibration masses 1' and 2' is given as

$$F_{1',2'} = \cos(\gamma) G \frac{m_{tm} m_{cal}}{(r - R \sin(\alpha))^2 + (R \cos(\alpha))^2} \quad (\text{F.5})$$

and for mass 3'

$$F_{3'} = G \frac{m_{tm} m_{cal}}{(r + R)^2}. \quad (\text{F.6})$$

The resulting force,  $F_B$  is larger than  $F_A$ , because in this case two of the calibration masses are near to the mirror.

$$F_B = G \cdot m_{tm} m_{cal} \left( \frac{1}{(r + R)^2} + \frac{2 \cos(\gamma)}{(r - R \sin(\alpha))^2 + (R \cos(\alpha))^2} \right) \quad (\text{F.7})$$

The effective force seen by the mirror,  $\Delta F$ , is given by the difference of  $F_A$  and  $F_B$ .

$$\Delta F = F_A - F_B \quad (\text{F.8})$$

We simplify this expression by using the fact that  $\alpha$  is 30 degrees in the current setup. This reduces the denominators as follows:

$$(r \pm R \sin \alpha)^2 + (R \cos \alpha)^2 = r^2 \pm rR + R^2. \quad (\text{F.9})$$

With this we get

$$\Delta F = G \cdot m_{tm} \cdot m_{cal} \left[ \frac{1}{(r + R)^2} + \frac{2 \cos \beta}{r^2 - rR + R^2} - \frac{1}{(r - R)^2} - \frac{2 \cos \gamma}{r^2 + rR + R^2} \right] \quad (\text{F.10})$$

Now we can take some reasonable numbers for the different parameters:

- $r = 1 \text{ m}$
- $R = 0.2 \text{ m}$

- $m_{tm} = 5.6 \text{ kg}$
- $m_{cal} = 2.0 \text{ kg}$

which leads to a force:

$$\Delta F \approx 6.71 \cdot 10^{-10} \text{ N}. \quad (\text{F.11})$$

This force corresponds to a strain amplitude of  $h_{\text{grav-cal}} = 6 \cdot 10^{-20} / \sqrt{\text{Hz}}$ . Assuming the gravity calibrator rotates with a frequency of 30 Hz (that is the frequency a common washing machine motors provides), a signal at 90 Hz,  $h_{\text{grav-cal}}$ , would be generated. Comparing  $h_{\text{grav-cal}}$  to the actual sensitivity of GEO 600 (see Figure 1.3), we find the gravity calibrator signal to show up in the detector sensitivity with a snr of about 5 for an integration time of one second.

## Appendix G.

### Matlab script: Statistical veto with amplitude consistency-check

```
% Script for applying a statistical veto with amplitude
% consistency check in the full GEO veto pipeline.
% Actual case: MIDVIS_veto for Sep 2006.

% Input:
% - 2 Sets of triggers: MIDVIS and H
% - veto list for science, nullstream and  $\chi^2$ 
% - Amplitude ratio of H and MIDVIS
% Output:
% - List of veto intervals

% sthild, November 2006

%-----
clear;

%% settings
% September 06
s1      = UTC2GPS('2006-09-01 00:00:00');
s2      = UTC2GPS('2006-10-01 00:00:00');
config = 'chacr_200609S5';
outdir = '0906';

%% load triggers
he = load(sprintf('%s/DER_DATA_H_events_%s', outdir, config));
```

```
xe = load(sprintf('%s/LSC_MID_VIS_events_%s', outdir, config));
he = he.events;
xe = xe.events;
t0 = min([he.gps_start(1) xe.gps_start(1)]);

he.a = sqrt(10.^(he.totPower/10));
xe.a = sqrt(10.^(xe.totPower/10));

%% Apply science veto

svi = viload(sprintf('%s/science_veto_%s.txt', outdir, outdir));
disp(sprintf('+ applying non-science veto to h'));
[hes, hvidx] = applyvi(he, svi);
disp(sprintf('+ applying non-science veto to MID_VIS'));
[xes, xvidx] = applyvi(xe, svi);

%% Apply chi^2 veto

cvi = viload(sprintf('%s/chi2_dqflag_%s.txt', outdir, outdir));
disp(sprintf('+ applying chi^2 to h'));
[hesc, hvidx] = applyvi(hes, cvi);
disp(sprintf('+ applying chi^2 to MID_VIS'));
[xesc, xvidx] = applyvi(xes, cvi);

%% Apply Nullstream veto

cvi = viload(sprintf('%s/nullstream_%s.txt', outdir, outdir));
disp(sprintf('+ applying nullstream to h'));
[hescn, hvidx] = applyvi(hesc, cvi);
disp(sprintf('+ applying nullstream to MID_VIS'));
[xescn, xvidx] = applyvi(xesc, cvi);

%% Choose events
hidx = find(hescn.gps_start > s1 & hescn.gps_start < s2);
xidx = find(xescn.gps_start > s1 & xescn.gps_start < s2);

out.he = structidx(hescn, hidx, 'serverInfo');
out.xe = structidx(xescn, xidx, 'serverInfo');
save('hx_events', 'out');
```

---

```

out.he.time = out.he.gps_start+out.he.gps_offset;
out.xe.time = out.xe.gps_start+out.xe.gps_offset;

h_t = out.he.time;
vis_t = out.xe.time;
h_freq = out.he.freq_central;
vis_freq = out.xe.freq_central;
h_dur = out.he.duration;
vis_dur = out.xe.duration;
h_snr = out.he.totPower;
vis_snr = out.xe.totPower;
h_snr = undb(h_snr);
vis_snr = undb(vis_snr);

%read in TF data
TF = fig2data('TF_nfest_mag.fig');
TF_freq = TF.line(1).x
    TF_mag = TF.line(1).y*2;
    TF_mag_or = TF_mag/2;

twin = 0.008
fwin = 1000

snr_ratio_l = [];
snr_ratio_h = [];
vis_snr_all = [];
vis_freq_all = [];
h_snr_all = [];
h_freq_all = [];
snr_ratio_h_freq = [];
snr_ratio_l_freq = [];
snr_ratio_all = [];

result = 1:1:length(h_t);
result2 = [];

%% Applying the statistical veto with amplitude consistency-check

```

```
%      for n=1:400
%          timeshift = (n-200)*0.3
%          h_shift = h_t +timeshift;
%          fprintf('%d', n)

      for j=1:length(h_t)
          step = j;
          tdiff = vis_t - h_t(j);
          idx = find(abs(tdiff) < (twin));
          if sum(idx)>0.5
              %      for u=1:length(idx)
                  freq_diff = h_freq(j)-vis_freq(idx) ;
                  idx2 = find(abs(freq_diff)<(fwin));
                  if sum(idx2)>0.5
                      result(j) =1;
                      snr_ratio = [];
                      snr_ratio = vis_snr(idx)./h_snr(j);
                      snr_ratio_all = [snr_ratio_all snr_ratio];
                      fre = round(h_freq(j));
                      comp=snr_ratio./TF_mag(fre);
                      idx3 = find(comp<1);

                      if idx3>0.5;
                          result2(j) =1;
                          snr_ratio_h = [snr_ratio_h snr_ratio];
                      else
                          result2(j) =0;
                          snr_ratio_l = [snr_ratio_l snr_ratio];
                      end

                      else
                          result(j) = 0;
                      end

              else
                  result(j) = 0;
              end

          end

      end
```

---

%% Plotting the results

```
figure
semilogy(snr_ratio_h_freq, snr_ratio_h, 'bx', snr_ratio_l_freq,
          snr_ratio_l, 'rx', TF_freq, TF_mag, 'r', TF_freq, TF_mag_or, 'r');
xlabel('Frequency [Hz]')
ylabel('Ratio of total power in H and MID\VIS')
legend('TotPower\_H devided by TotPower\_MID\_VIS, fwin = 1000 Hz,
       twin = 0.008sec, FULL SEPTEMBER 2006', 'TotPower\_H devided
       by TotPower\_MID\_VIS, fwin = 1000 Hz, twin = 0.008sec, FULL
       SEPTEMBER 2006' )
title(sprintf('triggers in h(t) = %d : triggers in auxiliary channel = %d
\n Efficiency = %d (no amp cut) : Efficiency = %d amp cut applied'
, length(h_t) , length(vis_t), sum(result)/length(h_t)*100,
(sum(result)-sum(result2))/length(h_t)*100));
axis(50,2000);
grid on;

sum(result)
sum(result2)
veto = [];

%% Writing the list of veto intervals

idx_veto = find(result>0.5);
for i = 1:length(idx_veto)
    i
    veto(1,i)= hescn.gps_start(idx_veto(i))+hescn.gps_offset(idx_veto(i));
    veto(2,i)= hescn.duration(idx_veto(i));
end
```





## Appendix H.

### FINESSE input file of GEO 600 for DC-readout

```
#-----
# File used to determine the optimal dark fringe offset for #
using a DC readout scheme. # sthild, 12/2006
#-----
# geo600-main.kat $Rev: 8 $ # Andreas Freise
(adf@star.sr.bham.ac.uk) # $Date: 2007/01/04 13:34:10 $ # # Input
File for FINESSE (www.rzg.mpg.de/~adf) # # Optical layout of GEO
600 with "real" parameters . #
#-----
# # History: # # 12.12.2006 by  Andreas Freise
(adf@star.sr.bham.ac.uk) # - changed distribution of losses to be
130ppm on each #   surface inside the DR MI # # 12.12.2006 by
Andreas Freise (adf@star.sr.bham.ac.uk) # # - changed MC mirror
parameters according to labbok page 4027 # - changed laser power
to be at (70deg ->) 4.82W (page 3984) # - changed node names of
MPR and MSR # - changed mirror specs of MCN, MFN, MCE. MFE
according to #   labbok page 4028, results are exactly as stated
there by Hartmut # - not yet done: mode-matching, curvature,
compensation check, .... #

# 21.11.2006 by  Andreas Freise (adf@star.sr.bham.ac.uk)
#               Stefan Hild   (stefan.hild@aei.mpg.de)
#
#   Restarting GEO 600 file maintenance, see Labbok page 4011
```

```
# Staring from a file called power_evl_curr_8_car.kat
# (26.06.2006, labbok page 3656)
#
# - changed syntax to Finesse version 0.99.4
# - put Mode cleaners back in
# - updated modulation indices (see page 4011)
# - added telescope in south output port (Hartmut)
# - added dymanic thermal lens (for BS) computation
#
#-----

1 i1 3.2 0 nMU3in1                # corresponds to 75 deg
                                   # (nominal S5)
gauss beam_in i1 nMU3in1 268u -550m # beam parameter roughly
                                   # matching PRC
## (old value used:  i1 nMU3in 248u -550m)    ** to be checked **
mod eom3 $fPR $midxPR 2 pm 0 nMU3in1 nMU3in # PRC control
##

mod eom4 $fSR $midxSR 2 pm 0 nMU3in nMU3_2    # Schnupp1 (SR control)
mod eom5 $fMI $midxMI 2 pm 0 nMU3_2 nMU3_3    # Schnupp2 (MI control)

lens lpr 1.8 nMU3_3 nMU3_4
# some rather arbitrary thermal lense for the isolators and the EOMs:
lens therm 5.2 nMU3_4 nMU3_5                # ** to be checked **
isol d2 120 nMU3_5 nMU3out                  # Faraday Isolator

# 070502 corrected length with respect to OptoCad (Roland Schilling)
s smcpr3 4.391 nMU3out nBDIPR1
bs1 BDIPR 50u 30u 0 45 nBDIPR1 nBDIPR2 dump dump
s smcpr4 0.11 nBDIPR2 nMPR1

##-----
## main interferometer ##
##
## New MPR; values for MPR005 page 2264 (check with Harald)
## first (curved) surface of MPR
```

---

```

m    mPRo 0 1 0 nMPR1 nMPRi1
attr mPRo Rc -1.85
s    smpr 0.0718 1.44963 nMPRi1 nMPRi2
# second (inner) surface of MPR
m1   MPR 900u $LMPR 0. nMPRi2 nMPR2          # T=900 ppm, L=50 ppm

s    swest 1.1463 nMPR2 nBSwest      # new length with T_PR=900 ppm
                                     # * to be checked **

##-----
## BS
## basic data from old GEO files
##
##
##
##              nBSnorth      ,'-
##              |      +      '
##              |      ,      :
##      nBSwest      |      +1      +
##      ----->      ,:._ i2 ,
##              + \      '-. +      nBSseast
##              , i3\      , -----
##              +      \      +
##              , i4.'
##              '-.      ..
##              '-. , | nBSsouth
##              -      |
##              |
##              |
bs2   BS 0.485998 $LBS 0.0 42.834 nBSwest nBSnorth nBSi1 nBSi3
s     sBS1a 0.040 1.44963 nBSi1 nBSi1b
##-----
# Thermal lense of beam splitter
lens bst 14.5k nBSi1b nBSi1c # static value for 1.9kW at BS
## -----
# Alternative: dynamic thermal lens computation, as in:
# S. Hild et al, Applied Optics IP, vol. 45, Issue 28, pp.7269-7272
# assuming 0.25ppm/cm absorption, w=0.88cm, d=9cm
/*
pd prcpower nBSwest # we need 2* power in BS, so we measure power in

```

```

west arm
noplplot prcpower
set bspow prcpower re
func flength = 1.6635E7 / ( $bspow + 0.0000000001)
#noplplot flength
put bst f $flength
*/
s    sBS1 0.051 1.44963 nBSi1c nBSi2
s    sBS2 0.091 1.44963 nBSi3 nBSi4
bs2  BS2 60u $LBSAR 0 27.9694 nBSi2 dump nBSeast nBSAR # R=60 ppm, L=30ppm
bs2  BS3 60u $LBSAR 0 -27.9694 nBSi4 dump nBSsouth dump # R=60 ppm, L=30ppm
# two measured values for R_AR: labbook page 2418 (44ppm), 3996 (64ppm)

##-----
## north arm
s snorth1 598.5682 nBSnorth nMFN1 # ** to be checked **

bs1 MFN 8.3u $LMFN 0.0 0.0 nMFN1 nMFN2 dump dump # T=8.3 ppm
attr MFN Rc 666

s snorth2 597.0241 nMFN2 nMCN1 # ** to be checked **

m1 MCN 13u $LMCN -0.0 nMCN1 dump # T=13 ppm
attr MCN Rc 636

##-----
## east arm
s seast1 598.4497 nBSeast nMFE1
bs1 MFE 8.3u $LMFE 0.0 0.0 nMFE1 nMFE2 dump dump # T=8.3 ppm
# ** the Rc(T) below need to be checked, they certainly look wrong **
attr MFE Rcx 664 # 90 W
attr MFE Rcy 660 # 90 W
#attr MFE Rcx 665 # 71 W
#attr MFE Rcy 662 # 71 W
#attr MFE Rc 663.75 # perfect curvature
#attr MFE Rcx 666.41 # 66W
#attr MFE Rcy 663.75 # 66W
#attr MFE Rcy 660.75 # 75W
#attr MFE Rcx 663.75 # 75W

```

---

```

s seast2 597.0630 nMFE2 nMCE1
m1 MCE 13u $LMCE 0.0 nMCE1 dump          # T=13ppm
attr MCE Rc 622

##-----
## south arm
s ssouth 1.109 nBSsouth nMSR1

m MSR 0.9805 0.01945 0.7646 nMSR1 nMSR2    # R=0.9805, T=0.01945, L=50 ppm
# tuning = f_tune/FSR_SR * 180, FSR_SR=125241 Hz ** to be checked **
# e.g f_tune 532 Hz -> 0.7646 deg
##-----
## output optics telescope

s sout1 1.8 nMSR2 nBD01i
bs1 BD01 0.01 0.0 0.0 5.0 nBD01i nBD01o dump dump    # T=1%
attr BD01 Rc 6.72

s sout2 4.855 nBD01o nL01i # BD02 and BD03 are flat and omitted in this path
lens L01 0.5 nL01i nL01o  # 1. lens on detection bench
s sout3 0.703 nL01o nL02i # computed telescope length, 2 flat mirrors
                        # omitted in this path
lens L02 -0.03 nL02i nL02o # 2. lens on detection bench
# actual lens -0.05m ?
s sout4 1.0 nL02o nout    # length to quad. camera

##-----
## further settings and commands

# Modulation frquencies
const fSR 9016865    ## corresponding to 532 Hz on tune.vi, (10/2006 S. Hild)
const fMI 14.904929M ## (10/2006 S. Hild)
const fPR 37.16M
const midxPR 0.13 # see page 4011
const midxSR 0.17 # see page 4011
#const midxMI 0.38 # see page 4011
const midxMI 0.019

```

```
# Michelson losses
const LMPR 130u
const LMCN 130u
const LMFN 130u
const LMCE 130u
const LMFE 130u
const LBS 130u
const LBSAR 130u

# PR cavity (north arm)
cav prc1 MPR nMPR2 MCN nMCN1
# PR cavity (east arm)
cav prc2 MPR nMPR2 MCE nMCE1
# SR cavity (north arm)
cav src1 MSR nMSR1 MCN nMCN1
# SR cavity (east arm)
cav src2 MSR nMSR1 MCE nMCE1
```

```
##-----
```

```
## Simualtion commands
```

```
/*
# power detectors
#pd MC1out nMU2_2
#pd MC2out nMU3_5
#pd MPRrelf nMPR1
#pd MPRin nMPR1*
#pd PRC nMPR2
pd BSpow nBSwest
pd MSRpow nMSR1
#pd darport nBD01i
xaxis BS phi lin -1 1 100
*/
```

```
maxtem 2
retrace off
time
phase 3
```

---

```
fsig sig1 MCN 10 0
fsig sig2 MCE 10 180

pdS1 hpd_DC 10 max nout
xaxis sig1 f log 50 2000 200
put hpd_DC f1 $x1
x2axis MCE phi lin 0 0.1 100
func t = 0-$x2
put MCN phi $t

yaxis log abs
scale meter hpd_DC

pause gnuplot windows
```





## Appendix I.

# Measurement of the bulk-absorption of the GEO 600 beam splitter

### I.1. Introduction

The four large-scale laser-interferometric gravitational wave projects, LIGO [Waldman06], VIRGO [Acernese06], TAMA 300 [Ando05] and GEO 600 [Hild06c], have dedicated much effort to commissioning the detectors and improving their sensitivity. Soon the initial projects will have reached a sensitivity limited by fundamental noise sources like, for instance, shot noise. Second generation projects such as Advanced LIGO [AdvLIGO], Advanced VIRGO [AdvVIRGO] and GEO HF [Willke06] aiming at strain sensitivities in the region of  $10^{-23}$  to  $10^{-24}/\sqrt{\text{Hz}}$  will operate at much higher light powers than the initial detectors, in order to reduce the influence of shot noise. Accordingly, one major problem will be the absorption of laser light in the optical elements like beam splitters and test masses. Even though techniques for thermal correction and compensation have been developed (e.g., [Lück04, Lawrence02]), the use of low-absorption materials is a key point of future detector research.

The beam splitter substrate currently installed in GEO 600 was manufactured by Heraeus, Hanau [Heraeus] and consists of Suprasil 311 SV which provides extremely low bulk absorption due to an OH-content of less than 50 ppm [Loriette03]. Recent measurements of OH-reduced fused silica showed an absorption below 0.5 ppm/cm which was the lowest absorption of fused silica reported so far [Loriette03]. Therefore it is of great interest to obtain a lower absorption value, as presented in this work.

In Section I.2 I will explain the principle of a new method for a more sensitive estimation

of the bulk absorption in the beam splitter by using the GEO 600 interferometer itself as a measuring tool. Realization and details of this measurement are described in Section I.3 while the result is discussed in Section I.4.

## I.2. A new method for measuring bulk absorption

Large Michelson interferometers such as GEO 600 working at high optical powers can be used to measure small effects of thermally induced distortion of their optical elements [Ottaway06]. One of the most sensitive optical components in GEO 600 is the beam splitter which is placed inside a high-finesse cavity: the power-recycling cavity (Figure I.1.1). The absorption of the bulk material causes a weak lens building up inside the beam splitter [Winkler91, Strain94]. This lens disturbs mainly the beam passing through the beam splitter substrate, whereas the beam reflected to the other arm (in case of GEO 600 this is the north arm) is only slightly influenced (Figure I.1.3). This means that depending on the strength of the lens we see a change in the interference pattern at the ports of the interferometer. Since GEO 600 is operated on a dark fringe at the output port, this effect can most easily be visualized there, using, for example, a CCD camera.

Due to the fact that the thermal lens does not build up instantaneously, we can compare the beam pattern at the output port for a cold state and a hot state of the beam splitter (as shown in Figure I.2). The high gain of the alignment control system guarantees a stable alignment and good suppression of first order higher modes [Grote04a]. Using GEO 600 parameters we can reproduce the pattern of the cold state using a FINESSE [Freise04] simulation. Now we can add to the simulation an additional lens inside the beam splitter and vary its focal length until it matches the experimentally observed beam pattern for the hot state. If the light power transmitted through the beam splitter is known, an estimate of the bulk absorption can be derived from the focal length of the simulated thermal lens as described below.

Absorption of light power from the transmitted beam heats the substrate non uniformly. Because of the temperature dependence of the index of refraction a path difference  $\delta s$  occurs between a light path measured along the beam axis and a light path measured

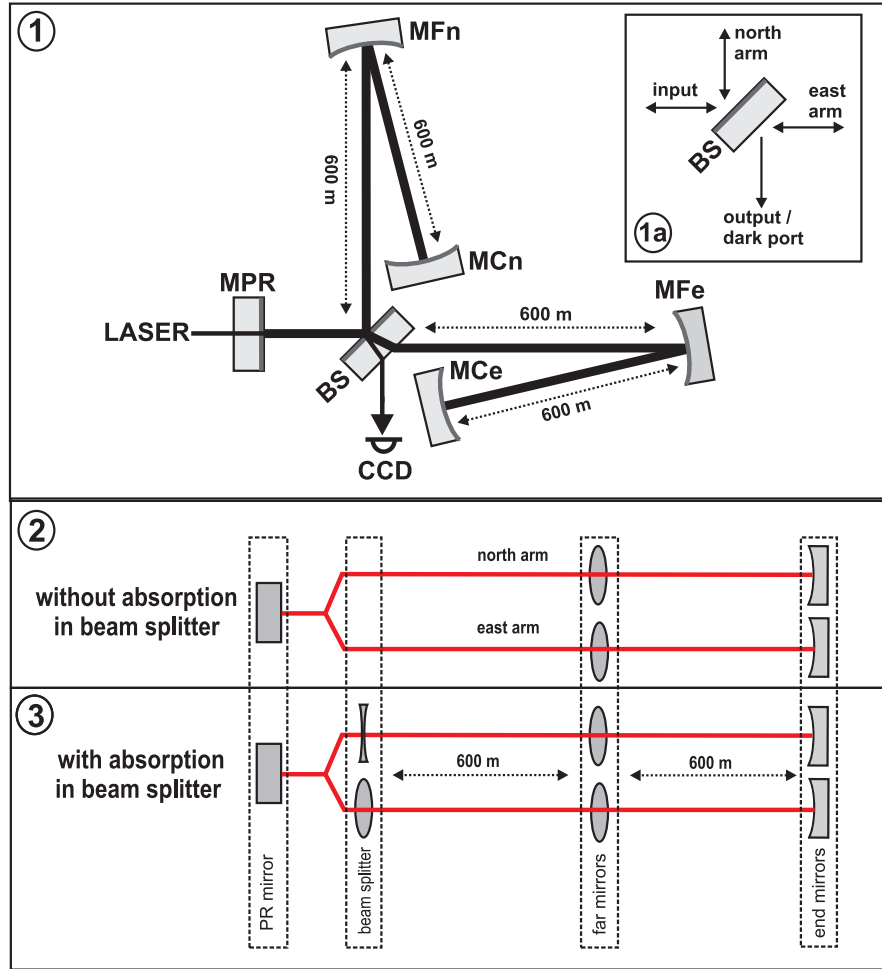


**Figure I.1.:** 1. Simplified optical layout of the GEO 600 main interferometer with folded arms. The Laser beam enters the Michelson interferometer through the power-recycling mirror (MPR), gets split at the beam splitter and transverses the two folded arms, each of 2400 meter round trip length. At the output port of the interferometer the beam pattern is observed using a CCD camera. 2. Optical imaging inside the interferometer arms expressed in an equivalent lens diagram for the case of no absorption inside the beam splitter substrate. 3. Bulk absorption inside the beam splitter can be modelled by an additional convex lens inside the east arm (dominant effect) and an concave lens in the north arm.

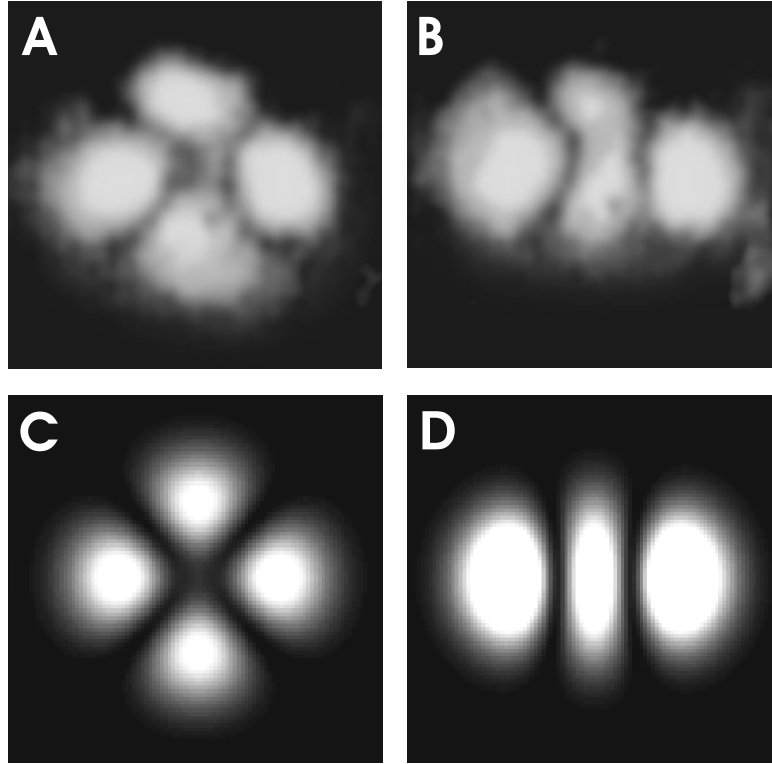


**Figure I.2.:** Beam pattern of the GEO 600 dark port for the case of a power-recycled Michelson interferometer. **A:** Observed dark port pattern for a cold beam splitter. **B:** Observed dark port pattern for a hot beam splitter, i.e., thermal lens present. **C:** Corresponding simulation of the cold beam splitter. **D:** Corresponding simulation of the hot beam splitter, i.e., thermal lens present.

along the  $1/e^2$  point of the intensity distribution [Winkler91].

$$\delta s = 1.3 \cdot \frac{\beta}{4\pi\kappa} \cdot p_a \cdot d \cdot P \quad (\text{I.1})$$

Here  $\kappa$  is the thermal conductivity,  $p_a$  is the absorption per unit length,  $P$  is the light power and  $d$  is the geometrical path length inside the substrate. The temperature dependence of the index of refraction is given by  $\beta = dn/dT$ . Expressing  $\delta s$  by the focal length of the thermal lens induced in the beam splitter as  $f_{\text{therm}} = w^2/2\delta s$ , where  $w$  is the beam radius at the beam splitter, Equation (I.1) transforms to

$$p_a = \frac{4 \cdot \pi}{2.6} \cdot \frac{w^2 \cdot \kappa}{\beta \cdot d \cdot P \cdot f_{\text{therm}}}. \quad (\text{I.2})$$

Up to here we only took absorption inside the beam splitter and the corresponding thermo-refractive effect into account. Of course, in reality the optical imaging in GEO 600 is also slightly influenced by two other effects: the thermal expansion and the absorption of the dielectric coatings. Nevertheless ignoring these two effects still gives a valid upper limit for the bulk absorption of the beam splitter, as we will show in the following sections.

The principle of our absorption measurement relies on the thermally induced change in the difference of the wavefront curvature of the two interferometer arms. Therefore we can neglect absorption at any coating of the four main interferometer mirrors (MFe, MFn, MCn and MCe in Figure I.1) and the corresponding thermal deformation of the mirror surfaces, because this effect would influence the wavefront curvature similarly in both interferometer arms (assuming symmetric absorption in both arms of the interferometer). Nevertheless we can give a rough estimate of the change in radius of curvature of the mirror and the resulting change in the beam diameter caused by coating absorption of the four main interferometer mirrors. In that respect the far mirrors (MFe, MFn) are the most critical ones. Assuming a coating absorption at one of the far mirrors of 2 ppm, would increase the radius of curvature which is 666 m by about 10 cm. The beam diameter  $w$  which is about 8.8 mm would change by roughly 6 microns. Therefore the coating absorption of the main interferometer mirrors is totally negligible.

Assuming symmetrical absorption in the two arms of the interferometer the beam splitter is the only optical component that can change the wavefront curvatures of the two arms differentially. In the case of the bulk absorption it is reasonable to neglect the thermal

expansion because it is first of all ten times smaller than the thermo-refractive effect and second would enhance the strength of the thermal lens.

Finally we have to consider light absorption at the two dielectric coatings of the beam splitter and the related thermal effect. For the east arm these effects can be modelled by adding an additional convex lens, while in the north arm we have to insert a concave lens.

All of the effects discussed above would cause a differential change of the two wavefront curvatures, which would increase the strength of the observed thermal lens and by this lead to a smaller value of the bulk absorption  $p_a$ . Hence Equation I.2 gives a valid upper limit for the bulk absorption inside the beam splitter.

### I.3. Setting an upper limit for the bulk absorption in the GEO 600 beam splitter

To investigate the thermal lensing of the beam splitter, the GEO 600 detector was used in the configuration of a power-recycled Michelson interferometer. To avoid the influence from mode healing [Grote04b], the signal-recycling mirror was misaligned, such that it can just be considered as an attenuator at the dark port. Figure I.2A shows the dark port image for a cold state beam splitter, i.e., immediately after lock acquisition. Figure I.2C shows the result from a FINESSE simulation for the same configuration using our best estimate of the parameters of the GEO 600 detector.

The cross shape of the dark port image is caused by an astigmatic mismatch of the radii of curvature from the two far mirrors (MFe and MFn in figure I.1.1) [Lück04]. Due to this astigmatism the dark port image changes quite strongly with the beam splitter's lensing, which makes it easier to match measurements and simulations. Furthermore this fact also makes our method more accurate in obtaining the focal length of the thermal lens.

Figure I.2B shows the dark port image for the hot state of the beam splitter, after the lens has fully developed and the beam splitter is in thermal equilibrium, which takes about 30 minutes. The result of the corresponding simulation is shown in Figure I.2D. An additional thermal lens with a focal length of  $f_{\text{therm}} = 13 \text{ km}$  best matches the simulation to the observed dark port shape.

The light power inside the beam splitter for this measurement was  $P = 1.4$  kW. The beam radius is  $w = 0.88$  cm and the geometrical path length inside the beam splitter is  $d = 9$  cm. Using these parameters and  $\beta/\kappa = 10^{-5}$  m/W for Suprasil [Takke] Equation (I.2) gives an upper limit for the bulk absorption of the GEO 600 beam splitter of

$$p_a = 0.25 \pm 0.1 \text{ ppm/cm.} \quad (\text{I.3})$$

The main contributions to the error budget are uncertainties in the measurement of the radii of curvature of the far mirrors, the intra-cavity power,  $P$ , and the beam radius  $w$ .

## I.4. Conclusion

A new method was developed to estimate the bulk absorption of beam splitter substrates in a large scale power-recycled Michelson interferometer. Using this method we obtained an upper limit of the bulk absorption of the GEO 600 beam splitter of  $p_a = 0.25 \pm 0.1$  ppm/cm. This is, to the knowledge of the author, the lowest value ever measured for absorption in fused silica at a wavelength of 1064 nm.





# Bibliography

- [Acernese06] *"The Virgo status"*, F Acernese et al., Class. Quantum Grav. **23** No 19 (2006) S635–S642.
- [Adhikari04] *"Sensitivity and Noise Analysis of 4 km Laser Interferometric Gravitational Wave Antennae"*, R Adhikari, PhD thesis (2004) Massachusetts Institute of Technology.
- [Adhikari06] *"Enhanced LIGO"*, R Adhikari, P Fritschel, S Waldman, LIGO Technical Note, LIGO-T060156-01-I (2006)
- [AdvLIGO] <http://www.ligo.caltech.edu/advLIGO/>
- [AdvVIRGO] *"Advanced Virgo White Paper"*, R Flaminio, A Freise, A Gennai, P Hello, P La Penna, G Losurdo, H Lueck, N Man, A Masserot, B Mours, M Punturo, A Spallicci, A Vicer'è for the Virgo Collaboration, 2005
- [Ajith06] *"Robust vetoes for gravitational-wave burst triggers using known instrumental couplings"*, P Ajith, M Hewitson, J R Smith and K A Strain, Class. Quantum Grav. **23** No 20 (2006) 5825–5837.
- [Ajith06a] *"Null-stream veto for two co-located detectors: implementation issues"*, P Ajith, M Hewitson and I S Heng, Class. Quantum Grav. **23** No 19 (2006) S741–S749.
- [Akutsu] *"Veto analysis for gravitational wave burst signals in TAMA300 data using an ALF filter"*, T Akutsu, M Ando, N Kanda, D Tatsumi, S Telada, S Miyoki, M Ohashi and the TAMA Collaboration, Class. Quantum Grav. **23** No 8 (2006) S23–S28.
- [Anderson01] *"Excess power statistic for detection of burst sources of gravitational radiation"*, W G Anderson et al, Phys. Rev. D **63** No 4 (2001) 42003

- [Ando05] "*Current status of the TAMA300 gravitational-wave detector*", Masaki Ando and the TAMA Collaboration, *Class. Quantum Grav.* **22** No 18 (2005) S881–S889.
- [Ansys] ANSYS, Inc., *www.ansys.com*
- [Astone02] "*Resonant mass detectors: present status*", P Astone, *Class. Quantum Grav.* **19** (2002) 1227–1235.
- [Balasubramanian05] "*Results from the first burst hardware injections performed on GEO 600*", R Balasubramanian, H Grote, I S Heng, M Hewitson, H Lück, J R Smith, K A Strain, H Ward and B Willke, *Class. Quantum Grav.* **22** No 14 (2005), 3015–3028.
- [Beauville05] "*A first comparison of search methods for gravitational wave bursts using LIGO and Virgo simulated data*", F Beauville, M-A Bizouard, L Blackburn, L Bosi, P Brady, L Brocco, D Brown, D Buskulic, S Chatterji, N Christensen, A-C Clapson, S Fairhurst, D Grosjean, G Guidi, P Hello, E Katsavounidis, M Knight, A Lazzarini, F Marion, B Mours, F Ricci, A Viceré and M Zanolin (The Joint LIGO/Virgo Working Group), *Class. Quantum Grav.* **22** No 18 (2005) S1293–S1301.
- [Blair] "*The Detection of Gravitational Waves*", D G Blair [Editor]:, Cambridge University Press 1991.
- [Buonanno03] "*Quantum noise in laser-interferometer gravitational-wave detectors with a heterodyne readout scheme*", A Buonanno, Y Chen, and N Mavalvala, *Phys. Rev. D* **67**, 122005, (2003)
- [Candonati04] "*Coherent waveform consistency test for LIGO burst candidates*", L Cadonati, *Class. Quantum Grav.* **21** No 20 (2004) S1695–S1703.
- [Candonati05] "*CorrPower: a cross-correlation-based algorithm for triggered and untriggered gravitational-wave burst searches*", L Cadonati and S Márka, *Class. Quantum Grav.* **22** No 18 (2005) S1159–S1167.
- [Chatterji04] "*Multiresolution techniques for the detection of gravitational-wave bursts*", S Chatterji et al, *Class. Quantum Grav.* **21** (2004) S1809.
- [Clapson05] "*A gravitational wave burst search method based on the S transform*", André-Claude Clapson, Matteo Barsuglia, Marie-Anne Bizouard, Violette Brisson,

- Fabien Cavalier, Michel Davier, Patrice Hello, Stéphane Kreckelberg and Monica Varvella, *Class. Quantum Grav.* **22** No 18 (2005) S1381–S1390.
- [Cutler/Thorne] "*AN OVERVIEW OF GRAVITATIONAL-WAVE SOURCES*", C CUTLER and K S THORNE, submitted to World Scientific on May 17, 2006
- [DiCredico05] "*Gravitational wave burst vetoes in the LIGO S2 and S3 data analyses*", Alessandra Di Credico (for the LIGO Scientific Collaboration), *Class. Quantum Grav.* **22** No 18 (2005) S1051–S1058.
- [Dupuis05] "Bayesian estimation of pulsarparameters from gravitational wave data", R J Dupuis and G Woan, *Phys. Rev. D* **72**, (2005) 102002.
- [Finesse] "*FINESSE 0.99.4, Frequency domain INterferomEter Simulation SoftwarE*", Andreas Freise, <http://www.rzg.mpg.de/adf/download/Finesse-0.99.4.pdf>.
- [Freise03] "*The Next Generation of Interferometry: Multi-Frequency Optical Modelling, Control Concepts and Implementation*", A Freise, Dissertation, Universität Hannover (2003).
- [Freise04] "*Frequency-domain interferometer simulation with higher-order spatial modes*", A Freise et al, *Class. Quantum Grav.* **21** (2004) S1067–1074.
- [Giaime] "*Adavnced LIGO*", J Giaime et al, Amaldi6 Conference (2005).
- [Gossler02] "*The modecleaner system and suspension aspects of GEO 600*", S Gossler, M M Casey, A Freise, H Grote, H Luck, P McNamara, M V Plissi, D I Robertson, N A Robertson, K Skeldon, K A Strain, C I Torrie, H Ward, B Willke, J Hough and K Danzmann, *Class. Quantum Grav.* **19** No 7 (2002) 1835–1842.
- [Gossler04] "*The suspension systems of the interferometric gravitational-wave detector GEO600*", S Goßler, Dissertation, Universität Hannover (2004).
- [Grote] "*High-power, low-noise, and multiply resonant photodetector for interferometric gravitational wave detectors.*", H Grote, submitted to *Rev. of Sci. Instruments*.
- [Grote03] "*Making it Work: Second Generation Interferometry in GEO600 !*", H Grote, PhD thesis, Hannover 2003.
- [Grote04a] "*Alignment control of GEO 600*", H Grote et al, 2004, *Class. Quantum Grav.* **21**, S441–449.

- [Grote04b] *"Dual recycling for GEO 600"*, H Grote et al, 2004, Class. Quantum Grav. **21**, S473–480.
- [Grote05] *"The Status of GEO 600"*, H Grote et al, Class. Quantum Grav. **22** (2005) S193–S198.
- [Hanna06] *"Reducing gravitational wave false alarms using signals at the antisymmetric port in LIGO detectors"*, C R Hanna (for the LIGO Scientific Collaboration), Class. Quantum Grav. **23** No 8 (2006) S17–S22.
- [Harms06] *"Shot Noise and Heterodyne Detectors"*, J Harms, internal document, 2006
- [Heraeus] *"Quarzglas für die Optik, Daten und Eigenschaften"*, Heraeus Quarzglas GmbH & Co.KG, Hanau (1999).
- [Heinzel98] *"Experimental Demonstration of a Suspended Dual Recycling Interferometer for Gravitational Wave Detection"*, G. Heinzel, K.A. Strain, J. Mizuno, K.D. Skeldon, B. Willke, W. Winkler, R. Schilling, A. Rüdiger, and K. Danzmann, Phys. Rev. Lett. **81** (1998) 5493–5496.
- [Heng03] *"Methods for multi-detector burst gravitational wave search"*, I S Heng, F Salemi and A Ortolan, Class. Quantum Grav. **20** No 17 (2003) S617–S622.
- [Heng04] *"First steps towards characterizing the hierarchical algorithm for curves and ridges pipeline"*, I S Heng, R Balasubramanian, B S Sathyaprakash and B F Schutz, Class. Quantum Grav. **21** No 5 (2004) S821–S826.
- [Hewitson04] *"Principles of calibrating the dual-recycled GEO 600"*, M Hewitson et al, Rev. Sci. Instrum., **75** (2004) 4702
- [Hewitson04a] *"On aspects of characterising and calibrating the interferometric gravitational wave detector, GEO 600"*, M Hewitson, PhD thesis, University of Glasgow, 2004.
- [Hewitson05] *"Optimal time-domain combination of the two calibrated output quadratures of GEO 600"*, M Hewitson et al, Class. Quantum Grav. **22** (2005) 4253–4261
- [Hewitson05a] *"Using the null-stream of GEO 600 to veto transient events in the detector output"*, M Hewitson and P Ajith, Class. Quantum Grav. **22** No 22 (2005) 4903–4912.

- 
- [Hild04] "*A new calibration method*", S Hild, presentation at the GEO meeting, April 2004, Hannover.
- [Hild06a] "*Towards gravitational wave astronomy: Commissioning and characterization of GEO600*", S Hild, H Grote, J R Smith, M Hewitson, J. Phys.: Conf. Ser. **32** (2006) 66–73.
- [Hild06b] "*Measurement of a low-absorption sample of OH-reduced fused silica*", S Hild, H Lück, W Winkler, K Strain, H Grote, JR Smith, M Malec, M Hewitson, B Willke, J Hough and K Danzmann, Appl. Opt. 45, 7269-7272 (2006).
- [Hild06c] "*The status of GEO 600*", S Hild (for the LIGO Scientific Collaboration), Class. Quantum Grav. **23** No 19 (2006) S643-S651.
- [Hild07a] "*A statistical veto method using auxiliary channels sensitive to gravitational wave signals*", S Hild, P Ajith and M Hewitsion, submitted to Class. Quantum Grav.
- [Hild07b] "*Demonstration and comparison of tuned and detuned signal recycling in a large-scale gravitational wave detector*", S Hild, H Grote, M Hewtison, H Lück, J R Smith, K A Strain, B Willke and K Danzmann, submitted to Class. Quantum Grav.
- [Hulse] "*The discovery of the binary pulsar (PSR 1913+16)*", R A Hulse, Rev. Mod. Phys., 66, 699, (1994).
- [ILIAS06] "*2nd Report on WG1: Antennas commissioning and characterization*", M Barsuglia, A Freise, I Fiori, H Grote, H Heitmann, S Hild, P LaPenna, G Losurdo, H Lück, J Smith, L Taffarelli, G Vajente, M Visco, B Willke, 2006.
- [Klimenko04] "*A wavelet method for detection of gravitational wave bursts*", S Klimenko and G Mitselmakher, Class. Quantum Grav. **21** (2004) S1819–S1830.
- [Koetter03] "*PQMon: a powerful veto for burst events*", K Kötter, I S Heng, M Hewitson, K A Strain, G Woan and H Ward, Class. Quantum Grav. **20** No 17 (2003) S895-S902.
- [Kuroda06] "*The status of LCGT*", K Kuroda (and the LCGT Collaboration), Class. Quantum Grav. **23** No 8 (2006) S215–S221

- [Lawrence02] "*Adaptive thermal compensation of test masses in advanced LIGO*", R Lawrence et al, 2002, Class. Quantum Grav. **19** S1803–1809.
- [LIGO05] LLO electronic log 2005-08-19 (B O Reilly, personal communication).
- [Loriette03] "*Absorption of low-loss optical materials measured at 1064 nm by a position-modulated collinear photothermal detection technique*", V Loriette and C Boccara, 2003, Applied Optics, **42** 649–656.
- [Lück04] "*Thermal correction of the radii of curvature of mirrors for GEO 600*", H Lück et al, Class. Quantum Grav. **21** (2004), S985–989.
- [Lück06] "*Status of the GEO600 detector*", H Lück et al, Class. Quantum Grav. **23** S71–S78 (2006).
- [Mantone06] "*Benefits of Artificially Generated Gravity Gradients for Interferometric Gravitational-Wave Detectors*", L Mantone et al, in preparation.
- [Malec06] "*Commissioning of advanced, dual-recycled gravitational-wave detectors: simulations of complex optical systems guided by the phasor picture*", M Malec, PhD thesis, Hannover 2006.
- [Meers] "*Recycling in laser-interferometric gravitational-wave detectors*", B J Meers: , Phys. Rev. **D 38** (1988) 2317–2326.
- [Mossavi06] "*A photon pressure calibrator for the GEO 600 gravitational wave detector*", K Mossavi, M Hewitson, S Hild, F Seifert, U Weiland, J R Smith, H Luck, H Grote, B Willke, K Danzmann, Phys. Letters A **353** (2006) 1–3.
- [Ottaway06] "*In-situ measurement of absorption in high power interferometers using beam diameter measurements*", D Ottaway et al, Optics Letters, 31 (4) pp. 450–452, 2006.
- [Rakhmanov05] "*A cross-correlation method for burst searches with networks of misaligned gravitational-wave detectors*", M Rakhmanov and S Klimenko, Class. Quantum Grav. **22** No 18 (2005) S1311–S1320.
- [Rowan/Hough] "*Gravitational Wave Detection by Interferometry (Ground and Space)*", S Rowan, J Hough:, Living Rev. Relativity, 3, (2000), 3. [Online Article]: cited on 9.9.2003, <http://www.livingreviews.org/Articles/Volumes3/2000-3hough/>.

- [Saulson] *"Fundamentals of Interferometric Gravitational Wave Detectors"*, P R Saulson, World Scientific Publishing, 1994.
- [Savage06] R Savage, P Kalmus, E Goetz, personal communication.
- [Schnupp] L Schnupp, Presentation at European Collaboration Meeting on Interferometric Detection of Gravitational Waves, Sorrent, 1988.
- [Sigg04] *"Commissioning of LIGO detectors"*, D Sigg, Class. Quantum Grav. **21** (2004) S409–S415.
- [Smith04] *"Mechanical quality factor measurements of monolithically suspended fused silica test masses of the GEO 600 gravitational wave detector"*, J R Smith, G Cagnoli, D R M Crooks, M M Fejer, S Goßler, H Lück, S Rowan, J Hough and K Danzmann, Class. Quantum Grav. **21** (2004) S1091–S1098.
- [Smith06] *"Formulation of Instrument Noise Analysis Techniques and Their Use in the Commissioning of the Gravitational Wave Observatory, GEO600"*, J R Smith, PhD thesis, Hannover 2006.
- [Strain91] *"Experimental Demonstration of Dual Recycling for Interferometric Gravitational-Wave Detectors"*, K. Strain, B. Meers, Phys. Rev. Lett. **66** (1991) 1391–1394.
- [Strain94] *"Thermal lensing in recycling interferometric gravitational wave detectors"*, K Strain et al, 1994, Phys. Let. A, **194**, 124–132.
- [Strain] K A Strain, personal communication.
- [Stuver06] *"A first comparison of SLOPE and other LIGO burst event trigger generators"*, Amber L Stuver and Lee Samuel Finn, Class. Quantum Grav. **23** No 19 (2006) S733-S740.
- [Takahaschi04] *"Direct measurement of the scattered light effect on the sensitivity in TAMA300"*, R Takahashi, K Arai, S Kawamura and M R Smith, Phys. rev. D, (70) No 6 (2004) 062003.1–062003.4
- [Takke] Personal communication with R. Takke from Heraeus.
- [Taylor] *"Binary pulsars and relativistic gravity"*, J H Taylor, Rev. Mod. Phys. 66, (1994) 711.

- [Vinet96] "*Scattered light noise in gravitational wave interferometric detectors: Coherent effects*", J Y Vinet, V Brisson, S Braccini, Phys. Rev. D **54**, (1996) 1276 – 1286
- [Waldman06] "*Status of LIGO at the start of the fifth science run*", Samuel J Waldman (for the LIGO Science Collaboration), Class. Quantum Grav. **23** No 19 (2006) S653-S660.
- [Weber] "*Evidence for discovery of gravitational radiation*", J. Weber Phys. Rev. Lett. **25** (1970) 180.
- [Weiland04] "*Preparing for gravitational wave astronomy: A verification of the GEO600 detection chain by generation, injection, and extraction of continuous signals*", U Weiland, PhD thesis, Hannover 2004.
- [Wen05] "*Coherent network detection of gravitational waves: the redundancy veto*", L Wen and B F Schutz, Class. Quantum Grav. **22** No 18 (2005) S1321-S1335.
- [Willke04] "*Status of GEO 600*", B Willke et al, Class. Quantum Grav. **21** S417-S423 (2004).
- [Willke06] "*The GEO HF project*", B Willke et al, Class. Quantum Grav. **23** S207–S214 (2006).
- [Winkler] "*Eine optische Verzögerungsleitung für ein Breitband-Gravitationswellenexperiment*", W Winkler, Doktorarbeit, Max-Planck-Institut für Quantenoptik, 1983.
- [Winkler91] "*Heating by optical absorption and the performance of interferometric gravitational wave detectors*", W Winkler et al, 1991, Phys. Rev. A, **44**, 7022.



## Acknowledgement

Joining the GEO-project, then seeing and feeling it grow and proceed was an exciting experience for me and I would like to thank all the people who contributed to GEO 600.

First I would like to thank Karsten Danzman for giving me the chance to work right at the core of the GEO 600 detector. It is unusual for a nearly unexperienced student to get the opportunity to ‘play’ with such an exciting device as GEO 600.

The people who contributed most to this work are the members of the GEO commissioning team: Hartmut Grote, Harald Lück, Martin Hewitson, Joshua Smith, Ken Strain and Benno Willke have been for me an infinite supply of motivation, creativity and knowledge. I am happy and proud to be a member of such a great team. I’m very grateful to these people for sharing their knowledge and work with me, - nearly everything I know about building, commissioning and running a gravitational wave detector I learned from these bunch of scientists. Finally I want to add that working at GEO was not only scientifically interesting, but also always good fun and I enjoyed the familiar atmosphere in Ruthe very much. Thank you !!!

Furthermore I would like to thank many people from outside the Ruthe-team who contributed to this work: Keita Kawabe for introducing me to the ‘real-live’ interferometry at the Garching prototype interferometer. Stefan Goßler for teaching me how to build a proper suspension. Andreas Freise for many fruitful discussions and his help in doing simulations. Iain Martin, Stuard Reid and Jim Hough for providing the FEM analysis of the photon pressure induced mirror deformation. Peter Kalmus, Rick Savage and Brian O’Reilly for interesting discussions about the photon pressure calibrators used in GEO and LIGO. Simon Chelkowski for motivating me to use 3D AutoCAD. Ajith Parameswaran for giving me a background in veto analysis. Andreas Weidner and Heiko zur Mühlen for help in building electronics. Walter Winkler and Roland Schilling for sharing their knowledge with me and answering endless rows of questions. All members of the ILIAS Working group 1 for the interesting discussions and the nice atmosphere at all the meetings we had. Finally I thank Andre Thuering, not only for sharing an office in Hannover with me, but also for always being a friend.

For proof reading of this thesis I thank: Andreas Freise, Jan Harms, Hartmut Grote, Martin Hewitson, Harald Lück, Kasem Mossavi, Joshua Smith, Ken Strain and Benno Willke. However, I am of course responsible for all remaining mistakes in this thesis.

I am deeply grateful to Marion for all her patience and love.

# Curriculum vitae

Stefan Hild  
Meterstrasse 6  
30169 Hannover

Born on April 1<sup>st</sup>, 1978 in Celle, Germany  
Marital status: unmarried

12. 2003 – to date	Scientific Assistant, Max-Planck-Institut für Gravitationsphysik (AEI), Hannover
12. 2003 – 2. 2007	Doctoral Studies in Physics, University of Hannover
11. 2003	Physik Diplom, University of Hannover (Thermally tunable Signal-Recycling for GEO 600)
10. 2002 – 02.2003	Max-Planck Institute für Quantenoptik, Garching (Internship on the Garching prototype)
10. 1998 – 11.2003	Diploma Studies in Physics, University of Hannover
08. 1997 – 09.1998	Alternative civilian service
06. 1997	Abitur
08. 1990 – 06.1997	Hölty Gymnasium Celle
08. 1988 – 07.1990	Orientierungsstufe Ovelgönne
08. 1984 – 07.1988	Grundschule Hambühren



# Publications

## 2007

- S Hild, H Grote, M Hewitson, H Lück, JR Smith, KA Strain, B Willke and K Danzmann, "Demonstration and comparison of tuned and detuned signal recycling in a large-scale gravitational wave detector", accepted for publication in Class. Quantum Grav.

## 2006

- S Hild for the LIGO Scientific Collaboration, "The Status of GEO600", Class. Quantum Grav. 23 S643-S651 (2006).
- S Hild, H Lück, W Winkler, K Strain, H Grote, J Smith, M Malec, M Hewitson, B Willke, J Hough and K Danzmann, "Measurement of a low-absorption sample of OH-reduced fused silica", Appl. Opt. 45, 7269-7272 (2006).
- JR Smith, P Ajith, H Grote, M Hewitson, S Hild, H Lück, KA Strain, B Willke, J Hough and K Danzmann, "Linear projection of technical noise for interferometric gravitational-wave detectors", Class. Quantum Grav. 23 527-537 (2006).
- K Mossavi, M Hewitson, S Hild, F Seifert, U Weiland, JR Smith, H Lück, H Grote, B Willke and K Danzmann, "A photon pressure calibrator for the GEO600 gravitational wave detector", Phys. Lett. A 353 1-3 (2006).
- S Hild, H Grote, JR Smith and M Hewitson, "Towards gravitational wave astronomy: Commissioning and characterization of GEO600", J. Phys.: Conf. Ser. 32 66-73 (2006).
- H Lück et al, "Status of the GEO600 detector", Class. Quantum Grav. 23 S71-S78 (2006).

- B Willke et al, "The GEO HF project", *Class. Quantum Grav.* 23 S207-S214 (2006).
- The LIGO Scientific Collaboration, "Joint LIGO and TAMA300 search for gravitational waves from inspiralling neutron star binaries", *Phys. Rev. D* 73, 102002 (2006).
- The LIGO Scientific Collaboration, "Search for gravitational waves from binary black hole inspirals in LIGO data", *Phys. Rev. D* 73, 062001 (2006).

## 2005

- JR Smith, H Grote, M Hewitson, S Hild, H Lück, M Parsons, KA Strain and B Willke, "Feedforward correction of mirror misalignment fluctuations for the GEO 600 gravitational wave detector", *Class. Quantum Grav.* 22 3093-3104 (2005).
- M Hewitson, H Grote, S Hild, H Lück, P Ajith, JR Smith, KA Strain, B Willke and G Woan, "Optimal time-domain combination of the two calibrated output quadratures of GEO600", *Class. Quantum Grav.* 22 4253-4261 (2005).
- M Hewitson for the LIGO Scientific Collaboration, "Preparing GEO 600 for gravitational wave astronomy: a status report", *Class. Quantum Grav.* 22 S891-S900 (2005).
- H Grote et al, "The status of GEO 600", *Class. Quantum Grav.* 22 S193-S198 (2005).
- The LIGO Scientific Collaboration, "Search for Gravitational Waves Associated with the Gamma Ray Burst GRB030329 Using the LIGO Detectors", *Phys. Rev. D* 72, 042002 (2005).
- The LIGO Scientific Collaboration, "First All-sky Upper Limits from LIGO on the Strength of Periodic Gravitational Waves Using the Hough Transform", *Phys. Rev. D* 72, 102004 (2005).
- The LIGO Scientific Collaboration, "Limits on Gravitational-Wave Emission from Selected Pulsars Using LIGO Data", *Phys. Rev. Lett.* 94, 181103 (2005).
- The LIGO Scientific Collaboration, "Search for Gravitational Waves from Galactic and Extra-galactic Binary Neutron Stars", *Phys. Rev. D* 72, 082001 (2005).

- The LIGO Scientific Collaboration, "Search for Gravitational Waves from Primordial Black Hole Binary Coalescences in the Galactic Halo", Phys. Rev. D 72, 082002 (2005).
- The LIGO Scientific Collaboration, "Upper Limits on Gravitational Wave Bursts in LIGO's Second Science Run", Phys. Rev. D 72, 062001 (2005).
- The LIGO Scientific Collaboration, "Upper limits from the LIGO and TAMA detectors on the rate of gravitational-wave bursts", Phys. Rev. D 72, 122004 (2005).

## 2004

- JR Smith et al, "Commissioning, characterization, and operation of the dual-recycled GEO 600", Class. Quantum Grav. 21 S1737-S1745 (2004).
- B Willke et al, "Status of GEO 600", Class. Quantum Grav. 21 S417-S423 (2004).
- KA Strain et al, "The status of GEO 600", Optical Fabrication, Metrology, and Material Advancements for Telescopes. Edited by Atad-Ettinger, Eli; Dierickx, Philippe. Proceedings of the SPIE, Volume 5500, pp. 25-36 (2004).
- H Lück, A Freise, S Goßler, S Hild, K Kawabe and K Danzmann, "Thermal correction of the radii of curvature of mirrors for GEO 600 ", Class. Quantum Grav. 21 S985-S989 (2004)

## 2003

- S Hild, "Thermisch durchstimmbares Signal-Recycling für den Gravitationswellendetektor GEO600", Diploma Thesis, University Hannover, 2003.

## Submitted

- S Hild, P Ajith and M Hewitson, "A statistical veto method using auxiliary channels sensitive to gravitational wave signals", submitted to Class. Quantum Grav.

